FAU-PI1-DISS-07-001

Design studies for the KM3NeT Neutrino Telescope

Den Naturwissenschaftlichen Fakultäten
der Friedrich-Alexander-Universität Erlangen-Nürnberg
zur
Erlangung des Doktorgrades

vorgelegt von
Sebastian Kuch

aus Nürnberg

Als Dissertation genehmigt
von den Naturwissenschaftlichen Fakultäten
der Universität Erlangen-Nürnberg.

Tag der mündlichen Prüfung: 18. Juli 2007

Vorsitzender der Prüfungskomission: Prof. Dr. Eberhard Bänsch

Erstberichterstatter: Prof. Dr. Ulrich F. Katz

Zweitberichterstatter: Prof. Dr. Els DeWolf

Zusammenfassung

Die Entdeckung der kosmischen Strahlung durch Viktor Hess 1912 markiert den Beginn der Astroteilchenphysik. Das Ziel dieser Disziplin ist die Erforschung kosmischer Phänomene durch die Detektion von kosmischen Teilchen auf der Erde. Dies beginnt bei den Protonen und leichten Kernen der kosmischen Strahlung selbst, die in Luftschauerexperimenten nachgewiesen werden. Diese Experimente liefern Informationen über die Zusammensetzung und das Energiespektrum der kosmischen Strahlung. Sie konnten jedoch bis jetzt keine Informationen über den Ursprung ihrer hochenergetischen Teilchen liefern, da diese geladen sind und, außer bei den höchsten Energien ($E > 10^{19}\,\mathrm{eV}$) durch das galaktische Magnetfeld abgelenkt werden, wodurch sie ihre Richtungsinformation verlieren.

Vielversprechender ist hier das Neutrino, das mangels Ladung nicht in elektromagnetischen Feldern abgelenkt wird. Da Neutrinos nur schwach wechselwirken, werden sie im interstellaren Medium oder kosmischen Staubwolken kaum absorbiert. Weiterhin erlauben Neutrinos dem Beobachter ins Zentrum von heissen und dichten Objekten zu blicken, die für elektromagnetische Strahlung undurchlässig sind. Wenn ein Objekt Protonen auf die Energien der kosmischen Strahlung beschleunigt wechselwirken diese mit der Materie oder der Strahlung um das Objekt, wobei über Zwischenschritte geladene Pionen erzeugt werden, bei deren Zerfall Myon- und Elektron-Neutrinos entstehen. Die Entdeckung von kosmischen Neutrinoquellen käme also der Entdeckung des Ursprungs der kosmischen Strahlung gleich. Es gibt viele Kandidaten für solche individuellen Quellen hochenergetischer ($E > 1\,\mathrm{GeV}$) kosmischer Neutrinos, wie z.B. Aktive Galaktische Kerne, Supernova-Überreste oder sogenannte Gamma-Ray-Bursts, die auch Kandidaten für Quellen der kosmischen Strahlung sind.

Die gleichen Eigenschaften, die das Neutrino zu einem idealen Botenteilchen für die Astroteilchenphysik machen, erschweren seine Detektion. Durch den sehr geringen Wirkungsquerschnitt werden riesige Targetvolumina benötigt. Für Neutrinoteleskope werden deshalb natürliche Volumina wie das Wasser in der Tiefsee und das antarktische Eis instrumentiert. Interagiert ein Neutrino mit den Nukleonen des Targetmaterials, so entstehen geladene Sekundärteilchen, die sich mit einer Geschwindigkeit bewegen, die grösser ist als die Lichtgeschwindigkeit im Detektormedium. Deshalb senden diese Teilchen Cherenkov-Photonen aus, die Hilfe von Lichtsensoren (Photomultipliern, PMn) detektiert werden. Aus den Ankunftszeiten und Amplituden der Photonen-Treffer in den PMn kann die Richtung und die Energie des einfallenden Neutrinos rekonstruiert werden. Ein Neutrinoteleskop ist also im wesentlichen eine dreidimensionale Anordung von Photosensoren. Die Signatur einer Neutrinoreaktion im Detektor hängt vom Neutrino-*flavour* ab. Am bedeutendsten sind hierbei Myon-Neutrinos, die bei ihrer Wechselwirkung (geladener Strom)

Myonen erzeugen (und einen hadronischen Schauer). Myonen haben in Wasser und Eis eine sehr große Reichweite ($> 1\,\mathrm{km}$ für $E > 1\,\mathrm{TeV}$) und erzeugen lange Spuren von Cherenkov-Licht, was eine Rekonstruktion der Richtung erleichtert. Die große Reichweite ermöglicht auch die Detektion von Myonen, die weit außerhalb des Detektorvolumens erzeugt wurden. Andererseits ist die Energierekonstruktion schwierig, da unbekannt ist welcher Teil der Myonenspur ausserhalb des Detektors verlief. Bei den Wechselwirkungen von Elektron- und Tau-Neutrinos, sowie bei allen Wechselwirkungen über den neutralen Strom entstehen hadronische und elektromagnetsiche Schauer, die ihre Energie schnell an das Medium verlieren und deshalb Reichweiten von nur etwa 10 m haben. Dies erschwert die Richtungsrekonstruktion. Für Schauer im Innern des Detektorvolumens ist allerdings die Energierekonstruktion einfacher, da die gesamte Energie des Schauers im Detektor deponiert wird.

Weltweit sind einige Neutrinoteleskope im Betrieb oder im Aufbau. Am Südpol befindet sich das AMANDA-Teleskop das schon seit Ende der neunziger Jahre Daten nimmt. Im russischen Baikal-See befindet sich das Baikal-Experiment, das erste funktionierende Wasser-Neutrinoteleskop. Im Mittelmeer ist das ANTARES-Experiment im Aufbau vor der südfranzösischen Küste und wird 2007 fertiggestellt sein. Das griechische NESTOR-Projekt hat bereits erfolgreich Prototypen getestet und mit ihnen erste Daten genommen. Diese Experimente demonstrieren die Funktionalität der Technolgie von Neutrinoteleskopen in der Tiefsee (oder dem tiefen Eis). Dennoch ist bereits jetzt absehbar, das die Volumina dieser Teleskope zu klein sind, um das volle Potential der Neutrinoastronomie auszuschöpfen. Detektoren mit einem intrumentierten Volumen von (mindestens) einem Kubikkilometer werden dazu nötig sein.

Am Südpol hat der Bau des Nachfolgers des AMANDA-Teleskops, des IceCube Detektors, bereits begonnen. Im Mittelmeer betreibt das italienische NEMO-Projekt seit einiger Zeit Vorstudien für ein Kubikkilometer-Teleskop. Da Neutrino-Teleskope die Erde als Abschirmung gegen atmosphärischen Untergrund (Myonen aus Luftschauern) benötigen, sind zwei Teleskope notwendig, um den gesamten Himmel abzudecken, eines auf der Nord- und eines auf der Südhalbkugel. Der schnelle Fortschritt des IceCube-Projekts legt die Zeitskala für ein Kubikkilometer-Experiment auf der Nordhalbkugel fest. Deshalb haben sich die europäischen Neutrino Teleskop-Experimente ANTARES, NEMO und NESTOR zusammengeschlossen mit dem Ziel einer Designstudie für ein Kubikkilometer-Neutrinoteleskop im Mittelmeer, dem KM3NeT-Projekt.

Diese Designstudie erfordert zunächst intensive Simulationen zur Optimierung des Detektordesigns. Da bis jetzt keine dedizierte KM3NeT-Software existiert und der Zeitplan der Designstudie knapp ist, wurde in dieser Arbeit die ANTARES-Software verwendet. Die NEMO-Kollaboration verwendet diese Software bereits seit einiger Zeit für die Simulation des NEMO Detektor-Konzepts, was ihre Anwendbarkeit auf größere Geometrien beweist. Die ANTARES- Simulationskette enthält im Prinzip alle für eine breite Studie nötigen Komponenten. Dies beginnt bei der Erzeugung eines Software-Modells des zu simulierenden Detektors. Dies besitzt im wesentlichen zwei Ebenen. Die kleinste Einheit ist das sogenannte Stockwerk, eine lokale Anordnung von PMn mit definierten Eigenschaften wie Richtung und Ort der Photomultiplier im Stockwerk, sowie deren technische Daten. Die zweite Ebene ist die Geometrie, also die Anordnung dieser Stockwerke im instrumentierten Volumen. Die technischen Details der Positionierung der Stockwerke, also die

Frage ob sie an Kabeln (strings, ANTARES) oder semifesten Türmen (towers, NEMO, NESTOR) in der Tiefsee verankert werden, wurden hier nicht betrachtet, da für eine Abschätzung der Leistung eines Detektors zunächst nur die Positionen und Eigenschaften der PM relevant sind. Der nächste Schritt in der Simulationskette ist die Simulation der einfallenden Neutrinos und ihrer Wechselwirkungen im Medium. Die entstehenden geladenen Sekundärteilchen werden anschliessend zum bzw. durch den Detektor propagiert. Hier wird die Cherenkov- Lichterzeugung simuliert und die Antwort des Detektors in Form von Photon-Treffern in PMn (Zeiten und Amplituden) bestimmt. Aus den Treffern wird schließlich mit Hilfe eines Rekonstruktionsalgorithmus die Richtung des Neutrinos bestimmt. Die meisten dieser Komponenten sind mit geringen technischen Änderungen auf eine Vielzahl verschiedener Detektor-Konzepte anwendbar. Die einzige Ausnahme ist der Rekonstruktionsalgorithmus, der trotz einiger Änderungen, auf die ANTARES-Konfiguration optimiert ist. Eine gleichartige Effizienz für die verschiedenen untersuchten Detektor-Konfigurationen ist daher unwahrscheinlich.

Für diese Studie wurden ausschliesslich Myon-Neutrinos im Energiebereich zwischen 10 GeV und 10 PeV simuliert. Dieser Energiebereich deckt das gesamte Spektrum der Physikziele von Neutrinoteleskopen ab. Beginnend bei der Suche nach Neutrinos aus den Annihilationen von dunkler Materie (WIMPs) in Schwerkraftzentren wie der Sonne ($E < 1\,\text{TeV}$), über die Suche nach individuellen Quellen kosmischer Neutrinos ($1\,\text{TeV} < E < 100\,\text{TeV}$), bis zur Suche nach Neutrinos aus dem diffusen Fluss aller kosmischen Neutrinoquellen ($E > 100\,\text{TeV}$). Der optische Untergrund (aus ^{40}K-Zerfällen und Biolumineszenz) wurde mit einer Rate von 90.9 Hz pro cm^2 Photokathodenfläche simuliert (entspricht 40kHz pro 10PM). Für die übrigen Umgebungsparameter wurden die ANTARES Standardwerte verwendet.

Um die verschiedenen Detektor-Konfigurationen vergleichen zu können, wurde die Effektive Neutrinofläche berechnet, die ein Maß für die Effizienz des Detektors ist und die einfache Berechnung von Ereignisraten für gegebene Neutrinoflüsse ermöglicht. Weiterhin wurde die Winkelauflösung bestimmt (der Median der Verteilung der Winkelabweichung zwischen 'wahrem' Neutrino und rekonstruiertem Myon), was die Anwendung des Rekonstruktionsalgorithmus erfordert. Um möglichst unabängig von der Rekonstruktion zu bleiben, wurde ein Satz von Kriterien definiert, der es erlaubt, das Potential eines Detektormodells einzuschätzen. Die wichtigsten sind das sogenannte *minimal*-Kriterium welches das absolute Minimum an Treffern in PMn verlangt, das für eine Rekonstruktion der Myon-Spur nötig ist, das *selected*-Kriterium, das auf der Rekonstruktion basiert und das *moderate*-Kriterium das mindestens 6 (Signal-)Treffer in 6 verschiedenen Stockwerken verlangt. Ersteres ist die optimistischste (und wahrscheinlich unrealistischste) Option, das *selected*-Kriterium stellt den schlechtesten Fall dar, während die *moderate*-Bedingung die wahrscheinlich realistischste Abschätzung ist.

Zunächst wurden verschiedene Photomultiplier-Konfigurationen untersucht. Im wesentlichen handelt es sich dabei um Anordnungen von drei verschiedenen PM-Typen. Der in ANTARES und AMANDA verwendete 10PM (Hamamatsu R7081-20), ein sehr viel kleinerer 3PM (Photonis XP53X2), der eine bessere Quanteneffizienz, einen kleineren Transit Time Spread (TTS) und bessere Photonseperation bietet, sowie ein 20PM. Für den Vergleich der verschiedenen Anordnungen (schematisch dargestellt in Abb. 1) wurden die jeweiligen Stockwerke in einem homogenen quaderförmigen Gitter mit horizontalen

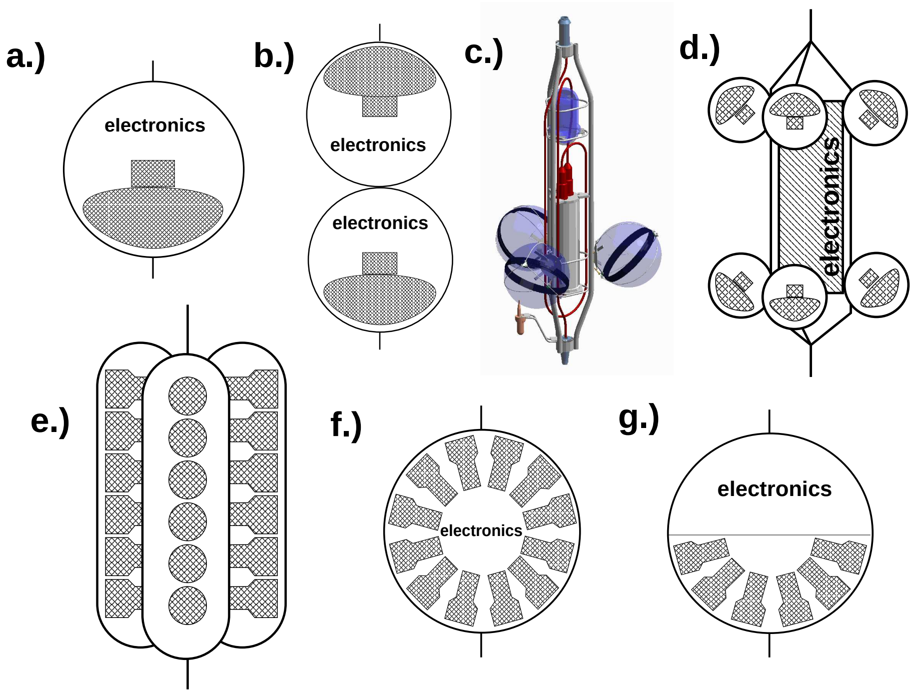

Abbildung 1: Schematische Darstellung der simulierten Stockwerktypen. a.) Stockwerk mit einem einzelnen 10öder 20PM; b.) Stockwerk mit 2 10PMn; c.) ANTARES Stockwerk, 10öder 20PM; d.) Zwillings-ANTARES Stockwerk mit sechs 10PMn; e.) Multi-PM Zylinder-Stockwerk mit 36 3PMn; f.) Multi-PM Kugel-Stockwerk mit 36 oder 42 3PMn; g.) Multi-PM Kugel-Stockwerk mit 21 3PMn.

(string-) und vertikalen (Stockwerk-)abständen von 63 m angeordnet. Das Volumen dieser Geometrie beträgt nahezu genau einen Kubikkilometer, der mit 4840 Stockwerken instrumentiert ist. Zusätzlich wurde für alle Stockwerk-Typen die deutlich weniger oder mehr Photokathodenfläche besitzen eine zusätzliche Geometrie erzeugt, wobei die Anzahl der Stockwerke pro ßtringßo angepaßt wurde, dass die gesamte Photokathodenfläche einem Referenzdetektor entspricht. Diese Konfigurationen wurden *candidate*-Detektoren genannt. Dem zugrunde liegt die Annahme, dass die Kosten für ein Neutrinoteleskop im wesentlichen proportional zur Photokathodenfläche sind. Als Referenzstockwerk wurde das Standard ANTARES-Stockwerk verwendet.

Wie zu erwarten, sind Detektoren mit größerer Photokathodenfläche im allgemeinen besser (mehr effektive Fläche, bessere Winkelauflösung). Detektoren mit nur einem PM pro Stockwerk verlieren bei der Rekonstruktion drastisch an Effizienz, da der Algorithmus unter anderem lokale Koinzidenzen benötigt, also Treffer in mehreren PMn eines Stockwerkes innerhalb eines definierten Zeitfensters. Dies dient der Unterdrückung des optischen Untergrundes. bei einem Stockwerk mit einem einzelnen PM gibt es offensichtlich keine lokalen Koinzidenzen. Zwar können auch Treffer mit Amplituden über einer definierten Schwelle verwendet werden, doch ist deren Anzahl im Allgemeinen zu klein. Da lokale Koinzidenzen mit großer Wahrscheinlichkeit auch bei einer dedizierten KM3NeT-

Rekonstruktionsstrategie verwendet werden, sind Stockwerke mit einzelnen PMn stark im Nachteil. Die Stockwerke mit 3PMn, 36 davon in verteilt auf drei Glaszylinder oder 42 bzw. 21 in einer Glasskugel pro Stockwerk, zeigen unter etwa 10 TeV zu niedrigen Energien deutlich ansteigende effektive Flächen. Dies wird vor allen Dingen durch die höhere Quanteneffizienz der PM verursacht. Die Winkelauflösung ist ähnlich wie für die Stockwerke mit 10PMn. Besonders effizient scheint dabei die Version mit 21-PM-Kugelstockwerken. Durch die größere Anzahl von Stockwerken pro string ist die hier die Instrumentierung dichter, was die Lichtausbeute verbessert. Dabei wurde die besseren Photonseparations-Eigenschaften der 3PMs in der Simulation noch nicht berücksichtigt. Zwei Stockwerk-Konfigurationen wurden mit 20PMn bestückt. Das erste entspricht dem ANTARES Stockwerk (also 3 20PMn), während das zweite einen einzelnen 20PM trägt. Letzteres leidet unter den gleichen Nachteilen wie die Variante mit einzelnen 10PMn pro Stockwerk und liefert trotz höherer Photokathodenfläche als beim Referenzdetektor keine besseren Ergebnisse. Die erste Variante ist allen anderen Detektoren bei Energien unter 100 TeV überlegen. Es muss aber berücksichtigt werden, dass es sich nicht um eine '*candidate*-Version' handelt (die hätte nur zwei Stockwerke pro string, was ziemlich unrealistisch ist). Die Kosten für einen derart ausgestatteten Detektor wären also deutlich höher (die 20PM sind teurer und erfordern größere Druckbehälter). Der Nutzen dieser Konfiguration hängt somit von den genauen Kosten ab.

Um die verschiedenen Detektorgeometrien zu vergleichen, wurden die jeweiligen Detektormodelle mit den 36-PM-Zylinder-Stockwerken bestückt. Einige Besipiele für untersuchte Geometrien werden in Abb. 2 gezeigt. Zunächst wurden verschiedene ringförmige Konfigurationen simuliert. Da die Reichweite von Myonen mit Energien über 1 TeV in Wasser die Größenordnung von 1 km (also in etwa die Dimension des Detektors) überschreitet, erreichen die meisten Myonen den Detektor von außerhalb. Daher ist bei diesen und höheren Energien eine große Querschnittsfläche wichtiger als ein großes instrumentiertes Volumen. Dieser Effekt könnte genutzt werden, um die Anzahl an Strings (und damit Strukturen und Kosten) zu reduzieren. Ringgeometrien sind eine einfache Möglichkeit dieses Konzept umzusetzen. Die Anzahl der Strings wurde bei annähernd gleicher Anzahl von Stockwerken um mehr als ein Drittel reduziert. Die resultierenden effektiven Flächen sind verglichen mit dem Quader bei niedrigen Energien aufgrund der dichteren Instrumentierung im Ring etwas besser, für Energien über etwa einem TeV (abhängig vom verwendeten Kriterium) jedoch etwa 10% schlechter. Die Ursache für die geringere Effizienz bei hohen Energien ist der Anteil von Myonen, der den Detektor nahezu vertikal passiert. Die Querschnittsfläche ist für solche Ereignisse aufgrund des Lochsïm Ring geringer. Bei gleicher Photokathodenfläche scheinen die Ringe also gemäß der Annahme zu funktionieren. Bei einer Reduktion der Photokathodenfläche nimmt die Effizienz jedoch drastisch ab. Das Konzept kann also eine geringere Anzahl von Stockwerken nicht kompensieren. Um die Effizienz bei niedrigen Energien zu erhöhen, muss die Dichte der Instrumentierung erhöht werden. Um bei konstanter Anzahl an Stockwerken dennoch eine gute Effizienz bei hohen Energien zu erreichen, können 'Cluster'-Geometrien verwendet werden. Das Volumen von einem Kubikkilometer wurde mit einigen (hier acht) dicht instrumentierten Stringgruppen (Clustern) ausgefüllt. Myonen mit niedrigen Energien können innerhalb dieser Cluster mit hoher Effizienz detektiert werden, während hochenergetische ($E > 1$ TeV) Myonen mehrere Cluster treffen, und so vom großen Volumen profitieren können. Die

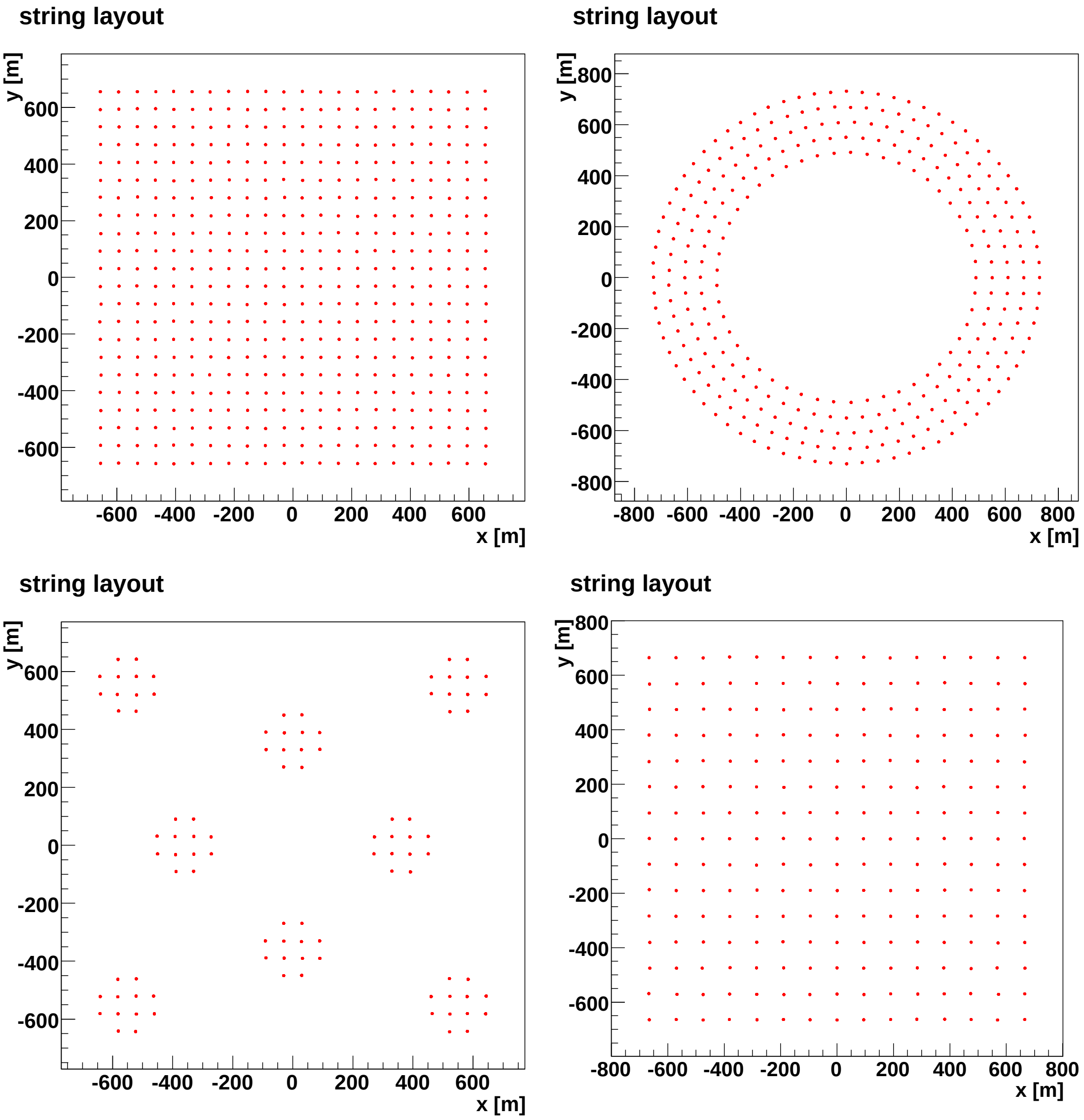

Abbildung 2: Beispiele für simulierte String-Geometrien. Die Punkte bezeichnen die Positionen von Strings auf dem Meeresboden. Oben links: Homogener Quader (Standard-Geometrie); Oben rechts: Ring-Geometrie (*ring1*); Unten rechts: Cluster-Geometrie (*cluster1*); Unten links: Variante des Quaders (verwendet unter anderem beim *Conclusion detector*)

effektiven Flächen dieser Strukturen sind tatschlich für Energien unter einigen hundert GeV signifikant höher, bei größeren Energien sind sie jedoch bis zu 20% niedriger als bei der homogenen Quader-Konfiguration. Die Winkelauflösung verhält sich ähnlich, sie ist sehr gut bei niedrigsten Energien und deutlich schlechter bei hohen. Viele der höherenergetischen Myonen, speziell im Bereich einiger TeV (lange Reichweite, aber geringe Abstrahlung von Cherenkov-Photonen) gehen in den Cluster-Zwischenräumen verloren. Mit dieser Konfiguration kann also die Effizienz für niedrige Energien verbessert werden, aber auf Kosten der Effizienz bei höheren Energien. Schließlich wurden noch Varianten des Quaders simuliert. Dabei wurde die Anzahl der Strings reduziert und die Anzahl der Stockwerke pro String erhöht. Die Varianten mit 324, 225 und 144 Strings zeigen nahezu identische Ergebnisse wie der homogene Quader (mit 484 strings), trotz der deutlich geringeren Anzahl an Strukturen. Lediglich im Bereich von einigen TeV (speziell für *selected* events) sind die effektiven Flächen für die Quader mit weniger Strings etwas niedriger. Die Winkelauflösung ist in allen vier Fällen sehr ähnlich. Der nach diesen Ergebnissen vielversprechendste Detektor (der *Conclusion detector*) ist ein Quader mit 225 strings und 21-(3")-PM-Kugelstockwerken. Er kombiniert eine relativ geringe Anzahl an Strukturen mit einer guten effektiven Fläche und ausreichender Winkelauflösung. Effektive Flächen für diese Konfiguration und einige andere Beispiele sind, unter Verwendung verschiedener Selektions-Kriterien, in Abb. 3 gezeigt.

Um den Einfluss des instrumentierten Volumens zu untersuchen wurden einige Varianten der Ring- und Quader-Geometrien mit einem instrumentierten Volumen von zwei Kubikkilometern erzeugt. Wurde dabei die Anzahl der Stockwerke nicht erhöht, so nimmt die Effizienz bei niedrigen Energien etwas ab oder bleibt vergleichbar (geringere Dichte der Instrumentierung), während sie bei hohen Energien ansteigt (größere Querschnittsfläche). Wurde die Anzahl der Stockwerke erhöht, so steigt die effektive Fläche in etwa proportional zur Photokathodenfläche, speziell bei Energien unter 1 TeV. Bei doppelter Photokathodenfläche ist die effektive Fläche bei größeren Energien weniger als doppelt so groß, wie bei der entsprechenden 1 km^3-Variante, da sie wie bereits erwähnt weitgehend von der Querschnittsfläche des Detektors bestimmt wird, die schwächer als linear mit dem Volumen steigt. Um die Relationen zwischen den verschiedenen Geometrie-Konzepten zu prüfen, und weil die Softwaregruppe des KM3NeT-Konsortiums sich auf einen IceCube-artigen Vergleichsdetektor verständigt hat, wurden schließlich einige mit IceCube-artigen strings ausgestattete Konfigurationen simuliert (IceCube Comparable, ICC). Die Ergebnisse für die originale IceCube-Geometrie, den ICC-Quader, den ICC-Ring, sowie den ICC-Cluster bestätigen die bisherigen Resultate.

Als weiterer Test wurden die Ergebnisse der vielversprechendsten Detektorkonfigurationen mit dem unter gleichen Bedingungen simulierten ANTARES-Detektor verglichen. Die Relationen der effektiven Flächen und der Winkelauflösung verhalten sich dabei der Erwartung entsprechend, was die Simulationsergebnisse weiter bestätigt. Bei diesem Vergleich und auch schon zuvor entstand der Verdacht, dass der verwendete Rekonstruktionsalgorithmus ANTARES-artige Strukturen (Stockwerke, dichte String-Geometrien) bevorzugt. Um diesen Verdacht zu erhärten, wurden einige einfache Tests durchgeführt. Tatsächlich zeigen Detektoren mit ANTARES-Stockwerken oder ANTARES-ähnlichen String-Konfigurationen erkennbar bessere Rekonstruktionsergebnisse.

Eine weitere Studie diente einer systematischen Analyse des Einflusses der Abstände

minimal

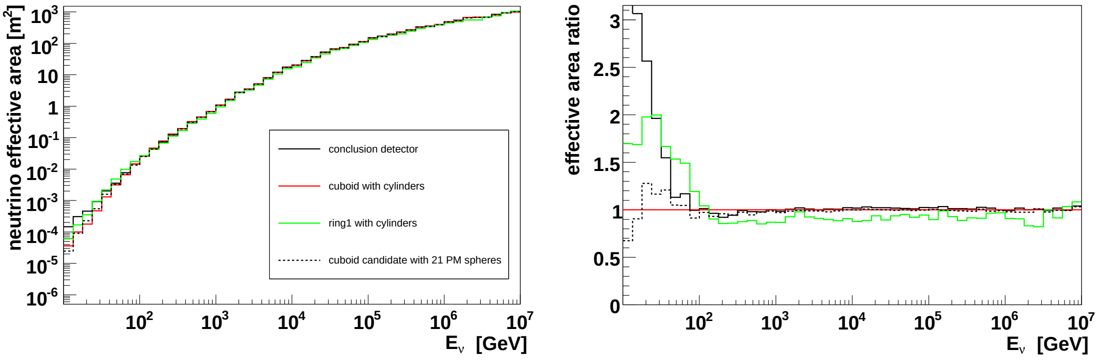

hit

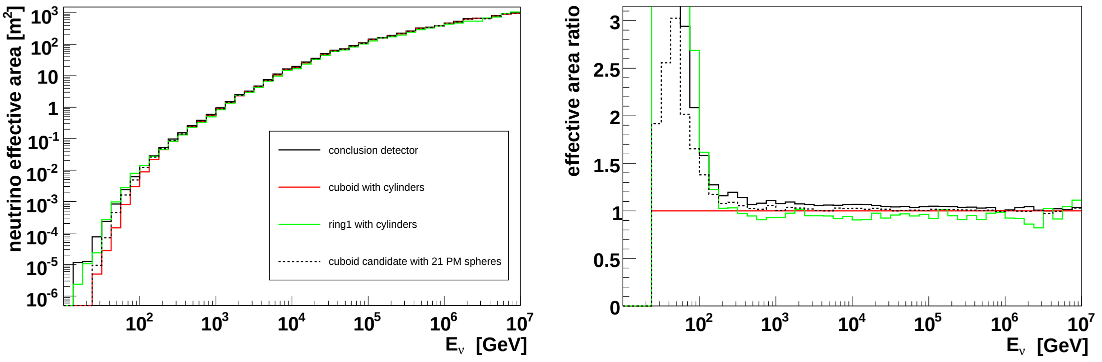

moderate

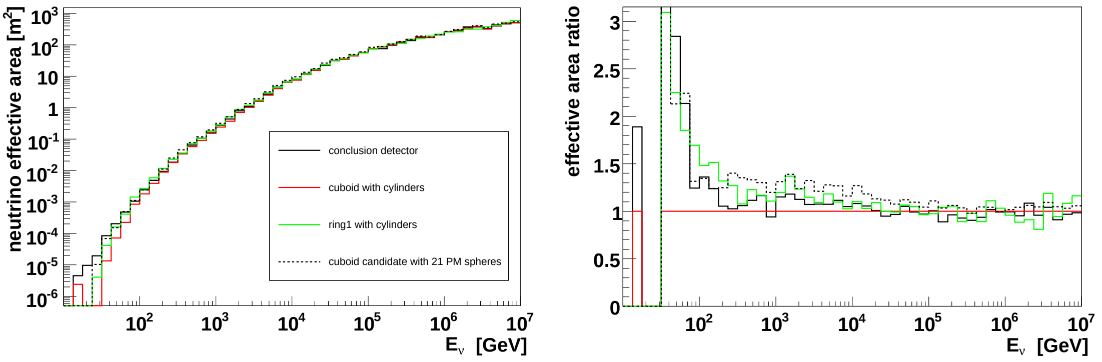

Abbildung 3: Effektive Neutrinoflächen und deren Verhältnisse für verschiedene Detektormodelle. Unter Verwendung der (von oben nach unten) *minimal*-, *moderate*- und *selected*-Kriterien.

zwischen den Stockwerken auf die Ergebnisse für die grundelegenden Geometrie Klassen (Quader, Ring, Cluster). Es zeigt sich, dass die effektiven Flächen bei steigenden Abständen bei niedrigen Energien sinken und bei hohen Energien steigen. Der Übergang zwischen fallender und steigender effektiver Fläche steigt dabei mit steigendem Abstand von etwa 1-10 TeV an. Ursache ist wieder die durch die größeren Abstände abnehmende Dichte der Instrumentierung (niedrige Energien) und die zunehmende Querschnittsfläche (hohe Energien).

Schließlich wurde das Physik-Potential für die wichtigsten Detektor-Konfigurationen abgeschätzt. In Abb.4 werden die Neutrinofluss-Grenzen für den diffusen kosmischen Neutrino-Fluss bei einem Konfidenzlevel von 90% und einer Beobachtungszeit von einem Jahr, für bestehende Experimente und den *Conclusion detector* verglichen, wobei das *selected*-Kriterium angewandt wurde. Bei der Berechnung des Limits, wurde die Bartol-Parameterisierung des atmosphärischen Neutrino-Flusses [1], sowie die Paramterisierung des Prompt-Neutrino Anteils nach dem QGSM-Modell verwendet [2]. Es sei darauf hingwiesen, das bei diesem Ergebnis keinerlei Energierekonstruktion angewendet wurde, es wurden die Monte-Carlo Neutrino- Energien verwendet. Ebenso wurde der Untergrund atmosphärischer Myonen vernachlässigt. Es handelt sich also um eine optimistische Abschätzung.

In Abbildung 5 sind die Flusslimits für eine generische Punktquelle als Funktion ihrer Deklination angegeben. Der Verlauf der Kurve für den *Conclusion detector* ergibt sich aus der variierenden Sichtbarkeit der Quelle für einen Detektor im Mittelmeer. Die Zenithwinkelabhängigkeiten der effektiven Fläche und des atmosphärischen Neutrino Untergrunds wurden bei der Berechnung berücksichtigt. Die für den *Conclusion detector* angegebenen Werte beziehen sich erneut auf die Ergebnisse für das *moderate*-Kriterium, es wurde also keine Rekonstruktion angewendet. Als weiteren Indikator für die Sensitivität auf individuelle Neutrino-Quellen wurden mit dem in [3] verwendeten Code Ereignisraten für den Supenova-Überrest RXJ1713.7-3964 bestimmt, eine der vielversprechenden potentiellen galaktischen Neutrino-Quellen. Mit dem *Conclusion detector* sind unter Anwendung des *selected*-Kriteriums, im Mittel etwa ein Neutrino bei einem mittleren Untergrund von drei atmosphärischen Neutrinos und einer Beobachtungszeit von einem Jahr zu erwarten. Diese Zahlen ermöglichen eine signifikante Detektion nach einigen Jahren Detektorlaufzeit.

Um die Sensitivität auf Neutrinos aus den Annihilationen von Teilchen der dunklen Materie (WIMPS) in der Sonne abzuschätzen, wurden integrierte Ereignisraten für drei beispielhafte Neutrino-Flüsse berechnet [4]. Hierbei stellt der *Bulk*-Fluss eine pessimistische Variante dar, während die beiden *Focus Point*-Flüsse optimistischere Möglichkeiten sind (einer ist sehr groß, der andere erstreckt sich bis zu relativ hohen Energien). Die Ereignisraten für einige der simulierten Detektoren, unter Anwendung des *selected*-Kriteriums, sind in Abb. 6 gezeigt. Für den *Conclusion detector* ergeben sich Raten zwischen sechs (*Bulk*-Fluss) und etwa 400 (*Lower Focus Point*- Fluss) Ereignissen pro Jahr. Die Möglichkeit der Detektion hängt vom realen Neutrino-Fluss ab. Der zukünftige KM3NeT-Detektor wird aber die bestehenden Modelle für die kalte Dunkle Materie einschränken.

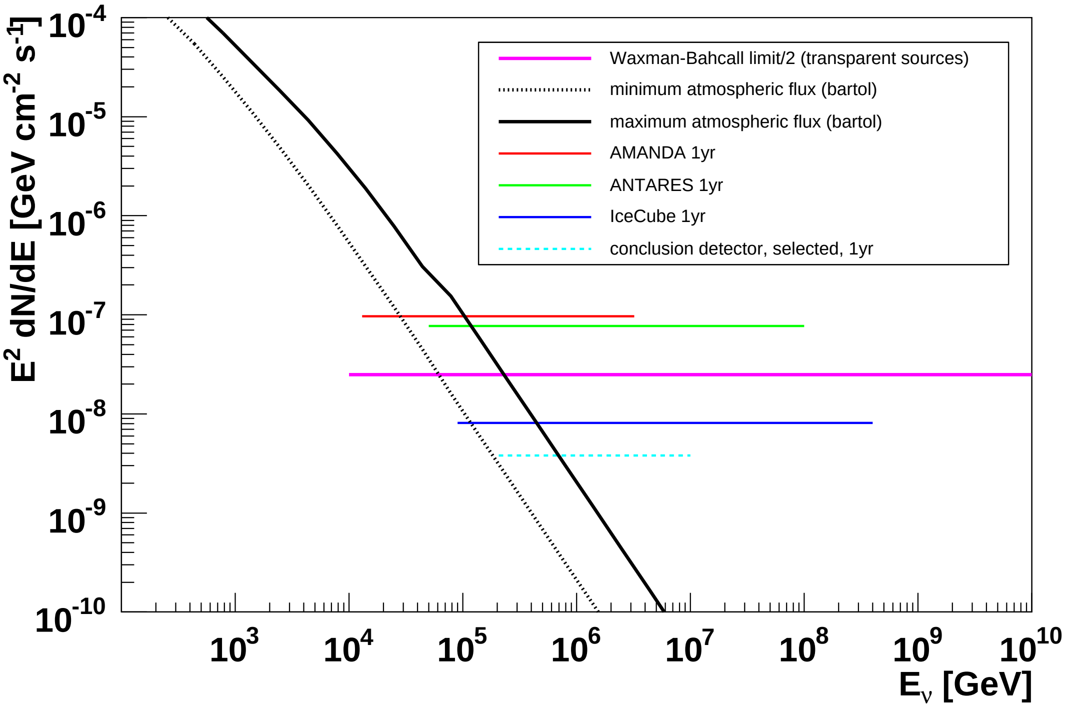

Abbildung 4: Vergleich von Neutrino-Flussgrenzen auf den diffusen Fluss kosmischer Neutrinos für verschiedene Experimente und Modelle, sowie den *Conclusion detector*. IceCube Limit aus [5], ANTARES limit aus [6], AMANDA limit aus [7], Waxman-Bahcall Flussgrenze aus [8].

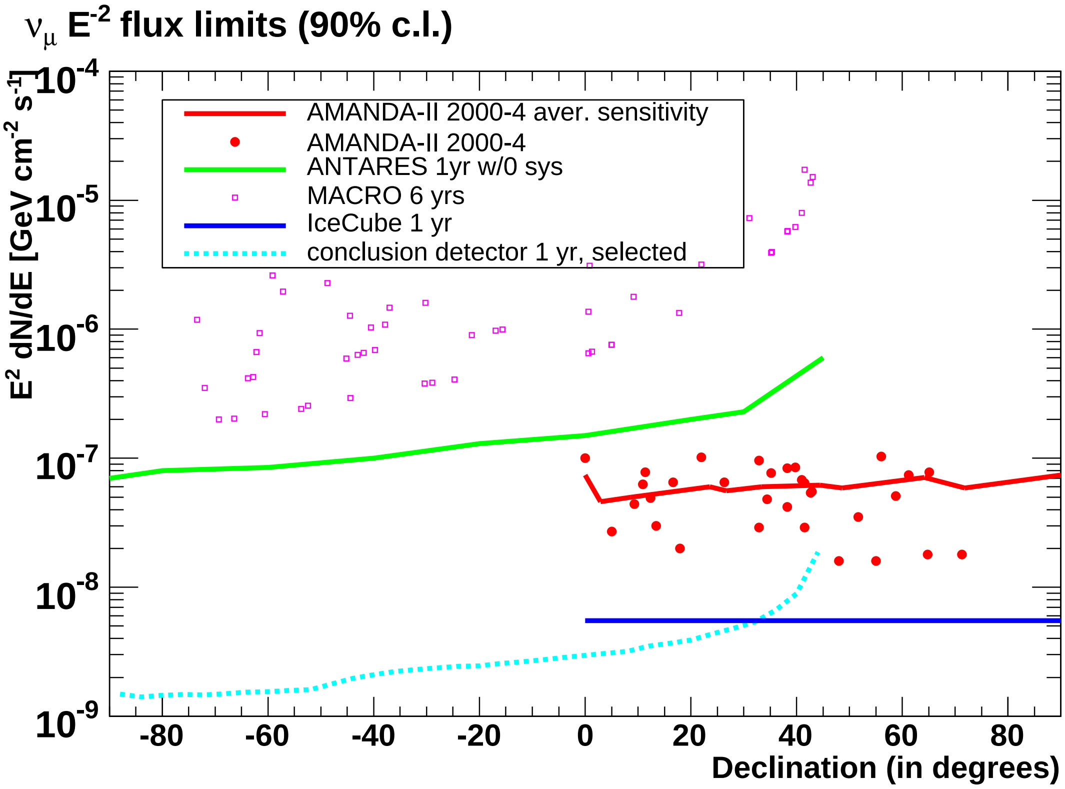

Abbildung 5: Vergleich von Flusslimits auf den Fluss einer generischen individuellen Neutrino-Quelle für verschiedene Experimente und den *Conclusion detector*.

minimal

moderate

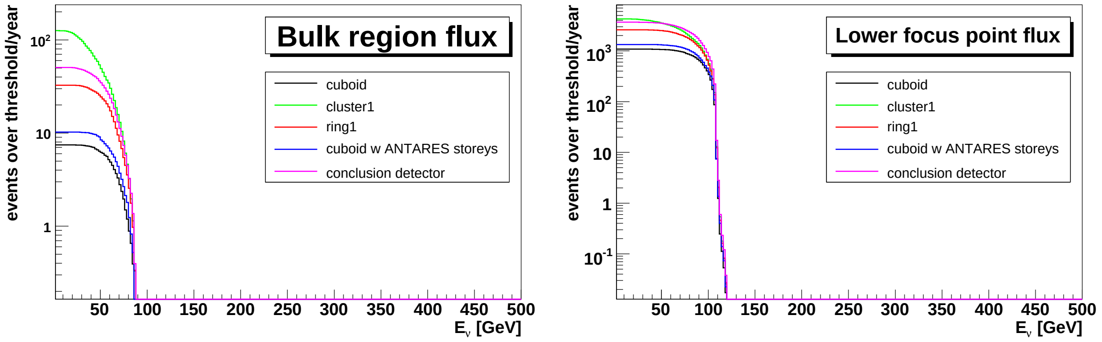

selected

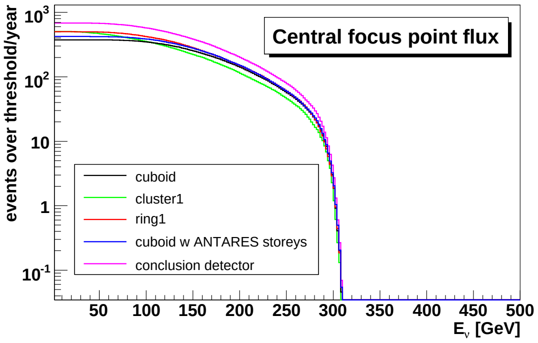

Abbildung 6: Integrierte Ereignisraten für verschiedene Detektormodelle und Voraussagen des Neutrino-Flusses aus Annihilationen dunkler Materie in der Sonne. Dabei wurden die effektiven Flächen unter Verwendung des *selected*-Kriteriums benutzt.

Contents

Chapter 1

Introduction

In the recent years, astronomers have acquired an enormous wealth of knowledge about the universe and the cosmic objects that populate it. By utilising multi-wavelength-techniques and aquiring data from radio, infrared, optical, ultraviolet and x-ray instruments, our knowledge of the cosmos has grown dramatically. Yet the methods of conventional astronomy are limited by the properties of its primary messenger, the photon. There are a lot of interesting objects in the universe like Supernovae (SN) and Active Galactic Nuclei (AGN) that consist of very dense, hot matter that is opaque for photons. At high energies conventional methods are no longer suitable for photon detection as fluxes decrease and photo interactions in the atmosphere render their direct detection increasingly difficult. Finally photons with very high energies (above 100 TeV) interact with the cosmic infrared and microwave backgrounds, thereby limiting their range depending on their energy.

In order to overcome these limitations a new field of astroparticle-physics has emerged in the past decades, high energy neutrino-astronomy. Theory predicts many potential astrophysical sources of cosmic high energy ($\mathrm{E} > 10\,\mathrm{GeV}$) neutrinos and their detection would be a major step toward further understanding of high energy phenomena in the universe, cosmic acceleration and the yet unknown origin of the cosmic rays. High energy neutrino astronomy provides several advantages, but also challenges. Neutrinos only interact weakly and are therefore able to pass the interstellar medium, obstructing gas clouds and leave the central regions of hot dense objects unhinderedly. Having no electrical charge, neutrinos are not deflected by interstellar magnetic fields, like other cosmic particles such as protons.

These properties also make neutrinos very elusive and their detection requires the instrumentation of huge volumes. The only way is to use natural resources in the form of large volumes of water or ice in the sea and Antarctica. The instrumentation of such a detector volume in the deep sea or ice poses a major challenge.

Several experiments took on this challenge starting with the DUMAND [9] experiment, which has produced first experiences for the detection of Cherenkov radiation produced by neutrino induced secondary particles. Two neutrino telescopes are fully operational at the moment, the BAIKAL-telescope [10] in Lake Baikal and AMANDA [11] at the South Pole. The construction of the ANTARES [12] neutrino telescope in the Mediterranean Sea will be finished in early 2008, while the parts that have already been deployed are continuously taking data. The second Mediterranean experiment, NESTOR [13], is in the prototyping phase and has concluded successful tests including the deployment of a prototype structure and the reconstruction of atmospheric muons from its data.

While these experiments demonstrate the feasibility of the method and produce promising results, it has become clear that larger detectors are necessary to explore the full potential of neutrino astronomy. The first of these larger telescopes the cubic-kilometer IceCube [14] experiment, the successor of AMANDA, is already under construction at the South Pole. Together with NEMO [15], an earlier R&D project for a Mediterranean km^3-size detector, the ANTARES and NESTOR collaborations have united their efforts to develop and build the km^3-scale next generation neutrino telescope in the Mediterranean Sea, KM3NeT. This collaboration includes all of the European expertise in deep-sea neutrino telescopy. Its first aim is the production of a Technical Design Report (TDR) by 2009, which is developed in an EU-funded [16] Design Study since the beginning of 2006. The first step for of the Design Study is of course a phase of intensive simulation for the optimisation of detector geometries, optical sensor layouts and photo detection techniques. This thesis is a first step toward this goal, utilising the software tools also used in the ANTARES and NEMO projects.

This thesis is organised as follows:

The next chapter introduces the basics of neutrino astronomy, starting with a short introduction to astroparticle physics in general. It includes an overview of the different experimental techniques and the corresponding experiments.

In Part I, the production mechanisms of cosmic neutrinos and their sources are described. This is followed by the technical aspects of neutrino telescopes and an overview of existing experiments. There will also be a short outlook towards the next generation of telescopes and new promising detection techniques.

Part II includes detailed descriptions of the software tools and methods used for this work. Starting from event generation and ending with analysis methods and tools used for comparison of the different concepts simulated for KM3NeT.

Part III deals with the different concepts themselves, their motivation and their implementation in the software. It will give the results of the work and finally discuss the merits and flaws of the various ideas investigated.

Chapter 2

High energy astroparticle physics - a short introduction

Starting with the first detection of cosmic rays by Victor Hess in 1912, physicists have begun to detect different particles from outer space, thus marking the starting point of astroparticle physics. Since then many experiments have gathered knowledge about the composition and the energy spectrum of cosmic rays. Today we know that the cosmic rays are high energy particles, mainly protons and nuclei. Their energy spectrum spans several orders of magnitude up to energies of over $10^{20}\,\mathrm{eV}$ and follows a power law. The differential flux can therefore be written as

$$\frac{dN}{dE} \propto E^{-\gamma} \tag{2.1}$$

where γ is called the spectral index.

The measured cosmic ray spectrum is shown in Fig. 2.1. With increasing energy the spectrum shows some very distinct features. Below about $4.5 \times 10^{15}\,\mathrm{eV}$ the spectral index is 2.7. At this energy it rises to 3, producing a break in the spectrum that is commonly referred to as the 'knee'. The spectrum becomes even steeper at $4 \times 10^{17}\,\mathrm{eV}$, which is called the 'second knee'. At $10^{19}\,\mathrm{eV}$ there is another break, as the spectral index changes back to about 2.7 at the so called 'ankle'. The cosmic ray composition changes along the spectrum. Below the knee the flux is dominated by protons, while in the knee region the contribution of heavier nuclei is larger [17]. Starting from energies of $10^{18}\,\mathrm{eV}$ the Larmor Radius of the protons in the Galactic magnetic field is larger than the dimension of the Galaxy, therefore particles with higher energies cannot be contained in the Galaxy. Because of this it is widely assumed, that the contribution to the flux above this energy is caused by extra-Galactic sources. Protons with energies above a few times $10^{19}\,\mathrm{eV}$ start to interact with the cosmic microwave background and produce Δ-resonances. This limits their range to $\sim 50\,\mathrm{Mpc}$. This is called the Greisen-Zatsepin-Kuz'min-cutoff (or GZK-cutoff in short [19,20]). The effect also affects heavier nuclei at the corresponding resonance energies. If particles with higher energies were observed, their accelerators would have to be in the limited range of the cosmic ray particles at this energy. As there are no known candidates for such sources in the vicinity of our galaxy, the cosmic ray flux should drop above GZK energies.

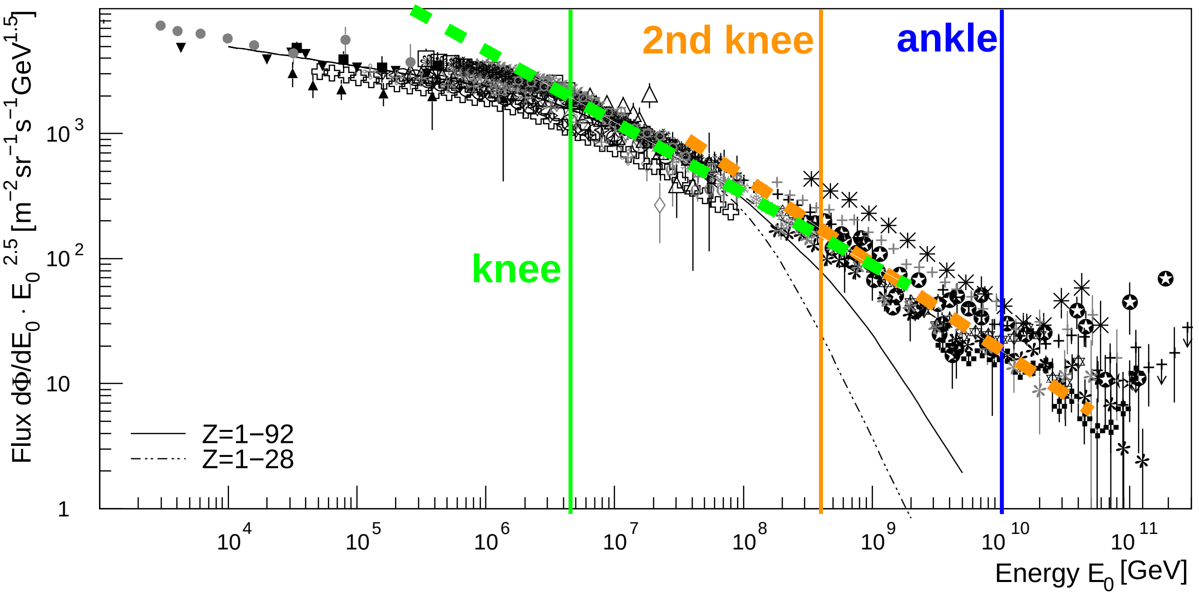

Figure 2.1: All-particle cosmic ray spectrum measured by different experiments, and according to model calculations, taken from [18].

In order to produce high energy particles, powerful accelerators are necessary. The search for these cosmic accelerators and the origin and properties of cosmic rays are central questions of astroparticle physics.

To find the answers to these questions the first step is obviously the direct measurement of the cosmic ray particles. This can be done with balloon and satellite experiments. As the flux becomes very low above 10^{15} eV, the small detection areas of balloon and satellite borne detectors no longer suffice. The only reasonable way is to build arrays of detectors with large areas on the ground. As cosmic ray particles interact with the nuclei of the atmosphere, it is not possible to detect them directly on the ground. However, through the primary interactions, particle showers are produced, that contain electromagnetic and hadronic components, which are detected in so called extensive air shower (EAS) arrays. By utilising Monte Carlo simulations, the properties of the primary particle can be reconstructed from the properties of the shower. There are two basic detection methods for air shower experiments. The first one is based on a large number of rather conventional particle detectors, like scintillators and water-Cherenkov detectors, that are distributed over a wide area. The shower particles are detected inside these units which allows for the reconstruction of the properties of the shower. Examples of experiments using this method are KASCADE [21] or AGASA [22]. Obviously a detector like this only detects a horizontal profile of the shower at the ground level. The second possibility is the observation of fluorescence light, produced by the air shower in the atmosphere, with suitable optical telescopes. This allows to follow the development of a shower, but due to the low fluorescence light yield is only applicable in very dark moonless nights. The Fly's Eye [23] and HiRes [24] experiments are using this technique. Interestingly, experiments of

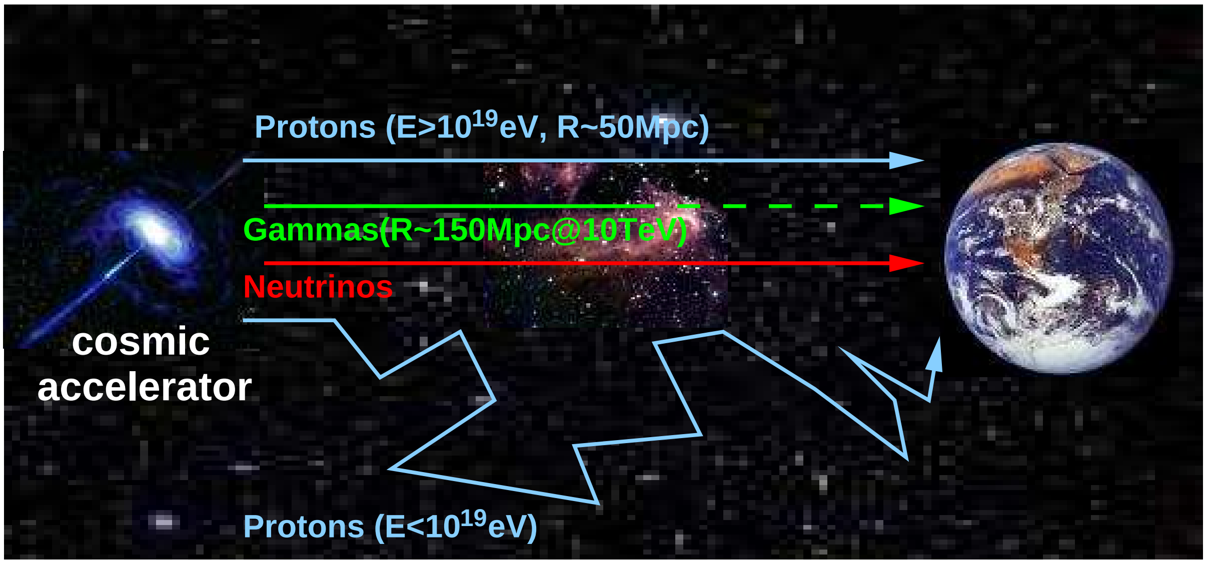

Figure 2.2: Overview of messenger particles for astroparticle physics. Protons are deflected from their original direction by interstellar magnetic fields, except at highest energies. However at these energies their range is limited due to the GZK effect. High energy photons are not influenced by magnetic fields, but can interact with the cosmic infrared background or be absorbed in interstellar gas clouds and therefore have a limited range of approximately 150 Mpc (at 10 TeV). Neutrinos are not deviated nor absorbed and reach the Earth on a straight trajectory.

the two different types claim different results concerning the GZK-cutoff. While the Fly's Eye Experiment observes a drop of the flux above GZK-energies, the AGASA experiment claims to have measured a spectrum that flattens back to smaller spectral indices. However both experiments suffer from limited statistics. The next generation of EAS-experiments, the Pierre-Auger observatory [25] combines both methods and is expected to solve this contradiction. It is the largest cosmic ray experiment so far. In its final configuration, 1600 water tanks equipped with Photomultipliers (PMs) will be spread out over an area of 3000 km^2 in Argentina and will be supplemented by several fluorescence telescopes.

But unfortunately, the observation of cosmic radiation, except at highest energies, does not help to find its sources, as the trajectories of protons and nuclei (and electrons) are influenced by interstellar magnetic fields, effectively destroying any direction information (see Fig. 2.2). The flux of cosmic ray particles that have sufficient energy to resist the influence of the magnetic fields is extremely low and experiments of the size of the Pierre-Auger observatory are needed to detect them with reasonable statistics. These extremely high energy particles are also, as explained above, most probably of extra-Galactic origin. Therefore other messengers are necessary for the search for the accelerators of Galactic cosmic ray particles.

Accelerated protons or nuclei of very high energies are likely to interact with the matter around the accelerator and the interstellar medium. In these reactions large amounts of secondary high energy photons and neutrinos are produced. Photons can be absorbed by interstellar matter or interact with the cosmic infrared or microwave backgrounds and are therefore limited in range, but their trajectories are not influenced by magnetic fields and hence their origin can be identified. However there are other sources of high energy photons. Electrons can be accelerated to very high energies and then produce high energy photons through bremsstrahlung in the medium surrounding the source or through inverse compton scattering (see section 3.1). Therefore, sources of high energy gamma rays cannot be unambiguously identified as the sources of cosmic rays.

The experimental method for the detection of such photons is based on detecting the Cherenkov light produced by showers induced by their interactions in the atmosphere. Well known experiments using this so called imaging air Cherenkov technique (IACT) are H.E.S.S. [26] and MAGIC [27].

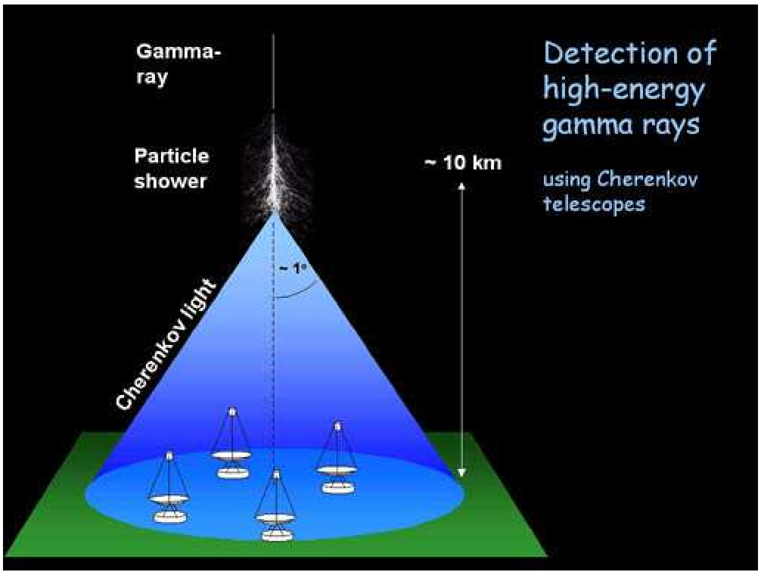

Figure 2.3: Schematic illustrating the imaging air Cherenkov technique.

The incident high-energy photon interacts in the atmosphere and produces a shower of secondary particles, which reaches its maximum at a height of about 10 km above ground. As these particles travel faster than the speed of light in the medium (air), the charged particles will produce Cherenkov light that is emitted in a cone. This light cone illuminates an area on the ground with a diameter of a few hundred meters (Fig. 2.3). For a TeV energy primary photon, about 100 photons arrive per m^2. The time interval of their arrival is only a few nanoseconds long. Telescopes on the ground can detect these Cherenkov photons with photomultipliers that form the pixels of a camera. The primary photon direction and its energy can be reconstructed from shape and intensity of the resulting image. The main background, consisting of showers induced by cosmic ray particles, can be rejected using the shape of the Cherenkov images.

The IACT experiments have produced spectacular results. The H.E.S.S. experiment has discovered more than 30 sources of TeV gamma rays in the Galaxy [28]. Some of these have been confirmed by observations by MAGIC. Due to the good pointing accuracy of the H.E.S.S. detector many of these sources could be identified with known sources at other wavelengths, like supernova-remnants (SNRs), binary systems, or Pulsar Wind Nebulae (PWNe). One of the best studied examples is the SNR RXJ1713.7-3946. Due to its good angular resolution, the H.E.S.S. instrument was able to resolve the morphology of this extended source. The strong signal allowed detailed spectral and morphological studies. A picture of RXJ1713 in TeV gamma-rays is shown in Fig. 2.4. The good spatial correlation of the gamma-ray flux with the X-rays proves that SNRs are indeed accelerators of high energy particles. A multi-wavelength analysis of RXJ1713 favours hadronic acceleration, the acceleration of protons or nuclei, over leptonic acceleration [29].

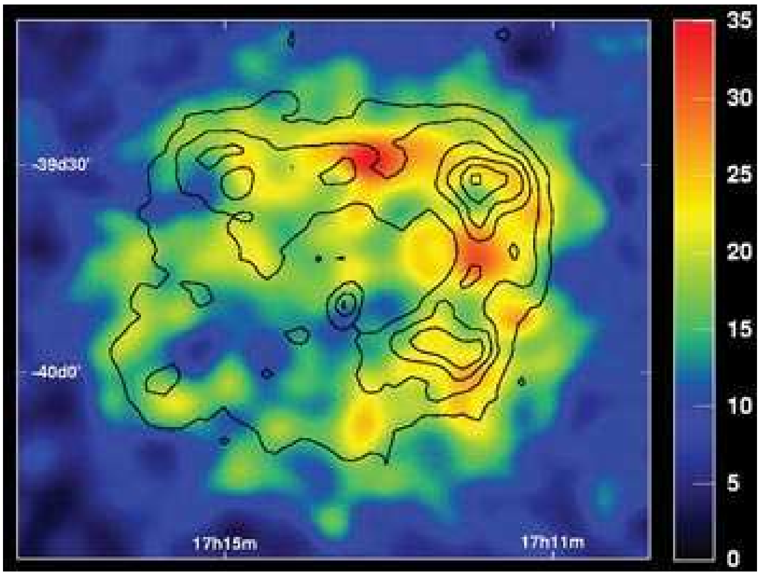

Figure 2.4: Image of the SNR RXJ1713.7-3946 in High energy gamma-rays. The colour scale corresponds to excess counts of gamma events, the contours correspond to the x-ray emission measured by the ASCA satellite.

Apart from photons, proton reactions with interstellar matter also yield large numbers of neutrinos. With no electrical charge and only weak interaction, neutrinos provide an extremely promising window to the universe. They are not absorbed in the interstellar medium, their trajectories are not influenced by magnetic fields and they have virtually unlimited range. Unfortunately the same properties, that make them an almost ideal messenger for astro-particle-physics, also render their detection a challenging task, to which this thesis is devoted.

Part I

Neutrinos and Telescopes

Chapter 3

Neutrinos from cosmic sources

This first part of the thesis focuses on the basics of neutrino astronomy, beginning with the production of neutrinos by cosmic accelerators. The acceleration mechanism most probably responsible is explained and the most prominent classes of cosmic phenomena that are candidates for the acceleration of particles to cosmic ray energies are listed. Furthermore, the production of high energy neutrinos through dark matter annihilation and other hypothetic, more exotic, scenarios are shortly discussed.

3.1 Neutrinos from cosmic accelerators

3.1.1 The acceleration mechanism

As explained in the preceding chapter, the search for the origin of cosmic rays is one of the most prominent topics of astroparticle physics. To produce the energy of the cosmic ray protons observed, powerful natural accelerators are necessary. Several candidates are considered to be capable of accelerating protons to energies of 10^{20} eV, like AGNs and Gamma Ray Bursts (GRBs), others, like SNRs, are expected to accelerate particles to energies of 10^{15} eV. The responsible mechanism is basically the same. This mechanism is commonly known as 'first order Fermi acceleration' [30–33] or simply shock acceleration as it requires the presence of a shock in two colliding plasmas. Particles inside these plasma filled spaces can be elastically scattered by irregular magnetic fields and are magnetically bound to the source. The shock acceleration mechanism is schematically shown in fig 3.1. The shock front, for example caused by a supernova explosion, moves with a velocity of $\vec{v}_s$ relative to the surrounding medium, which is considered to be at rest. The shocked gas trailing the shock front moves with a velocity of $-\vec{v}_r$ relative to the front. Its velocity $\vec{v}_g$ in the laboratory frame is accordingly given by

$$\vec{v}_g = \vec{v}_s - \vec{v}_r. \tag{3.1}$$

If a relativistic particle passes the shock front from the unshocked to the shocked medium it is scattered at magnetic irregularities in the gas behind the shock front. Through this scattering the particles' direction is randomised and there is a probability to cross the shock into the unshocked medium and have its direction randomised again. At each

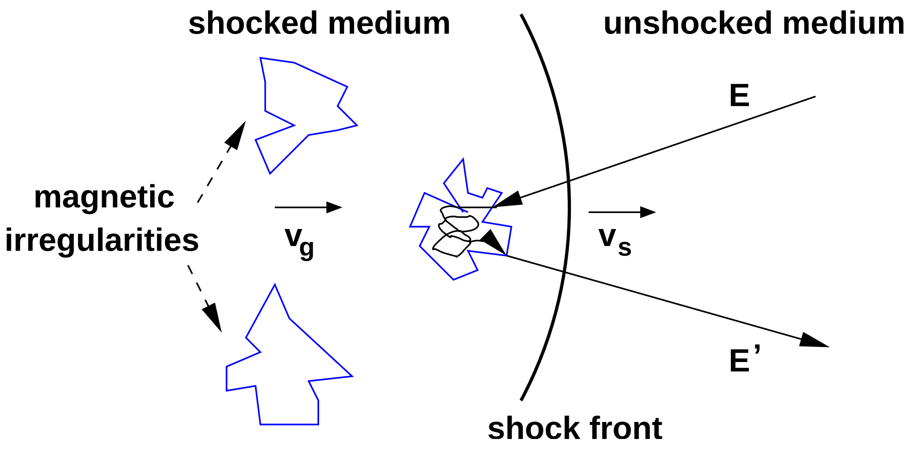

Figure 3.1: Schematic illustration of the shock acceleration mechanism: A shock front moves with velocity v_s through the surrounding medium. A particle with energy E passes the shock front and is scattered back by a magnetic irregularity in the gas following the shock front with velocity v_g. The particle is accelerated to an energy of E'.

crossing the particle gains an energy ΔE proportional to the velocity $\vec{v}_g$ in the shocked medium.

$$\frac{\Delta E}{E} \propto \frac{v_g}{c} = \beta. \tag{3.2}$$

In order to reach energies in the TeV range, this process has to be repeated many times. The spectral index of the flux of particles accelerated by this mechanism can be estimated by assuming a constant probability P that a particle escapes the acceleration region. Of N particles starting with energies E, $N' = N(1-P)^n$ particles will remain after n cycles, with energies of $E_n = E(1+\beta)^n$. With this the number of particles $N_{E \geq E_n}$ reaching or exceeding an energy E' through acceleration can be derived:

$$N_{E \geq E_n} = N \left(\frac{E_n}{E}\right)^{\frac{\ln(1-P)}{\ln(1+\beta)}} . \tag{3.3}$$

From this the number of particles within an energy interval $E \to E + dE$ can be obtained by differentiation:

$$\frac{dN(E')}{dE'} \propto E_n^{\frac{\ln(1-P)}{\ln(1+\beta)}-1} \tag{3.4}$$

Although the above calculation is based on simplified assumptions it yields the power law spectrum corresponding to the observations. Detailed calculations yield spectral indices of $\gamma = 2.1$ to $\gamma = 2.4$ [34]. The maximum energy that a particle can reach through this acceleration mechanism depends on the lifetime of the shock front and the strength of the magnetic irregularities in the medium.

3.1.2 The production of neutrinos

As mentioned above, the accelerated particles (mostly protons for $E < 3 \times 10^{15}$ eV) lose any directional information due to their deflection by cosmic magnetic fields. Fortunately the probability of an accelerated proton to interact with photons or matter fields near its source is quite high. The reactions,

$$p + \gamma/p \longrightarrow N_1\pi^+ + N_2\pi^- + N_3\pi^0 + X \tag{3.5}$$

produce charged and neutral pions in about equal amounts ($N_1 + N_2 \sim N_3$). The charged pion decays produce neutrinos (to the benefit of neutrino telescopes), while the neutral pion decays into high energy photons (to the benefit of airshower Cherenkov telescopes).

$$\begin{aligned} \pi^+ \quad &\rightarrow \quad \mu^+ + \nu_\mu && (3.6)\\ &\qquad \hookrightarrow e^+ + \nu_e + \overline{\nu}_\mu && (3.7) \end{aligned}$$

$$\begin{aligned} \pi^- \quad &\rightarrow \quad \mu^- + \overline{\nu}_\mu && (3.8)\\ &\qquad \hookrightarrow e^- + \overline{\nu}_e + \nu_\mu && (3.9) \end{aligned}$$

$$\pi^0 \rightarrow \gamma + \gamma. \tag{3.10}$$

As the fraction of the proton energy carried by the neutrinos after these reactions is roughly independent of the proton energy, the spectrum of the neutrinos follows the spectrum of the protons.

As can be seen from the reactions 3.7 and 3.9, two muon- and one electron-neutrino are produced in the decay of a charged pion. It can be shown that this ratio of $\nu_e : \nu_\mu : \nu_\tau = 1 : 2 : 0$ is changed to about $1 : 1 : 1$ due to neutrino oscillation, for distances larger than one kiloparsec.

3.1.3 Neutrino sources

Photons with energies of GeV or more cannot be produced by thermal processes, they must be the result of an acceleration process as described above. If the accelerated particles are protons (hadronic acceleration), high-energy neutrinos are produced in the interactions of these protons with ambient matter as well. Therefore all sources emitting GeV gamma rays are of special interest for neutrino telescopes. However, electrons accelerated to high energies also produce high-energy photons through bremsstrahlung or inverse Compton scattering, in which case no neutrinos would be produced. In the following the most important candidates for cosmic accelerators are described.

Supernova Remnants (SNR)

The explosion of a massive star that has reached the end of its lifespan, a so called supernova explosion, produces a large amount of neutrinos. These neutrinos with energies of only a few MeV are not detectable by a deep-sea neutrino telescope, which generally has an energy threshold of a few GeV. The remnant of the star can form a neutron star or a black hole. In the common shell-type Supernova remnants, the ejected matter forms an expanding shell around the resulting object. This shell of matter is the source of photons from radio wavelengths up to TeV energies. Multi-wavelength analyses of the photon energy spectrum of SNR RXJ1713.7-3946 measured by H.E.S.S. [29], favour hadronic acceleration, therefore making Supernova remnants candidates for the emission of high-energy neutrinos.

Pulsars and Pulsar Wind Nebulae (PWN)

The remnant of the star after a supernova explosion can be a neutron star. If the axis of its magnetic field points into the direction of the observer it is called a pulsar. The magnetic field of this object is extremely strong. Within the pulsars magnetosphere particles (electrons or ions) are accelerated to relativistic energies and interact with the surrounding matter. This acceleration mechanism is not yet understood. A surrounding nebula powered by this relativistic 'wind' of the pulsar is called a pulsar wind nebula.

Some of the brightest sources detected by TeV gamma-ray telescopes are PWNe, for example the Crab and Vela pulsars [35,36]. It is generally assumed that this gamma emission is produced through inverse Compton scattering (leptonic acceleration), but the existence of a significant fraction of nuclei in pulsar winds has been suggested. In this case PWNe might be potential neutrino sources [37].

Microquasars

Microquasars are binary systems consisting of a neutron star or black hole of approximately solar mass and a single star. The neutron star or black hole constantly accretes mass from its companion and produces a relativistic jet perpendicular to the accretion disk similar to an AGN. The pattern of the emitted gamma rays is similar to that of a quasar but the emission is about six magnitudes weaker. Calculations have shown that microquasars are candidate sources for high-energy neutrinos [38,39].

Active Galactic Nuclei (AGN)

Seyfert galaxies, radio galaxies, quasars and blazars are all special types for the objects classified as Active Galactic Nuclei, galaxies with a super-massive black hole in its center and an accretion disk surrounding it. Relativistic jets are formed perpendicular to the disk. The classification into the different groups depends on the special properties of the AGN (most prominently the angle between the jet emission and the observers line of sight).

These objects are known to emit high-energy gamma rays. If the gamma rays are produced by hadronic acceleration in the accretion disk, neutrinos should also be produced. In addition it is expected that neutrinos are produced in the jets as well. As the models describing AGNs are still speculative, the detection of neutrinos from an AGN would be an important input for the explanation of these objects [40,41].

Gamma Ray Bursts (GRB)

Gamma Ray Bursts are a transient phenomena that produce enormous amounts of gamma rays, outshining all other gamma ray sources during their lifetime of a few seconds. Several theoretical models for Gamma ray burst exist at the moment.

Some GRBs can be explained by the so called Hypernova explosions of rapidly rotating very massive stars, that in the process transform into also rapidly rotating black holes with accretion disks. High energy gamma rays are emitted in bursts perpendicular to the disk during the process. Those GRBs that can not be associated with Hypernova explosions can be explained by the merging of a binary system of a neutron star and/or a black hole. The result is a black hole with an accretion disk emitting bursts of high energy photons in the same way as a hypernova.

The mechanism of acceleration in these objects is still not completely understood, but it is expected that along with the gamma rays high-energy neutrinos are emitted [42].

3.2 Dark matter - Neutrinos from WIMP annihilations

It is well known that the observable, light-emitting mass of spiral galaxies does not suffice to explain their measured rotation curves. Calculations indicate that 90% of the mass of these galaxies has to be composed of dark matter, which is invisible with common astronomical instruments. As the searches for large-scaled candidates for this cold dark matter like MACHOs (Massive Compact Halo Object, massive objects that do not emit light like brown dwarf stars or small black holes) did not result in enough detected objects to the explain measured rotation curves [43], the focus of research has turned on elementary particles as dark matter candidates.

As dark matter is obviously not visible a potential dark matter candidate can only be an uncharged, weakly interacting particle. In the Standard Model (SM) of particle physics this leaves neutrinos. The results of the WMAP mission [44] show that the abundance of dark matter is much larger than that of visible matter, and neutrinos do not provide enough mass to explain these results. The structure of the universe as observed today also rules out neutrinos as dark matter candidates, as they are fast moving and the observed large-scale structures would have been washed out.

The dark matter candidate particle has to be slow moving and therefore massive. In order to find a suitable candidate for such a weakly interacting massive particle (WIMP) one has to go beyond the SM. The supersymmetric theory (SUSY) provides an option with the Lightest Supersymmetric Particle (LSP). These particles have a high mass and are assumed to be stable due to the conservation of the supersymmetric R-parity, which suppresses the decay into non-supersymmetric particles. The exact nature of the LSP greatly depends on the supersymmetric model and its parameters. For the Minimal Supersymmetric model (MSSM) this is the neutralino, a linear combination of the supersymmetric partners of the Z-boson, the photon and the neutral Higgs-boson. This proposed particle has all the necessary properties to form the cold dark matter.

WIMPs move rather slowly through the galaxy and can lose further energy through weak elastic scattering on matter. Thereby WIMPs can get gravitationally trapped by a massive objects like a star or planet. WIMPs that are captured in this way will accumulate in the center of the object and neutrinos may be produced by WIMP-WIMP annihilations (the neutralino, being a majorana particle, is its own antiparticle). The energy of neutrinos from such annihilation reactions is lower than the WIMP mass.

The observation of an increased neutrino flux from the center of the sun or Earth (or the Galactic center) would be a strong indicator for the existence of WIMPs and would allow to give constraints on their properties, especially their mass. Current calculations suggest WIMP masses below 1 TeV, therefore the typical neutrino energies would be of the order of hundreds of GeV or even lower.

3.3 Other sources

Another explanation of the origin of cosmic rays with energies as high as 10^{20} eV are the so called 'top-down'-scenarios. These theories assume that cosmic ray particles do not obtain their energy by acceleration through cosmic objects, but that they are decay products of super-massive relic particles from the Big-Bang. These would have masses of $10^{24} - 10^{25}$ eV (GUT-scale masses). Until now 'top-down' models have not been proven, but also not disproven. However, one would expect a large number of high-energy photons to be produced in such decays, which have not been found in studies on the composition of highest energy cosmic particles [45,46]. This fact disfavours these scenarios.

Chapter 4

Neutrino telescopes

The neutrino is a lepton with a very small mass [47] and no charge, which makes it a very elusive particle, as it only interacts through the weak force and gravitation (the latter is negligible in most cases). This fact is the reason for its usefulness for astroparticle physics. Unfortunately this also prevents direct detection and renders indirect detection difficult, as the extremely small cross sections require extremely large target masses.

The first neutrino detectors, like the famous Homestake experiment [48], used tanks filled with chemicals of known composition as targets and, after some time, counted the number of nuclei which went through a neutrino induced reaction. Therefore these experiments only measured an integrated (over energy and angle) flux of neutrinos. Apart from the fact that the used reactions do not work at energies above those of solar neutrinos (MeV) knowing the energy and direction of single neutrinos is essential for neutrino astronomy and because of this a new detection method was necessary.

The common strategy for neutrino detection is to use a dense, transparent medium in a large volume, for example water or ice, and instrument it with optical sensors. For relatively small volumes man-made caverns can be utilised like in Super-Kamiokande [49], which is designed for the measurement of solar neutrinos and therefore has a relatively low energy threshold. For high energy neutrino astronomy, where very high neutrino energies are interesting and the neutrino flux is much smaller, only natural environments such as the deep sea (or lakes) or the antarctic ice, provide sufficient detection volumes. In these media neutrinos can interact with the nucleons in the water and produce secondary particles. These particles generally travel with highly relativistic velocities larger than the speed of light in that medium. This leads to light production via the Cherenkov effect. Some of the Cherenkov photons will hit the photo-sensors and produce signals. The times and amplitudes of these signals are recorded, which are then used to reconstruct the direction and energy of the incident neutrino. Because of the extreme environment (high pressure, corrosive sea water, no access) this comprises a major challenge.

In this chapter the basics of neutrino telescopes are presented. The detection principle is explained in more detail and the signatures of neutrinos of different flavours in the detector are discussed. Basic reconstruction principles and the treatment of the background is explained. After a short review of possible future alternative methods for neutrino detection, an overview over existing neutrino telescope projects is presented.

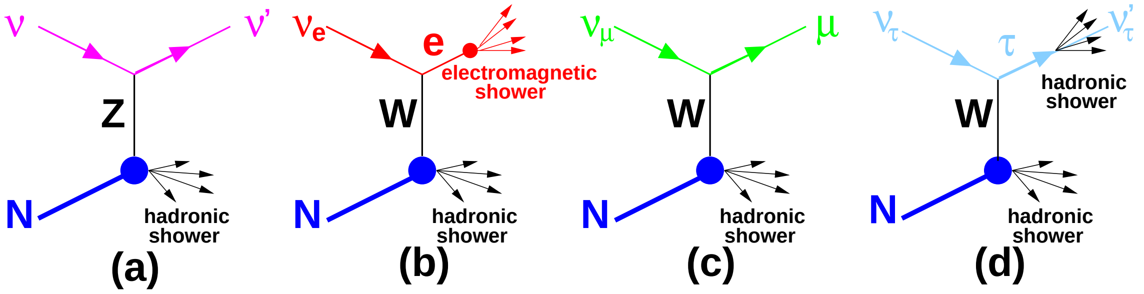

Figure 4.1: Schematic illustration of neutrino interactions relevant for neutrino telescopes. (a) Neutral current reaction resulting in a scattered neutrino and a hadronic shower; (b) Charged current reaction of an electron-neutrino resulting in an electromagnetic and a hadronic shower; (c) Charged current reaction of a muon neutrino resulting in a muon and a hadronic shower; (d) Charged current reaction of a tau-neutrino resulting in a double bang event. For leptonic decays of the τ-particle the signature is equivalent to (a) and (c) (see text).

4.1 Principles of neutrino optical detection

4.1.1 Neutrino Interactions

Neutrinos can interact with target nucleons through deep inelastic scattering. The different event classes produced by the different neutrino flavours are illustrated in Fig. 4.1. The type of the interaction, charged current or neutral current, and the neutrinos flavour greatly affect the signature of the neutrino event in the detector. There a two basic classes of signatures in the detector, long muon tracks and showers with a length generally smaller than 10 m. The latter are basically seen as point sources of Cherenkov light, due to the relatively large distances between the PMs.

Neutral current interactions are similar for all flavours: The neutrino will react with a nucleon, resulting in a lower energy scattered neutrino and a hadronic shower in the final state that carries a part of the primary neutrino's energy,

$$\nu + N \rightarrow \nu + X. \tag{4.1}$$

For charged current interactions the situation is more diverse. They will produce a relativistic charged lepton and a hadronic shower,

$$\nu_l + N \rightarrow l + X. \tag{4.2}$$

Electron-neutrinos will therefore produce electrons and thereby an electromagnetic shower overlapping with the hadronic shower. Tau neutrinos will produce a τ-lepton which will travel a certain distance and then decay, producing, among other possibilities, another hadronic shower (depending on the type of decay). This type of event with two separated hadronic showers is often called a 'double-bang' event.

The most interesting flavour for neutrino telescopes is the muon neutrino, as this produces a muon in the interaction. In the energy ranges interesting for neutrino telescopes

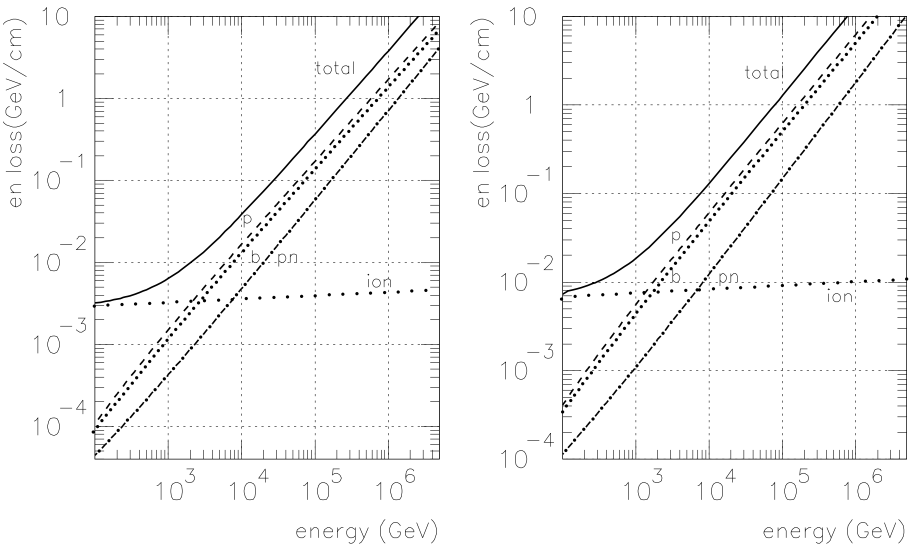

Figure 4.2: Energy loss of muons in water (left) and standard rock (right). The solid line is the total energy loss, 'p' denotes pair production (dashed line), 'b' bremsstrahlung (densely dotted line), 'pn' photo-nuclear interaction (dash-dotted line) and 'ion' ionisation (sparsely dotted line). Taken from [50].

muons lose energy relatively slowly and therefore can traverse large distances before being stopped. A high energy muon looses energy through ionisation, bremsstrahlung, pair production and nuclear interactions. The relative importance of these mechanisms at different energies can be seen in Fig. 4.2. The maximum range of the muon in water depends on its energy; at energies of about 1 TeV it is already above 1 km and increases further with energy (Fig. 4.3).

These long muon tracks are the primary event signature for neutrino telescopes. The long muon range allows us to detect muons produced far outside the instrumented detector volume and provides a long lever arm for direction reconstruction. It should be noted that there is a small angle between the neutrinos and the produced muons direction, that is caused by the kinematics of the interaction. As only the muons direction can be reconstructed, this imposes a limit on the achievable angular resolution. This kinematic angle decreases with energy, so that the angular resolution of a neutrino telescope is dominated by the reconstruction above energies of typically a few TeV and by the kinematics of the neutrino interaction below.

The neutrino-nucleon cross section increases with energy in the relevant energy range of 10 GeV to 10 PeV (Fig. 4.4). However, the cosmic neutrino fluxes are expected to be proportional to E^{-2} to $E^{-2.5}$ (see section 3.1). The expected interaction rates therefore decrease with increasing energy.

For neutrino energies around 6.3 PeV, the cross section for antineutrino-electron scattering shows a resonance peak due to W production and exceeds the νN cross section

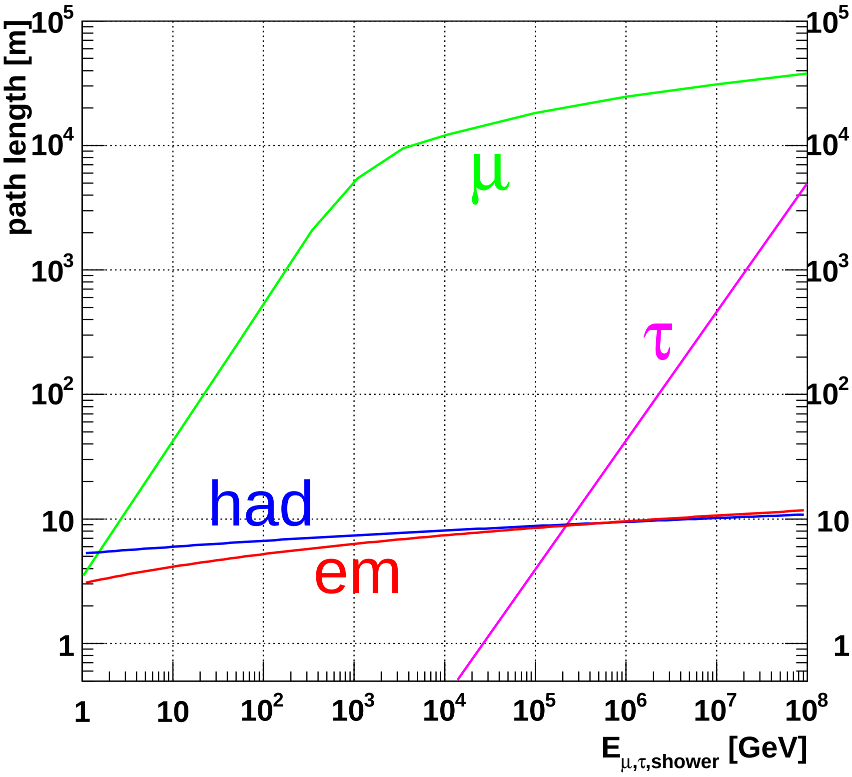

Figure 4.3: Path lengths of muons (μ), taus (τ) and electromagnetic (*em.*) and hadronic (*had.*) showers in water. Taken from [51].

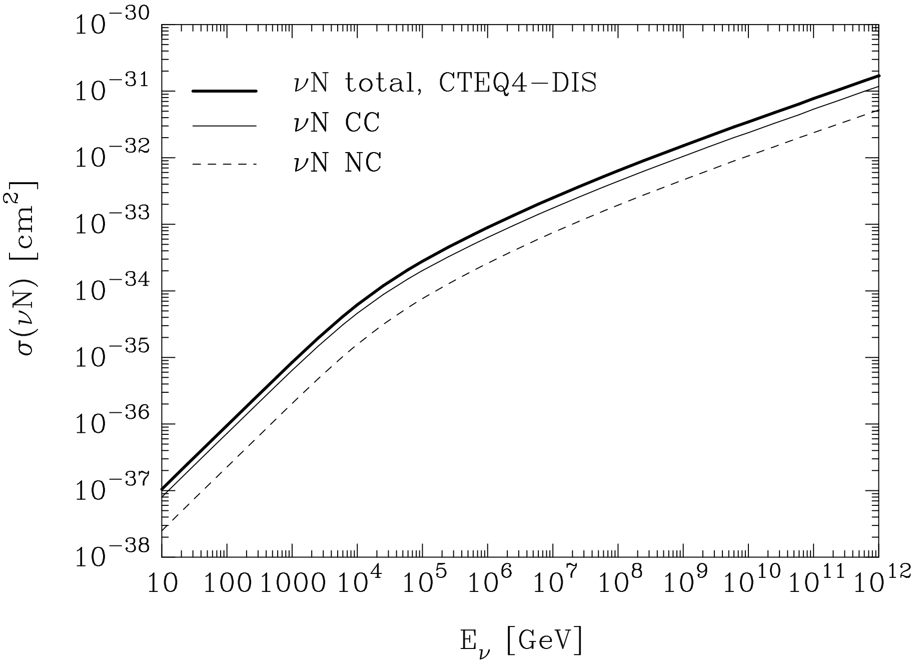

Figure 4.4: Cross sections for ν-N-interactions, using the CTEQ4-DIS parton distribution functions. The dashed line corresponds to NC-interactions, thin line to CC-interactions and the thick line to the overall cross section. Taken from [52].

(*Glashow resonance*). The reactions with these highest cross sections are:

$$\bar{\nu}_e + e^- \rightarrow \bar{\nu}_l + l_l^- \tag{4.3}$$

$$\bar{\nu}_e + e^- \rightarrow \text{hadrons.} \tag{4.4}$$

As can be seen from the reactions, the Glashow resonance is relevant only for $\bar{\nu}_e$ events.

4.1.2 Light propagation and detection

The Cherenkov effect

Charged particles traveling through a medium with a velocity greater than the speed of light in that medium, emit Cherenkov light. The light is emitted in a cone with a characteristic angle, depending on the refractive index n of the medium and the velocity β of the particle (in units of the vacuum light speed c). This Cherenkov angle given by,

$$\theta_{\mathrm{C}} = \arccos \frac{1}{\beta n}. \tag{4.5}$$

In the case of water with about $n \sim 1.35$ (in the relevant wavelength region) and a highly relativistic particle with $\beta \sim 1$ this leads to an angle of $\theta_{\mathrm{C}} = 42°$. The wavelength spectrum of the Cherenkov radiation is in the ultraviolet and visible range.

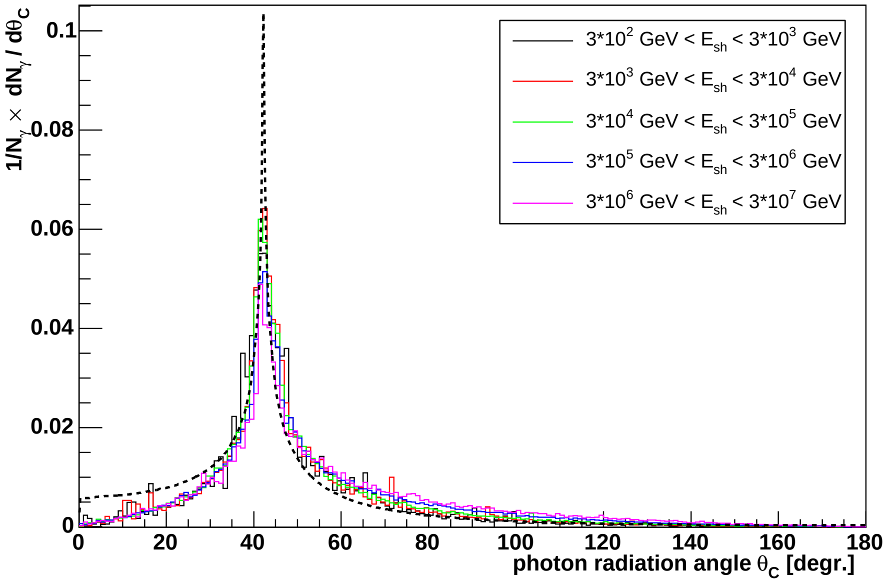

Figure 4.5: Distribution of Cherenkov photon emission angle for hadronic showers at various energies (histograms) and for electromagnetic showers (dashed line). Taken from [54].

The number of emitted photons can be calculated as [53],

$$\frac{dN_\gamma}{dx d\lambda} = \frac{2\pi\alpha}{\lambda^2}\left(1 - \frac{1}{n^2\beta^2}\right) \tag{4.6}$$

where λ is the wavelength of the photon and α is the fine structure constant. In the wavelength range from 300 nm to 600 nm, where water is transparent, this results in about 3.4×10^4 emitted photons per meter of particle track.

The signature of neutrinos

The charged particles in a shower-type event produce Cherenkov light until their energy drops below the Cherenkov threshold. The shower range in water is of the order of 10 m even at energies of about 100 TeV. The emitted particles move mostly about parallel to the primary particle (due to kinematics) but the remaining variation and the fact that velocities $\beta < 1$ occur in the shower lead to a smearing of the Cherenkov cone. The distribution of the Cherenkov angle around the shower axis is shown in Fig. 4.5. The shower emits a large number of photons within a very short distance. This is an advantage for energy reconstruction as the number of photons deposited inside the detector is proportional to the shower energy. On the other hand a shower is basically a point like light source, as the typical distance between sensors in a neutrino telescope is of the order of a few tens of meters. This is a disadvantage for direction reconstruction.

The long tracks of muons emit Cherenkov light over their whole length. Additionally secondary showers are produced by bremsstrahlung and pair production, whose energy and number depend on the muon energy. This continuous and more or less homogeneous emission of light under a well-defined angle facilitates direction reconstruction. The energy reconstruction of muons uses the energy loss per track length dE/dx. For energies below about one TeV, dE/dx is independent of the muon energy and energy reconstruction is difficult. Above this threshold, dE/dx increases with increasing muon energy, which allows to estimate the muon energy through the number of detected photons (see Fig. 4.2).

Reconstruction principles

The input for any reconstruction algorithm is a set of photon hits in photomultipliers, with hit times and amplitudes. The task of the algorithm is to use this information to obtain an estimate of the direction and energy of a muon or shower, using the known Cherenkov angle, the speed of light in water and the positions of the PMs. Of course the contamination with background hits should be reduced as much as possible before applying the reconstruction algorithm. Among other methods, a causality filter can be applied rejecting all those hits, that are not causally connected to hits that have a high probability of being signal hits (high amplitudes, coincident).

For the final reconstruction maximum likelihood methods are used that require a probability density function. The fundamental part of this function is the distribution of the time residuals of the hits, which are the differences between the theoretical arrival times of photons from a given track and the measured arrival times. Maximum likelihood methods have the tendency to depend on the starting point for the minimisation process. Therefore (geometric) prefits are applied as a first step to provide a first estimate of the track parameters as an input for the likelihood algorithm.

The performance of a neutrino telescope depends as much on the efficiency of the reconstruction software as it depends on the technical design of the detector.

4.1.3 Background and optical noise

There are several different types of sources all resulting in the production of background light obscuring the signature of cosmic neutrinos. Some can be drastically reduced, others are irreducible.

^{40}K decays

The target medium of deep-sea neutrino telescopes is sea water, which contains salt including small amounts of the radioactive isotope Potassium 40 (^{40}K). ^{40}K decays through β-decay ($^{40}\mathrm{K} \rightarrow^{40} \mathrm{Ca} + \overline{\nu}_e + e^-$,branching ratio 89.3%) releasing β-electrons with energies around 1 MeV, sufficient to produce light via the Cherenkov effect. The other important decay channel ($^{40}\mathrm{K} \rightarrow^{40} \mathrm{Ar}^* + \nu_e + e^+ \rightarrow^{40} \mathrm{Ar} + \gamma + \nu_e$, branching ratio 10.5%) yields a photon with an energy of about 1.5 MeV, that produces electrons via compton-scattering. These electrons can also carry enough energy to produce Cherenkov light.

Cherenkov photons from ^{4}0K decays form a steady, isotropic background in the sea water with rates of the order of 100 Hz per square centimeter of photocathode area.

Although the rates per PM are moderate compared to the time it takes a muon to pass the detector (which is in the range of a few µs depending on the muon direction and the size of the detector), there is a chance that a random pattern of ^{40}K hits may mimic the signature of a muon track or shower, thus producing a 'fake' event. Even more important is the effect that the background photon signals obscure the hit pattern of a neutrino-induced muon or shower-event.

Higher energy muon tracks and showers generally produce a lot of Cherenkov photons, thus reducing the chance that ^{40}K noise can mimic such an event. However at energies below 1 TeV, where only few photon signals are produced by a muon or shower, the probability for fake events increases. The ^{40}K background can be greatly reduced by requesting local coincidences in clusters of photomultipliers. The probability for random coincidences by ^{40}K-hits is low. Another common measure is to apply a threshold on the amplitudes of the hits. As hits caused by ^{40}K generally have amplitudes corresponding to one photo electron (pe), a cut on the hit amplitudes will help to reduce the number of surviving noise hits. As Signal hits have a higher probability of larger amplitudes (at least at higher energies), they are not as strongly affected by the threshold.

Bioluminescence

The deep sea is inhabited by a large number of life forms, ranging from protozoans to larger animals like fish. Most of these creatures emit light through different processes in a broad range of wavelengths. This bioluminescence interferes with neutrino telescopy. The bioluminescence background has two components. The first produces light with steady baseline frequencies of up to kHz per square centimeter of photocathode area and is generally attributed to bioluminescent bacteria (actually it is not easy to decide which part of a steady baseline rate is due to ^{40}K decays and which is due to bioluminescence). The second component produces sharp, localised bursts of light with high rates and is most probably connected to larger animals passing the detector.

The experience of the ANTARES experiment implies that bioluminescence follows seasonal variations depending on currents and the vertical movement of nutrient-rich water due to cooling/warming effects on the surface [55]. Rates as high as a several MHz (per 10"PM) have been measured by ANTARES in spring, severely hampering neutrino detection. As the bioluminescence background depends (among other things) strongly on the depth this is of course site dependent (as measurements by the NEMO and NESTOR collaborations show [56,57]).

As for ^{40}K background the bioluminescence background can be reduced by coincidence methods. Of course this is only feasible if the rates are low enough.

Atmospheric muons

Cosmic rays entering the atmosphere produce extensive air showers (see chapter 2). One component of these air showers are high energy muons that are produced in large numbers. Of course there is no basic way to differentiate between a neutrino-induced muon produced outside the detector and an atmospheric muon. This is one of the reasons why the deep sea is chosen as detector site, as the thousands of meters of sea water above the detector

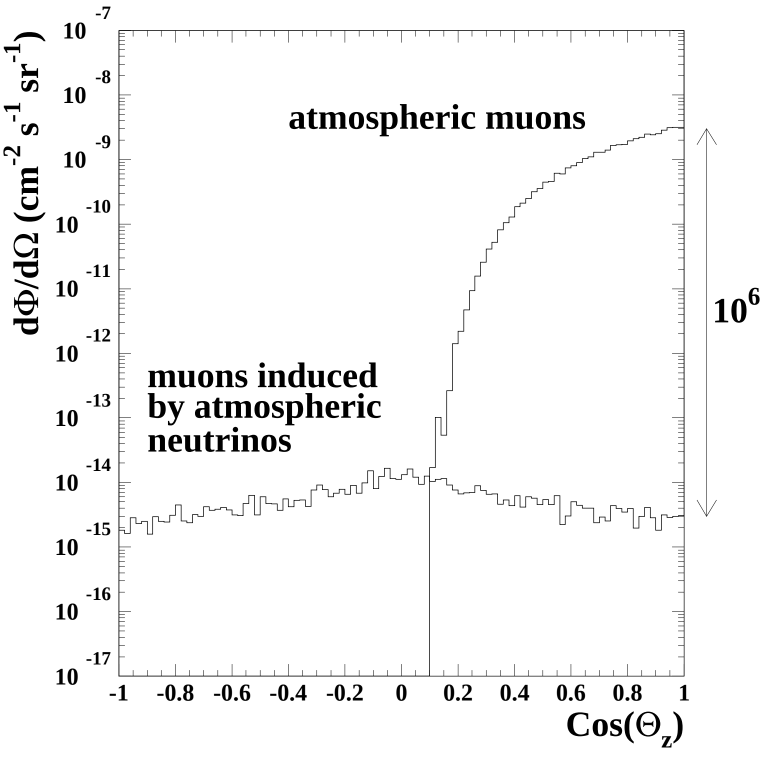

Figure 4.6: Flux of atmospheric muons and atmospheric neutrino induced muons as function of zenith angle at detector level. Taken from [58].

shield it against atmospheric muons. However as the flux of these muons is very high, a large number still reaches the detector.

To get rid of this background, existing neutrino telescopes concentrate on upgoing muons, thus using the Earth as a shield against the atmospheric muons. In Fig. 4.6 the flux of atmospheric muons and of muons induced by atmospheric neutrinos is shown as a function of the zenith angle. The flux of downgoing atmospheric muons exceeds the flux of neutrino induced muons by a factor of 10^6, whereas muons coming from below are definitely neutrino-induced. However, multiple coincident downgoing muons can produce a photon hit pattern that resembles the one of an upgoing muon. The rate of these fake events is fairly low, but significant with respect to the estimated rates of cosmic neutrinos.

For km^3-scale detectors, neutrinos with energies above a few hundred TeV are also of interest, as the larger effective detector volume compensates for the lower flux. The neutrino-nucleon cross section increases with energy to a level where at about 100 TeV-1 PeV the Earth starts to become opaque for neutrinos. Therefore it is necessary to look upwards at these energies. In Fig. 4.7 the interaction lengths of neutrino nucleon interactions are shown as a function of neutrino energy. Starting at about 40 TeV the interaction length gets shorter than the diameter of the Earth, so that at higher energies a significant part of the incident neutrinos is absorbed in the Earth. Simulations of the atmospheric muon background for ANTARES [59] lead to the result that at these energies the flux of atmospheric muons at the detector is low enough to allow us to identify cosmic

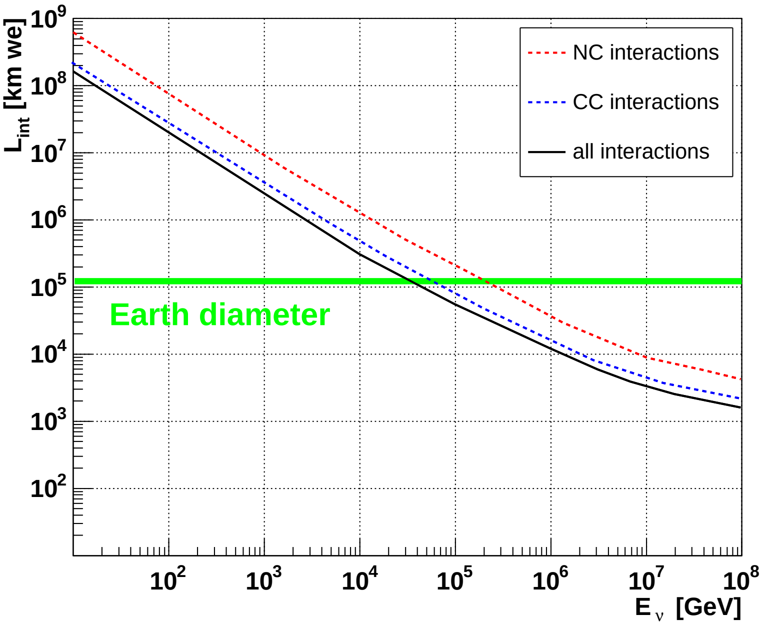

Figure 4.7: Interaction lengths for different types of neutrino-nucleon interactions, given in km water equivalent. The diameter of the Earth has been calculated, according to the parameterisation given in Fig. 6.1. Taken from [60].

neutrinos coming from above.

Atmospheric neutrinos

The cosmic ray interactions in the atmosphere produce large amounts of charged pions and kaons, whose decay produces neutrinos, resulting in a large flux of atmospheric high-energy neutrinos. These form an irreducible background for the detection of cosmic neutrinos. However, the energy spectrum of atmospheric neutrinos is softer than the expected spectrum of the diffuse flux of cosmic neutrinos (see Fig. 4.8), so that it is possible to search for an excess of neutrinos over the expectation of atmospheric neutrinos at higher energies. For the search for point-like sources, the size of the search cone, which is directly connected to the angular resolution, defines the influence of the atmospheric neutrino background on the detection probability. On the other hand, the flux of atmospheric neutrinos is important for detector calibration and testing.

Several parametrisations of the atmospheric neutrino flux are shown in Fig. 4.8 and compared to the cosmic diffuse flux limit by Waxman and Bahcall [8]. In addition to the energy the atmospheric neutrino flux depends on the zenith angle. For horizontal directions, the mean free path length in the atmosphere of pions and kaons produced by cosmic ray primaries is longer than for small zenith angles (more of the path is in the less dense upper atmosphere). This increases the decay probability (compared to the interaction probability) and therefore the neutrino flux. The atmospheric neutrino flux as a function of energy and zenith angle is shown in Fig. 4.9.

In addition to pions and kaons, charmed particles are produced in the interactions of

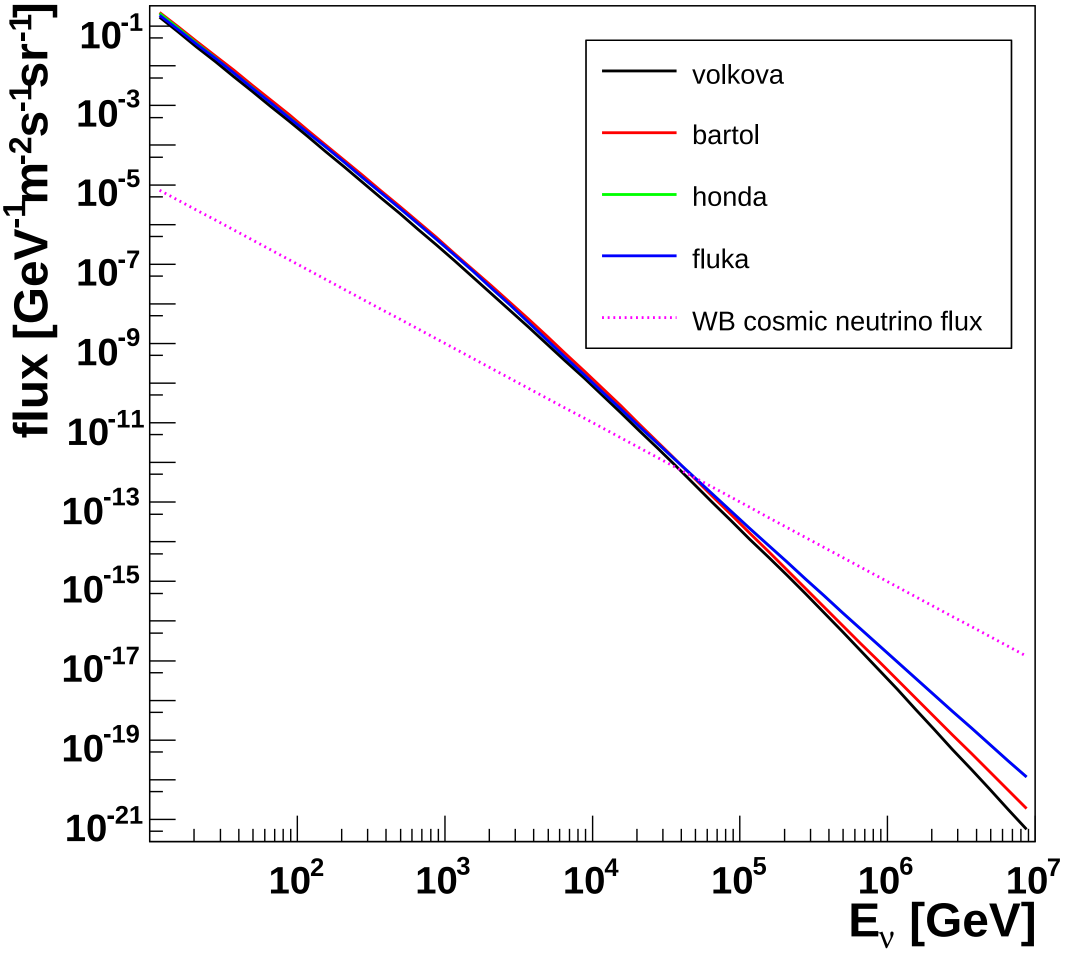

Figure 4.8: Zenith-averaged atmospheric neutrino flux, calculated from different parametrisations (Volkova [61], Bartol [1,62], Honda [63], Fluka [64]). The differences are small at lower energies, where the fluxes are high. The cosmic neutrino flux limit of Waxman and Bahcall [8] is included to illustrate the different energy spectra (see section 6.5).

cosmic rays in the atmosphere. The decays of these particles also induce a small neutrino flux, generally called the 'prompt' flux (while the flux produced through pions and kaons is called 'conventional' flux). This flux is less well known than the conventional flux and the different models differ significantly (by orders of magnitude). Some of these models, combined with the conventional Bartol flux, are compared in Fig. 4.10. The prompt flux starts to dominate at energies above 100 TeV, which is exactly the region of interest for the search for cosmic neutrinos from the diffuse flux. For the diffuse flux limit calculations in this work an intermediate model, the QGSM model ('qgsm_pe' in Fig. 4.10), was chosen. For the flux limits for point-like sources the prompt contribution was neglected, as the search for point-like sources focuses on lower energies, where the prompt contribution is negligible compared to the conventional atmospheric neutrino flux.

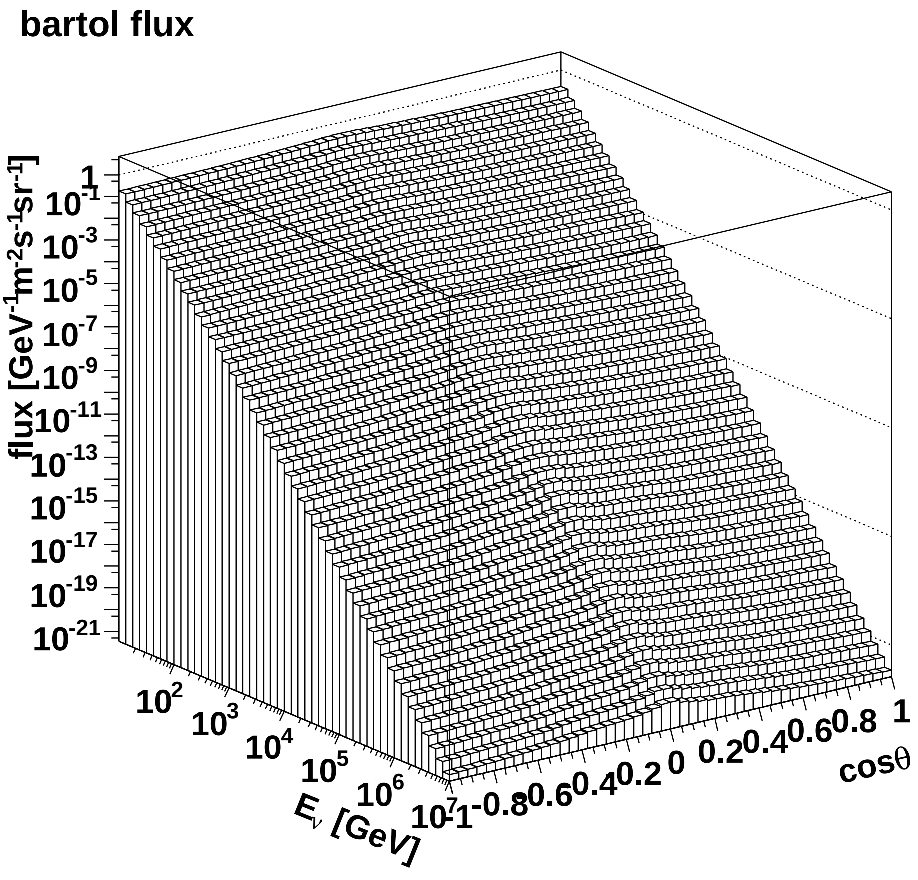

Figure 4.9: Energy and zenith angle dependence of the Bartol flux. For horizontal directions the flux increases due to the increased mean free path length of the particles producing the neutrinos in the atmosphere.

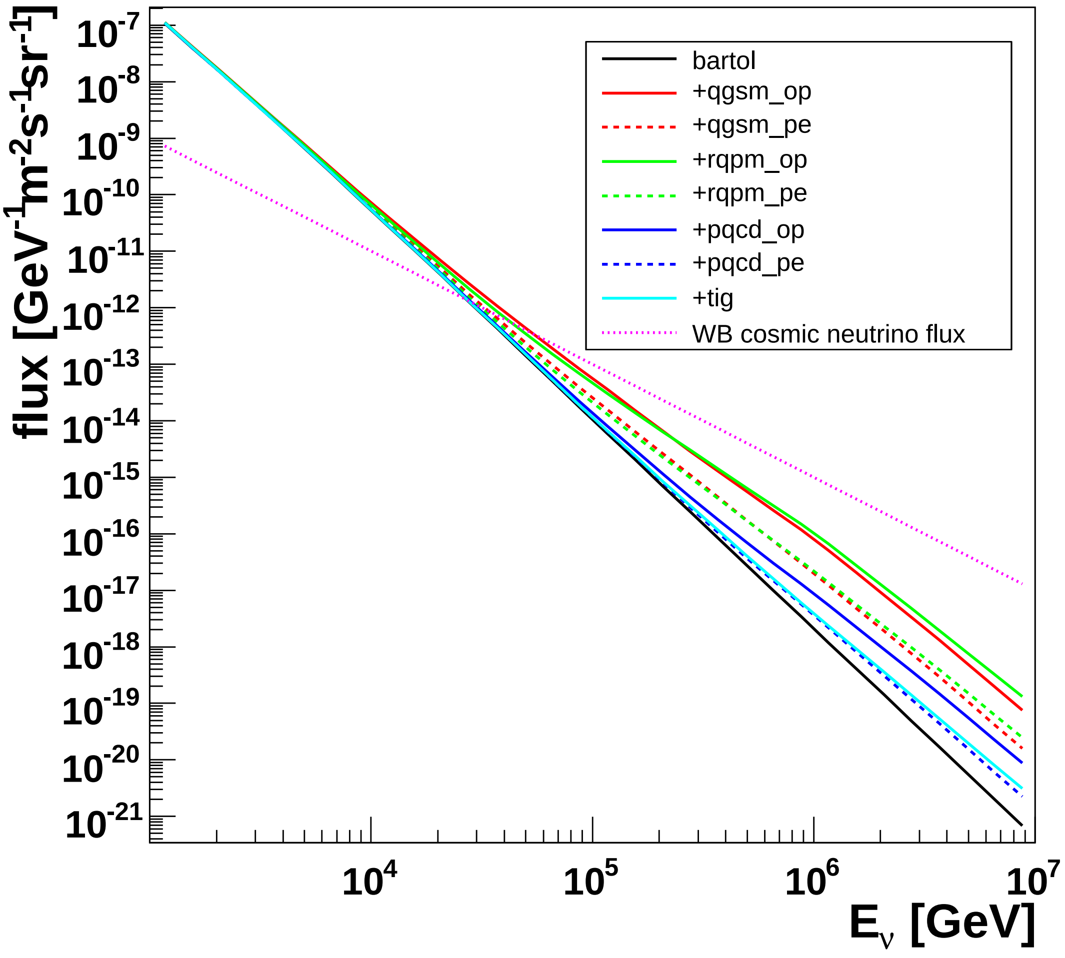

Figure 4.10: Comparison of different parametrisations of the prompt atmospheric neutrino flux. The calculation of these fluxes and the models used are described in [2]. The TIG model is described in [65]. The fluxes presented here were calculated using the ANTARES software neutrino flux library.

4.1.4 The influence of the medium

The performance of a neutrino telescope depends on the medium and environmental parameters. For detectors in the deep glacial ice, the ^{40}K background rates are negligible and obviously there is no bioluminescence. Therefore there is almost no optical background for the photomultipliers. Furthermore, the absorption length is large compared to sea water. On the other hand there are several disadvantages: The transparency of the ice depends on the depth, which has to be measured and included in any analysis. The probably most important advantage of water over ice is the light scattering length which in ice is in the range of 20 m implying that almost all the photons detected will have scattered repeatedly and will have lost their directional information. The effective scattering length [1] in water for blue light (UV) is about 250 m (120 m) [66] and therefore of the order of typical distances between detector components. Because of this, the spread of the arrival times of the photons in the PMs in sea water is smaller compared to ice, resulting in better timing.

4.2 Alternative methods - the future of neutrino telescopes?

Apart from the optical detection of cosmic neutrinos in water or ice, other options have been discussed in the past and are under consideration. Though they are based on very different techniques, they all focus on very high neutrino energies, where the flux becomes very low and huge detector volumes are required. As the distances between sensors in a Cherenkov telescope are limited by the absorption length in water, it is difficult to instrument such large volumes using the common optical detection.

Radio Cherenkov technique

Neutrinos interacting with the target medium induce an electromagnetic cascade or a hadronic cascade with an electromagnetic component. As the positrons in the cascade annihilate in the medium and electrons accumulate through Compton scattering and pair production, an excess of negative charge is created. This propagating negative charge cloud emits Cherenkov radiation, which is coherent for wavelengths larger than the dimension of the cascade. Since ultra-high energy cascades in matter have a typical length of several meters, the emission is in the radio frequency range. This coherent radio-emission was first postulated by G.A. Askaryan in 1962 [67]. If the medium is transparent for radio waves, they have a huge range and large target volumes could be instrumented with few sensors. In the antarctic ice the transmission of radio waves in the generated frequency band is almost lossless and scattering is minimal. Two experiments aim to use this for neutrino detection: One of the experiments is RICE (Radio Ice Cherenkov Experiment) [68]. The underlying idea of the RICE (Radio Ice Cherenkov Experiment [68]) experiment is to bury an array of radio receivers in the ice to detect the radio emission.

---

[1] The effective scattering length λ_{scat}^{eff} is defined by $\lambda_{scat}^{eff} = \lambda_{scat}/(1-\overline{cos\theta})$, where λ_{scat} is the scattering length and θ is the scattering angle.

The other experiment is ANITA (Antarctic Impulsive Transient Antenna) [69] which uses a balloon equipped with radio antenna to detect the radio signature of neutrino interactions in the ice from a height of about 37 km, allowing for an observed area of 1.5 million km^2 (area limited by the horizon). The balloon circles around the South Pole, driven by the circumpolar winds and travels for about 30 days (first flight in December 2006). The detectable energy range of neutrinos is between 0.1 and 100 EeV.

Horizontal Air Showers

When an extended cosmic ray air shower is induced by an almost horizontal cosmic ray primary in the high atmosphere its electromagnetic component will be attenuated by the atmospheric slant depth. Cosmic high energy neutrinos, on the other hand, may interact deeper in the atmosphere and can therefore produce showers with a large electromagnetic component at the surface. This can be detected by air shower arrays. The AUGER observatory might have a chance to detect neutrinos this way, with an energy threshold of about 1 EeV. A planned experiment using the same principle, but a different detection strategy is EUSO (Extreme Universe Space Observatory [70]). The EUSO detector is planned to be attached to the Columbus module of the International Space Station and would detect air showers by the fluorescence effects they induce in the atmosphere (similar to the HiRes experiment and the AUGER fluorescence telescopes). The advantage of EUSO over ground based detectors is that it actually uses all of the atmosphere visible from its position in orbit as detection volume. Due to this high position EUSO may also look for neutrinos that pass the rim of the Earth, interact in the rock and produce almost upward air showers (at the energies interesting for EUSO the Earth is opaque for neutrinos, but a bit below the horizon the depth of traversed rock may be small enough for the neutrino to pass). With this method neutrinos with energies from 10^{19} eV upward can be detected. Unfortunately the future of the EUSO project is uncertain.

Acoustic neutrino detection

In the 1970s G.A. Askaryan formulated the so-called thermo-acoustic model [71]. It describes the emission of acoustic signals by high-energy hadronic or electromagnetic cascades dumping their energy in a medium. This effect can be utilised for neutrino detection. A neutrino interacting in water or ice can induce a particle cascade which heats the surrounding medium locally forcing it to expand. This expansion produces a bipolar pressure pulse, or in other words an acoustic signal, with a frequency spectrum mainly in the range between 10 and 100 kHz. Such signals can be detected by underwater sound sensors, called hydrophones. The advantage of the acoustic method, compared to the optical detection, is the very long attenuation length of sound waves at these frequencies in water or ice, which is in the range of a few kilometers. This would allow to instrument large volumes as the maximum distance between sensors is closely related to the attenuation length. The principles of the thermo-acoustic model have been thoroughly tested over the last decades [72–75], and members of the ANTARES and IceCube collaborations have started with prototyping activities and first in situ tests of this technique. Further experiments aiming at acoustic neutrino detection are SAUND [76] and ACORNE [77].

The neutrino energy threshold is defined by the signal-to-noise ratio of the acoustic signals. In the relevant frequency band in sea water the dominant part of the noise is caused by sea state dependent surface noise and the thermal noise of the water molecules. This limits the threshold to about 100 PeV or probably more. The largely unknown acoustic background in ice is currently measured by the IceCube acoustic detection group. A detailed discussion on acoustic detection and studies for acoustic detectors in water can be found in [78].

4.3 Past and current water/ice Cherenkov telescopes

There are a number of neutrino telescope projects. Some of them are or have been running, while others are in the construction, prototype or planning phase. This section provides an overview of these experiments, their current status and their planned future.

DUMAND

The Deep Underwater Muon and Neutrino Detection project (DUMAND) [9] was the first deep sea neutrino telescope project. It started around 1976 and planned to deploy the detector in the Pacific ocean off Keyhole Point on the Big Island of Hawaii, at a depth of 4800 m. Among many preliminary studies, a prototype vertical string was suspended from a ship to demonstrate the technology. A major step was the deployment of a string of photodetectors, an instrumentation line with environmental instruments and a junction box to connect these components to a deep sea cable in 1993. Unfortunately after a while short circuits occurred in the electronics and the connection was lost. In 1995 the US DOE cancelled further funding on DUMAND. Despite the fact of its early end, the DUMAND project did a lot of fundamental work for the neutrino astronomy community, which is now utilised by its successors.

Baikal

This experiment is located in the Lake Baikal [10] which provides unique properties compared to other neutrino telescopes. First of all the Baikal lake consists of fresh water, thus greatly reducing the ^{40}K background. Additionally the lake freezes over in winter allowing for very easy deployment and maintenance procedures. On the other hand the absorption length in the lake is rather short ($< 20\,\mathrm{m}$) compared to the deep-sea sites. Furthermore the Baikal telescope is deployed at a relatively low depth and therefore suffers from a very high flux of atmospheric muons.

The first part of the detector was deployed in 1993 and consisted of three strings with 36 PMs in pressure resistant glass spheres (generally named optical modules or in short OMs), that were lowered to a depth of 1 km. This setup worked continuously for about a year. With the next step the detector was enlarged to 192 OMs on 8 strings, the so called NT-200 layout. It was the first deep-water neutrino telescope to detect several neutrinos in 1996.

The top of the detector houses the main control block and a calibration laser, from there the string support structure spreads out to hold the eight 68.5 m long strings in a

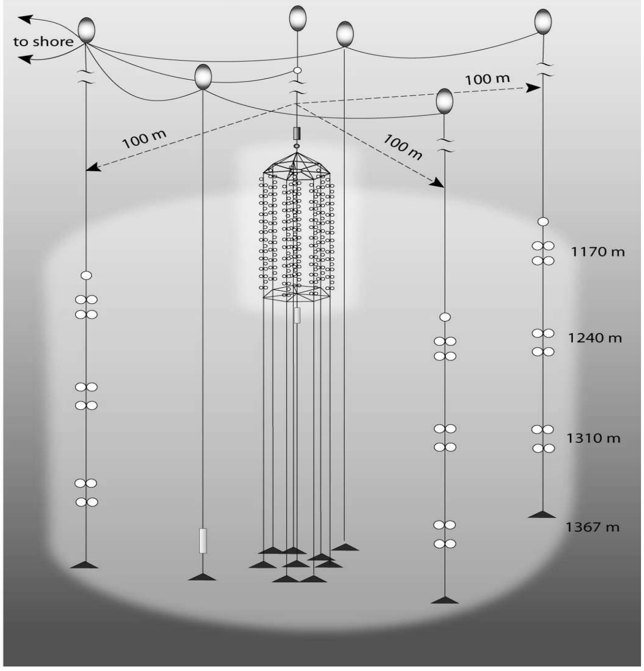

Figure 4.11: Schematic view of the Baikal NT-200+ telescope: Three additional strings, each equipped with 36 OMs, have been added to the NT-200 array to increase performance for shower detection (taken from [79]).

circle geometry with a radius of 21.5 m. Each string is equipped with a string control block on top and then an alternating series of photodetector and electronics units. The Photodetector storeys are equipped with two Russian 'Quasar' PMTs, looking downward.

Recently the detectors effective area for showers was increased, by deploying three additional, 200 m long strings with 36 PMTs each at a distance of 100m from the detector center (NT-200+) [10]. This layout is shown in Fig. 4.11. The promising results have triggered the idea to extend this shower optimised detector to a volume of one km^3 with minimal effort. The idea is to build an array of detectors that are shaped like the NT-200+ geometry, but with the core detector replaced by a single string. These structures would be arrayed to achieve a km^3 of detection volume. This layout is shown in Fig. 4.12 as a schematic. The detector would be optimised for the search for neutrino induced cascades. A Technical Design Report will be produced until 2008. The construction is scheduled to begin afterwards.

AMANDA

The Antarctic Muon And Neutrino Detector Array (AMANDA) [11] is the first operating deep-ice neutrino telescope. It was deployed in several stages at the South Pole, near the Amundsen-Scott South Pole station. The first important step was the deployment of the AMANDA B-10 detector with 10 strings carrying 302 8"PMTs in a depth between 1500 and 2000 m, finished in 1997. In the year 2000 the second stage was completed adding 9

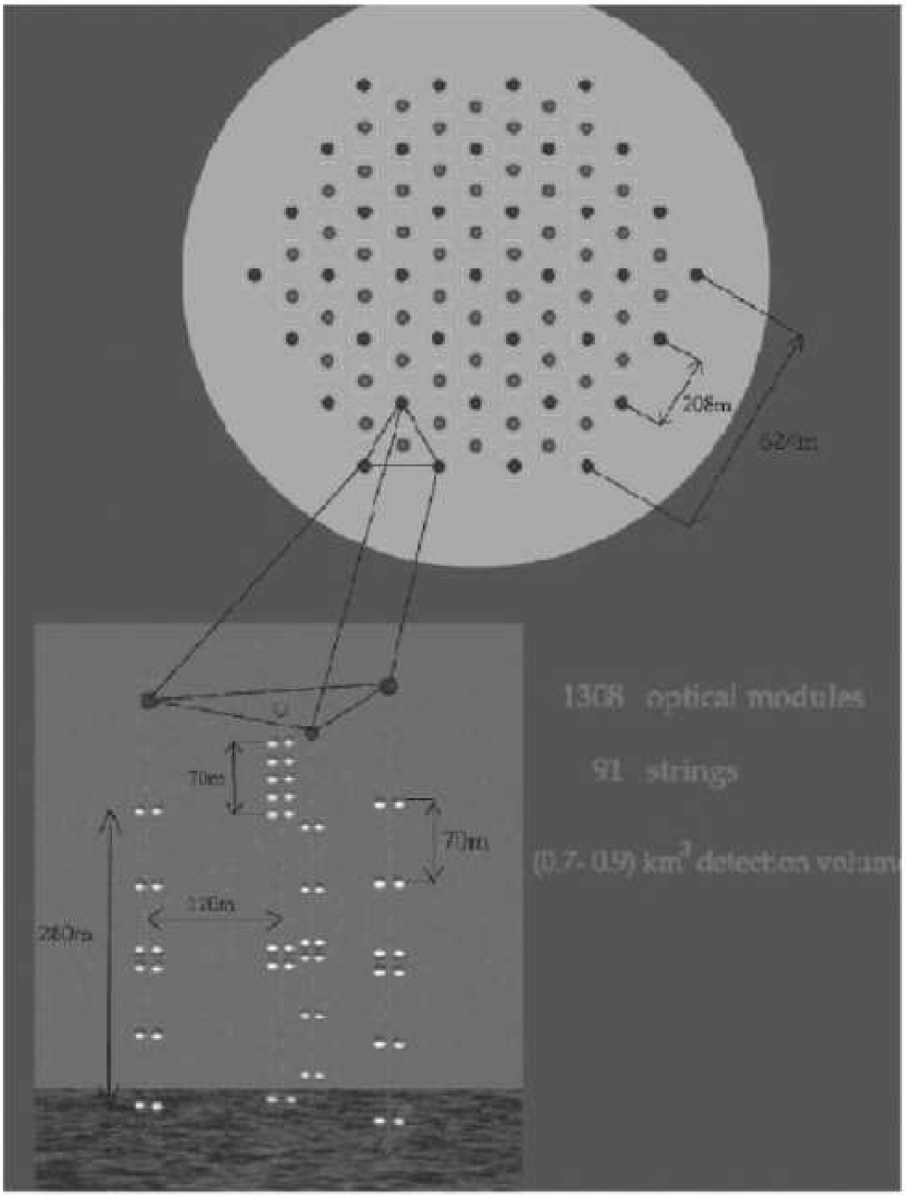

Figure 4.12: Concept Sketch for a km^3-detector in the Lake Baikal: On the bottom a schematic view of a substructure consisting of a reduced version of the NT-200+ array is depicted (with only a single string replacing the NT-200 part). In the upper part a schematic of a possible layout made of these substructures is shown (taken from [79]).

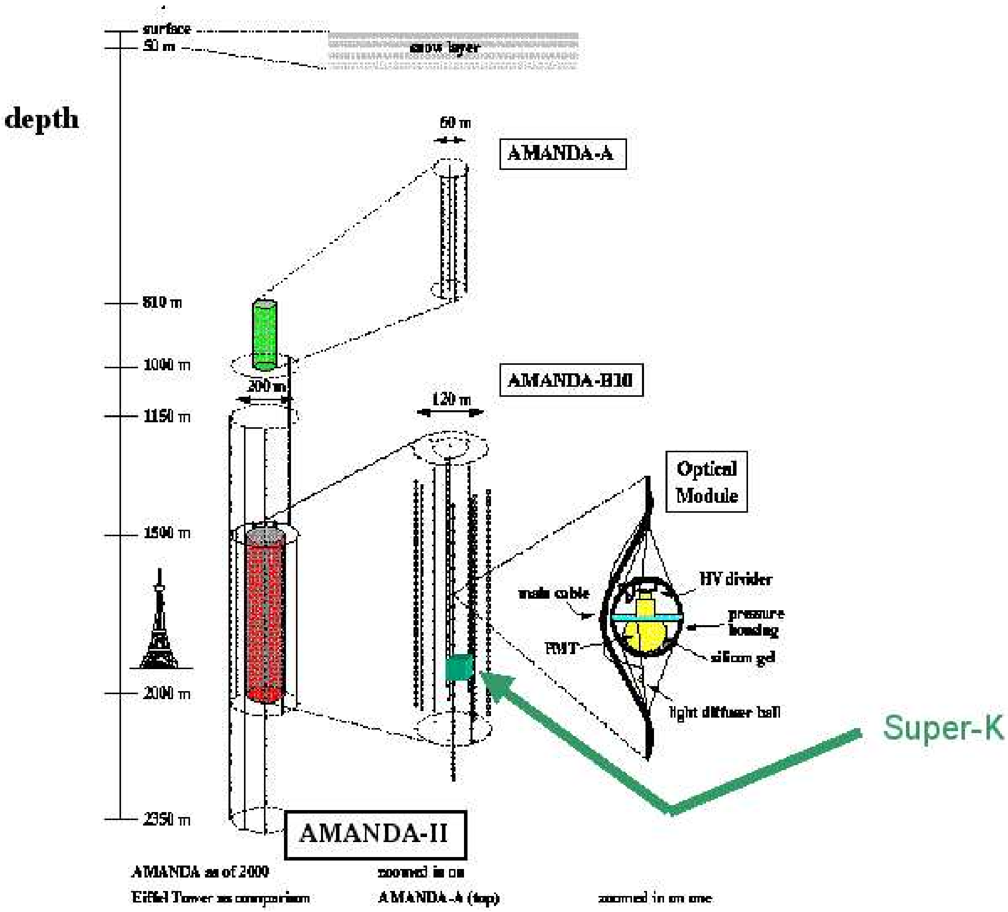

Figure 4.13: Schematic of the different stages of the AMANDA experiment with a scale for size comparison. On the right a schematic of the Optical module used is shown (taken from [80]).

additional strings to the B-10, three of them having OMs that extend to over 1000 m in depth. This so called AMANDA-II setup has a total of 677 PMs, its layout is depicted in Fig. 4.13. The analog signals of the PMs are read out and sent to the control room through copper wires. The AMANDA-II detector is taking data since 1997. A series of physics studies with the AMANDA data has been published (for example [81,82]) amongst them searches for point sources. So far, no detection of cosmic neutrinos has been reported.

NESTOR

NESTOR (Neutrino Extended Submarine Telescope with Oceanographic Research) [13] was the first neutrino telescope project in the Mediterranean Sea. Instead of flexible strings, tower-like structures are used, which consist of star-shaped rigid structures connected by cables. Each of these stars is equipped with one upward and one downward looking 13"PMT on each of its six arms (see Fig. 4.14). Several of these towers are planned to form the detector. A prototype has been tested in 2003 and atmospheric

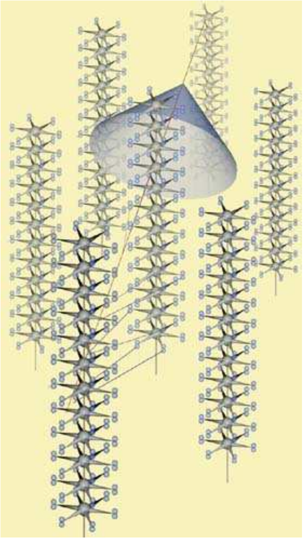

Figure 4.14: Artists view of the NESTOR detector: The detector is planned to consist of seven towers with 12 star shaped OM support structures each (taken from [83]).

muons were reconstructed successfully [84]. The NESTOR site is located 18 km of the coast of Pylos in Greece at a depth of 4000 m.

ANTARES

The ANTARES experiment (Astronomy with a Neutrino Telescope and Abyss Environmental Research) [58] is currently under construction in the Mediterranean sea, 40 km off the coast of Toulon in Southern France. When finished in the end of 2007, it will be the first fully operational neutrino telescope in the Mediterranean. In the final configuration the detector will consist of 12 strings, each equipped with 25 storeys at a distance of 14.5 m. Each storey houses an electronics container and three optical modules (OM). The OMs are equipped with 10”photomultipliers in standard pressure-resistant glass spheres and point downwards at an angle of 45°. The full detector will therefore be equipped with 900 photomultipliers. All elements are connected through electro-optical cables. Data is transferred through the optical fibre network, while power is distributed through the electrical cables. The data is transported to the bottom of the string and from there to the junction box, which connects the strings to a deep-sea cable to the shore. A Schematic view of the ANTARES detector including all the major elements is shown in Fig. 4.15, the sea floor layout is shown in Fig. 4.16. Each PM is read out by two ADC-chips (called ARS-chips, Analog Ring Sampler) which integrate the signals over a time window of 25 ns. After this it needs 250 ns to process the data. If another photon hits the PM within this time, the second chip takes over. Therefore a dead time occurs only when both chips have been hit and are processing signals. All data is sent to shore where it is processed by the onshore data filter.

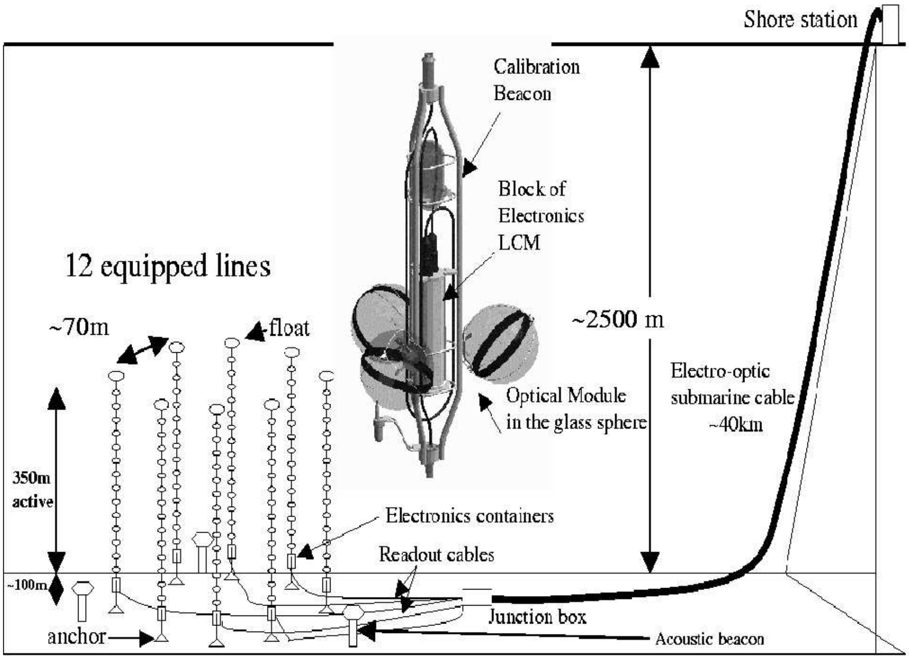

Figure 4.15: Schematic view of the ANTARES detector: The composition of the important components is shown as well as a picture of a complete storey. The storey contains the electronics container, three OMs and a LED beacon for calibration. The string layout is simplified for this picture (taken from [85]) .

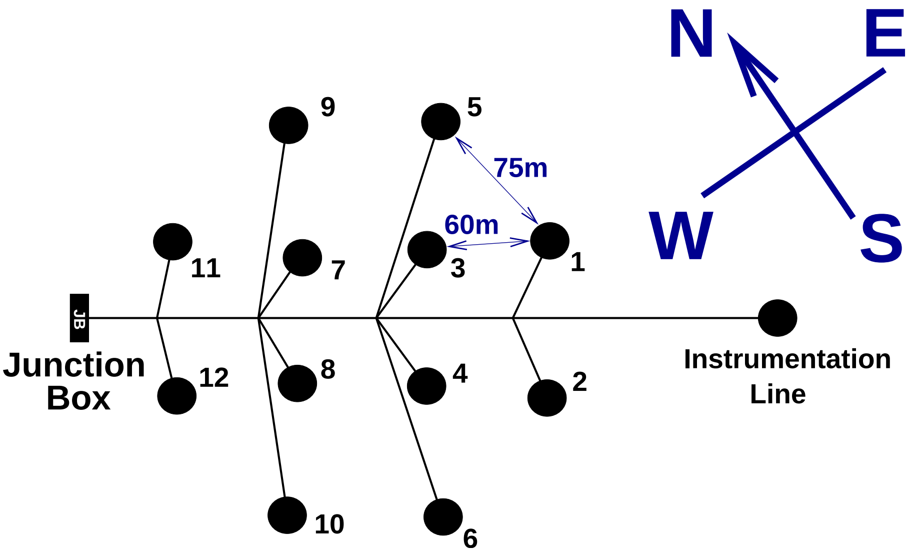

Figure 4.16: Sea floor string layout of the ANTARES detector. Each point marks the planned position of a string on the sea floor .

IceCube

The IceCube project [14] is the successor of the AMANDA experiment and is currently setting up a km^3 neutrino telescope at the South Pole in Antarctica. AMANDA will be integrated into IceCube as a sub-detector. A cubic kilometer of ice will be instrumented with 80 strings, each equipped with 60 OMs with a vertical spacing of 17 m. Each of the OMs is equipped with a downward looking 10”PMT. The string layout (Fig. 4.17) is a hexagonal grid with horizontal distances of about 125 m. Each string has a length of 1000 m. In addition a surface detector consisting of 160 water/ice tanks with two OMs each, called IceTop, will work alongside the deep-ice detector. It can be used for air shower physics, provides a veto for high-energy atmospheric muon background and will contribute to the calibration of the detector.

In contrast to AMANDA, the IceCube OMs will be read out digitally, where each of the 4800 digital OMs (DOMs) forms an autonomous data collection unit. IceCube will be the first km^3 neutrino telescope in operation.

NEMO

The NEMO (Neutrino Mediterranean Observatory) [15] project has been studying the prospects for a km^3 neutrino detector in the Mediterranean. The Italy-based collaboration has conducted extensive site exploration activities at their test site in Sicily. Additionally a concept for a km^3 neutrino telescope has been developed and prototypes are being tested.

The NEMO concept uses self unfolding towers made of 16 15 m long arms connected by cables with a spacing of 40 m (Fig. 4.18). Each arm is equipped with four OMs containing 10”PMTs, two at each end, one pointing down, the other horizontal (Fig. 4.19). The towers would be placed in a cuboid grid and connected to a junction box via secondary junction boxes (Fig. 4.20). The idea behind these tower structures is to reduce the number of structures and therefore the number of necessary deep sea connections.

A first size-reduced prototype is currently tested at a site nearer to the shore during the NEMO Phase-1. During Phase-2, a test of a full tower and all the deployment procedures is planned.

4.4 The KM3NeT project

Calculations of expected neutrino fluxes from cosmic sources, simulations of the performance of neutrino telescopes and the experiences with existing neutrino telescopes have led to the conclusion that at least a km^3 of instrumented volume is necessary for neutrino astronomy. These results have triggered the IceCube project to build a km^3 detector at the South Pole, profiting from the experiences with AMANDA.

As a neutrino telescope has to look downward to shield against atmospheric muons, and to look upward at energies above 100 TeV due to absorption of neutrinos in the Earth, it can only cover half of the sky. Situated at the South Pole, the field of view of the IceCube detector is the Northern sky (Southern sky above 1 PeV). In order to cover the whole sky a telescope in the Northern hemisphere is required. For such a detector,

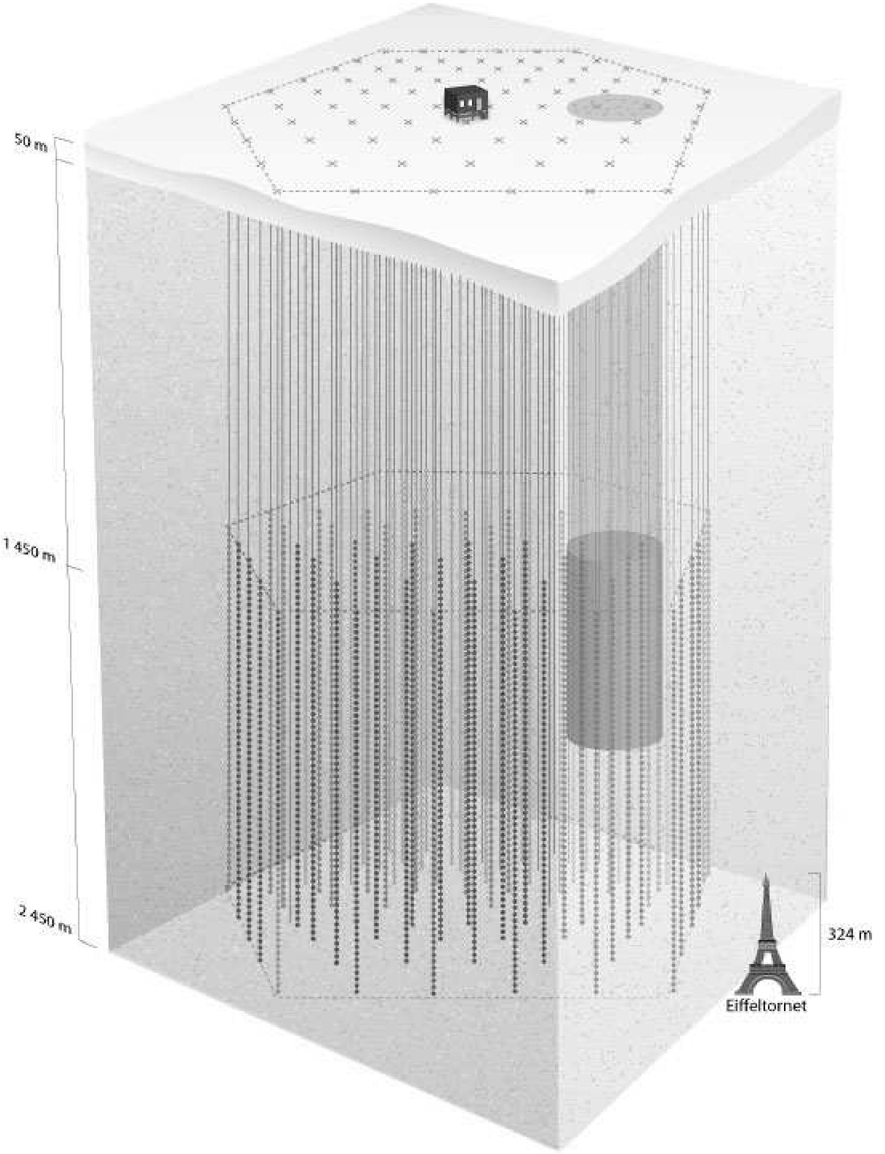

Figure 4.17: Schematic view of the IceCube detector. The grey cylinder corresponds to the position of the AMANDA detector. Taken from [86].

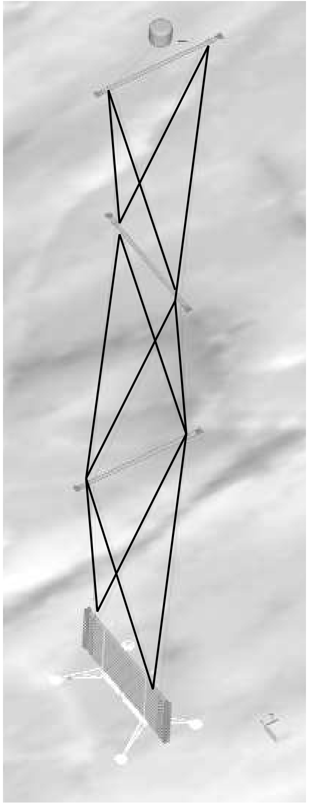

Figure 4.18: Schematic view of a NEMO tower with only three bars already unfolded. The bars are perpendicular to their neighbours and connected to them with cables. The rest of the bars is still attached to the socket (taken from [87]).

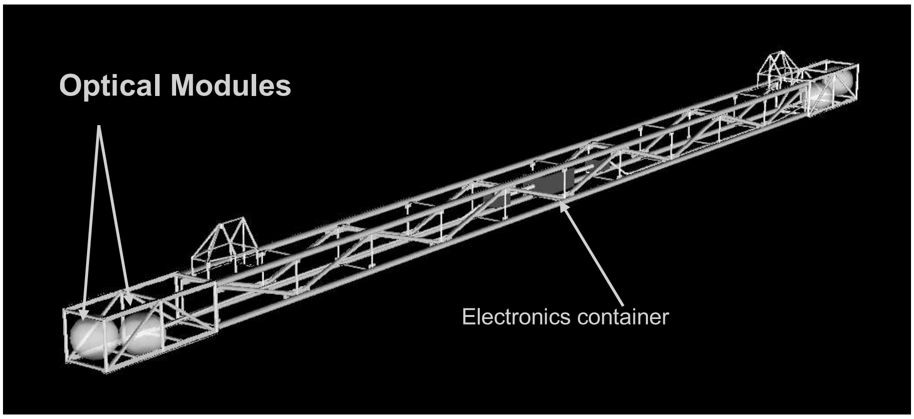

Figure 4.19: NEMO floor made of a frame containing the four OMs (2 pointing horizontally, two downwards) and the electronics container (taken from [87]).

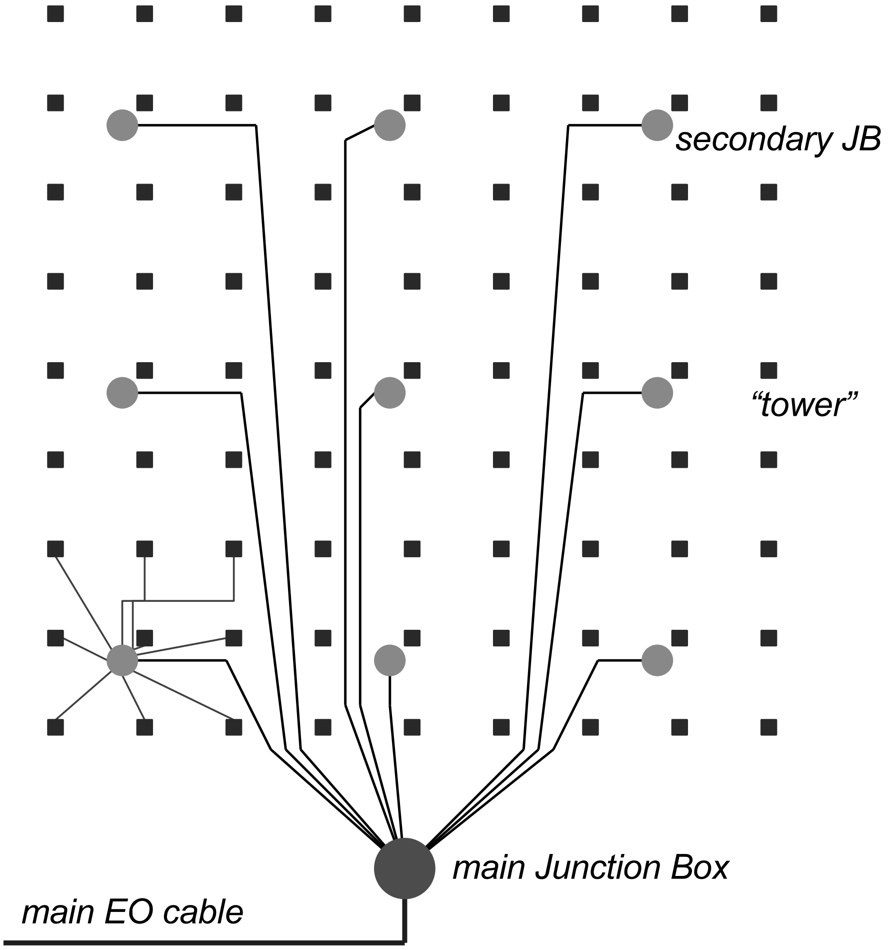

Figure 4.20: Sea floor layout proposed by NEMO. The 81 towers are positioned in a grid with distances of 140 m. Nine towers are connected to a secondary junction box. The nine secondary junction boxes are connected to the main junction box (taken from [87]).

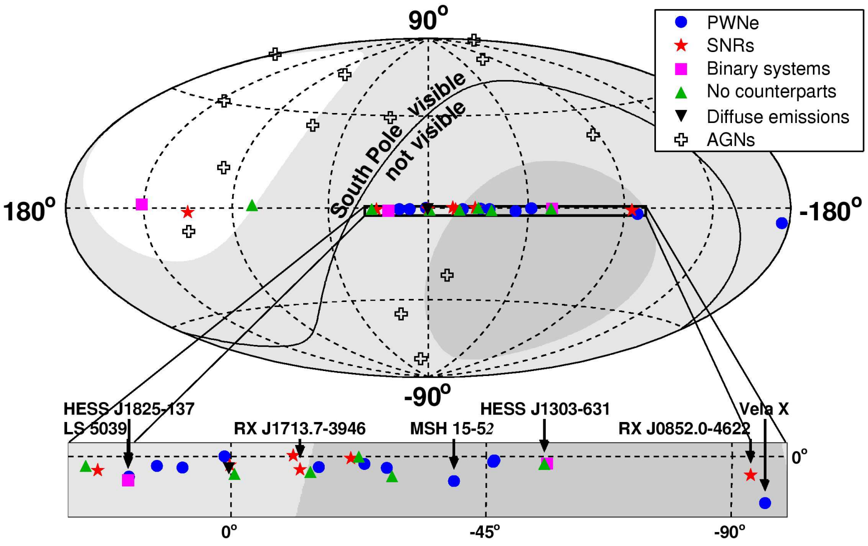

Figure 4.21: Sky coverage of IceCube and KM3NeT. A Mediterranean km^3 detectors field of view includes the galactic center and therefore a lot of the TeV gamma ray sources detected by HESS, that are also potential sources of high-energy neutrinos.

the Galactic center and many of the TeV gamma ray sources detected by HESS, that are also potential high-energy neutrino sources are visible (see Fig. 4.21). Additionally a detector in the Mediterranean sea is located closer to the equator and hence has a larger field of view. Therefore, the European neutrino telescope community decided to start the KM3NeT project [88,89] aiming for a design study and the construction for a km^3 neutrino telescope in the Mediterranean sea. With ANTARES, NEMO and NESTOR all European neutrino telescope collaborations participate in the KM3NeT Design Study, clustering all the European expertise in this field. The KM3NeT design study is funded by the European Union FP6 program [16].

The great challenge of this project is to optimise the sensitivity that can be achieved for the limited amount of money available. This prevents the use of the simple approach of expanding existing or planned neutrino telescopes to a cubic kilometer volume. As an example ANTARES has an instrumented volume of approximately 0.03 km^3. Applying the ANTARES production and deployment procedures on KM3NeT would be far too complicated and time consuming. Furthermore many factors like the power supply and the data transfer bandwidth are not easily scalable. The other simple approach is diluting the existing detectors, by increasing the distances between the detector components. As the maximum distance of photomultipliers is given by the attenuation length of light in water, which is about 60 m, a larger spacing leads to efficiency losses and hence higher energy thresholds. Therefore a completely new detector design has to be found in order to optimise the physics potential of the future km^3 detector under the given circumstances.

The KM3NeT Design Study has started in February 2006 and is scheduled to take three years. Until the end of 2007 a Conceptual Design Report (CDR) will be produced and in 2009 the final Technical Design Report (TDR), detailing all the technical aspects of the KM3NeT telescope, will be released. After this and a preparatory phase, the construction of the detector can begin in 2010 or 2011. The data taking can begin with the deployment of the first components in 2010.

This work is one of the contributions to the KM3NeT Design study.

Part II

Software and Analysis tools

Chapter 5

The ANTARES software

The task of the KM3NeT Design Study is to produce a Technical Design Report that contains all the necessary information for the construction of a km^3 neutrino telescope in the Mediterranean Sea. First of all, this requires extensive simulation studies to find the geometries, photodetection systems, and other detector components that are optimal to achieve the physics goals (see section 6.5). For this a full software chain from the simulation of neutrino interactions in the medium to the reconstruction of particle tracks and showers in a km^3-detector is required. As the time schedule of the design study is very tight, it is not possible to develop unique KM3NeT-software from scratch. Especially for first studies which have to yield results already in the early phases, existing software has to be used.

An obvious choice is to use software developed for the existing Mediterranean neutrino telescope experiments. The ANTARES and NEMO collaborations already use the same software tools, where the latter has proven that these tools can be used for different detector sizes, geometries and photodetection systems. This software package, which is quite heterogeneous, allows the full simulation from the creation of a detector model and the simulation of the detector response, including all the relevant backgrounds, to the reconstruction of simulated neutrinos, and the analysis of the results. A schematic overview of the simulation chain is shown in Fig. 5.1.

In the following sections the properties and peculiarities of the software used for this work are described. The basic functionality of the available code for the different simulation stages is briefly explained and then reviewed for adaptability and usability for km^3-detectors and different detection concepts. Finally, the necessary modifications of the code are detailed.

5.1 Detector modeling

General description

The first step of the simulation chain is the production of a software model of the desired detector, which is essentially a three-dimensional array of photomultipliers. The *gendet* code [90,91] developed for ANTARES allows to fill strings with components like optical modules (clusters of PMs) and calibration instruments like hydrophones for acoustic po-

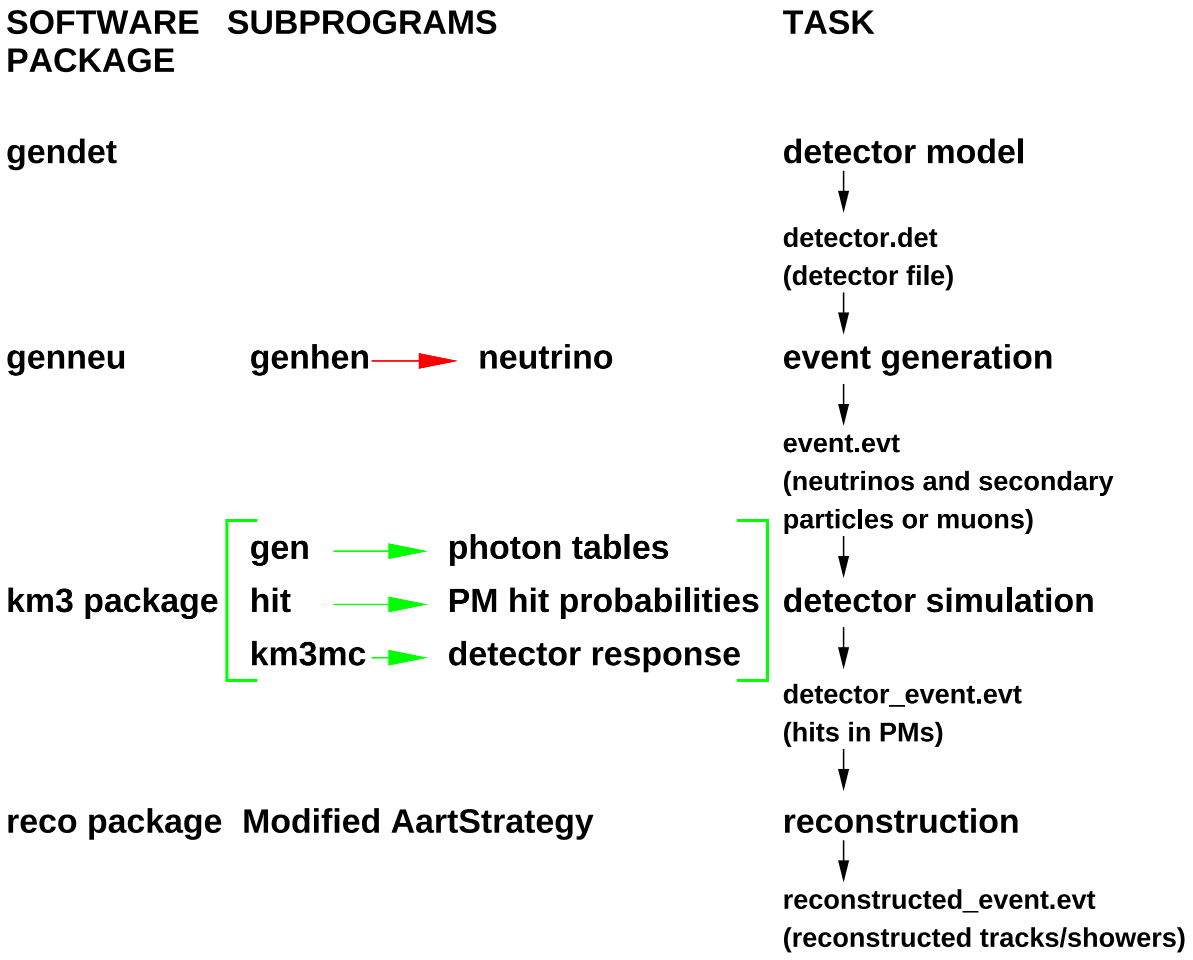

Figure 5.1: Overview of the simulation chain with the ANTARES software used in this work. The first column gives the names of the packages, the second shows the subprograms and their use (red optional, green sequential). The last column shows the task performed and the file produced by the relevant program.

sitioning and then arrange these strings according to user specified geometries (sea floor coordinates of the strings). The geometry of the clusters of PMs can be defined by giving their positions relative to the cluster center of gravity (c.o.g.) and the pointing directions. Furthermore, the diameter, effective photocathode area and Transit Time Spread (TTS) of the PMs have to be defined. Additionally the code includes the option to expose the layout to a simulated sea current and produce a therefore distorted geometry. The properties of secondary components (such as calibration instruments) can also be defined.

Usability for KM3NeT

On the first glance the *gendet* code is obviously limited to strings. But as long as one is not interested in the sea current effects (which are of minor importance for first studies) only the positions of PMs are of interest. Therefore it is possible to approximate tower structures by a corresponding placement of strings and PMs in clusters. A more severe problem might be the limitation to one type of string. In case of a detector layout with strings with different instrumentation some changes of the code would be necessary.

5.2 Event generation

General description

The next step of the simulation chain is to produce the particles incident on the detector. For this the *genhen* code (from the *genneu* package) is used.

This program includes a complete simulation of incident neutrinos, their interactions in the medium, and of the resulting secondary particles up to neutrino energies of 10^8 GeV. Produced muons are propagated to the detector and their energy loss is calculated in the process. Different atmospheric neutrino flux models are implemented in the code allowing the calculation of atmospheric neutrino event rates (see Fig. 4.8).

A cylindrical volume containing the instrumented volume of the detector, extended by three times the light absorption length in water.is defined as the 'sensitive area' (the so-called 'can-volume') The generation volume for neutrino interactions is defined as the volume given by the detector radius plus the maximum muon range at the maximum neutrino energy specified (limited by the sea surface). Neutrinos with energies according to a user defined power law spectrum are generated within this volume and their interactions are simulated, taking into account the different media, rock and water, around the detector. The neutrino direction is sampled isotropically in a user defined zenith angle range, or can be produced according to a point source with a given declination. The neutrino interactions are then simulated using LEPTO [92] (for deep inelastic scattering) and RSQ [93] (for resonant and quasi-elastic events), where a wide range of parton distribution functions can be chosen. In the case of muon neutrino outside the can, the muon is transported to the can using one of the muon propagation codes MUSIC [94], MUM [95] or PropMu [96].

Usability for KM3NeT

The *genhen* code can be used for km^3-detectors with only minor technical changes.

5.3 Detector simulation

General description

The task of the detector simulation is to define the detector response to incoming charged particles. Therefore it has to simulate the Cherenkov light emission from the particle tracks, transport the light to the photomultipliers and then transform the incoming photons to hits, optionally applying the simulation of the electronics. The ANTARES software includes two packages for this task.

The *km3* [97] package can only be used for incoming muons. It includes light scattering and is by default used for the simulation of muons in ANTARES. As tracking all the produced photons with a program like Geant [98] takes a lot of time, a different approach was chosen. The program *gen* is used to record the light output at different distances of a defined length of muon track (typically 1 or 2 m) or secondary electromagnetic shower. Several concentric spheres are placed around the track segment at different distances and all direct and scattered photons arriving on each of these spheres are stored (this uses full Geant [98] simulation). The inputs for *gen* include the absorption and scattering lengths. In addition the number of spheres and their distances can be specified.

The program called *hit* divides these shells into several angular bins and then transforms the photon fields into tables containing the hit probability in a PM with respect to the PM's distance and orientation relative to the segment. All the PM properties are defined in the *hit* code. In order to produce the hit probability tables the effective PM photocathode area is calculated according to,

$$A_{\mathrm{eff}}(\theta, \lambda) = q(\lambda)a(\theta)ct(\lambda) \tag{5.1}$$

where θ is the photon angle relative to the PM axis, λ the wavelength of the photon and q the quantum efficiency, a the angular acceptance, and the c the collection efficiency of the photomultiplier. The factor t is the wavelength-dependent transmissivity of the glass container in which the PM is placed and the gel used for the optical connection between the PM window and the glass of the container. No further properties of the PM are used. Generally, the photon tables from *gen* have to be produced only once, while the probability tables from '*hit*' have to be reproduced for every simulated photomultiplier type. It should be noted that these tables significantly influence the results of the detector simulation.

The actual detector simulation is done by the *km3mc* detector Monte Carlo. This program transforms the incoming tracks into a pattern of PM hits with amplitudes and arrival times. The muons are propagated through the medium using the MUSIC [94] muon propagation code, by generating track segments with a length corresponding to the one used for the photon field generation, until they are stopped or leave the detector. For each step, the energy loss, the start and end positions and the direction and time of the muon are stored in arrays. If the energy loss is above the energy loss by ionisation (or a user defined threshold), a secondary electromagnetic shower is produced at this location and added to the particle stack, to be processed afterwards. If the array is filled with the information for all the track segments, the probability distributions from '*hit*' are used to compute the PM hits (segment by segment). After the simulation of the response ^{40}K noise is added, with a user defined rate in a user defined time interval before the first and after the last signal hit. The rate per PM is sampled according to a Poissonian distribution. The hit times can then be smeared according to the TTS of the photomultiplier, the amplitudes can be modified according to a gain distribution of the PM that can be chosen from several options (Gaussian by default). Finally, a simplified electronics simulation can be applied, if required, simulating the ANTARES electronics. For this all hits arriving within a user-defined time window are integrated and then a dead time is applied (for a short description of ANTARES readout see section 4.3).

The second detector simulation code is called *geasim* [99] and is basically an interface to Geant (v3). Incoming particles and the Cherenkov photons are tracked with Geant. The obvious advantage is that all particle types can be processed, but on the other hand no light scattering is included. Generally *geasim* is used for shower simulation; it offers a mode where it can be used to simulate the response to the hadronic component of a muon-neutrino CC-interaction (where the muon is simulated with the *km3* package).

Usability and modifications for KM3NeT

For the Design Study a lot of different detector and PM geometries have to be simulated, as well as different types of photomultipliers. In addition, the detector configurations under study have many more optical sensors than ANTARES. This required several changes.

First of all the use of *geasim* for broad studies is limited by computing time requirements. Therefore the hadronic component of muon-neutrino CC interactions was neglected in this work (it contributes only if the vertex is inside or close to the instrumented volume). The *km3* code had to be modified as follows: Several technical problems had to be solved, like the adjustment of maximum detector size parameters or the adaptation of the output to larger numbers of PMs and hits. The *hit* subprogram was modified to easily allow for the simulation of different photomultiplier types (without having to change the source code). This required to add the relevant data for the quantum efficiency of the PMs in question and to provide functions for their angular acceptance. These properties can now be defined as a user input, along with the diameter of the PM. Further specific modifications were necessary for some of the photodetection layouts used in this work.

5.4 Trigger software

The ANTARES trigger is part of the Data Acquisition (DAQ) software, which is a very sophisticated piece of code and very specialised for the ANTARES detector. Therefore it is difficult to use it for detector layouts, that are very different. As the code structure is optimised for time performance it is also not easy to modify it. Because of this the trigger software has not been used for this work.

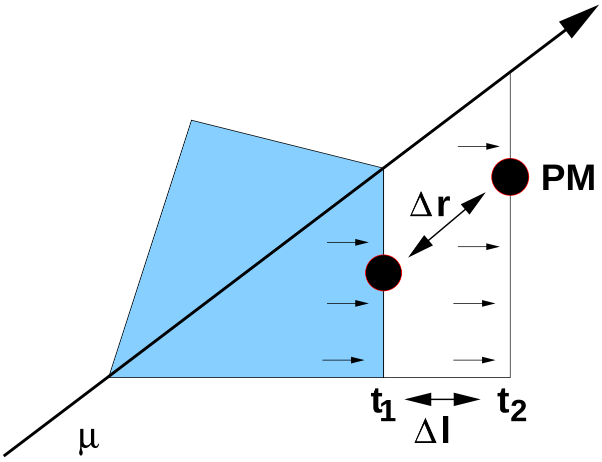

Figure 5.2: Schematic drawing of the Cherenkov light propagation from a muon track.

5.5 Reconstruction

General description

The ANTARES reconstruction code consists of a framework (called *reco*) that serves as an interface to different reconstruction strategies. Two of these strategies are commonly used for muon reconstruction, the *CarmonaStrategy* [100] and the *AartStrategy* [101], both named after their creators. The latter one is the standard reconstruction strategy for muons in ANTARES and will be explained in more detail.

All hits on the same cluster of PMs (a storey) within the coincidence time gate are part of a local coincidence. These hits are marked and the hit with the highest amplitude is used as input for the causality filter, which checks for all hits whether they are causally connected to this high-amplitude hit. A hit is called causally connected if the following condition is satisfied,

$$|\Delta t| - \frac{\Delta r}{c_n} < 100\,\text{ns}, \tag{5.2}$$

where Δt is the absolute time difference between the hits, Δr is the distance between the PMs that have been hit and c_n is the group velocity of light in water (at $\lambda = 460\,\text{nm}$). The situation is illustrated in Fig. 5.2. The front of light of the emitted Cherenkov photons moves with the velocity c_n. For the distance Δl between the position of the front at time t_1 and time t_2 one obtains,

$$\Delta l = c_n |t_2 - t_1|. \tag{5.3}$$

For the distance Δr between a PM on the front at t_1 and another PM on the front at t_2, one obtains $\Delta l \leq \Delta r$, yielding $\Delta l - \Delta r < 0$. The 100 ns threshold takes into account time delays due to light scattering in water and the jitter in the electronics. Only hits that pass the causality filter are used in the reconstruction algorithm.

The reconstruction process is outlined in Fig. 5.3. The muon reconstruction algorithm is basically a set of consecutive fits, where the result of one fit is used as a starting point for the next one. The first step is a geometric prefit, followed by three maximum likelihood fits. All of the likelihood fits use the time residuals, the differences between the theoretical expectation of the time of a hit (relative to a given track) and the measured time. The first of the fits, called the M-Estimator fit, uses a parameterised likelihood function of the time residuals. This function is robust, in the sense that it optimises the efficiency for finding the global minimum during the minimisation. This is followed by a likelihood fit using a likelihood function composed of the distribution of the time residuals and the angular acceptance of the PMs. The final fit uses the same function, extended by the expected optical background noise. For details of the likelihood functions see [102].

In order to increase the reconstruction quality, the prefit track is subjected to set of geometric transformations and the following two fits are used on all of these transformed tracks. The best solution, the one with the best likelihood, is then used as the starting point for the final fit.

The general idea of this reconstruction strategy is to provide increasingly better estimates of the muon track as starting points for increasingly sophisticated fits, as the dependence of the results on these starting points increases with the sophistication of the fitting method applied. For the prefit only hits that are part of a local coincidence or have amplitudes above a given threshold (3.0 photoelectrons) are used. For each of the consecutive likelihood fits, a subset of hits is selected, that is compatible with the track used as a starting point i.e. the location of the hit has to be within a given distance of the starting point track and the time residuals have to allow the hits to originate from it. This subset must have a defined minimum size in order for the reconstruction process to converge, i.e. a minimum number of (compatible) hits is required at several steps. The prefit requires at least three coincident hits or hits with high amplitudes, the M-Estimator fit 15 compatible with the prefit. The third fit requires ten hits compatible with the output of the M-Estimator procedure, while the final fit requires the minimum number of six (as a track is described by five parameters).

A quality cut on the likelihood value of the final fitted track can be applied to the reconstructed tracks. Two slightly different versions of this cut exist. The ’old’ version that is very strict, and the default version.

In addition there are several estimators for the muon energy, which can be chosen independently from the muon track reconstruction.

Usability for KM3NeT and modifications

The *AartStrategy* has already been modified to some extent for km^3-detectors [103–105]. This modified strategy is used by the NEMO collaboration. The most important modification is the causality filter, where an additional condition is introduced. In a km^3-detector the distances between PMs that have been hit can be much larger than in the current generation of neutrino telescopes. Because of this the situation shown in Fig. 5.2 is different as absorption of the emitted Cherenkov light starts to play a role. This different situation is shown in Fig. 5.4. The benefit of the causality filter is to provide a time window for the hits to be used in reconstruction and in this way reduce the number of noise hits in the sample. As the time window given by (5.2) increases with distance, the window gets longer for larger detectors, reducing the efficiency of the filter. In a large detector the time difference of two hits in PMs separated by a large distance is most strongly lim-

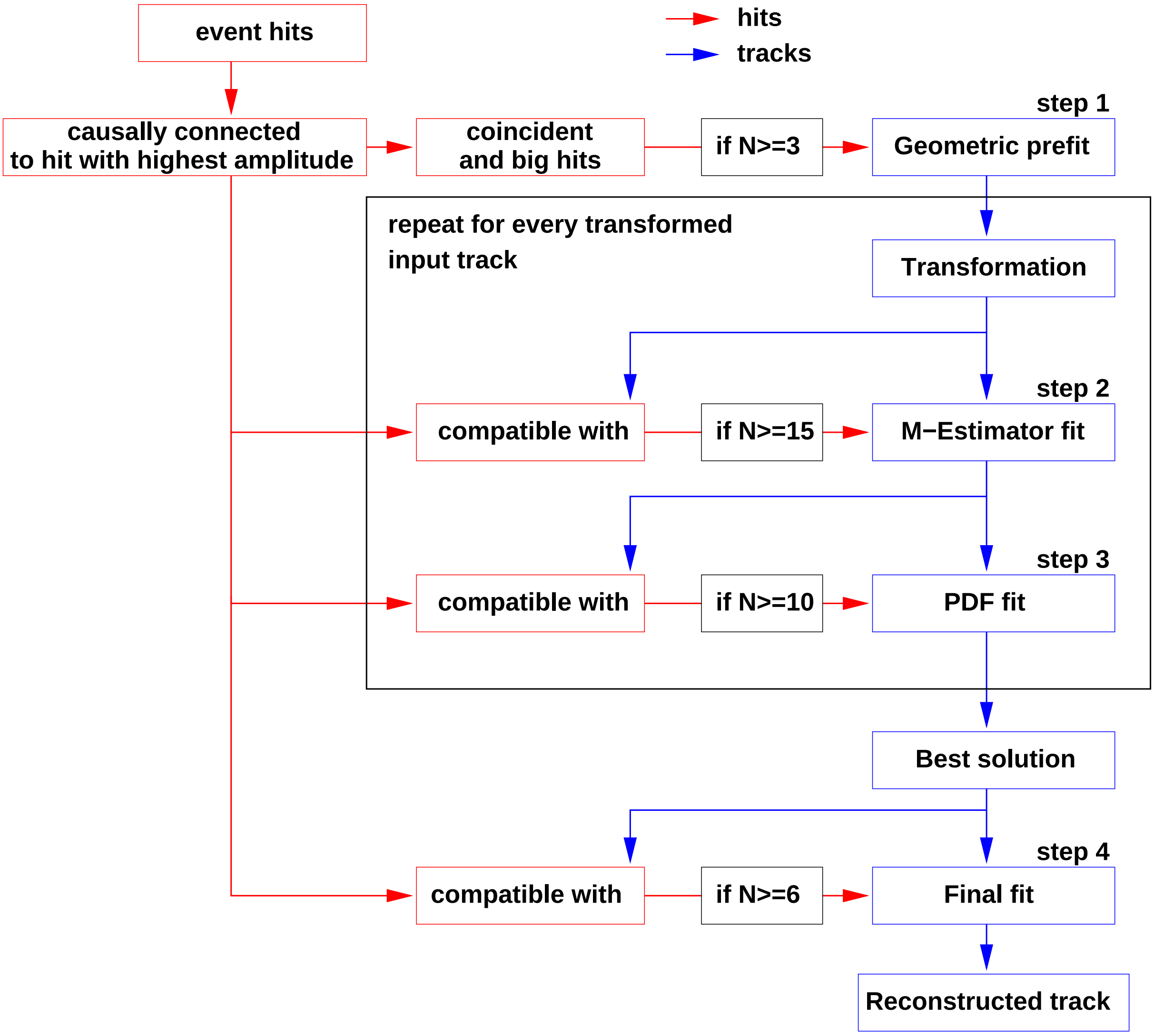

Figure 5.3: Scheme of the reconstruction process using the *AartStrategy*.

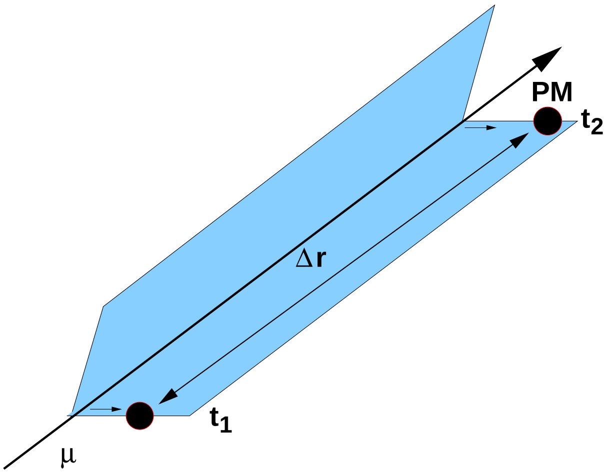

Figure 5.4: Schematic of the Cherenkov light propagation from a muon track for large distances between PMs.

ited by the muon velocity, i.e. the light velocity in vacuum, as light absorption prevents the Cherenkov photons to move that far from the track. This allows to formulate the additional causality condition,

$$||\Delta t| - \frac{\Delta r}{c}| < t_{\text{filter}}, \tag{5.4}$$

with c the speed of light in vacuum and t_{filter} being the causality time window, taking into account the delay of the Cherenkov light. The combination of both conditions increases the efficiency of the filtering process and therefore reduces the number of noise hits used for the prefit, which in the end leads to better reconstruction results.

A larger detector will generally be instrumented less densely, resulting in less hits per event for lower energies. In order to reduce resulting efficiency losses the internal minimum hit cuts in the reconstruction were loosened. The threshold for the hits to be used for the prefit was reduced to 2.0 photoelectrons and the minimum numbers of hits required for the different fitting steps were decreased (2 instead of 3 for the prefit, which is actually the minimum to draw a line, 10 instead of 15 for the M-Estimator fit and 7 instead of 10 for the first likelihood fit, the final fit still requires at least 6 hits). All these modifications result in a higher efficiency, but a somewhat lower reconstruction quality.

KM3 criteria

The reconstruction algorithm has been optimised for the ANTARES detector layout. Although it also works for other detector layouts, it is problematic to ensure that it works equally well for all the different detector models that will be considered in the Design Study. Especially the behaviour of the likelihood functions for different detectors is difficult to assess.

Because of this several selection criteria for events have been developed, that are potentially connected with the track reconstruction (by any algorithm). A special 'reconstruction strategy' was set up, that does not actually reconstruct the tracks but provides criteria for later analysis (see section 6.3).

Chapter 6

Analysis methods

This chapter describes the analysis methods and principles used for the detector studies. In order to compare different detector and PM geometries as well as different photodetection layouts, it is necessary to define a set of parameters, describing the performance of a given detector model. These are the effective area and the angular resolution. Furthermore, a set of selection criteria has been defined, in order to be able to obtain results which are independent from the ANTARES reconstruction algorithms. For studies of the sensitivity neutrino benchmark fluxes of cosmic neutrinos have been defined by the KM3NeT consortium. The underlying assumptions and the origin of these fluxes will also be detailed in this chapter.

6.1 Effective area

The most important property of a neutrino detector is its detection efficiency, i.e. the fraction of incident neutrinos the detector can reconstruct. Effective areas are a very useful way to display the efficiency as they take into account the relative size of different detectors and allow to easily calculate event rates for a given flux. There are different definitions of effective areas for muons and neutrinos [106,107]. For this work the neutrino effective area was used, defined as

$$A^{\nu}_{\text{eff}}(E_\nu, \theta_\nu, \phi_\nu) = V_{\text{eff}}(E_\nu, \theta_\nu, \phi_\nu) \cdot \rho N_A \cdot \sigma(E_\nu) \cdot P_{\text{Earth}}(E_\nu, \theta_\nu). \tag{6.1}$$

Here ρN_A is the target nucleon density (where ρ is the density of the target material and N_A is the number of particles per gram), $\sigma(E_\nu)$ is the neutrino-nucleon cross section, V_{eff} is the effective volume and P_{Earth} is the probability for neutrino absorption in the Earth. The effective volume is defined by

$$V_{\text{eff}}(E_\nu, \theta_\nu) = \frac{N_x(E_\nu, \theta_\nu)}{N_{\text{gen}}(E_\nu, \theta_\nu)} \times V_{\text{gen}}, \tag{6.2}$$

where V_{gen} is the generation volume, which depends on the neutrino energy and is generally much larger than the can volume (see 5.2) and N_x and N_{gen} are the numbers of selected (depending on the selection criterion) and simulated neutrino events. The absorption

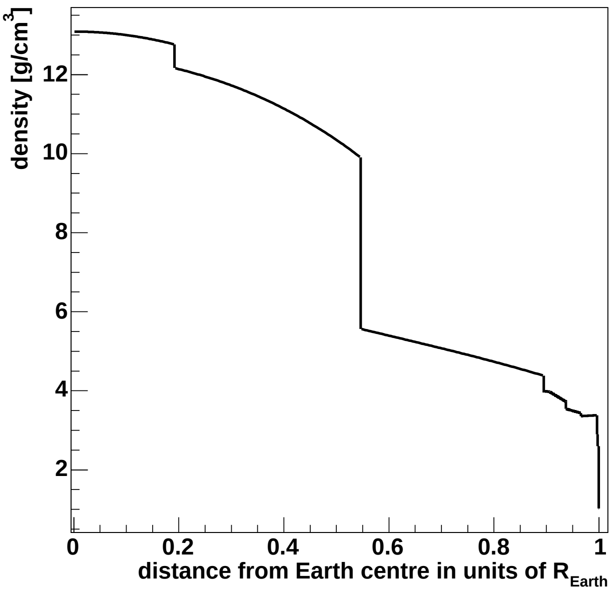

Figure 6.1: Earth density profile in units of the Earth radius, as parameterised in [108].

probability P_{Earth} is defined through:

$$P_{\text{Earth}}(E_\nu, \theta_\nu) = e^{-N_A \sigma(E_\nu) \int \rho dl}, \tag{6.3}$$

where $\int \rho dl$ is the Earth density integrated along the direction of the neutrino trajectory. For the calculation the density profile shown in Fig. 6.1 has been used. For a given neutrino flux $\frac{d\Phi_\nu}{dE_\nu d\Omega_\nu}$ the event rate N_ν can be calculated from the neutrino effective area:

$$N_\nu = \int A^\nu_{eff}(E_\nu, \theta_\nu) \frac{d\Phi_\nu}{dE_\nu d\Omega_\nu} dE_\nu d\Omega_\nu. \tag{6.4}$$

With the resulting event rates, sensitivities to these fluxes can be calculated.

6.2 Angular resolution

The angular resolution of a neutrino telescope is usually defined as the median of the angular deviation between the direction of reconstructed muon track or shower and the true neutrino direction obtained form the Monte Carlo. It strongly depends on energy. At higher energies it is dominated by the reconstruction quality of the muon track or shower, while at lower energies the kinematics of the neutrino interaction dominate the angular resolution, as the angular deviation between the incident neutrino and a resulting muon or shower grows with decreasing energy.

In addition to the angular resolution a point spread function can be defined from the angular deviations in the zenith and azimuthal angles.

The angular resolution is a critical parameter of a neutrino telescope, especially for individual sources of cosmic neutrinos, as the size of the search window and hence the background of atmospheric neutrinos scales with the square of the resolution.

6.3 Event selection criteria

In order to calculate effective areas, a set of events has to be chosen corresponding to a certain selection criterion, the most obvious being a good reconstruction. Unfortunately, no dedicated KM3NeT reconstruction algorithm is currently available. The ANTARES reconstruction code can be used, but it has been tuned for the much smaller ANTARES detector and is probably not optimal when used for KM3NeT geometries (see section 5.5. It is difficult to judge if the performance of the algorithm is influenced by the differences between the detectors, effectively introducing a bias of unknown severity to the results. This is even more true for the ANTARES selection cuts. Therefore a set of criteria is required that is maximally independent from the detector details and allows to compare the performances of the different detector models considered in this work on a fair level. However, in order to calculate the angular resolution, some kind of reconstruction is necessary.

6.3.1 Selection parameters

In the following several parameters will be listed that can potentially be used as selection criteria for the muon-neutrino events simulated in this work. Several stages of selection will be defined using these parameters.

Signal hits

A rather obvious criterion is the number of hits produced by the muon and its secondary showers. More hits in the detector PMs will result in a higher chance for a successful reconstruction. The ANTARES reconstruction in fact also utilises this, by requesting a given number of hits at its different stages. From Monte Carlo information, the number of signal hits before or after the application of the modified causality filter described in section 5.5 can be found and used as a criterion. The minimum number of signal hits is deteremined by the number of input parameters used for the description of a fitted track. A track is specified by a point in space (three space coordinates) and a direction (two angles), resulting in a minimum of at least six signal hits for a constrained fit.

A problem of using some number of hits as criterion is, that in this approach photodetection systems with a higher number of PMs are favoured. Consider a standard 10"PM and a set of smaller PMs with the same overall photocathode area and quantum efficiency pointing in the same direction. Two incident photons would be registered in the single large PM as one hit with an amplitude of 2 photoelectrons, while in the array of small PMs would produce two hits with 1 p.e. each. Thus cutting on the number of hits is biased towards the array. On the other hand cutting on numbers of hits is exactly what the reconstruction algorithm does and of course the minimum number of hits is still six as mentioned above.

Number of storeys with hits

If a large number of storeys are hit by photons originating from the muon track, the chances for a successful reconstruction of the track as well as the quality of the recon-

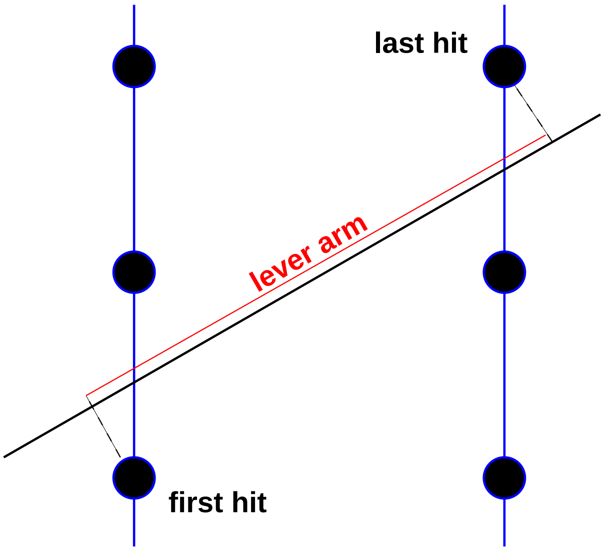

Figure 6.2: Illustration of the definition of the lever arm length.

struction are increased. Again, Monte Carlo information can be used to find this number. The minimum number of storeys required to draw a line is two (assuming that two hits in one storey are too nearby to be suitable). This criterion only depends on the probability of a hit in the storey and not on its actual substructure, like the number of hits.

Purity

The purity p of an event is generally defined as the proportion of signal hits in its hit pattern after some cut, or

$$p = \frac{N_{\mathrm{signal}}}{N_{\mathrm{signal+noise}}}. \tag{6.5}$$

Obviously the chances for a good reconstruction drop with the amount of noise hits used for it. In our case the purity after the application of the modified causality filter is a suitable criterion. This can be calculated for single hits or for hits that are part of a local coincidence.

Length of lever arm

The lever arm is defined as the distance between the position of the earliest and the latest hit, projected on the muon track (see Fig. 6.2). A long path of a muon through the detector increases the quality of the direction reconstruction, reducing the angular error and therefore implies a better angular resolution. As the range of muons in water depends on their energy, a lever arm cut also imposes an energy cut.

By requiring a given number of storeys to be hit, a lever arm cut is indirectly applied, with an arm length defined by the storey distances.

6.3.2 Selection steps

The results of simulations presented in this work are given for the following selection steps. The performance of the real detector will be somewhere between the minimal criterion and the full reconstruction, including a cut on the angular error. The effects of these selection criteria on the effective area of one of the example detectors under investigation are shown in Fig. 6.4. This detector is a homogeneous cuboid grid with ANTARES storeys (see section 4.3), for the actual detector layout and simulation parameters see chapter 8.

Minimal criterion

Assuming that the minimal necessary information will be sufficient, the minimal criterion requests six signal hits and two storeys to be hit before the application of the causality filter. This requires that the exact positions of PMs inside a storey are known. Otherwise several hits on a single storey do not represent additional degrees of freedom.

Hit criterion

This criterion requires the event to have at least ten signal hits and two signal coincidences or big hits after the application of the modified causality filter. This corresponds to the minimum hit requirement, that is applied during the reconstruction process with the modified *AartStrategy*. Therefore, assuming ideal noise reduction, any event satisfying this condition should be reconstructible.

Moderate criterion

This criterion requires six storeys to be hit by photons originating from the muon. It is the maximally unbiased criterion as it is completely independent of the storeys' substructure. By requesting six storeys to be hit, the minimal criterion and thus reconstructibility are automatically fulfilled.

Trigger criterion

This is essentially the same as the hit criterion with additional cuts on the purity of the hits and of the coincidences or big hits (larger than 10% and 80%, respectively). The idea is to simulate noise reduction or a trigger process by assuming, that only events with a certain purity will pass the trigger. This criterion is rather strict.

Selected events

Here, all events are used that are reconstructed by the modified ANTARES algorithm with an angular error better than five degrees. This might potentially produce biased results, as different detector designs might be treated differently by the algorithm. Nonetheless, it is necessary to define the angular resolution of the detector layouts, as this requires a fitted track. The cut on the angular error is used, since generally the algorithm produces some very badly reconstructed events (due to low purity and failed noise rejection). This criterion provides a worst case for the results presented in this work, and it is very likely, that with a dedicated KM3NeT reconstruction algorithm better results can be achieved.

criterion	**requires**	**causality filter**	**affected by optical noise**
minimal	6 signal hits 2 coincident or big signal hits	no	no
hit	10 signal hits 2 coincident or big signal hits	yes	no
moderate	6 storeys with signal hits	no	no
trigger	10 signal hits 2 coincident or big signal hits purity of hits > 0.1 purity of coincident/big hits > 0.8	yes	yes
selected	reconstructed angular error $< 5°$	yes	yes

Table 6.1: Overview of the selection criteria used in this work. The last two columns state whether the causality filter is applied and whether ^{40}K-noise is accounted for.

The effect of these different selection cuts summarised in Table 6.1 on the effective area and the number of events in the sample for a standard detector (homogeneous cuboid grid with ANTARES storeys, see section 8) are shown in Figures 6.3 and 6.4. The statistical errors on the effective areas are given as an example, as they will not be shown later to increase readability of the plots (they are anyway small compared to the differences due to selection criteria or detector models). From the differences in effective areas between the *selected* events and events fulfilling the less strict criteria (like the moderate criterion) it can be seen that there is definitely some space for improvement for a future reconstruction algorithm. When comparing the number of events for the hit criterion and for reconstructed events it is obvious that in fact most of the events satisfying the criterion are reconstructed. Unfortunately, as mentioned before, the quality of the reconstruction without any additional quality cuts, and therefore the angular resolution, is not very good, as can be seen in Fig. 6.5. Different additional quality cuts to the reconstructed events were tested. The first is a cut on the angular deviation between the fit and the prefit, assuming that reconstruction quality is increased if the starting point (the prefit) is good. The other two are slightly different cuts on the likelihood values of the fit results (see section 5.5, [101]). All of these cuts either leave a lot of badly reconstructed events in the final sample or cut away a significant part of the well reconstructed ones. Therefore the somewhat artificial cut on the angular error was chosen for the *selected* event criterion.

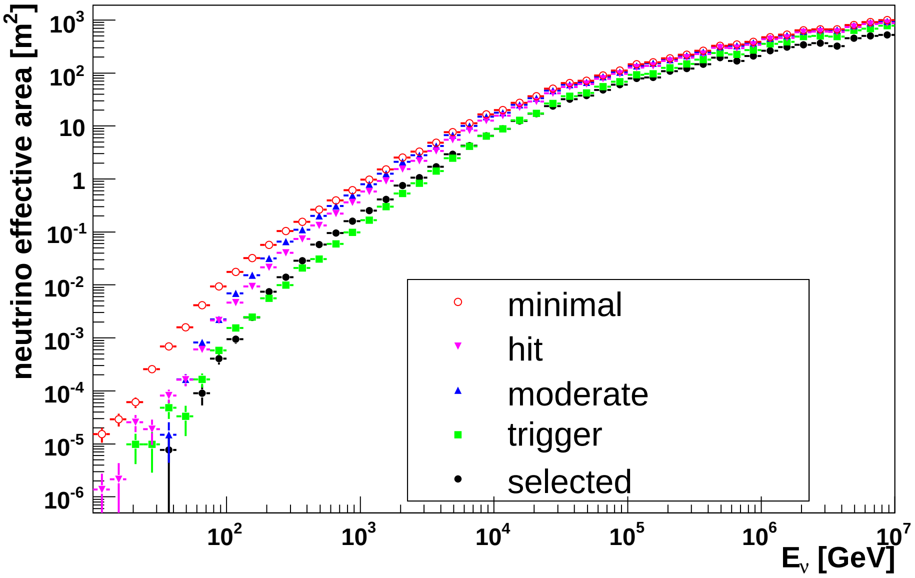

Figure 6.3: Neutrino effective area of a homogeneous cuboid grid detector equipped with ANTARES storeys, at different selection steps. The true achievable effective area lies between the minimal and the selected criterion and is approximated by the hit and the moderate criterion.

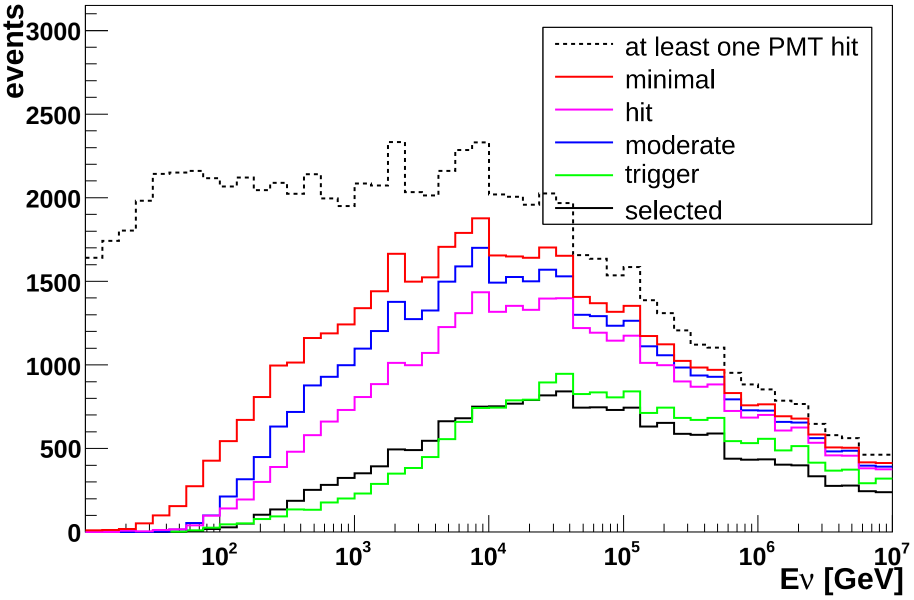

Figure 6.4: Number of events in the event sample (10^9 muon-neutrinos) of a homogeneous cuboid grid detector equipped with ANTARES storeys, at different selection steps.

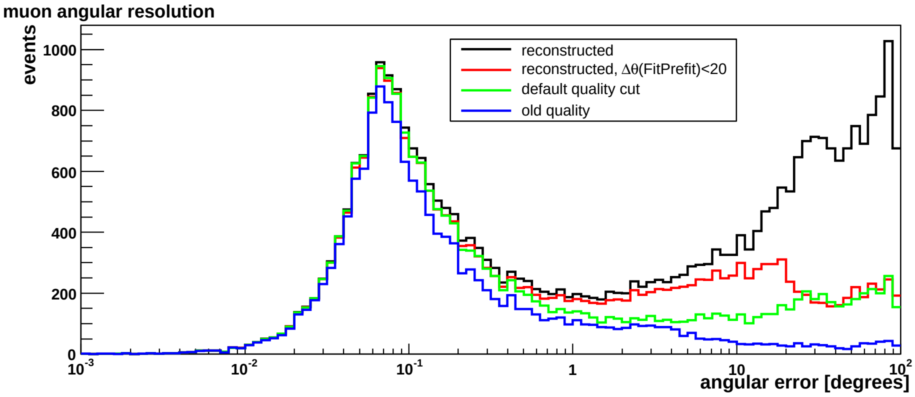

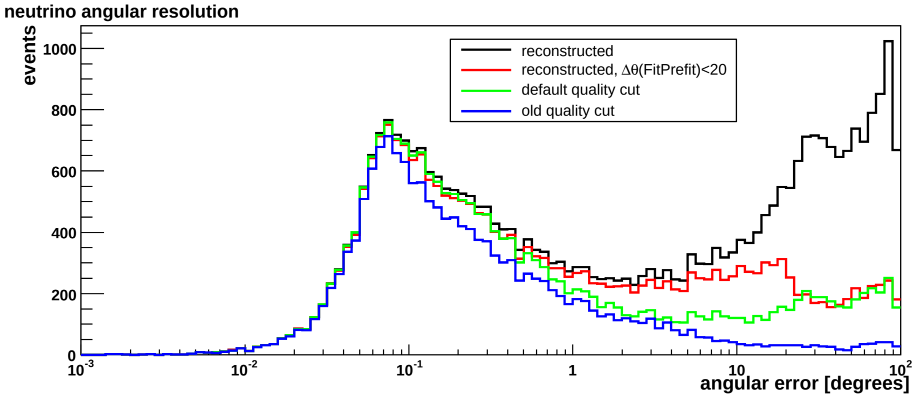

Figure 6.5: Distribution of angular errors for reconstructed events with different quality cuts, for a homogeneous cuboid grid detector equipped with ANTARES storeys. Top: Angular deviation between true and reconstructed muon direction. Bottom: angular deviation between incoming neutrino and reconstructed muon direction.

6.4 Calculation of flux limits

The first step for the derivation of flux limits for a neutrino detector is the calculation of event rates for the expected background (atmospheric neutrinos) and the source flux, which is assumed to follow the power law spectrum

$$\frac{d\Phi_\nu}{dE_\nu} = k_\nu E_\nu^{-\alpha} \tag{6.6}$$

typical for sources with hadronic acceleration. In the following an isotropic flux will be assumed. The number of background events ,N_b, and the number of events from the source flux, N_s, are both assumed to follow Poissonian distributions. As discussed in section 6.1, the event rate for this flux is:

$$N_s = \int A_{\text{eff}}^\nu(E_\nu) k_\nu E_\nu^{-\alpha} dE_\nu. \tag{6.7}$$

The task is now to find the normalisation constant k_ν^{limit} that defines the flux limit. Equation 6.7 can be rearranged to:

$$k_\nu = \frac{N_s}{\int A_{\text{eff}}^\nu(E_\nu) E_\nu^{-\alpha} dE_\nu}. \tag{6.8}$$

Generally some input flux $k_i E^{-\alpha}$ is used to calculate an event rate in the denominator from Monte Carlo information. From this k_ν^{limit} can be calculated as:

$$k_\nu^{\text{limit}} = \frac{N_s^{\text{limit}}}{\int A_{\text{eff}}^\nu(E_\nu) k_i E_\nu^{-\alpha} dE_\nu} k_i \tag{6.9}$$

or

$$k_\nu^{\text{limit}} = \frac{N_s^{\text{limit}}}{N_i} k_i. \tag{6.10}$$

The fraction N_s^{limit}/N_i is often called the Model Rejection Factor (MRF). Now a suitable value for N_s^{limit} can be chosen in order to derive the desired flux limit. As a very simple example, with $N_s = 1$, k_ν^{limit} will give the minimum flux required to detect one event.

In the presence of background the standard procedure is to employ the approach developed by Feldman and Cousins [109]. Here it is assumed that only background is detected. From the given number N_s of background events, an average upper limit of events $\langle N^{\text{limit}} \rangle$ is calculated that is compatible with the background at a given confidence level (C.L.) using the Feldman-Cousins method. If $N_s < \langle N^{\text{limit}} \rangle$, the observation will caused by a background fluctuation in a fraction of (C.L.)% of all cases. Usually the C.L. is chosen to be 90%. By using,

$$k_\nu^{\text{limit}} = \frac{\langle N^{\text{limit}} \rangle}{N_i} k_i, \tag{6.11}$$

k_ν^{limit} becomes the normalisation factor of the smallest flux that can be excluded by the detector with a C.L. of 90%. This is generally called the sensitivity of the detector.

Of course this procedure depends on the energy dependence (in this case $E^{-\alpha}$) of the expected neutrino flux and is therefore model dependent.

6.5 Physics goals and benchmark fluxes

The main aim of this work is to study different potential KM3NeT detectors regarding their properties and performance. Using effective areas and angular resolution is a suitable way to do so. A more sophisticated and at the same time more intuitive way is to use this information to derive the sensitivity for different predicted cosmic neutrino fluxes. This is the criterion that allows to decide on the detector configuration in view of the physics goals that will finally be pursued (and their weighting in importance). This requires the knowledge of the corresponding neutrino fluxes. There are three neutrino fluxes to be considered: The diffuse neutrino flux, the neutrino flux from individual cosmic ('point'-)sources and the flux from WIMP annihilations in the Sun or the Galactic center (which are individual sources as well).

Diffuse flux

The cosmic neutrino flux from the sum of all neutrino sources is generally called the diffuse flux. Several models for this flux, using different source assumptions exist. One of the most common is the neutrino flux upper bound derived by Waxman and Bahcall [8]. It corresponds to an upper limit on the neutrino flux originating from optically thin (transparent) sources. This results in the following neutrino flux limit:

$$\frac{d\Phi_\nu}{dE_\nu d\Omega_{nu}} = 5 \times 10^{-8} E^{-2} GeV cm^{-2} s^{-1} sr^{-1}. \tag{6.12}$$

Different flux limits are shown in Fig. 6.6. An analysis of the sensitivity of a neutrino telescope to these, requires calculating the experimentally achievable its flux upper limit at a given confidence level.

Due to the very high background of atmospheric neutrinos at low energies, a study of the diffuse flux has to focus on energies beyond 10-100 TeV.

Individual sources of cosmic neutrinos

The search for these point-like sources is probably the main goal for neutrino telescopes. In order to be able to define the sensitivity of a model detector, the fluxes of these sources have to be calculated. This has been done recently for some Galactic sources [3], where the neutrino flux spectra were derived from the TeV gamma-ray emission measured by HESS. The neutrino flux from a point source can be parameterised in the following form:

$$\frac{d\Phi_\nu}{dE_\nu} = kE^{-\Gamma} exp\left(-\sqrt{\frac{E_\nu}{\epsilon}}\right). \tag{6.13}$$

Here the neutrino energy is given in units of 1 TeV, k is the normalisation factor defining the absolute value of the flux, Γ is the spectral index defining the shape of the energy spectrum while ϵ defines a cutoff in the energy spectrum, that was observed in some TeV-gamma ray spectra by HESS and might be present in other sources at energies beyond the available measurement range of the current HESS setup. The existence or non-existence

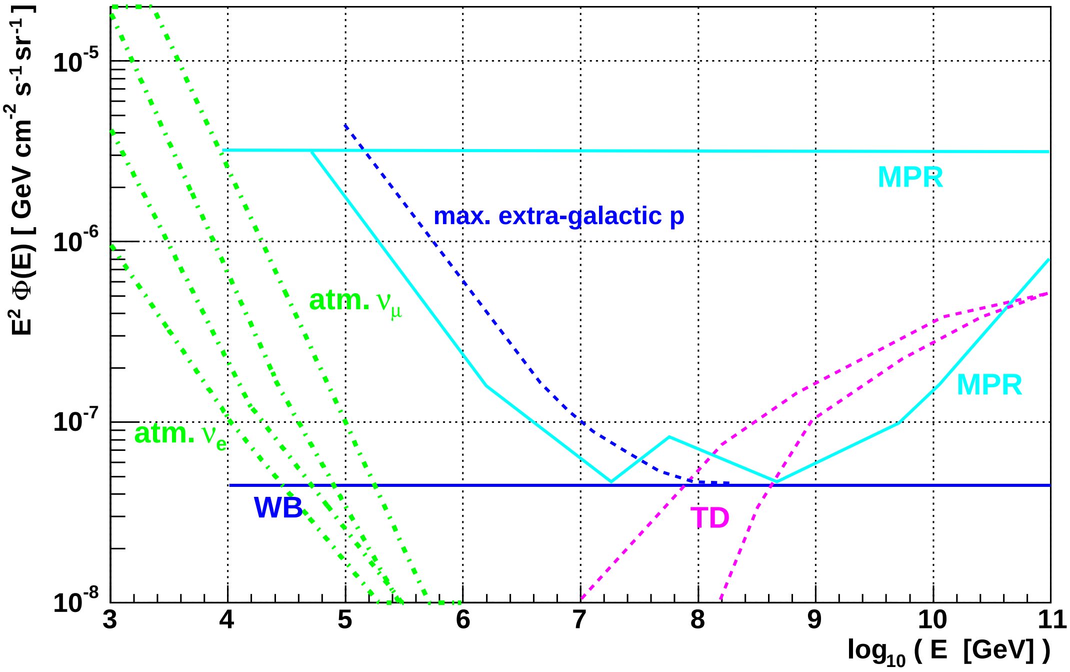

Figure 6.6: Theoretical prediction of diffuse neutrino fluxes for different models. Conventional [110] and prompt [111] atmospheric neutrinos (green lines), Waxman-Bahcall upper limit [8] (blue line) with maximum excess due to extra-galactic protons [112] (blue dashed line), Mannheim-Protheroe-Rachen limits [113] (upper cyan line for optically thick, lower line for optically thin sources), Top-down models [114] (as an example of a hyptthetical model, left magenta line with, right without SUSY). Taken from [54].

declination	**right-ascension**	**visibility**	k	Γ	ϵ
-39.5°	17:13:00	0.74%	15.52	1.72	1.35

Table 6.2: Spectral Data and other useful information on the SNR RXJ1713.7-3946 used as reference point source. k and ϵ are given in units of ($10^{-12}\mathrm{TeV}^{-1}\mathrm{cm}^{-2}\mathrm{s}^{-1}$). Taken from [3].

of a cutoff has a large impact on the number of events observed by neutrino telescopes, as their efficiency (effective area) generally increases with energy, while the atmospheric background decreases with energy. A cutoff at a relatively low energy, severely reduces the chances of detection.

In this work the SNR RXJ1713.7-3946 [29] was chosen as a standard source, as it is one of the promising candidates for Galactic neutrino sources known so far. Its celestial coordinates and spectral parameters are given in table 6.2. In addition a generic point source without a cutoff, with $\Gamma = 2$ and $k = 10^{-8}$ was used for the analysis of the sensitivity of the detector configurations considered.

The background of atmospheric neutrinos is greatly reduced for point sources as only atmospheric neutrinos within the search window enter the analysis. The size of the search window is defined by the angular resolution of the detector or by the dimension of the source if it is extended with respect to the detector resolution. Because of this the energy range relevant for an individual source analysis starts at lower energies, than for the diffuse flux, typically in the TeV region.

Neutrinos from WIMP annihilations

The neutrino flux from annihilations of Dark Matter particles in the Sun is another interesting physics topic for a km^3 neutrino telescope. The neutrino fluxes from the Sun for different assumptions on the neutralino mass have been calculated in [115]. In [4] the parameter space for the mSUGRA model has been scanned to estimate neutrino fluxes from the Sun. In Fig. 6.7, the neutrino flux is shown as a function of the mSUGRA parameters. Two regions are highlighted, the so called *bulk region* where fluxes are relatively low and the *focus point region*, where the flux reaches its maximum. Three fluxes were used in this work to calculate event rates for the simulated detector concepts, one from the *bulk region*, one from the lower *focus point* region and one from the central *focus point region.* The first one represents a worst case scenario, while the other two represent two potentially good cases, one with a very high flux, although at lowest energies, and the other at higher energies, although with lower fluxes at lower energies. The three fluxes are shown in Fig. 6.8.

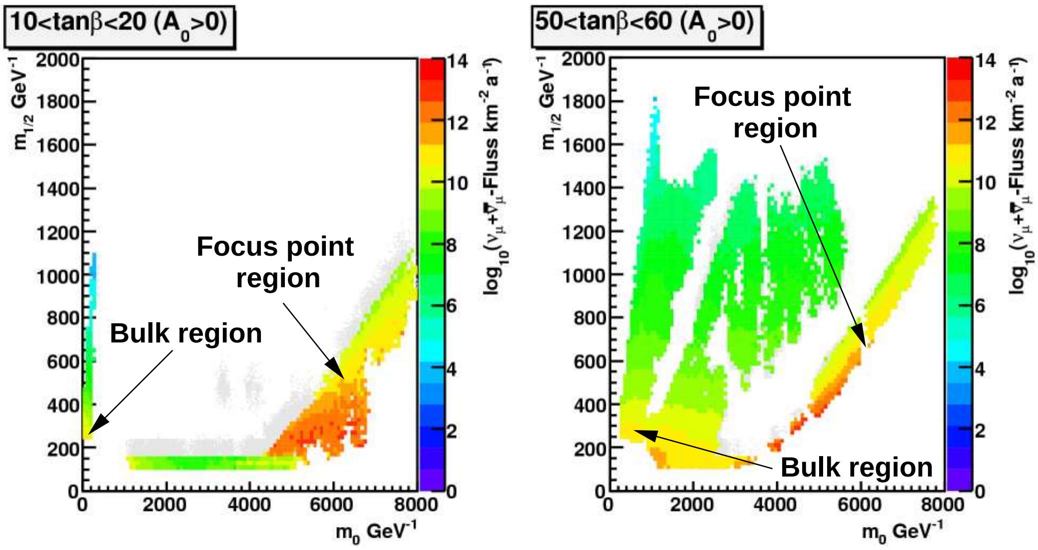

Figure 6.7: Neutrino flux on the Earth as a function of the mSUGRA parameters $m_{1/2}$, m_0 and $\tan(\beta)$. The plots represent slices through the $m_{1/2}$-m_0-plane at given values of $\tan(\beta)$. The regions of the flux models used in this work are marked. Taken from [4].

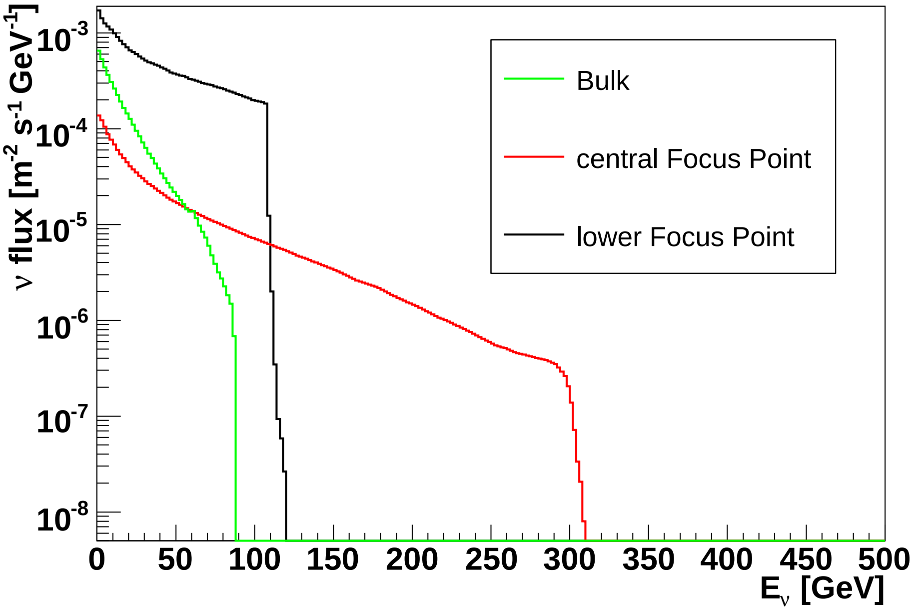

Figure 6.8: Example neutrino fluxes from dark matter decays used as benchmarks in this work. The bulk region flux represents a worst case, while the focus point region fluxes represent the best cases, one being very high and one extending to relatively large energies. Taken from [4].

Part III

Detector studies

Chapter 7

General considerations

This chapter will explain the basic principles for the detector studies. First the detector parameters used in the simulation are listed and in addition the site parameters are given (the impact of which is not studied in this work). Afterwards the principles for achieving an unbiased comparison between detector models are explained and finally the parameters for the simulation and the properties of the event samples used are given.

7.1 Detector parameters

The different detector models that can be studied are defined by their parameters, that are used as input for the simulation. There are two classes of such parameters, *geometric* parameters and *technical* parameters. The first class includes the quantities defining the overall geometry of the layout, which are the string and storey distances and the shape of the detector, as well as those describing the layout of the storeys themselves, i.e. the positions of the PMs within a storey. The second class includes the properties of the PMs used, their photocathode area, their quantum efficiency, their transit time spread (TTS) and their angular acceptance. Furthermore, this includes the optical properties of the PM housings, i.e. the transmissivity of the glass container and the optical gel that is commonly used to make the optical connection between the PM and the glass.

All these parameters influence the overall performance of the detector. The string and storey distances have a large impact on the performance at energies below $\sim 1\,\mathrm{TeV}$, where the lower light output and, in case of muons, the shorter track lengths reduce the size of the event signature in the detector. A denser spacing of storeys will therefore result in a lower energy threshold and a better low energy performance. A large photocathode area of the PMs will increase the chance to collect Cherenkov photons from an event. It is therefore expected that an increased photocathode area results in improved performance. The same applies to the quantum efficiency. Bad transmittivity through the glass and gel combination will obviously reduce the number of detected photons and therefore degrade the performance. The TTS of the PM is connected to the time resolution of the photon-induced electrical signals, where the timing properties of the electronics have to be taken into account. The time resolution of the signals is important for the achievable angular resolution. The influence of other parameters like the geometric layout of the detector,

	ANTARES (near Toulon)	NEMO Capo Passero	NESTOR near Pylos
depth (m)	2400	3400	4100
absorption length (m)	60@470 nm	70@440 nm	55@460 nm
scattering length (m)	50@470 nm	-	-
effective scattering length (m)	265@470 nm	-	-
background rate (kHz) (assuming 10”PM)	60	20-30	20-30

Table 7.1: Properties of the potential sites for the KM3NeT detector. Taken from [56, 116,117].

or the angular acceptance of the PMs, is harder to predict. For this work, most of these parameters were modified to analyse the different concepts that are considered for KM3NeT.

7.2 Site Parameters

Another set of important parameters are those defining the properties of the site of the neutrino telescope. These include the depth of the site and its exact location, where the latter defines the properties of the Earth magnetic field at the site and the visibility of given point sources. Furthermore the optical properties of the sea water at the site, the index of refraction as well as the absorption and scattering lengths, all depending on the wavelength, are included. These parameters have to be known, but are not nearly as critical as the rate of the ^{40}K and bioluminescence background.

In this work, the site properties are generally not studied, which implies that all parameters are set to the defaults given in the simulation software, which are the properties measured for the ANTARES site near Toulon. The only exception are the background rates, which probably have the largest impact on the results. Table 7.1 gives the most important parameters for the three potential KM3NeT sites. The refractive index of the sea water and the absorption and scattering lengths used in the ANTARES software are shown in Fig. 7.1 as functions of the wavelength.

7.3 Comparison of detector models

In this work several feasible detector designs were studied, that can be evaluated in the future using additional or alternative software tools. In addition basic dependencies on the parameters were studied. Therefore, two types of detector models were created. The first type is a 'realistic' detector, that could in principle be constructed, whereas the second type of detector models is used to analyse and illustrate basic dependencies, which may or may not result in rather unrealistic parameters (like for example very long strings or PM properties that do not exist in this combination). For the first type string distances of about 60 m were assumed, which is near the minimum distance achievable

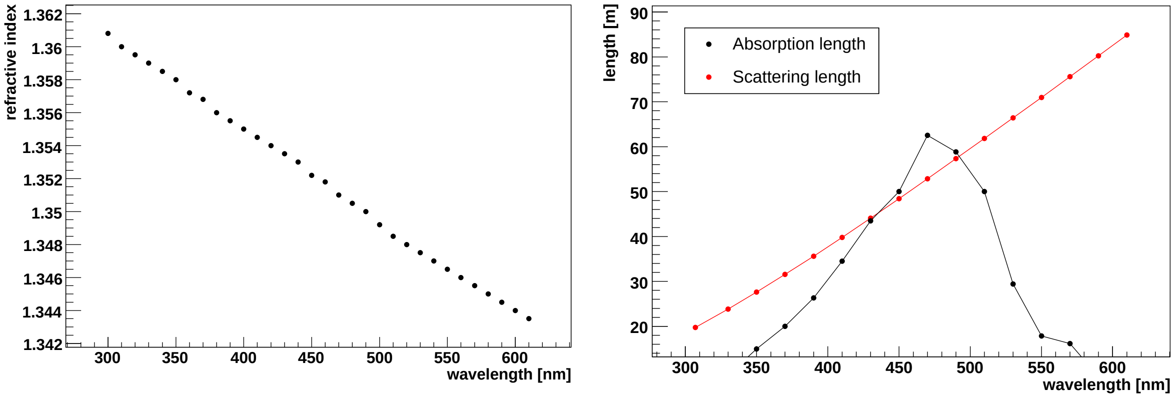

Figure 7.1: Left: The refractive index of sea water as a function of wavelength, Right: Absorption and scattering length as a function of wavelength for the water model used in the ANTARES simulation code (for more details on site properties see [116,117]).

with current deployment methods (exception: tower structures). The string height is limited to about 600 m, again due to deployment constraints. These *candidate* detectors all have an instrumented volume of 1 km^3 (with a deviation of less than 1%), to allow for giving their properties per cubic kilometer. In addition the overall photocathode area of the detector is kept constant within a deviation of less than 5%, to make different detectors approximately comparable in cost.

The problem with the comparison of different detector models is that most of the parameters are interrelated to some extent. To avoid overlaps as much as possible, different storey types have to be compared within the same detector geometry, while different detector geometries have to be compared with the same storey type.

For the second type of detector models this scheme can be broken to allow a general analysis of the influence of the different mainly geometrical parameters. This class of detector models also includes some unrealistic concepts to assess the extreme cases.

7.4 Event samples and simulation parameters

In this work only muon neutrinos (and therefore track like events) were simulated (i.e. no antineutrinos, no electron or tau neutrinos and no showers). In order to achieve sufficient statistics for the calculation of effective areas, 2×10^9 muon neutrinos were simulated using *genhen* (see section 5.2) as a standard sample for each type of detector geometry. This leads to at least 100 to 1000 events per bin in the effective area histograms above 100 GeV (see Fig. 6.4) which is reasonable statistics for the precision required in this study. On the other hand, smaller samples (1×10^9) were used for the systematic parameter studies to save time and disc space. The neutrinos for this sample were produced with energies from 10 GeV to 10 PeV, according to a $E^{-1.4}$ spectrum to yield good statistics also at high energies. The energy range covers all the relevant benchmark fluxes. The neutrinos are incident from the complete solid angle (4π, isotropic).

For most of the detectors the statistics below 100 GeV is somewhat low, especially in the range interesting for Dark Matter searches. Because of this an additional sample was created consisting of 5×10^7 neutrinos in an energy range from 1 to 500 GeV. Here more than 100 events per 10 GeV bin are reached even at the strictest selection level. This sample is called *low-energy sample* in the following.

For all detectors and simulations a ^{40}K-background rate of 90.9 Hz per square centimeter of photocathode area was assumed in the detector simulation (corresponding to 40 kHz in a 10" PM). As only the *km3* package (see section 5.3) was used any effects of the hadronic shower produced by the neutrino interaction are neglected. However this only affects muons that are produced inside or very near to the detector.

The simulation of the ANTARES electronics, which is basically the integration of incident hit signals performed by the ADC chips, is not used. However gain fluctuations were simulated (following a Gaussian distribution) and applied to the hit amplitudes. Also the arrival times of the hits were smeared according to the TTS of the PMT studied. Before the reconstruction process was started, an amplitude cut of 0.5 photoelectrons was applied to all hit amplitudes. This is a common procedure to reduce optical background and electronic noise and serves to increase the 'realism' of the process.

Chapter 8

Photo-detection layouts

A neutrino telescope is a three-dimensional array of photomulitpliers. It has two organisational levels. One is the photodetection/sensor unit, generally called a *storey*. It is described by the positions of photomultipliers within the storeys and their properties, i.e. a storey is essentially a cluster of PMs. The second level is the arrangement of the storeys in space, or in other words, the *geometry* of the detector. Existing neutrino telescopes generally use large hemispherical PMs (from eight to thirteen inches in diameter) placed in pressure-resistant glass spheres that either contain the necessary electronics or are connected to an external electronics container (see section 4.3). In current neutrino telescopes up to three of these structures form a single storey.

The following chapter is dedicated to the different storey layouts considered in this KM3NeT study. For comparison, the different structures were placed in a homogeneous cuboid grid with an instrumented volume of one cubic kilometer and storey distances of 63 m vertically and horizontally. The height of this geometry is 567 m, which is realistic for a string based detector (and probably also for a detector composed of rigid structures like towers). The total number of storeys is 4840, which compares nicely to the 4800 in IceCube. If considered to be composed of strings, this corresponds to 484 strings equipped with ten storeys each. This geometry is shown in Fig. 8.1 and will be referred to as the *cuboid* in the following. For storeys with different overall photocathode area this will not result in a fair comparison. Therefore an additional geometry was created, where the number of storeys per string is adjusted to obtain a total photocathode area for the whole detector being about equal to a given standard value. This standard value is, somewhat arbitrarily, defined by the standard *cuboid* grid equipped with ANTARES storeys. By comparing these *candidate* type detectors principle differences between photodetection systems (other than photocathode area) can be studied.

8.1 Detector storeys with 10"photomultipliers

As mentioned above, the use of large hemispherical PMTs is common in all neutrino telescope experiments currently in operation. Therefore, building a photodetection system with these well known instruments is a reasonable starting point. A widely used PM is the Hamamatsu R7081 10"PMT [118], which is the tube used in the ANTARES and IceCube

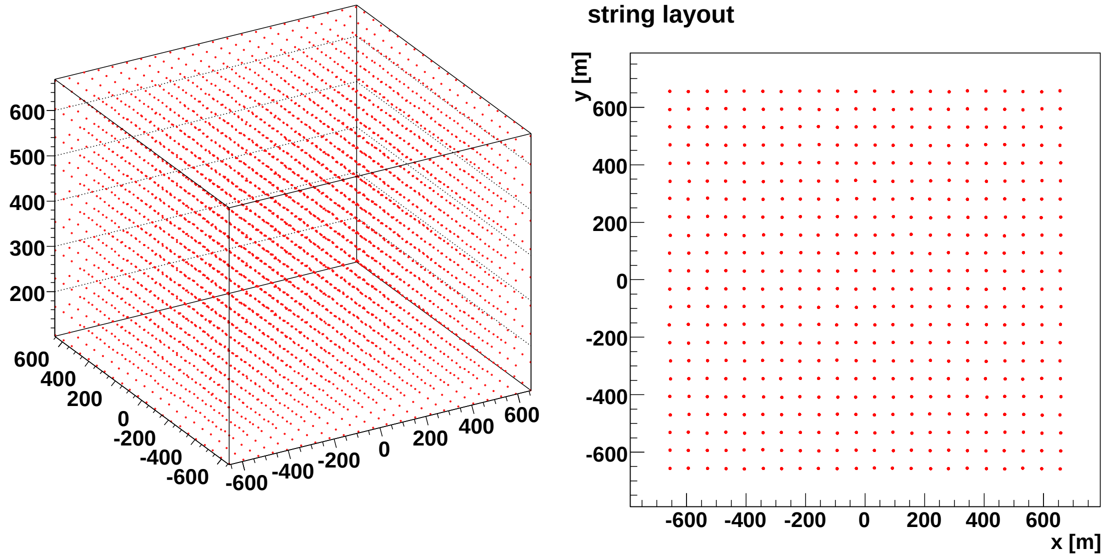

Figure 8.1: Left: Cuboid geometry used for the comparison of photodetection systems. Right: Sea floor layout of the strings used to simulate this geometry.

experiments. The properties that are used in the simulation, its quantum efficiency and angular acceptance, are shown in Fig. 8.2. These photomultipliers are placed inside a glass sphere to form an Optical Module (OM). The transmittivity of the glass sphere and the optical gel used for the simulation is shown in Fig. 8.3. Different arrangements of OMs in a storey were studied.

8.1.1 Storey layouts with 10”photomultipliers

The schematic layouts of the storeys with 10”PMs are shown in Fig. 8.4.

The single OM storey

A simple option is to use a single downward-looking 10”PM per storey, in principle the same as in IceCube. The reconstruction algorithm uses local coincidences inside one storey, therefore the single OM storey is at a disadvantage here. It could be possible to use nearest neighbour coincidences like in IceCube, but this might be difficult due to the lower absorption length in water. Nonetheless it is interesting to check the results for this simplest possible option. The corresponding *candidate* geometry has 30 storeys per string with distances of 21 m.

The double OM storey

The second simplest storey structure is one composed of two OMs. In order to increase angular acceptance, one would be looking downwards and the other upwards. In reality, however, sedimentation would cover the upward looking PM after some time. Also, looking directly upward increases the problems with the background of atmospheric muons,

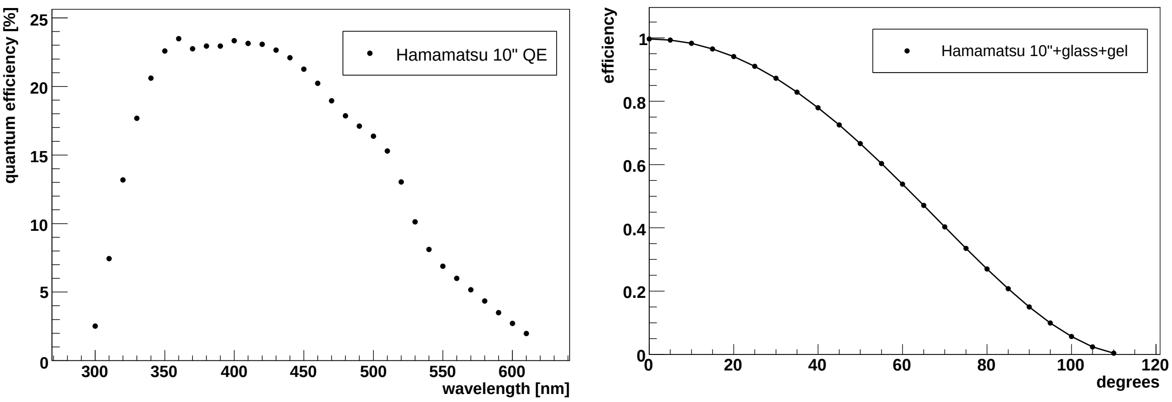

Figure 8.2: Left: Quantum efficiency of the Hamamatsu R7081 10"PM as a function of wavelength. Right: Angular acceptance of the Hamamatsu R7081 10"PM, taken from the source code of the *hit* program [97].

except at highest energies. But as many of the other structures are more or less sensitive to neutrinos from the whole solid angle and this layout is symmetrical it is still worthwhile to compare. The corresponding *candidate* geometry has 15 storeys per string with distances of 42 m.

The ANTARES storey

Another obvious choice is to use ANTARES storeys. These are composed of three OMs pointing downward at an angle of 45 degrees. For more details see section 4.3. The *cuboid* geometry with ANTARES storeys is used as a reference detector in this chapter.

The twin ANTARES storey

The main goal of the KM3NeT Design Study is to increase the volume by a factor of about 50 compared to existing deep sea neutrino telescopes, but limit the costincrease to a factor of ten or lower. Trying to reduce the number of structures and therefore save cost is essential. One possibility might be to reduce the number of structures by using an ANTARES storey with six instead of three OMs. The additional three OMs could be placed on top of the frame supporting the others and the electronics container, pointing upwards at an angle of 45 degrees and sharing the space for electronics with the downward-looking ones. The number of mechanical structures and electronics containers would be reduced by a factor of two, but the number of PMTs would stay the same.

The *candidate* detector equipped with the twin ANTARES storey has five storeys per string with distances of 142 m.

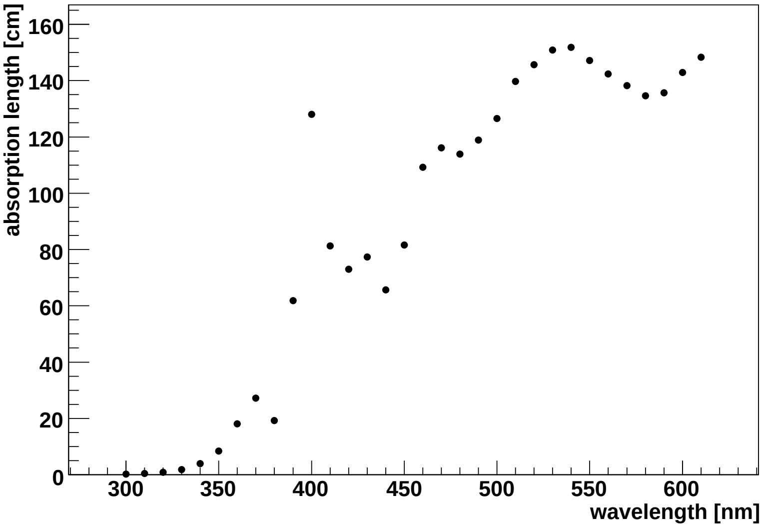

Figure 8.3: Absorption length of the glass of a glass sphere and the optical gel as a function of wavelength, taken from the source code of the *hit* program (see section 5.3).

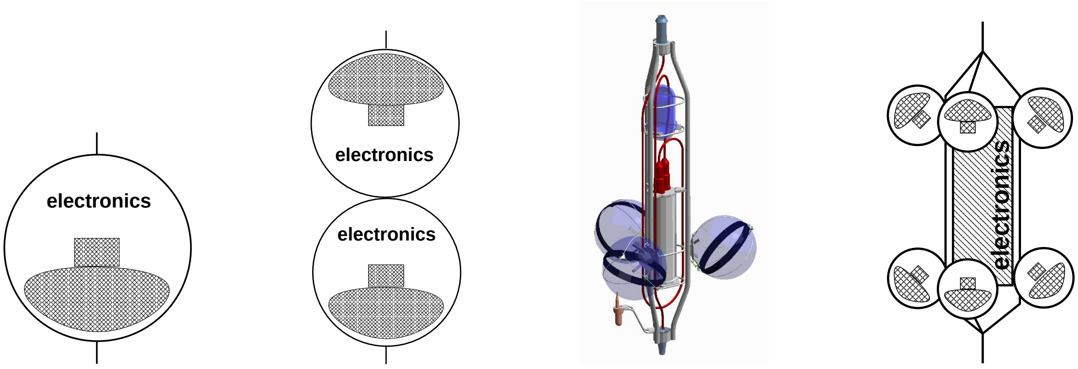

(a) (b) (c) (d)

Figure 8.4: Schematic layouts of the storeys with 10”PMs. (a) single OM storey; (b) double OM storey; (d) ANTARES storey; (c) twin ANTARES storey.

8.1.2 Results for storeys with 10"photomultipliers

Cuboid detectors

The neutrino effective areas at the five selection steps, along with ratio plots of the areas scaled to the cuboid with ANTARES storeys, are shown in Figures 8.6 and 8.7. The angular resolution for events satisfying the *selected* criterion is also shown in Fig. 8.7. With the *minimal* criterion applied it is clearly visible that the detectors with a larger number of PMs per storey are superior. At all energies the ratio of the effective areas corresponds to the ratio of total photocathode area and number of PMs per storey. The cuboid equipped with twin ANTARES storeys is the best followed by the standard ANTARES storeys, the double OM and then the single OM. The ratio of the effective areas is energy dependent. At energies up to 100 GeV the differences are very large, were the twin ANTARES storeys are more than factor three more efficient while the double and single OMs have only 10% or even less than 10% of the effective area of the cuboid with ANTARES storeys, respectively. The effective areas start to converge above energies of a few TeV until at 10 PeV the differences are only of the order of 10%.

The *hit* criterion amplifies the differences. The single and double OM detectors drop much more drastically, and at higher energies. The result for the *hit* and *minimal* criteria might still be due to the different number of PMs per storey. However, when comparing the effective areas for the *moderate* criterion the relations are very similar to the ones for the *minimal* criterion, except for a higher energy threshold. This increased threshold is caused by the limited range of muons at the low end of the energy spectrum, which drastically reduces the chances for them to cause hits in several different storeys. At lower energies, the effective area is roughly proportional to the photocathode area of the whole detector. The ranking of the detector performances is the same for the *trigger* criterion, but the differences at lower energies are less obvious. For *selected* events the behaviour is very similar to the *trigger* case, with the exception of energies below a few tens of GeV and the single OM detector which is massively worse here. This is most probably due to the fact that the reconstruction requires local coincidences in addition to big hits for the prefit. With only one PM per storey there are no coincidences and therefore only hits with amplitudes above the big hit threshold can be used for the prefit. In Fig. 8.5 a distribution of the failure codes of the reconstruction algorithm is given. It can be seen that most of the events are not reconstructed because there were not enough coincidences or big hits for the prefit.

The angular resolution is very similar for twin and single ANTARES storeys, with an advantage for the first one at energies below 300 GeV. The resolution for the double OM detector is comparable for energies above 30 TeV, but up to a factor 2-3 worse below. For these three detectors the angular resolution is lower than 0.1 degrees for energies higher than a few TeV. At lower energies it is dominated by the kinematics of the neutrino-nucleon interaction. The single OM detector is a factor two to three worse even at the highest energies.

The energy dependence of the effective area ratios is a consequence of the energy dependence of the muon light yield and the fact that all the criteria are equivalent to thresholds on the number of collected photons. At energies up to 1 TeV the muon is

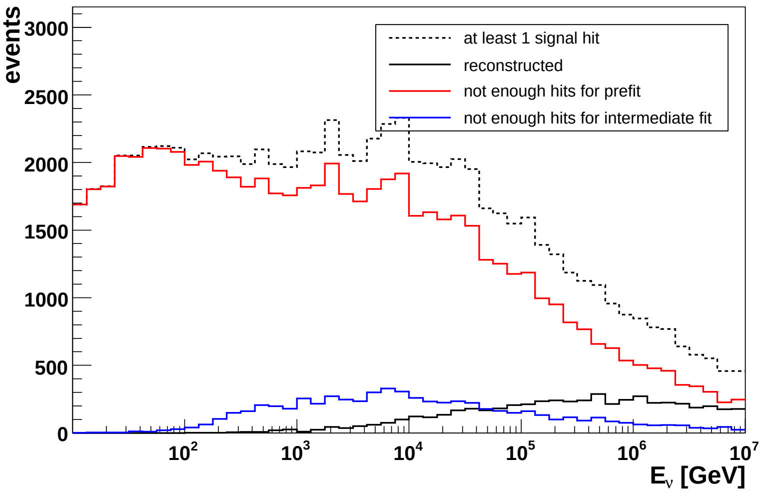

Figure 8.5: Distribution of the different outcomes of the reconstruction process for the single 10"PM cuboid detector. Only events with at least one signal hit are included in the sample. Most of the events that were not successfully reconstructed did not produce enough coincident or big hits for the prefit. In some cases the minimum number of compatible hits for the intermediate fits (step 2 and step 3 in the reconstruction process, see section 5.5) was not achieved.

minimally ionising, resulting in a more or less constant light output per track length. The range of the muon in water and with it the total light output increases roughly linearly with the muon energy in this region, from a few 10 m at 10 GeV to a few km at 1 TeV (see Fig. 4.3). Above 1 TeV the increase in range becomes increasingly slow, as other energy loss processes start to dominate (see Fig. 4.2), resulting in the production of larger numbers of secondary electromagnetic showers and a higher photon yield. At the low-energy end the low number of emitted photons increases the importance of large photocathode area as every extra photon collected can lift the event above the threshold of the relevant criterion. At high energies the number of photons is sufficiently large, so that most of the events passing a significant part of the instrumented volume will satisfy the criteria.

The low hit and coincidence purity of the events around 1 TeV is a consequence of the causality filter and the track length. The causality filter opens a time window starting near the starting time of the track. If the track is short there will be a short time window and only few noise hits will be inside this time window. At a TeV the track length is large enough for the muon to pass through the whole instrumented volume, but the overall light output is relatively small (compared to higher energies). This results in a small number of signal hits and a large number of noise hits in the time window opened by the causality filter and therefore in low purity. At higher energies the light output increases, while the track length in the instrumented volume, and therefore the number of noise hits in the time window, remains the same resulting in an increase of the purity.

The neutrino effective areas as a function of the nadir angle (180°-zenith) are given for the *minimal*, *moderate* and *selected* criteria in Fig. 8.8, where $\cos(\theta) = 1$ corresponds to upgoing events. The general shape of the distribution is the same for all of the selection steps. There is a significant peak in the horizontal direction, which is slightly shifted to downgoing directions. Both for up- and downgoing directions the effective area drops but only about 70% of the maximal value for the upward direction and much more for the downward direction. The smaller reduction of effective area for downward going events follows from the smaller interaction volume for incident neutrinos, as this volume (the volume above the detector) is limited by the distance between the detector and the sea surface. The interaction volume is larger for neutrinos incident close to the horizontal, as there is more than enough water (or rock) to interact with. The reduction for upward going neutrinos and the shift of the peak to a slightly downward direction is a consequence of the absorption of neutrinos with energies above a few 100 TeV in the Earth. The ratios between the detectors are similar for the *minimal* and *moderate* criteria, roughly following the ratio of the overall photocathode areas. At the *selected* level the single OM detector is much worse, the detector with ANTARES storeys is 10-20% better for upward going events than the twin storey detector. This is interpreted as a consequence of a bias in the reconstruction algorithm, which is tuned for ANTARES storeys and upward going events.

The differences between the effective areas as functions of the zenith angle are rather small when compared to the differences in the areas dependent on the energy. This is due to the sample being dominated by events with energies between 10 and 100 TeV (see e.g. Fig. 6.4), where most detectors have a very similar performance. The largest differences between detector configurations appear at lower energies. In order to illustrate this, the zenith-angle dependent effective area for events with energies below 10 TeV is given in Fig. 8.9. The differences between the detectors are clearly visible and also the general shape is different. There are clearly more upgoing events than downgoing ones and there is no peak in the horizontal. The reason for this is that below 10 TeV there is no absorption in the Earth and therefore the effect of the larger interaction volume below the detector is dominant.

Candidate detectors

The effective areas for the *candidate* versions of the detectors are shown in Fig. 8.10 and 8.11. For the minimal criterion, all the detectors have about the same effective area above 100 GeV, although the twin ANTARES and double OM versions appear to be slightly better at a few hundred TeV. Below statistics is very low. Regarding the *minimal* criterion, a similar photocathode area apparently results in similar effective areas. For the *hit* criterion the twin ANTARES storey *candidate* detector and the ANTARES storey detector are still very similar. The other two versions are clearly worse, with the single OM detector effective area being only at 70% of that of the ANTARES storey detector even at 10 PeV. The *hit* criterion depends strongly on the number of PMs per storey. When the *moderate* criterion is applied, this behaviour is inverted. Now the single OM detector is the best one, followed by the double OM version, the ANTARES storey detector and finally the twin ANTARES storey candidate. This is not surprising as in the *candidate* versions the number of storeys is different and as the *moderate* criterion requires six storeys to be hit, it is biased towards detectors with a large number of storeys. When using the *trigger* and *selected* criteria, the behaviour is similar to the *hit* case, with the exception of the twin ANTARES storey detector. Apparently the reconstruction is not very well suited for this layout, as its effective area drops significantly after reconstruction compared to the *trigger* and *hit* stages.

The angular resolution for the *candidate* configurations is shown in Fig. 8.11. The resolution of the single OM detector is a factor two to three worse than the ANTARES configuration over the whole energy range, while all others are comparable down to energies of 10 TeV, the twin ANTARES storey type has a resolution which is about 10% worse. Below 10 TeV, the double and twin ANTARES storey detectors are worse than the ANTARES storey type.

Section summary

- The effective area generally increases with increasing photocathode area.
- The ability to utilise local coincidences increases the performance for the *hit*, *trigger* and *selected* criteria.
- The reconstruction strategy appears to be slightly biased towards the ANTARES storey structure
- Even in the *candidate* case, the single and double OM detectors are significantly worse than the reference detector at the *hit*, *trigger* and *selected* levels.

8.2 Detector storeys with 3"photomultipliers

During the preparations for the KM3NeT Design Study, the idea to use several small PMs per storey instead of a few large hemispherical ones was developed [119,120]. The advantages of these small PMs are a higher quantum efficiency of more than 30%, a smaller TTS of about 0.5 ns and better two-photon separation capability. A further advantage is that they suffer less from gain degradation over time. Furthermore they are readily available in large numbers from the manufacturers. A disadvantage might be the increased amount of electronics required for the supply of high voltage and for the readout of the PMs.

One candidate under consideration is the Photonis XP53X2 3"PM [121]. While size, TTS and quantum efficiency are used in the simulation, the two-photon separation advantage is not accounted for. For the angular acceptance a 'flat disc' distribution was assumed, which means the angular acceptance is proportional to the cosine of the incidence angle of the photon. This and the quantum efficiency are shown in Fig. 8.12. As the pressure-resistant containers (glass spheres) and the optical gel are industrial standard, and no other data was available, the same transmissivity of the glass and gel combination as for 10"photomultipliers was used.

8.2.1 Storey layouts with 3"photomultipliers

Schematic layouts of the storeys with 3"PMs are shown in Fig. 8.13.

minimal

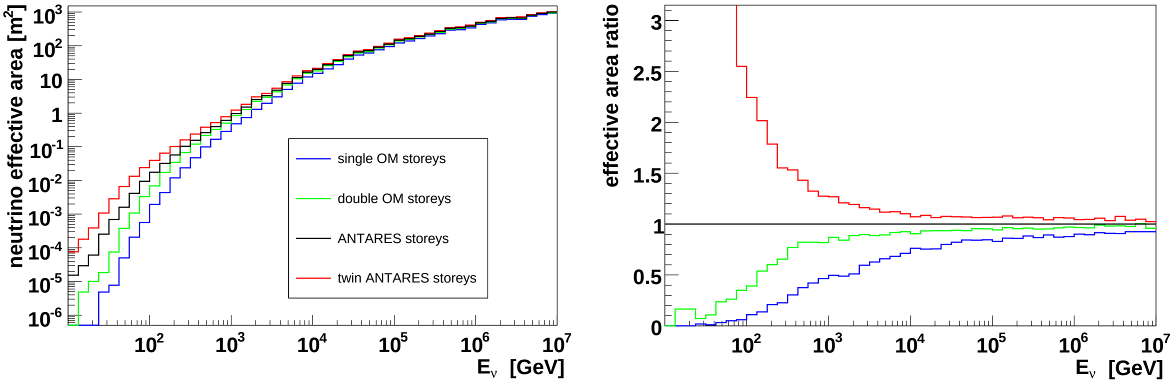

hit

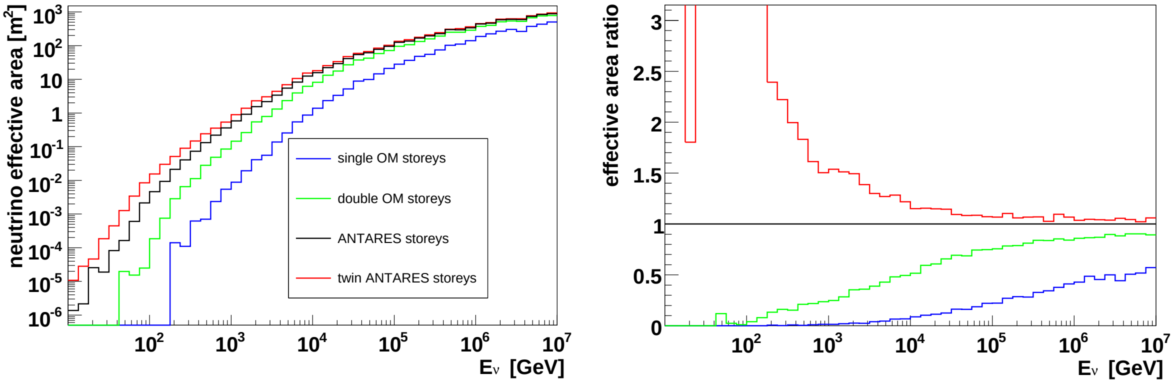

moderate

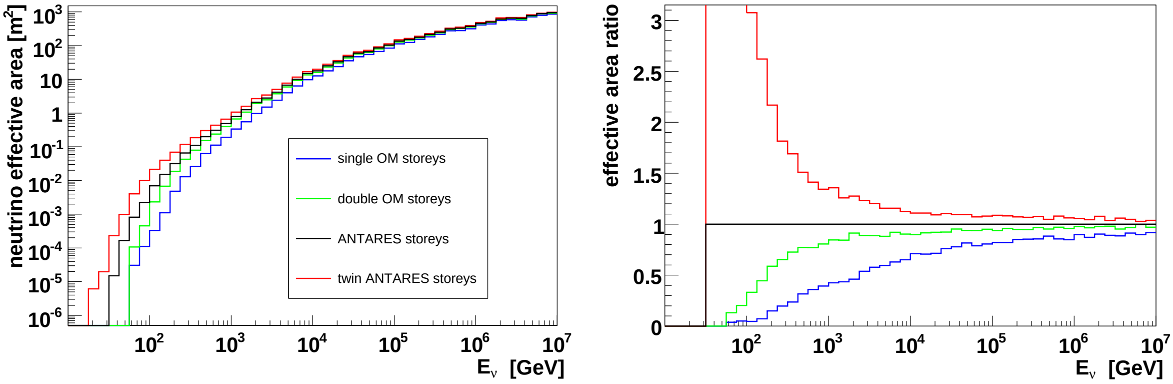

Figure 8.6: Neutrino effective areas and effective area ratios for *cuboid* detectors equipped with 10”PMs, with the *minimal*, *hit* and *moderate* criteria applied.

trigger

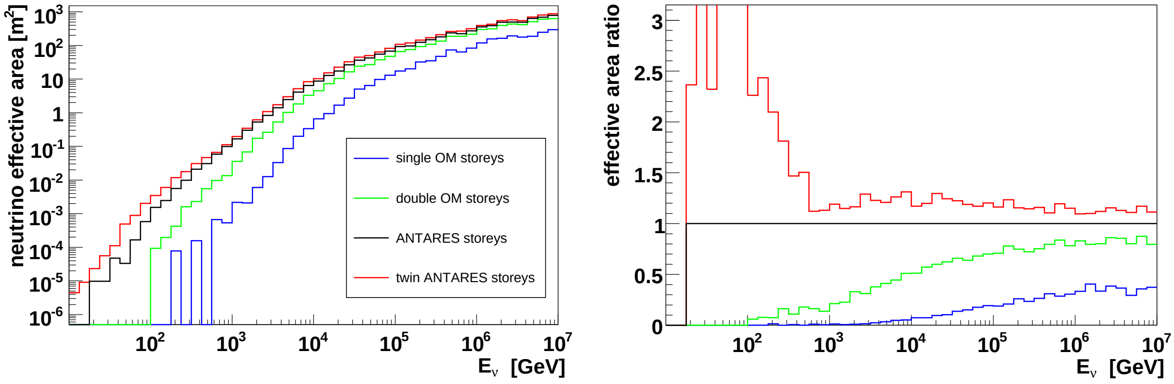

selected

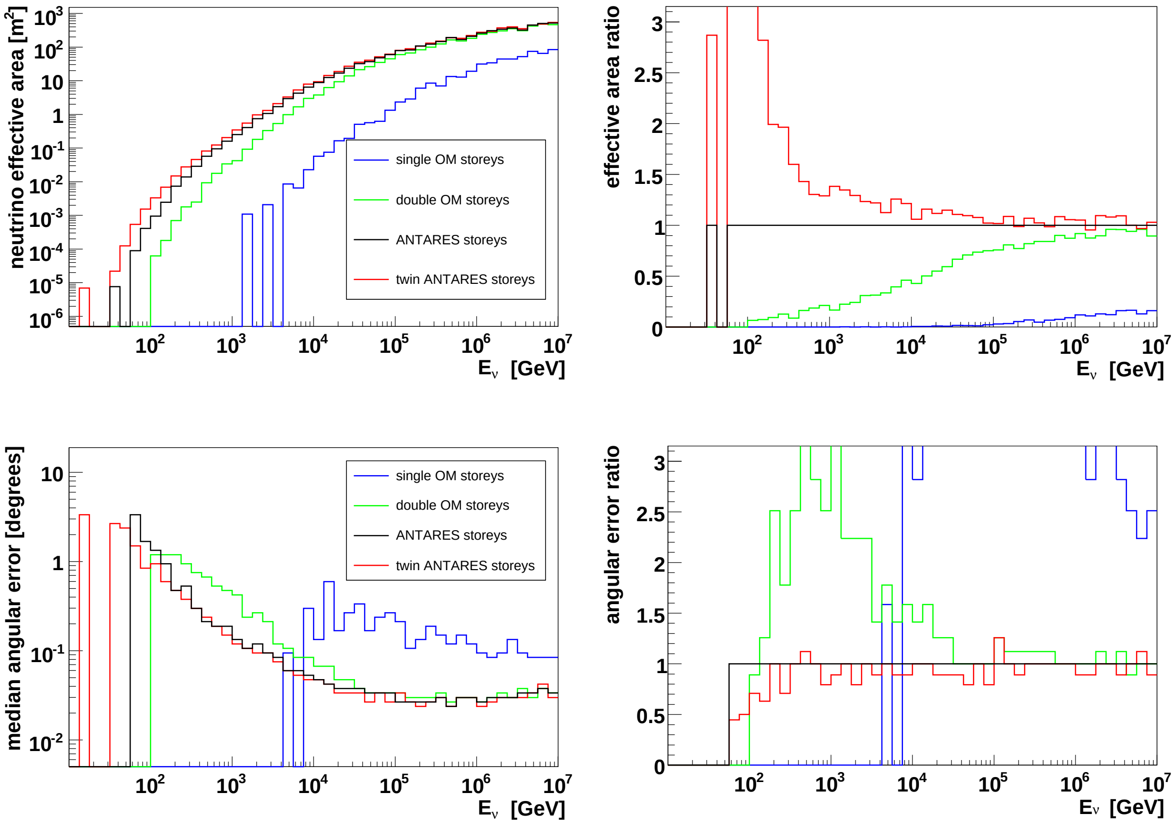

Figure 8.7: Neutrino effective areas and area ratios with the *trigger* criterion applied (top) and for *selected* events (middle) for *cuboid* detectors with 10”PMs. Angular resolution and resolution ratios for *selected* events (bottom).

minimal

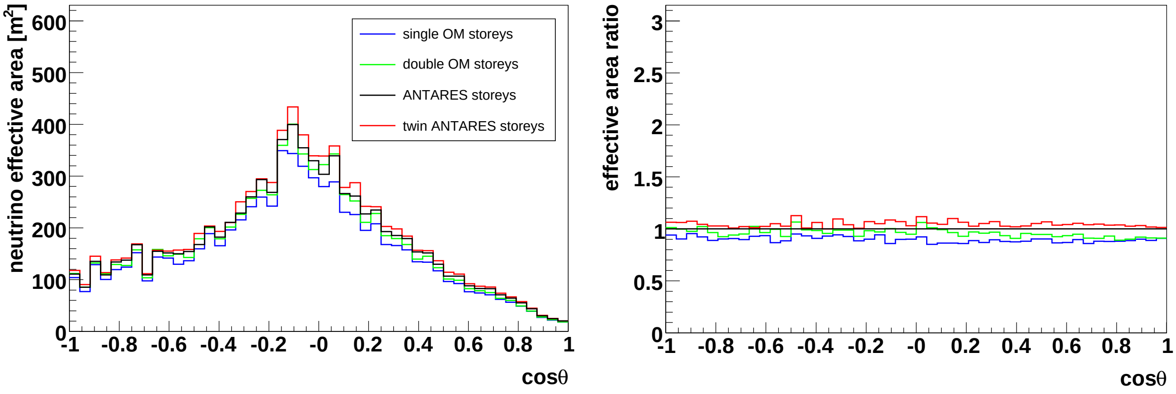

moderate

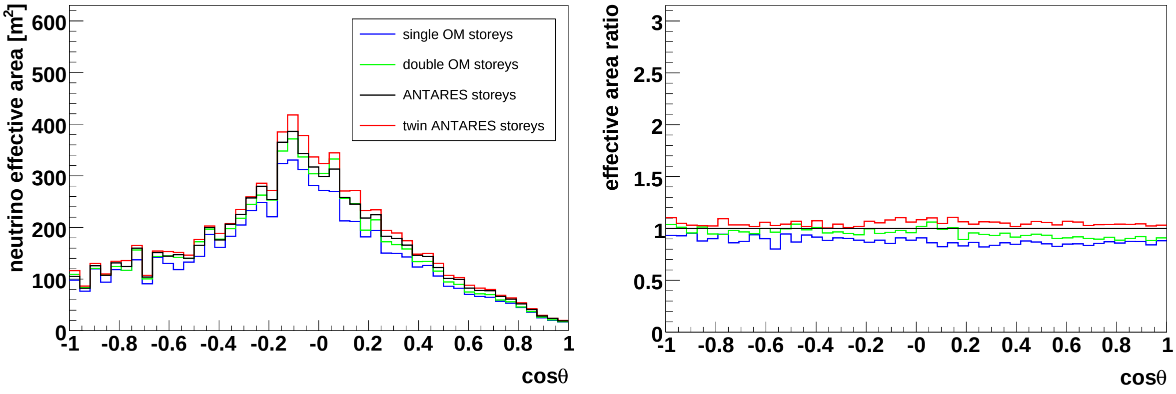

selected

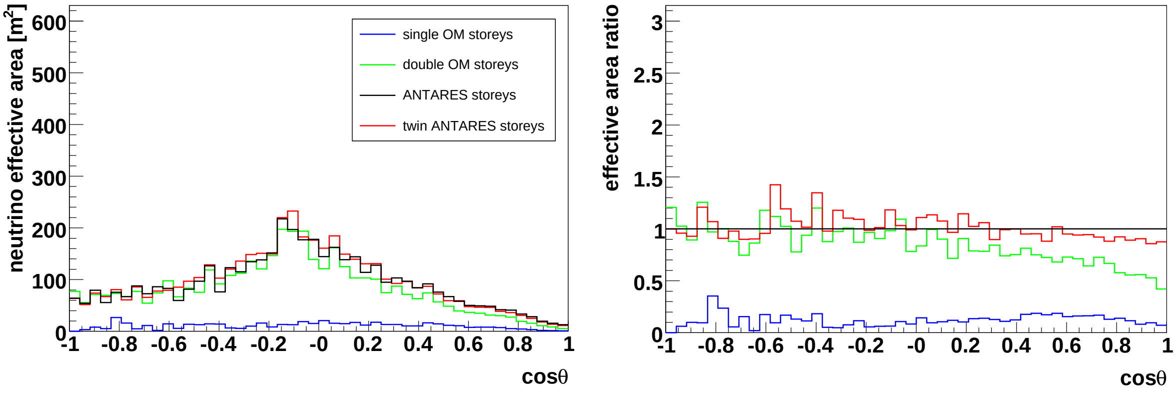

Figure 8.8: Neutrino effective areas and effective area ratios as a function of zenith angle for *cuboid* detectors equipped with 10”PMs with *minimal*, *moderate* and *selected* criteria applied.

minimal (E<10 TeV)

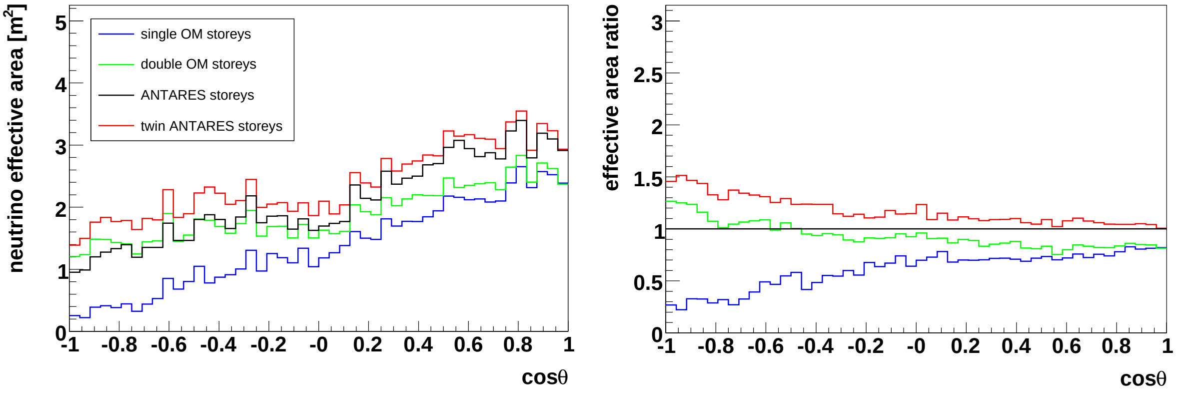

moderate (E<10 TeV)

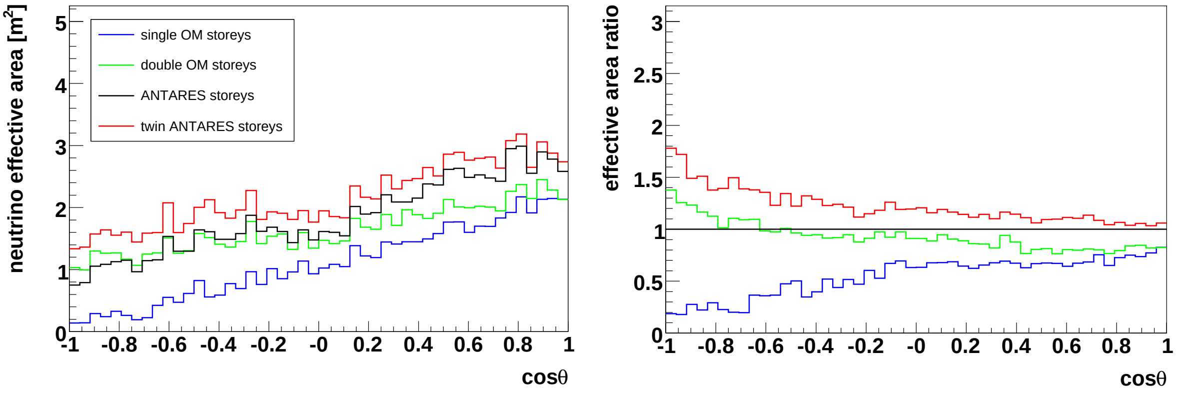

selected (E<10 TeV)

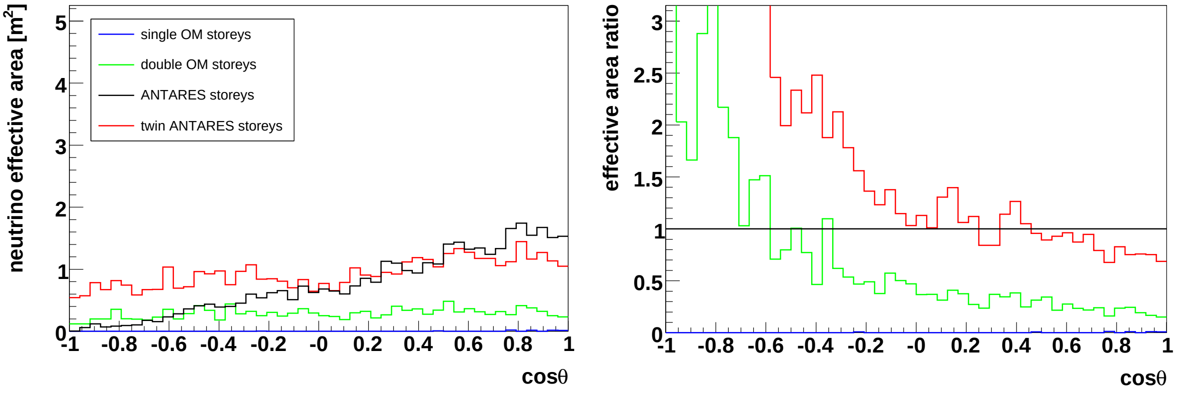

Figure 8.9: Neutrino effective areas and effective area ratios for events with E <10 TeV as a function of zenith angle for *cuboid* detectors equipped with 10" PMs with *minimal*, *moderate* and *selected* criteria applied.

minimal

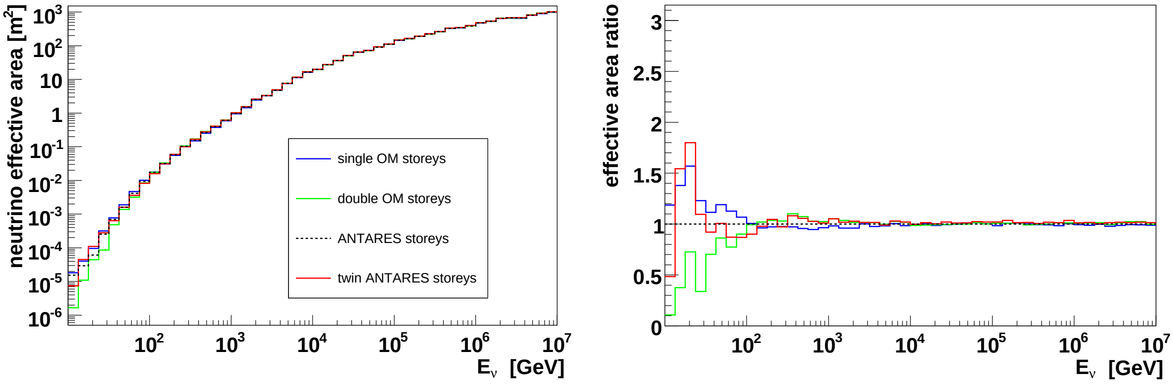

hit

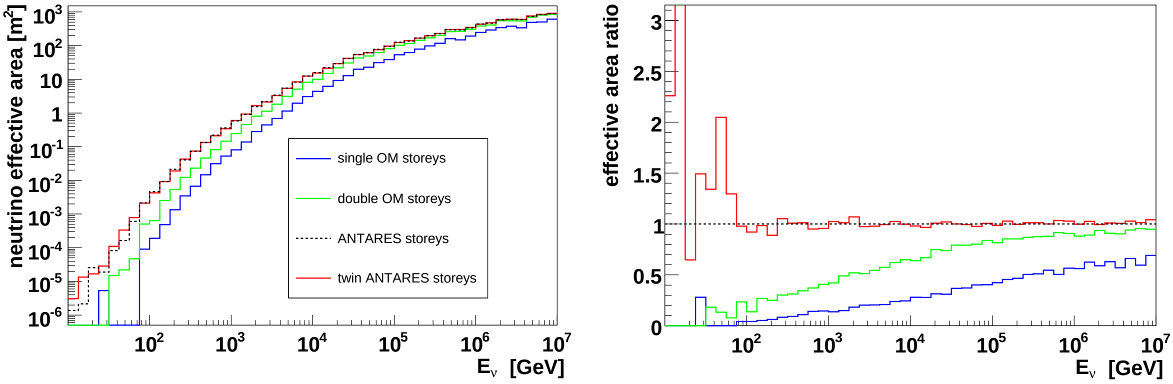

moderate

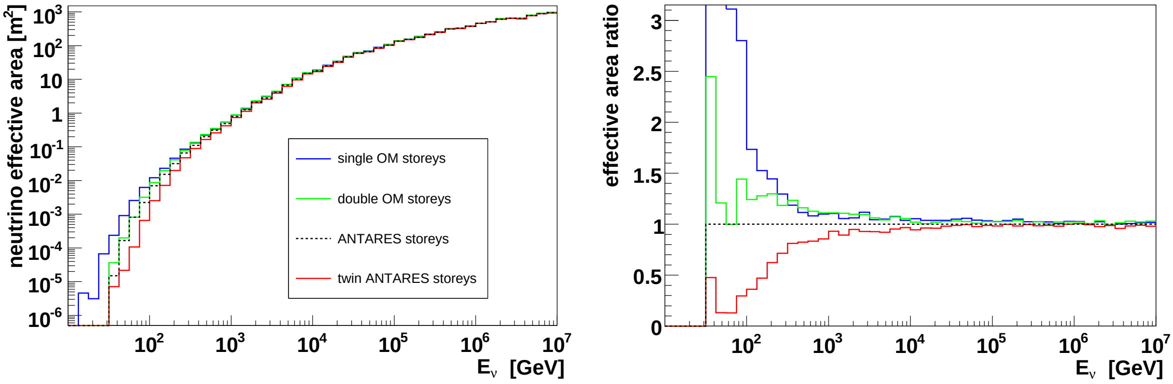

Figure 8.10: Neutrino effective areas and effective area ratios for *candidate* detectors equipped with 10”PMs, for the *minimal*, *hit* and *moderate* criteria applied.

trigger

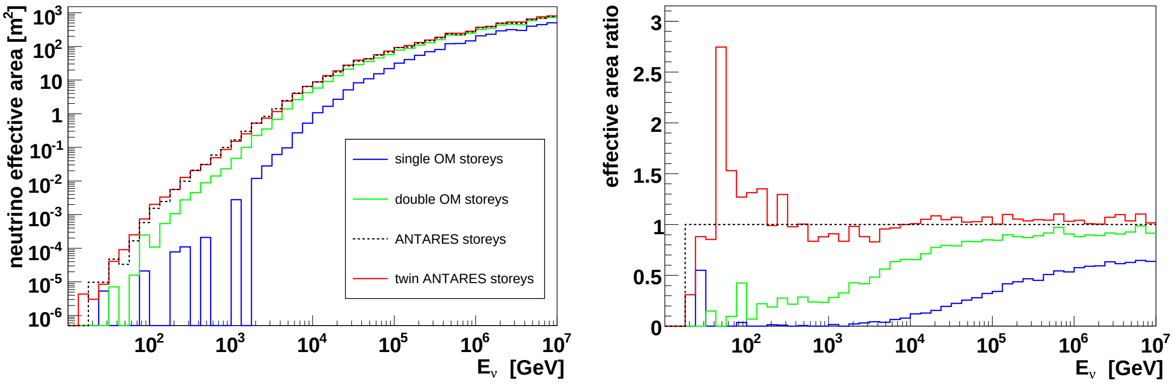

selected

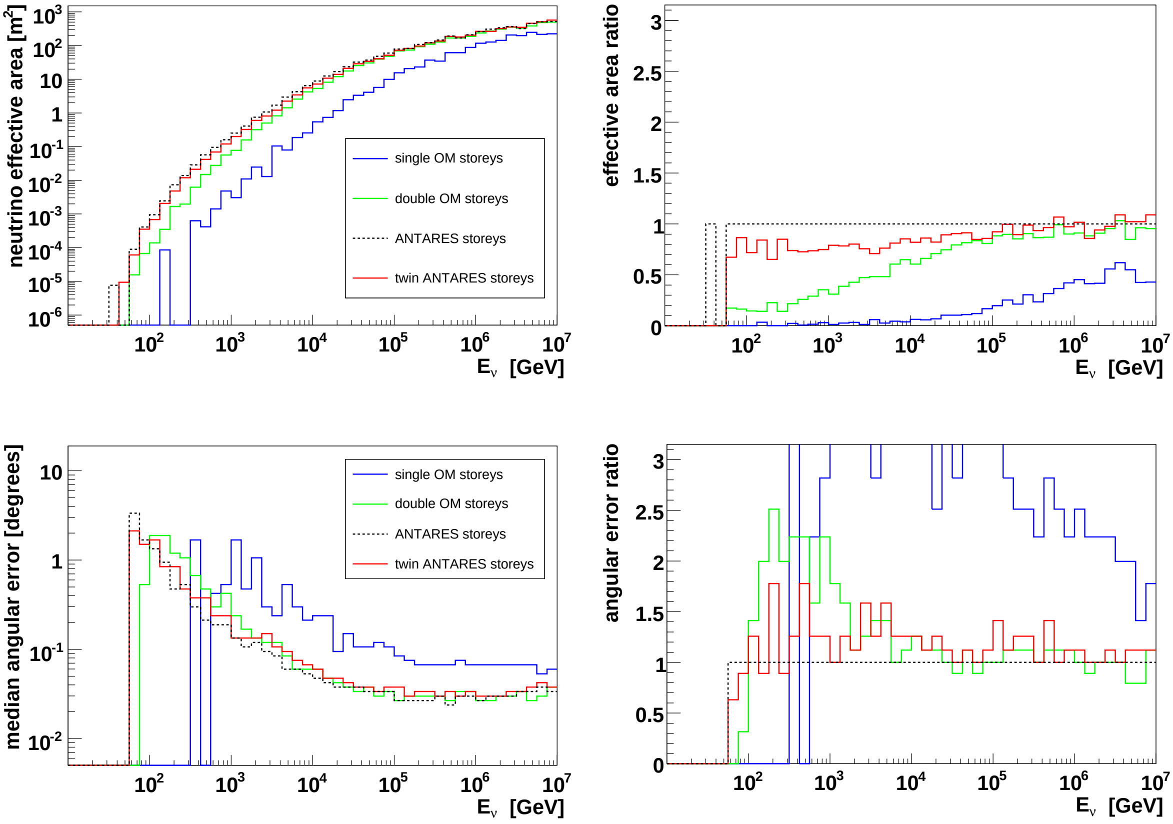

Figure 8.11: Neutrino effective areas and area ratios with the *trigger* criterion applied (top) and for *selected* events (middle) for *candidate* detectors with 10"PMs. Angular resolution and resolution ratios for *selected* events (bottom).

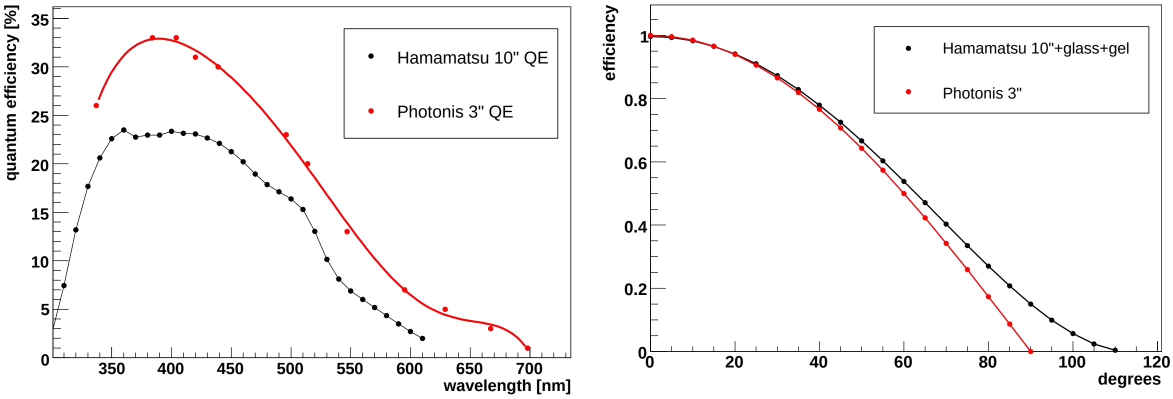

Figure 8.12: Left: Quantum efficiency of the Photonis XP53X2 3”PM compared to the values for the Hamamatsu R7081 10”as used in ANTARES (black). The numbers are taken from [122], the red line is the result of a fit. Right: Angular acceptance of the Photonis XP53X2 3”PM (red) compared to the values for the Hamamatsu 10”as used in ANTARES (black).

The MultiPMT cylinder storey

One option to arrange a number of small PMs into a storey is to place them into a standard pressure-resistant glass cylinder (see Fig. 8.14). Twelve 3”PMs would fit into one of these cylinders, which would add up to a similar photocathode area as a single 10”PM. By using three of these subcylinders to form a storey, about the same photocathode area as for a standard ANTARES storey is achieved.

The individual readout of all 36 PMs is probably difficult to realize due to the limited space for electronics. Therefore two optional readout principles have been studied for the cylinder storeys. For the first one it was assumed that one readout system is available for each of the subcylinders. All the hits that arrive in one subcylinder within a time window of 20 ns are added, effectively treating the twelve PMs as one with twelve times the photocathode area of a single 3”PM. The second assumes a readout method first proposed in [120]. This uses the time-over-threshold (TOT) of the PM signals, where the length of the resulting TOT signal is proportional to the logarithm of the signal amplitude and its starting time indicates to the photon arrival time. The TOT signals of one subcylinder would be added and sent to shore, where the hit amplitudes and the times can be reconstructed. For the simulation this implies, that amplitudes and times of individual hits are known, but not which of the PMs in one subcylinder was hit. Therefore not PM identifiers, but subcylinder identifiers and positions were used for the hits in the simulation and the reconstruction.

As the overall photocathode area of the *cuboid* with these cylinder storeys is similar to the reference detector, no *candidate* layout was required.

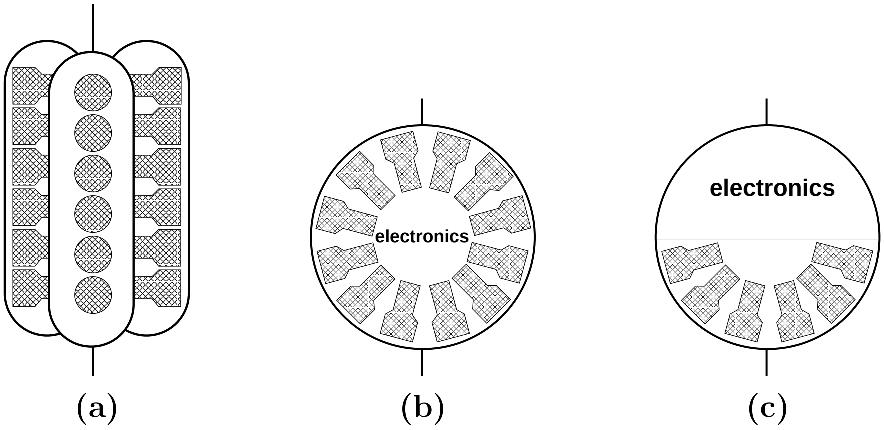

Figure 8.13: Schematic layouts of the storeys with 3"PMs. (a) MultiPMT cylinder storey with 36 3"PMs; (b) MultiPMT sphere storey with 36 or 42 3"PMs; (c) MultiPMT sphere storey with 21 3"PMs.

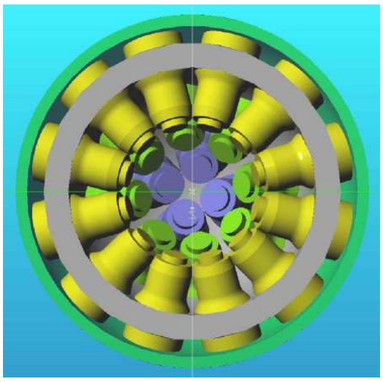

Figure 8.14: Standard pressure resistant glass cylinder (left) and schematic layout of the MultiPMT sphere storey (right).

The MultiPMT sphere storey

The optical connection of the (spherical) PMT surfaces with a cylindrical container surface using the optical gel might be difficult. An alternative is to position the 3"PMs in a glass sphere. It is possible to place up to 42 of these in one 17"sphere, still leaving a central spherical space with a radius of about 10 cm (see Fig. 8.14). In order to investigate the differences caused by the PM arrangement, a version with 36 PMs was used for the comparison with the cylinders. As some of the PMs are oriented almost straightly upward the storey will suffer from sedimentation. Additionally, the space for electronics is very limited. Therefore another version was simulated, were only the lower hemisphere was equipped with then 21 PMs. For the latter storey types *candidate* detectors were simulated. The 42 PM *candidate* configuration has 8 storeys per string with distances of 82 m, while the 21 PM version has 16 storeys per string at distances of 38.5 m.

8.2.2 Results for storeys with 3"photomultipliers

Cuboid detectors

The effective areas for the *cuboid* with MultiPMT storeys are shown in figures 8.17 and 8.18, the ratios are given relative to the *cuboid* with ANTARES storeys. The relations between the detectors with MultiPMT storeys is similar at all selection steps. The sphere with 42 PMs is the best due to the high photocathode area, and the sphere with 21 PMs is the worst because of its lower cathode area. The sphere and the cylinder with 36 PMs have almost the same effective areas, indicating that the shape of the PM arrangement has little effect. When comparing to the *cuboid* with ANTARES storeys the situation is a bit different. For the hit based criteria (*minimal*, *hit* and *trigger*) the MultiPMT modules (except the 21 PM version) have significant advantages at lower energies. In the *minimal* case their effective areas start to exceed the ANTARES-storey detectors area at 10 TeV and are a factor of two to three larger at energies below 100 GeV. The 21 PM version starts to get worse at the same energy and drops to 60% of the effective area of the reference detector at a few ten GeV. Considering the fact that it only has slightly more than half of the photocathode area, this is still remarkable (the double OM detector has two thirds of the area of the reference detector, but it is far worse at low energies). The low-energy efficiency further increases for the *hit* and *trigger* criteria where the energy at which the area ratio starts to rise increases and the maximum ratio is larger than three. In the *hit* case the 21 PM sphere is similar to the ANTARES-storey detector at larger energies, up to 20% worse between 100 GeV and 1 TeV, and better below 100 GeV.

Of course this advantage is to some extent caused by the larger number of PMs per storey, as the MultiPMT modules simply produce more individual hits. Any criterion just counting these will be biased toward such a structure. On the other hand, even at the *moderate* level the cuboids with the 3"PMs are better at energies below a few TeV (again except the 21 PM type). For selected events the ratio starts to rise at lower energies, starting from just below 1 TeV. Here the 21 PM type is almost comparable to the ANTARES-storey detector at all energies. The angular resolution is shown in Fig. 8.18. It is almost equal for all the detectors and below 0.1 degrees for energies larger than 2 TeV, despite the smaller TTS of the small PMs.

The results for detectors equipped with the MultiPMT cylinder storey using the different readout options are shown in Figs. 8.25 and 8.26. For the hit based *minimal* criterion the effective areas of the standard version and the version with TOT readout are virtually identical, as obviously the overall number of hits is the same. The effective area of the version where hits in one subcylinder are added starts to become increasingly worse for energies below 1 TeV. As adding the hits reduces their overall number, this is no surprise. If the *moderate* criterion is applied, all three versions show a nearly identical efficiency. Again this is is not surprising, as the properties per storey (photocathode area, quantum efficiency) are the same and the number of storeys hit is therefore not influenced significantly by the assumed readout option. For *selected* events the situation is a bit different. The TOT readout versions starts to get worse below 1 TeV. This is due to the fact that the exact position of hits on a storey is not known. An individual hit is taken to be at the cylinder standard position (rather than the exact PM position), causing problems in the reconstruction process. When the hits are added, the effective area is actually higher between 100 GeV and 20 TeV and drops quickly below. By adding the hits, the number of big hits is obviously increased, as all hits that would normally be coincident, are added. Therefore the number of hits usable for the prefit is not smaller. Apparently the performance is even increased at medium energies by this process. The angular resolution for the added hits readout is 20 to 40% worse at all energies, compared to the full readout. This is due to adding more noise hits for the reconstruction. The angular resolution of the TOT readout version shows a behaviour similar to its effective area. It is comparable to the standard version at energies above 1 TeV and a bit worse below due to the positional inaccuracy of the hits caused by the properties of the readout method.

Obviously, the MultiPMT modules produce a larger number of hits, partly due to a larger number of PMs per storey. But as the advantage is still present at the *moderate* level, there has to be an additional reason for this. The most probable one is the higher quantum efficiency. In order to analyse its effect two additional storey types were produced. The first one is identical to the cylinder with 36 PMs with the exception, that the quantum efficiency of the ANTARES PMs (Fig. 8.2) was used. The second one is an ANTARES storey, where the increased quantum efficiency of the 3"PMs (Fig. 8.12) was assumed for the 10"PMs. The effective areas for detectors equipped with these storeys are compared to their standard versions in Fig. 8.20 and 8.22. For the hit based criteria the high quantum efficiency version of the ANTARES-storey detector and the standard cylinder storey detector are similar over the whole energy range. The low quantum efficiency cylinders and the standard ANTARES storeys produce similar effective area above about 100 GeV. Below, the cylinders are still better, most probably due to the aforementioned larger number of individual hits. On the *moderate* level the detector pairs with the same quantum efficiency are almost equal above 100 GeV. To study the region below 100 GeV a simulation using the low energy sample was done. The result for the *moderate* case is given in Fig. 8.21. It shows that the cylinders are actually worse than the ANTARES storeys with increased quantum efficiency, below about 300 GeV. In Fig. 8.22, at the *selected* level, the cylinder versions seem to be clearly worse than their ANTARES OM counterpart with the same quantum efficiency, except at lowest energies. As at all other selection steps, the cylinders and ANTARES storeys with the same quantum efficiency are more or less similar, this points to a bias in the reconstruction towards the ANTARES

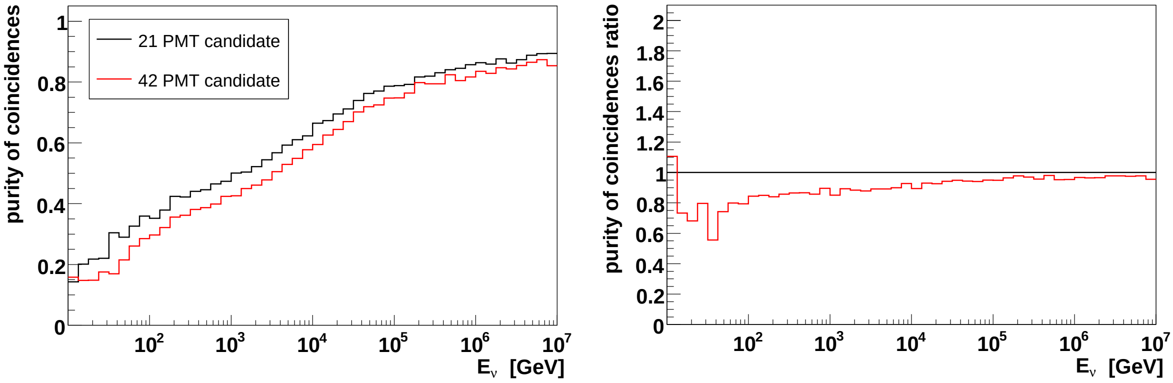

Figure 8.15: Left: Purity of the coincidences and big hits as a function of energy for the *candidate* 42 PM sphere storey detector (red) and the *candidate* 21 PM sphere storey model (black). Right: Ratio of the purity of the coincidences.

storey layout. Taking this into account, the higher quantum efficiency of the 3”PMs has proven to be the main reason for the increase of the performance of a detector, especially at low energies.

The neutrino effective areas as a function of nadir angle θ for the standard *cuboids* with MultiPMT storeys are given for the *minimal*, *moderate* and *selected* criteria in Fig. 8.19. The general shape of the distribution is the same as for the detectors with 10”PMs. The effective areas look very similar for the *minimal* and *moderate* criteria. For *selected* events, the reference detector equipped with ANTARES storeys is obviously more efficient for upward going events, as all of its PMs are pointing downward. The sphere modules are also better than the cylinder storey for this type of events, as they also contain PMs pointing more or less downward. The half sphere containing 21 PMs is the best of the MultiPMT storeys for upward going neutrinos, as all of its PMs are pointing into the lower hemisphere, but this is compensated in the downward going direction, where it is the worst of all.

Candidate detectors

The effective areas and ratios for the *candidate* versions compared to the *cuboid* detectors (in the cylinder and 36 PM sphere case) are shown in figures 8.23 and 8.24. For the hit based criteria the 21 PM sphere storey *candidate* is comparable to the *candidate* detector with 42 PMs, a bit better even for the *hit* and *trigger* criteria, between 100 GeV and 10 TeV. It is obviously significantly better below a few TeV at the *moderate* level, as it has twice the number of storeys. The most interesting result can be seen at the *selected* stage, where the 21 PM *candidate* is significantly better than the 42 PM *candidate* detector. Apparently this setup increases the reconstruction potential (although it might be that the reconstruction algorithm just favours strictly downward-looking storey-types as was already hinted at in section 8.1). The angular resolution, shown in Fig. 8.24, is also about 10 to 20% better, especially at energies below 1 TeV.

The *candidate* 21 PM module detector has a higher density of storeys in combination

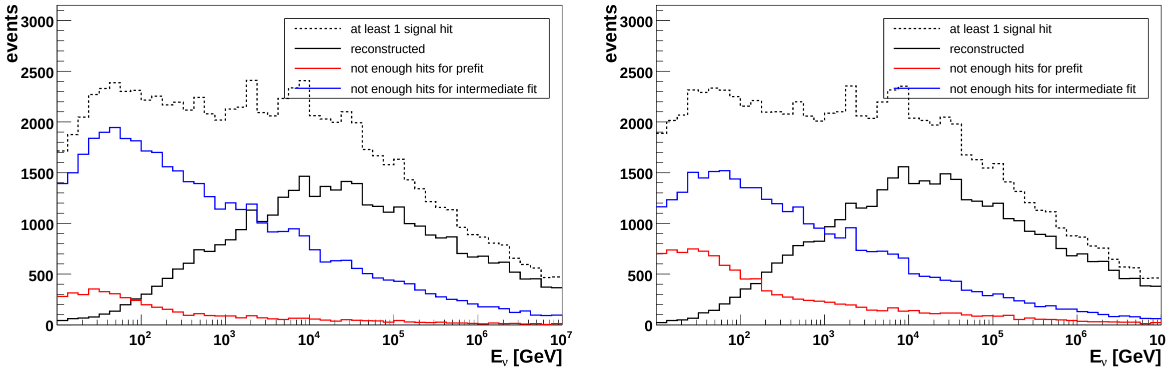

Figure 8.16: Distribution of the different outcomes of the reconstruction process for the *candidate* 42 PM sphere storey detector (left) and the *candidate* 21 PM sphere storey model (right).

with a storey type that can create local coincidences and has high hit probabilities. This is a big advantage for reconstruction, especially at low energies, where muon tracks are short and light output is low. In addition more storeys can have local coincidences hence a larger number of hits enters the prefit algorithm, which therefore provides better results for the subsequent fitting procedures. In Fig. 8.15 the purity of the hits in the prefit for the candidates with 21 and 42 PM sphere storeys is shown. The purity for the 21 PM *candidate* becomes increasingly better towards lower energies, where it is 20 to 30% higher than that of the 42 PM *candidate* detector. As a consequence the 21 PM version loses less events in the intermediate step of the fitting process (see section 5.5), as can be seen on the distribution of the failure codes for the two detectors, shown in Fig. 8.16.

Section summary

- Storeys with many small PMs (MultiPMT storeys) provide advantages at energies below a few TeV (depending on selection), mostly due to the higher quantum efficiency of the small PMs.
- Despite the smaller TTS of the small PMs, the angular resolution is not significantly better for detectors with MultiPMT storeys.
- The geometry of the arrangement of the PMs in a storey has almost no influence on the detector performance.
- A simplification of the readout method for the MultiPMT storeys does not reduce the effective areas significantly above a few TeV.
- Detectors with many storeys carrying few PMs are superior to detectors with few storeys carrying many PMs, as a high density of storeys provides better (coincidence) purity and therefore better reconstruction results.

minimal

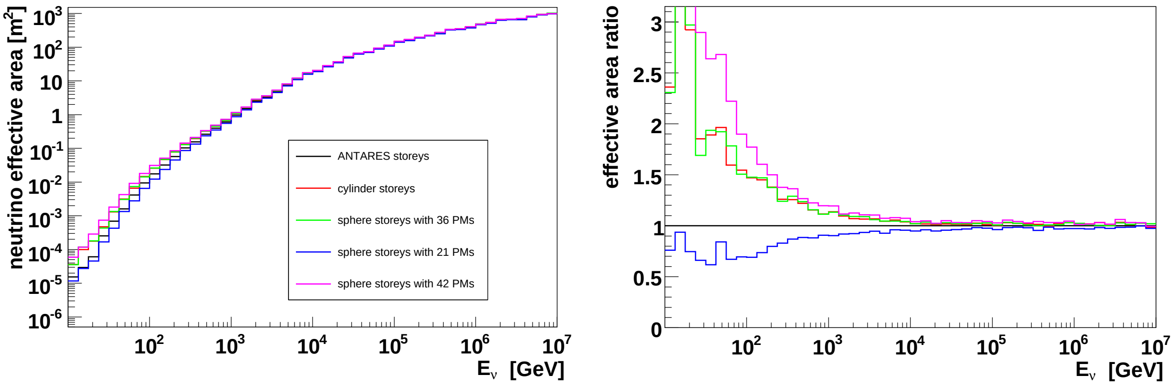

hit

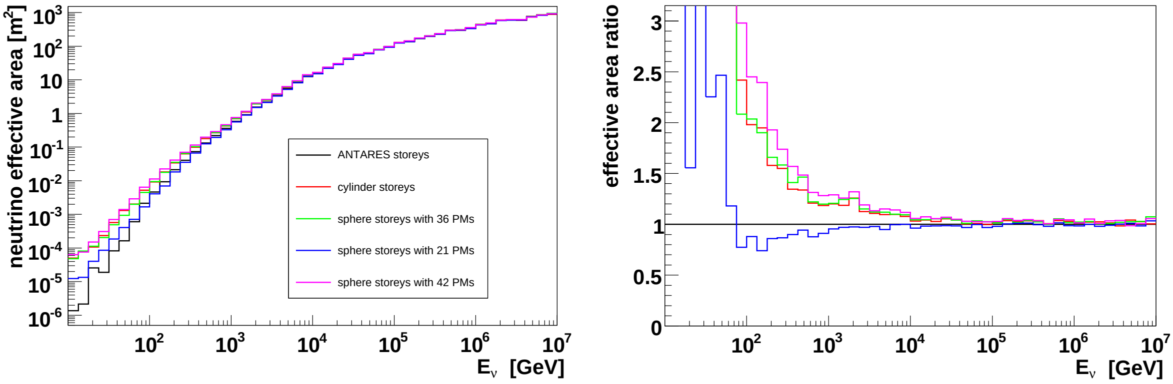

moderate

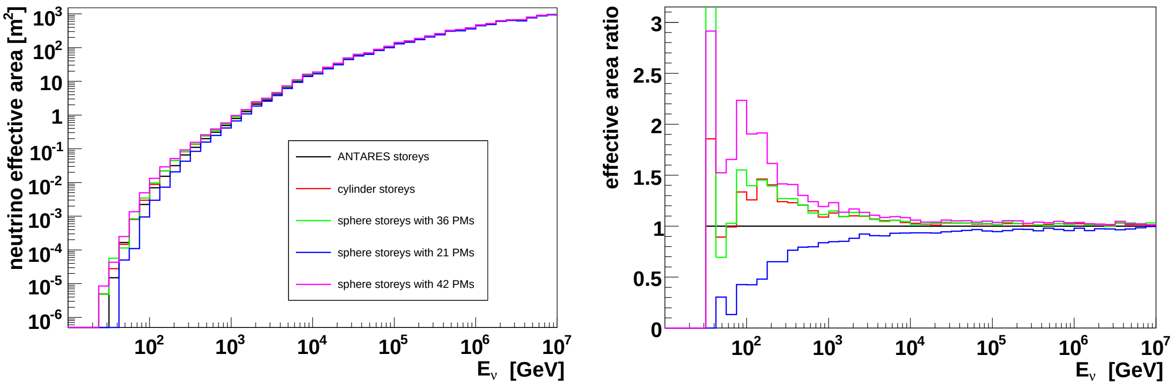

Figure 8.17: Neutrino effective areas and effective area ratios for *cuboid* detectors equipped with 3”PMs, for the *minimal*, *hit* and *moderate* criteria applied.

trigger

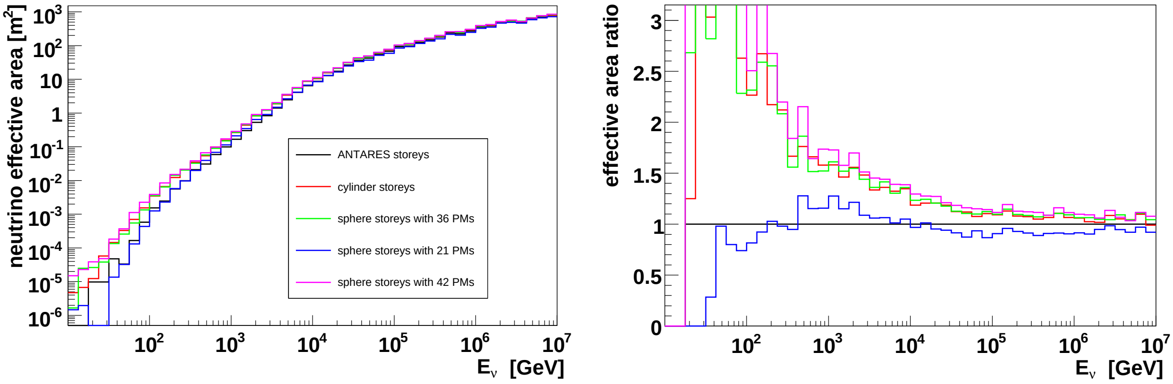

selected

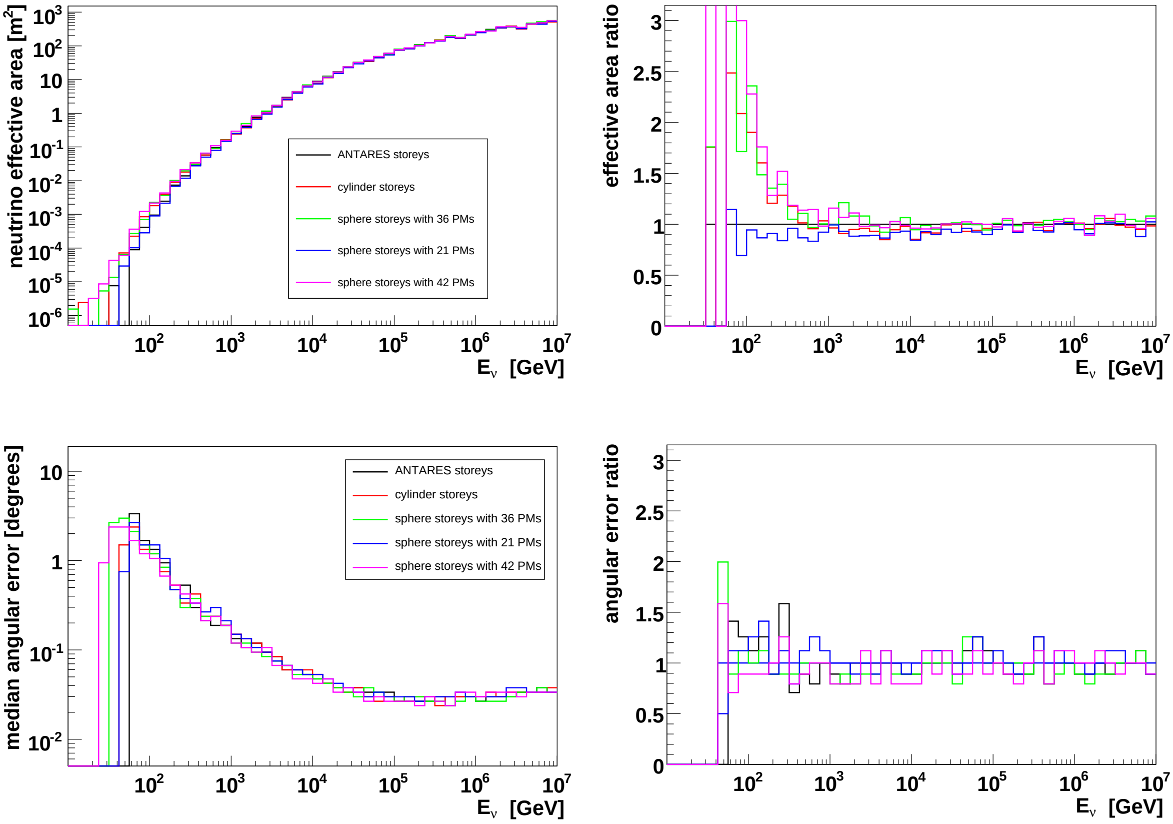

Figure 8.18: Neutrino effective areas and area ratios with the *trigger* criterion applied (top) and for *selected* events (middle) for *cuboid* detectors with 3”PMs. Angular resolution and resolution ratios for *selected* events (bottom).

minimal

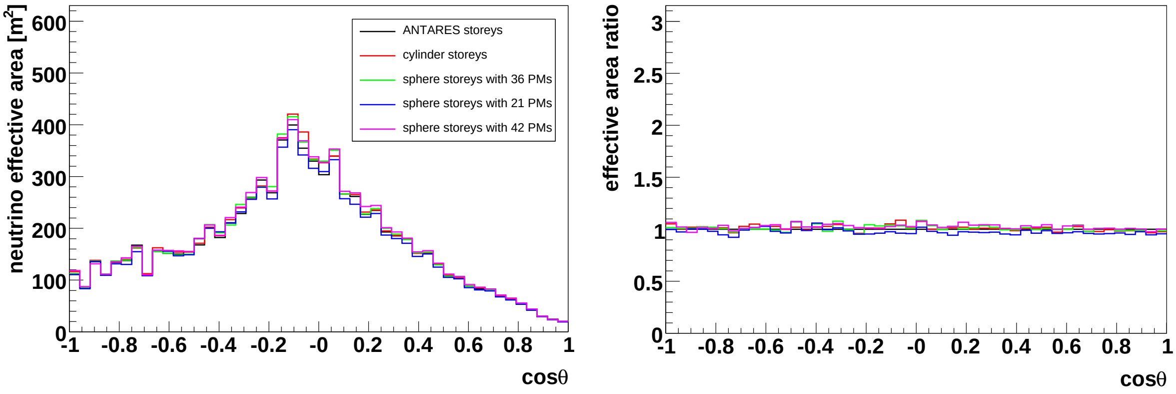

moderate

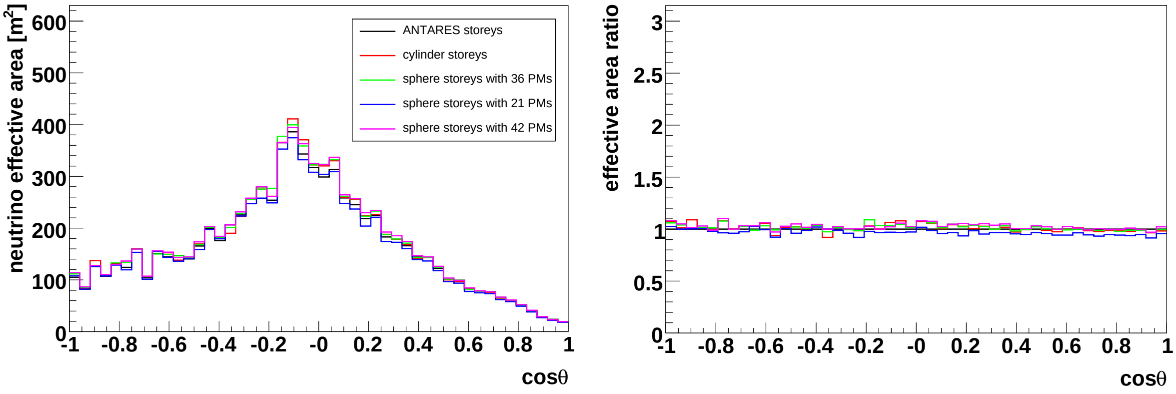

selected

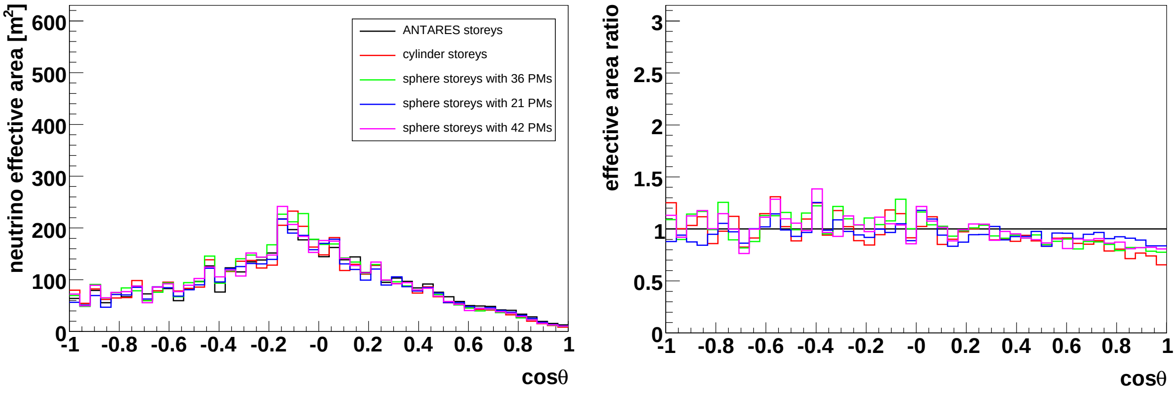

Figure 8.19: Neutrino effective areas and effective area ratios as a function of zenith angle for *cuboid* detectors equipped with 3”PMs with *minimal*, *moderate* and *selected* criteria applied.

minimal

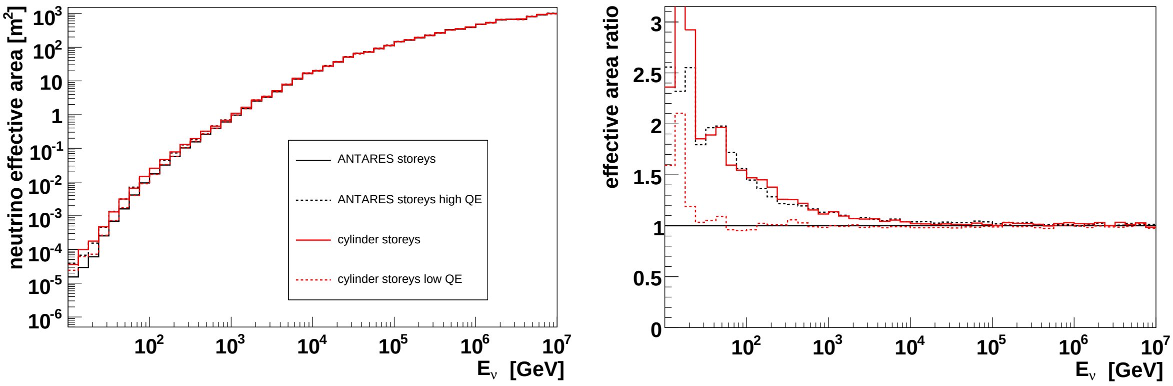

hit

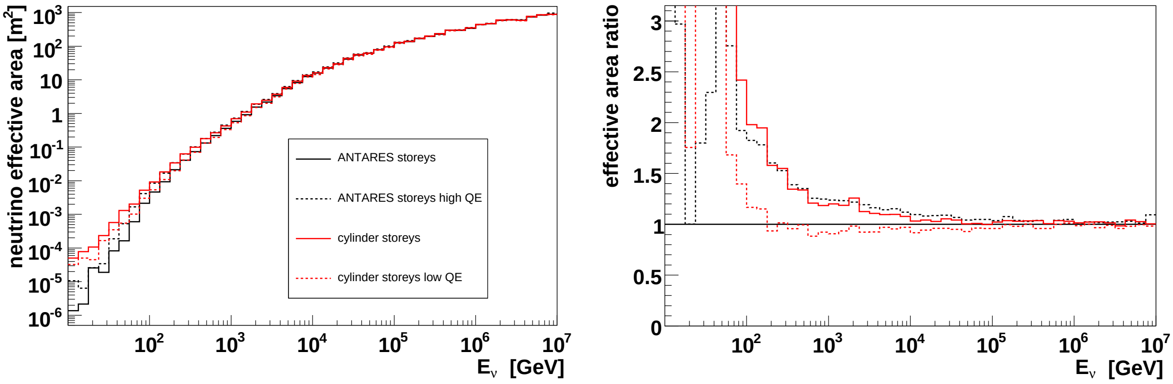

moderate

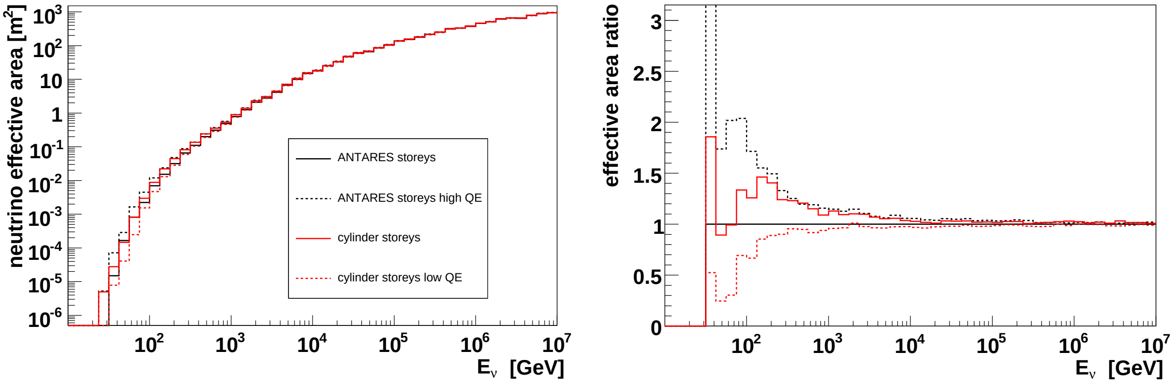

Figure 8.20: Neutrino effective areas for *cuboid* detectors and modules with modified quantum efficiencies with *minimal*, *hit* and *moderate* criteria applied.

moderate (low energy sample)

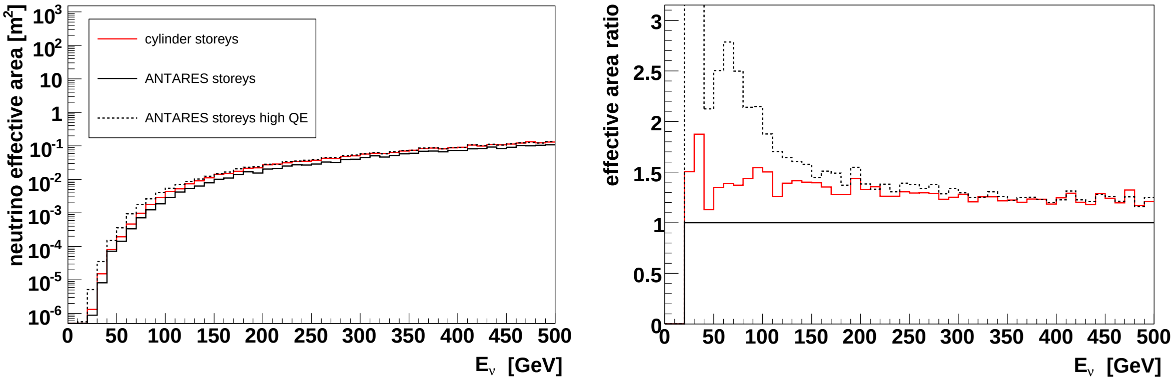

Figure 8.21: Neutrino effective areas for *cuboid* detectors and modules with modified quantum efficiencies for the low energy sample and the *moderate* criterion.

trigger

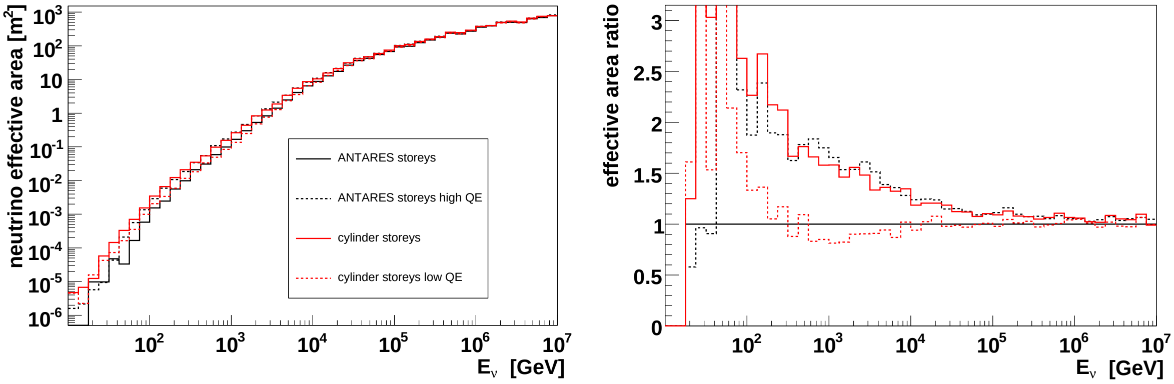

selected

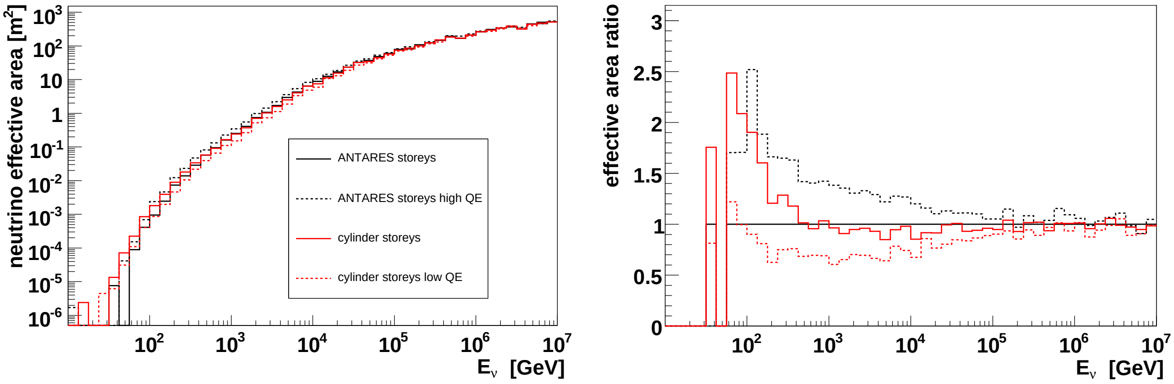

Figure 8.22: Neutrino effective areas for *cuboid* detectors and modules with modified quantum efficiencies for *trigger* and *selected* events.

minimal

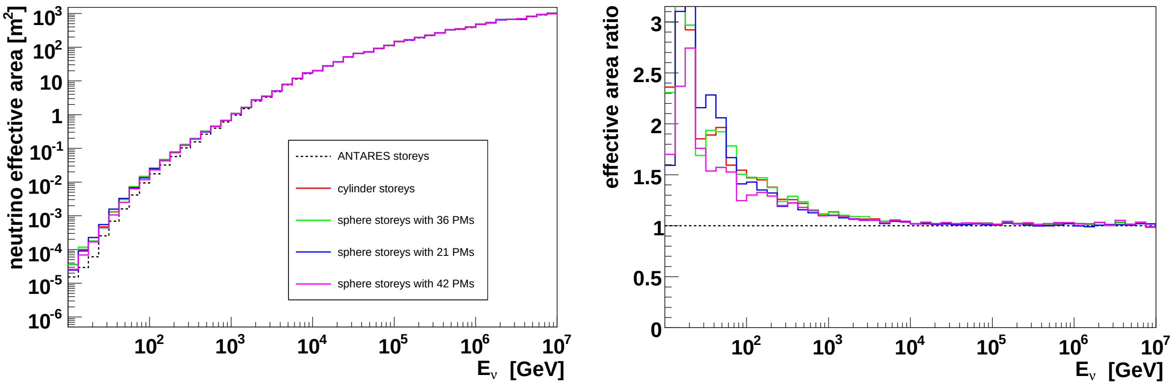

hit

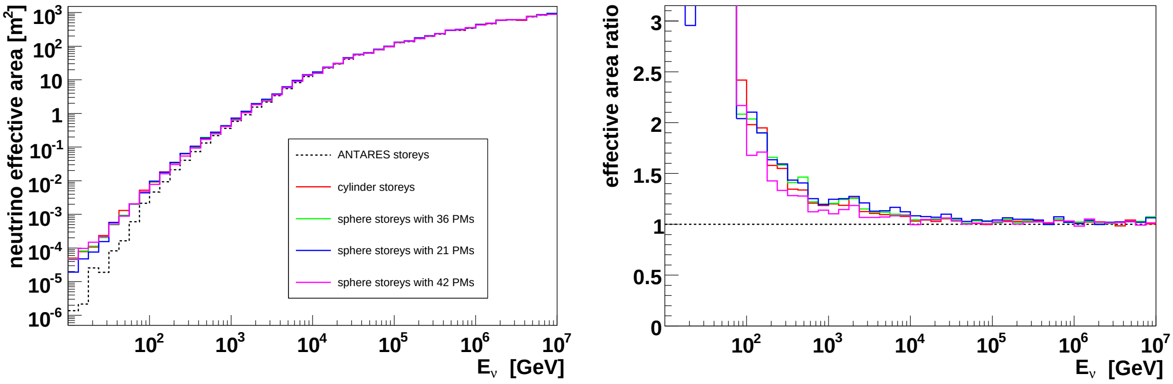

moderate

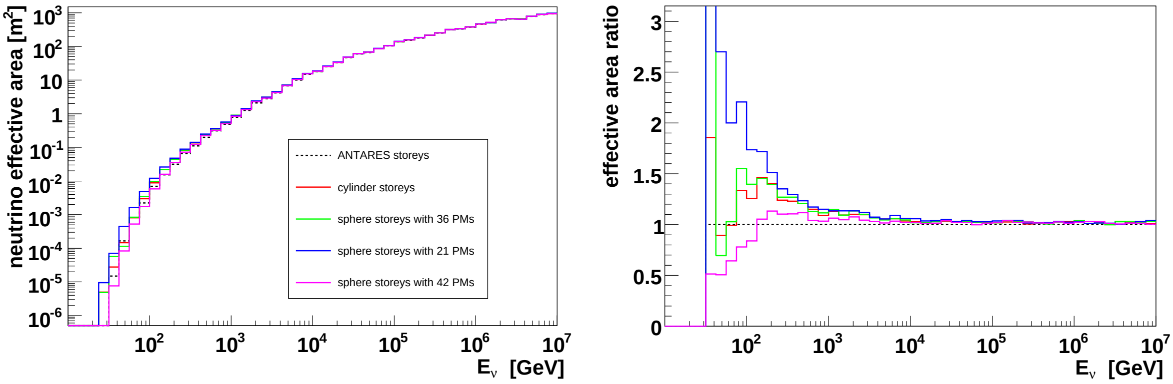

Figure 8.23: Neutrino effective areas and effective area ratios for *candidate* detectors equipped with 3"PMs, for the *minimal*, *hit* and *moderate* criteria applied.

trigger

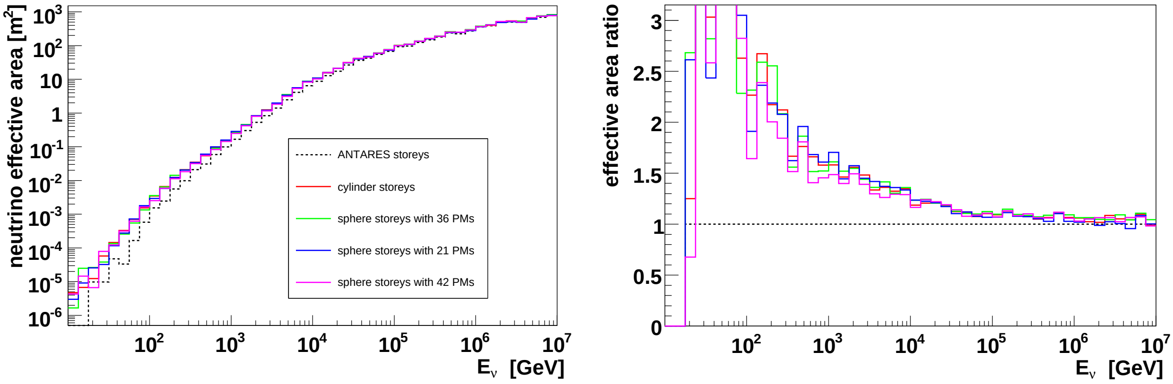

selected

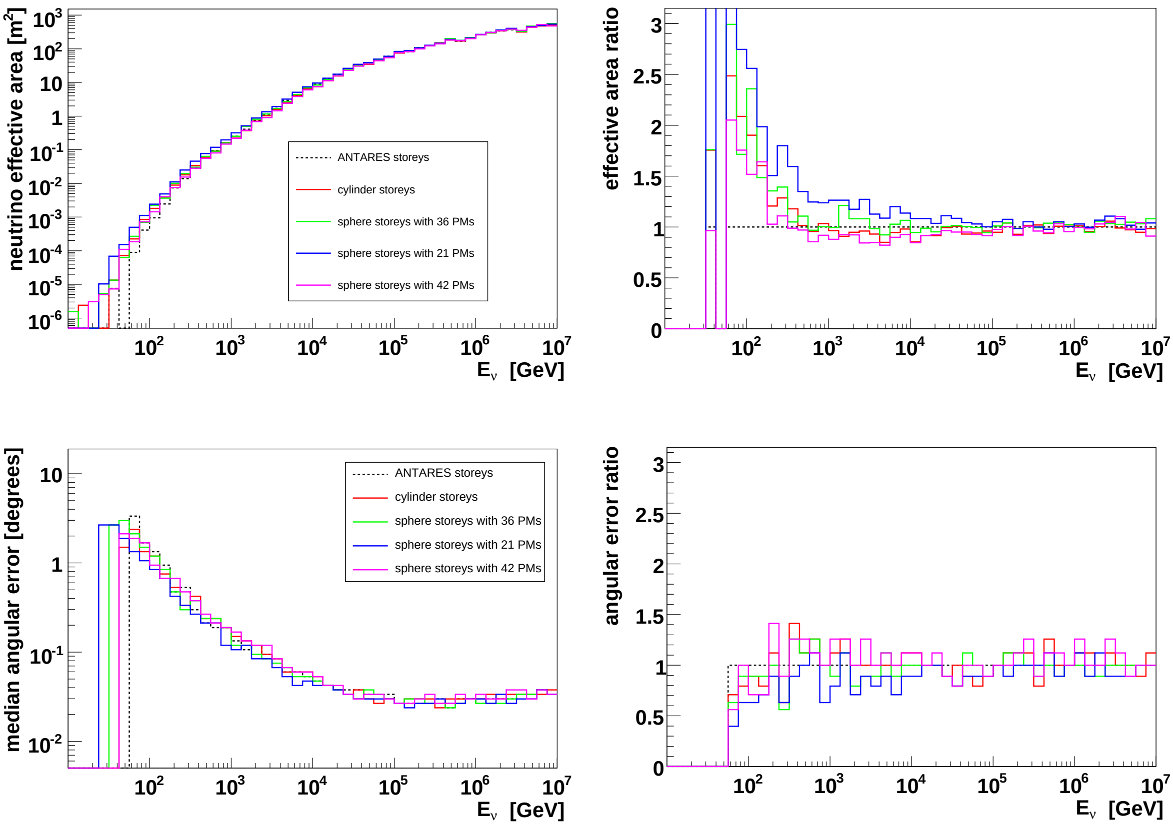

Figure 8.24: Neutrino effective areas and area ratios with the *trigger* criterion applied (top) and for *selected* events (middle) for *candidate* detectors with 3”PMs. Angular resolution and resolution ratios for *selected* events (bottom).

minimal

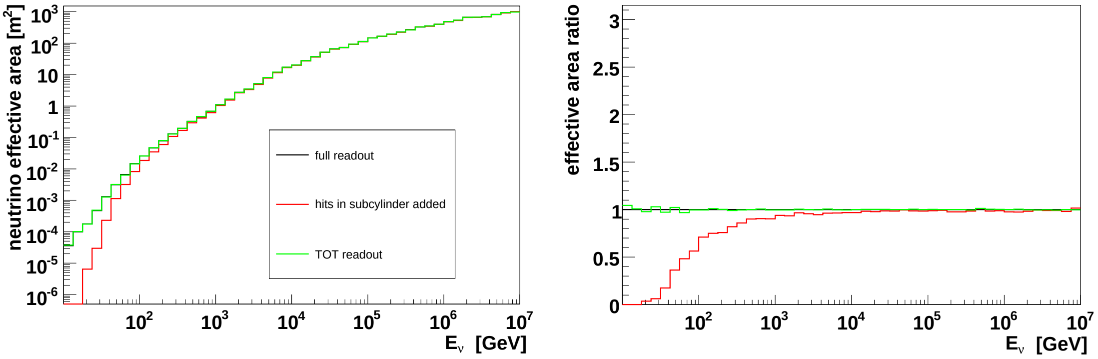

moderate

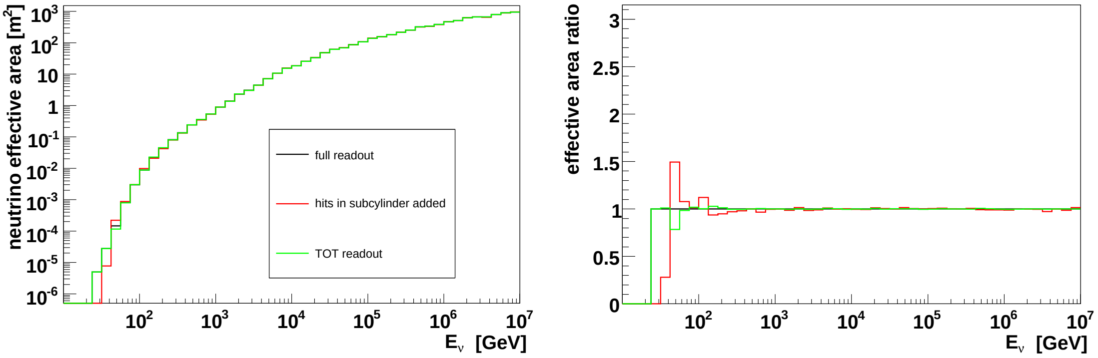

selected

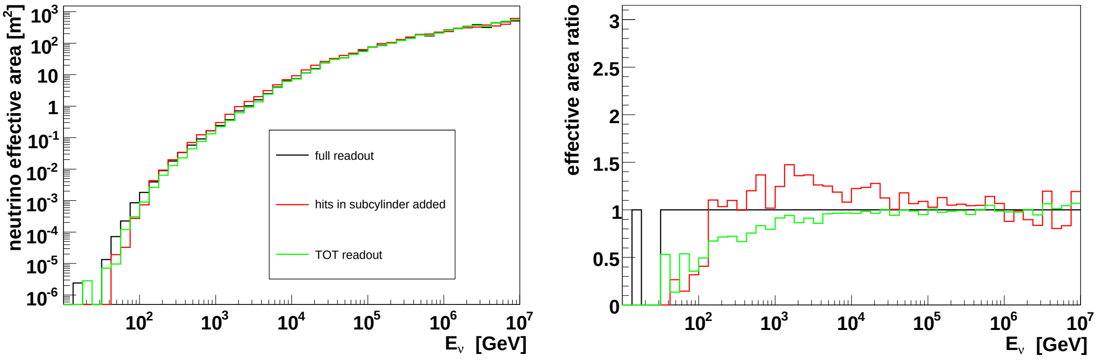

Figure 8.25: Neutrino effective areas and effective area ratios for *cuboid* detectors equipped with MultiPMT cylinder modules with modified readout, for the *minimal*, *moderate* and *selected* criteria applied.

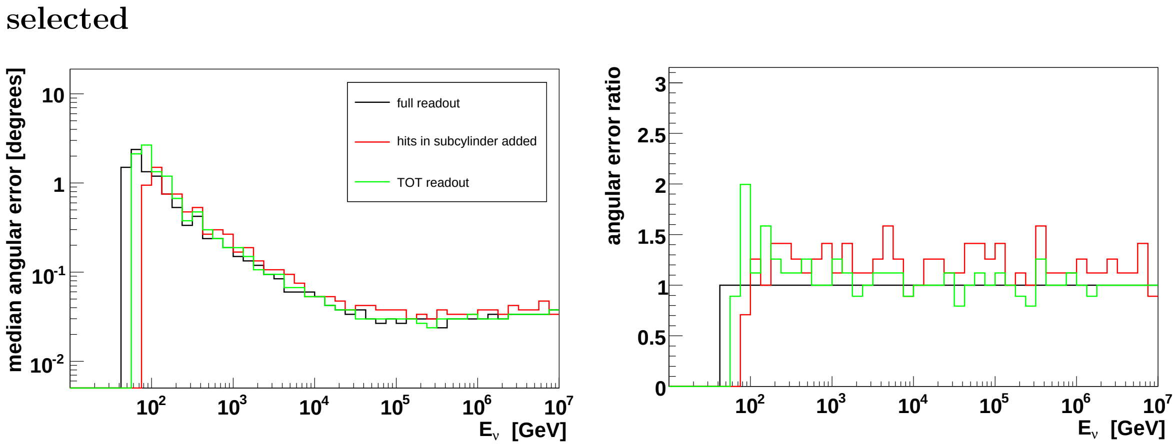

Figure 8.26: Angular resolution as a function of energy for *cuboid* detectors equipped with MultiPMT cylinder storeys with modified readout.

8.3 Detector storeys with 20”photomultipliers

Instead of using a large number of small Photomultipliers an alternative would be to use very large hemispherical photomultipliers, even though their quantum efficiency and TTS are worse than those of the 10”class. Furthermore, they are more expensive and will not easily fit into the standard glass sphere. Nonetheless, the larger collection area might compensate for these disadvantages.

A good example for a very large hemispherical PM is the Hamamatsu R3600 20”tube [123], which has four times the photocathode area of a 10”PM. It has a TTS of 3.5 ns and a maximum quantum efficiency of 20%. The spectral shape of the quantum efficiency was assumed to be the same as for the standard 10”PM. Therefore the quantum efficiency of the ANTARES 10”PMs was correspondingly scaled down. The same angular acceptance was assumed.

8.3.1 Storey layouts with 20”photomultipliers

The single 20”PM storey

The simplest option is to place one downward looking 20”PMT in each storey. This simple layout still has photocathode area about 30% larger than the standard ANTARES storey.

The ANTARES storey with 20”PMs

The second simplest option is to equip an ANTARES storey with 20”tubes instead of the 10”ones. The resulting detector has a four times larger photocathode area. No *candidate* version was used for this storey layout as it would have two storeys per string at a by far too large distance. When comparing detectors with this storey layout to others, it is important to keep in mind that they are presumably much more expensive. Unfortunately, it is difficult to judge the increase in cost and therefore to compare the results under this

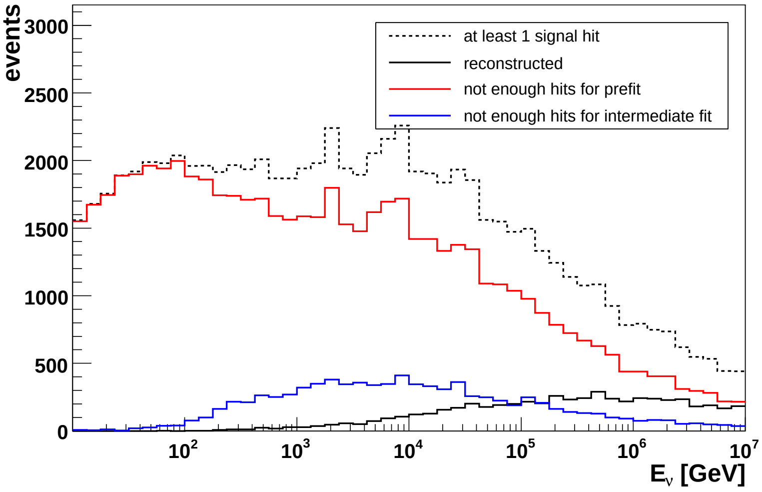

Figure 8.27: Distribution of the different outcomes of the reconstruction process for the single 20"PM cuboid detector. Most of the events are not reconstructed because of the lack coincidences necessary for the prefit.

aspect.

8.3.2 Results for storeys with 20"photomultipliers

Cuboid detectors

The effective areas for the *cuboid* detectors with 20"storeys compared to those with ANTARES storeys and MultiPMT cylinder storeys are shown in Fig. 8.28 and 8.29. The effective area of the detector equipped with ANTARES storeys with 20"PMs is of course highly superior at all selection steps, especially at lower energies. This is no surprise given that it has four times the photocathode area of the standard ANTARES storey cuboid. However, at the *trigger* level it is actually worse than the cylinder storey cuboid between energies of 100 GeV and 10 TeV where the purity of the events is worse. For *selected* events the detectors are very similar above a few hundred GeV. Below, the 20"ANTARES storeys are superior again. The angular resolution, shown in Fig. 8.29, is up to 50% worse than that for the reference detector, most probably due to the large TTS of the 20"PMs.

The detector equipped with a single 20"PM per storey shows effective areas comparable to the ANTARES storey. Its overall photocathode area exceeds the one of the other detectors, but it suffers from the same drawbacks as the 10"single PM detector. It does not utilise local coincidences (as there is only one PM per storey) and the angular coverage of the single PM is not very good. This also results in a low purity of the hits and a poor reconstruction quality with bad angular resolution. As even the *cuboid* version is worse than most other detector models, no *candidate* version (which would have even less storeys) was produced.

Section summary

- Replacing the 10"PMs in an ANTARES storey with the 20"PMs highly increases the performance of the detector as well as most probably its cost. The feasibility of using 20"PMs depends on the cost and is therefore difficult to judge.

- Although the overall photocathode area is larger for the *cuboid* with single 20"PMs than for the reference detector, the performance is actually worse at all selection steps. The single 20"PM *cuboid* detector suffers from the same drawbacks as the single OM detector with 10"PMs.

8.4 Conclusions

Under similar conditions, i.e. the same PM properties, the photocathode area is the most important factor defining the effective area. *Cuboid* detectors with more PMs per storey are generally more efficient (because they see more of the Cherenkov photons). The situation is somewhat different if different PM models are considered and the background noise is included in the analysis. PMs with a larger photocathode area also collect more background hits, often resulting in a bad purity and reduced performance for *selected* events.

Detectors with single PMs on the storey have some significant drawbacks. They do not produce local coincidences, which are required for the reduction of ^{40}K- and bioluminescence noise. Additionally their angular coverage is not very good. The example of the *cuboid* with single 20"PMs shows that even the larger photocathode area cannot compensate for these effects.

The MultiPMT storeys apparently provide a promising alternative to the more common setups, using a few large PMs. Their better performance, especially at lower energies is mainly caused by the higher quantum efficiency. Even the versions with simplified readout techniques are not significantly worse, eliminating one potential disadvantage. The smaller TTS of the small PMs does not significantly improve the angular resolution compared to the reference detector. It should be noted that the advantage of the better photon separation properties is not even included in this analysis. The actual arrangement of the small PMs in a single storey has almost no influence on the performance.

The gain of using very large hemispherical PMs greatly depends on the actual cost of such storeys. Because of the reasons mentioned before, more than one PM per storey is necessary and as the cost of a PM rises with its photocathode area huge tubes are much more expensive. Additionally they do not fit into the standard glass spheres commonly used in neutrino telescopes and larger spheres are also more expensive. Furthermore, at the *trigger* level and for *selected* events they are not significantly better than the MultiPMT storeys (except for extremely low energies). Finally the angular resolution is worse than for the reference detector, most probably due to the large TTS of the large PMs.

The example of the *candidate* detector with MultiPMT sphere storeys (21 PMs) shows that a larger number of storeys per string can be an advantage for the reconstruction, as a larger part of the volume is covered with detection units (using the number of storeys

minimal

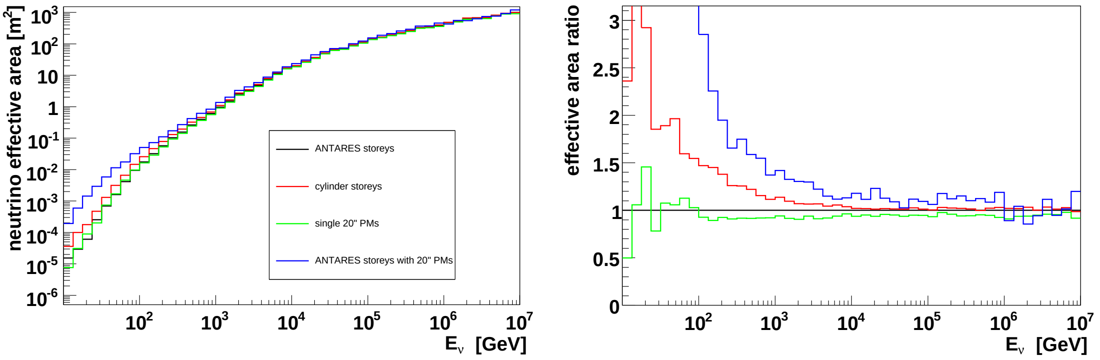

hit

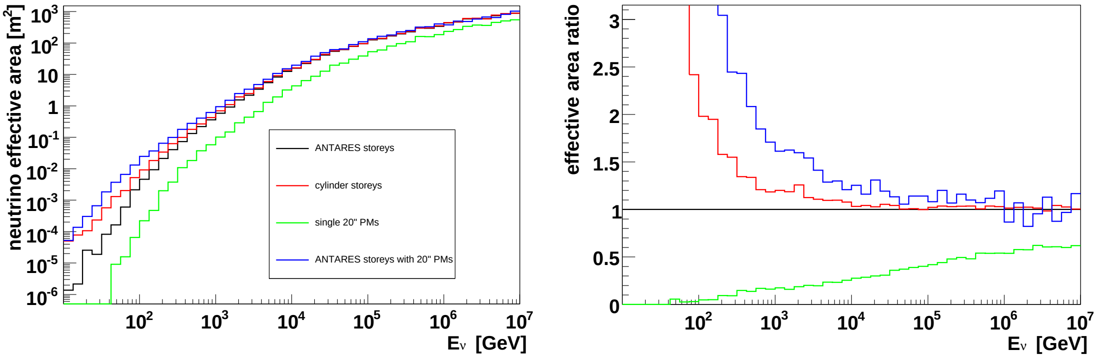

moderate

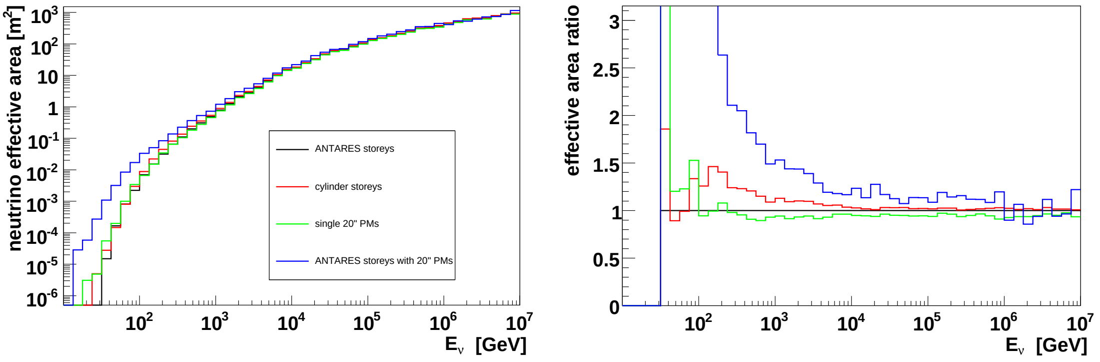

Figure 8.28: Neutrino effective areas and effective area ratios for *cuboid* detectors equipped with 20" PMs, for the *minimal*, *hit* and *moderate* criteria applied.

trigger

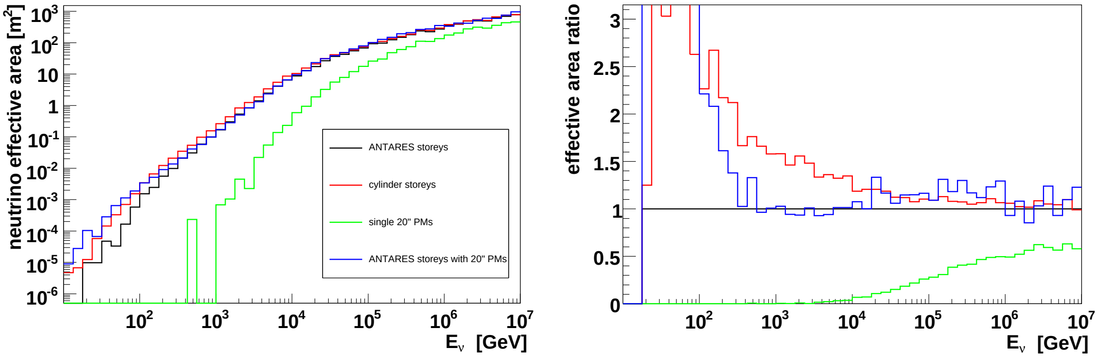

selected

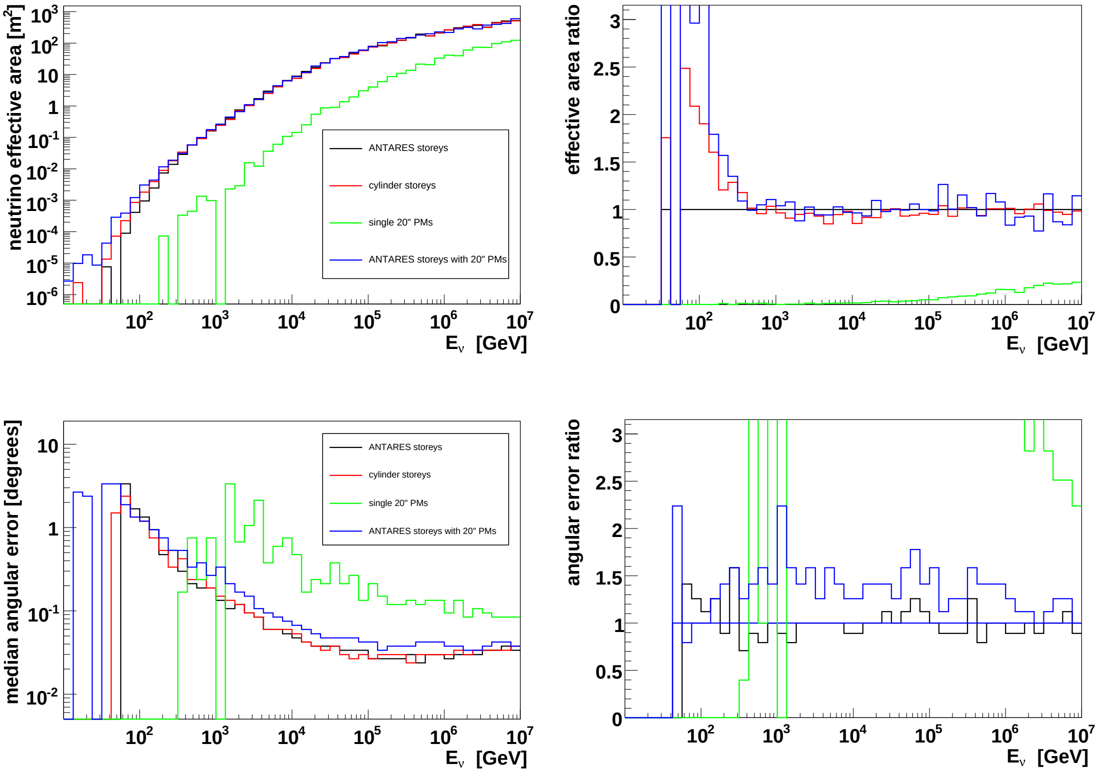

Figure 8.29: Neutrino effective areas and area ratios with the *trigger* criterion applied (top) and for *selected* events (middle) for *cuboid* detectors with 20" PMs. Angular resolution and resolution ratios for *selected* events (bottom).

minimal

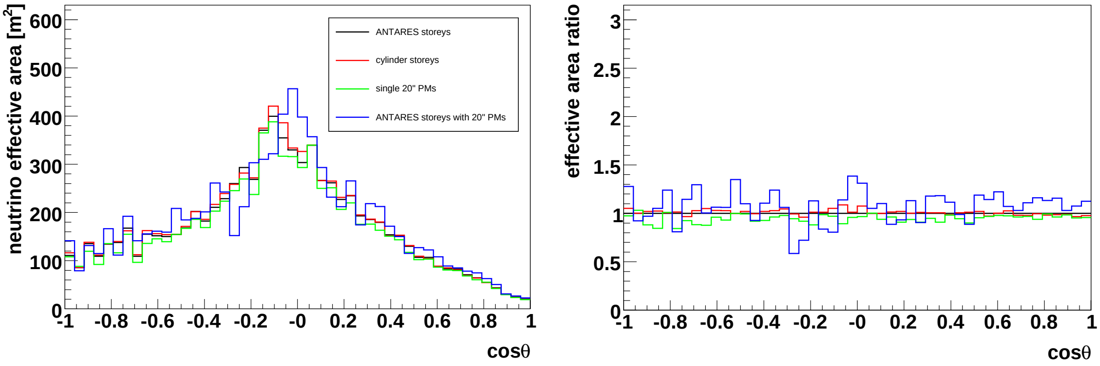

moderate

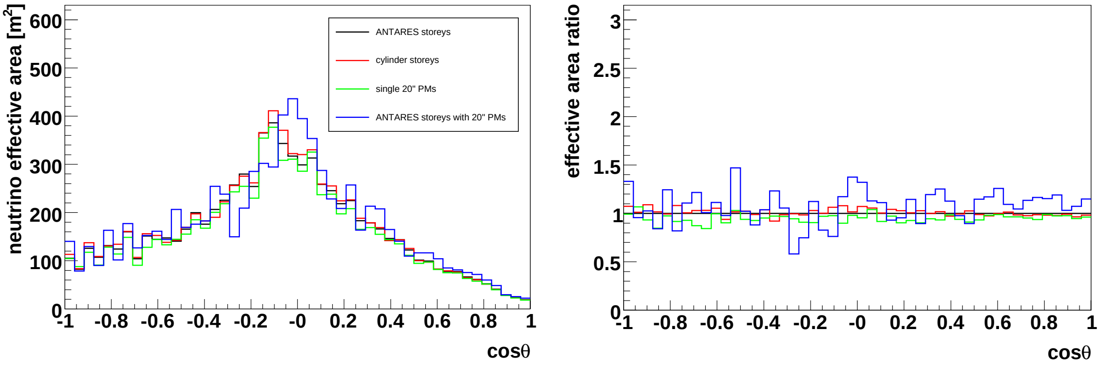

selected

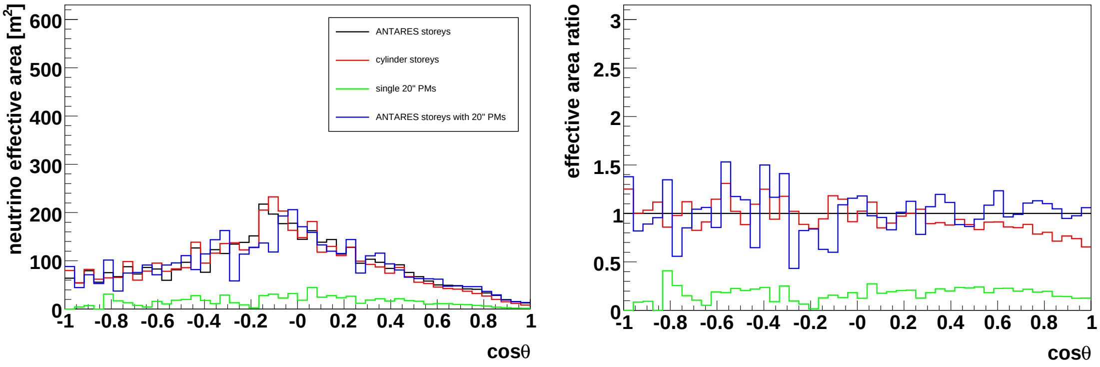

Figure 8.30: Neutrino effective areas and effective area ratios as a function of zenith angle for *cuboid* detectors equipped with 20"PMs with *minimal*, *moderate* and *selected* criteria applied.

hit for reconstruction is far more realistic, than using the positions of individual PMs inside one storey.) A detector equipped with these storeys could be a good choice. Most probably all the PMs can be read out individually as there is enough space for electronics in the upper hemisphere of the glass container. By having the PMs point downward and to the side, the most important region of zenith angles is well covered, without getting overwhelmed by the down-going atmospheric muons. Furthermore, no problems with sedimentation can arise with this storey type. All the advantages of the MultiPMT storeys are there, while most of the disadvantages are eliminated or reduced in effect. The only drawback is that twice the number of mechanical structures (storeys) is needed for a detector like this.

Chapter 9

Detector geometries

This chapter describes the analysis of different detector geometries, i.e. different arrangements of storeys in the instrumented volume. In this work it is generally assumed that the storeys are placed on detector strings, as for example in ANTARES or AMANDA. Since for the simulation a detector is only a three dimensional array of photodetectors and no environmental influences, like sea currents, have been simulated, the technical aspect of how the storeys are held in place is of no importance for this study. The simulation therefore effectively also covers tower-like geometries realised by appropriate configurations of strings.

This chapter will focus on *candidate* like detectors, i.e. the overall photocathode area and the instrumented volume will be left more or less constant. The first can be achieved by keeping the number of storeys similar (to within 10%) for all the different geometries, and by using the same storey type in all models. Partly for historical reasons, but mainly because it provides reasonable statistics even at lower energies, the MultiPMT cylinder storey was chosen as a standard. The instrumented volume is kept constant at one cubic kilometer.

9.1 Ring geometries

One concept considered, is a ring-shaped detector. Beginning at energies of about 1 TeV, the average muon range in water exceeds the typical dimension of a cubic kilometer detector (1 km), so that most of the incident muons are produced outside of the instrumented volume. In Fig. 9.1 the energy distribution of muon events in the standard sample is shown for muons that were produced inside or outside of the can volume. Only events that reach the can are included. As can be seen, above 1 TeV the events produced outside begin to dominate. As these muons will enter the detector from the outside, the important parameter is a large detector cross section rather than volume. A possibility to exploit this effect is to surround a large volume with photodetectors. This produces a large area and provides a long lever arm, if the particle enters and leaves the volume through this shell. As it is uneconomic to build strings (or towers) with only a few storeys at the bottom and the top, only the side walls can be instrumented. The easiest way is to design a detector with several concentric rings of detection strings. In this way less strings

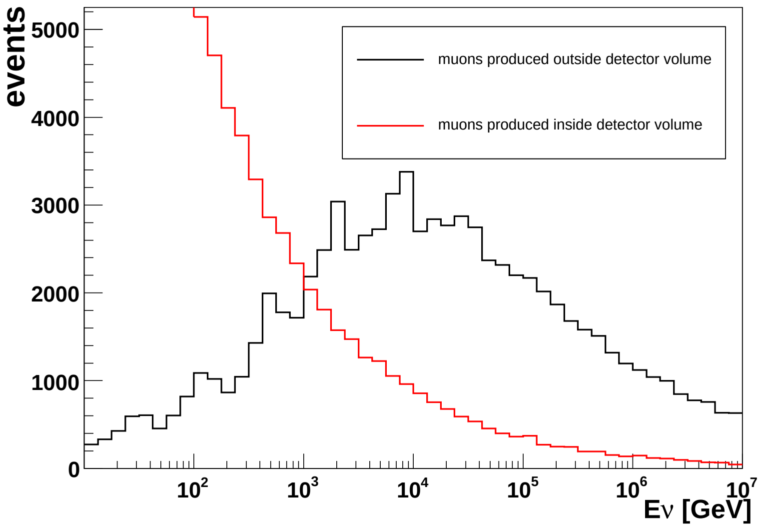

Figure 9.1: Energy distribution of muon events, that reach the detector, produced outside (black) and inside (red) of the instrumented volume, respectively.

can be used to instrument the same volume as with the homogeneous cuboid geometry. In order to keep the number of storeys constant, more of them have to be placed on the strings, as the density of the strings in the ring is limited by the minimal distance between them (which is defined by the procedures of the deployment). Nonetheless, the costs are reduced as less cabling (fewer strings) and fewer sea campaigns for the deployment are required.

An example ring layout is shown in Fig. 9.2. It has five concentric rings, where the string distance inside one of the rings is 60 m, as is the distance between the rings. A total of 312 strings is equipped with 16 storeys each, resulting in a storey distance of 40 m and 4992 storeys in total. This geometry will be called *ring1* in the following. A potential problem might be the effect of the core of the ring that is not instrumented and the resulting inefficiency for neutrinos incident under low (or very high) zenith angles. In order to analyse the effect of this problem a second ring geometry was simulated (see Fig. 9.3). In this case the distance of the rings decreases with increasing radius. The idea is to instrument the 'hole' with at least some strings, without giving up the overall concept. The number of strings and modules, as well as the distances between strings inside one ring and between the storeys remain the same. This layout is called *ring2*. A similar approach is followed for the geometry shown in Fig. 9.4. The core of three concentric rings with 60 m distance is filled with a smaller compact ring structure (with the same distances) to reduce the effect of the hole and to provide a densely instrumented volume for low energy events. This layout is called *ring3*. The last of the ring geometries is in principle a clone of the *ring2*, with the exception, that it has only half as many strings, resulting in larger string distances. To compensate for this the number of modules per string is doubled to 32, resulting in distances of 19.25 m. The idea of this concept is to increase the low energy performance by reducing the distances between storeys. This geometry, called *ring4*, is shown in Fig. 9.5.

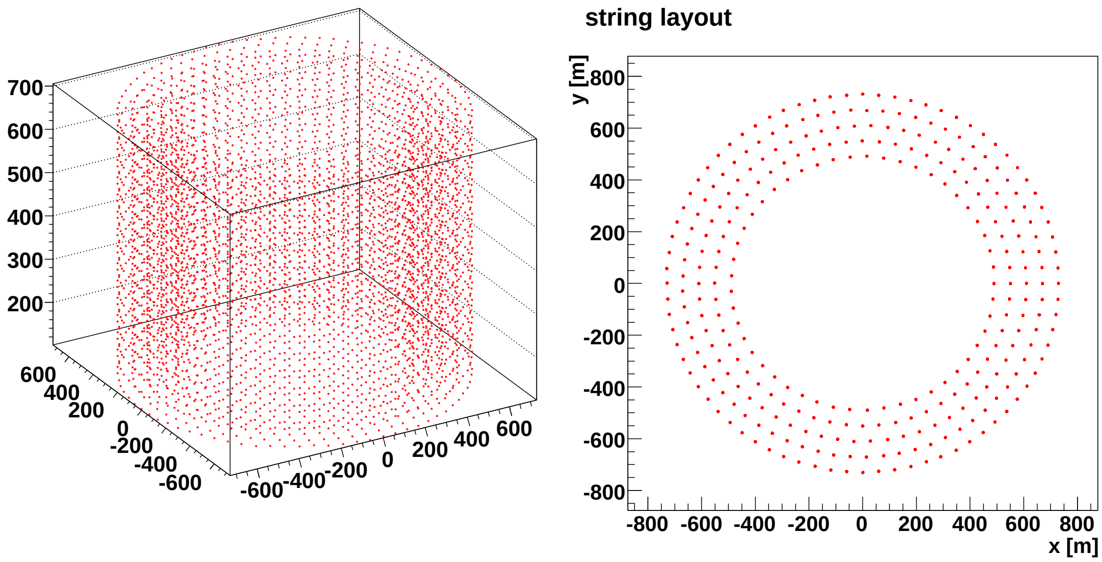

Figure 9.2: Left: *Ring1* geometry. Right: Sea floor layout of the strings used to simulate this geometry.

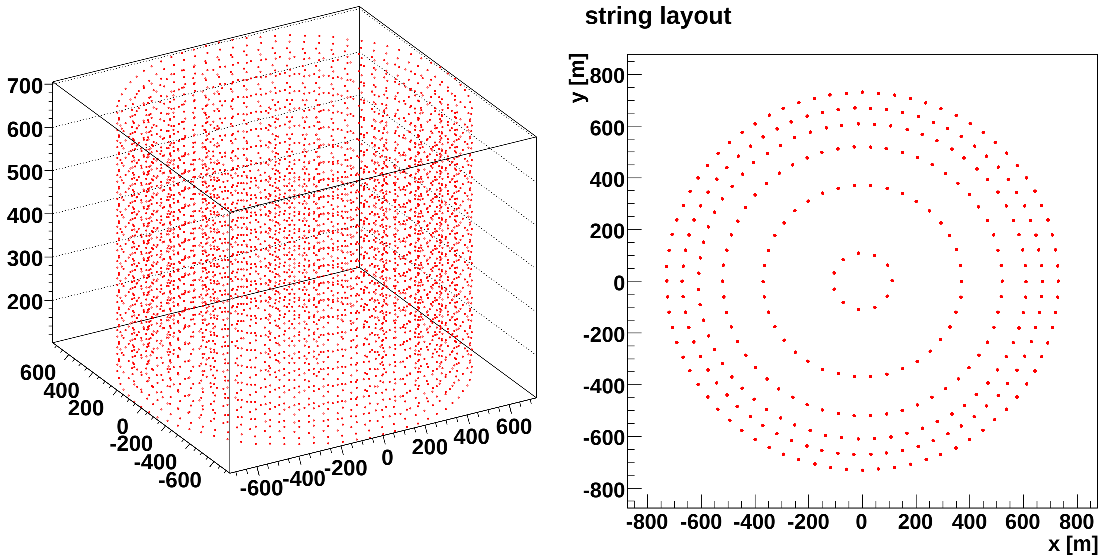

Figure 9.3: Left: *Ring2* geometry. Right: Sea floor layout of the strings used to simulate this geometry.

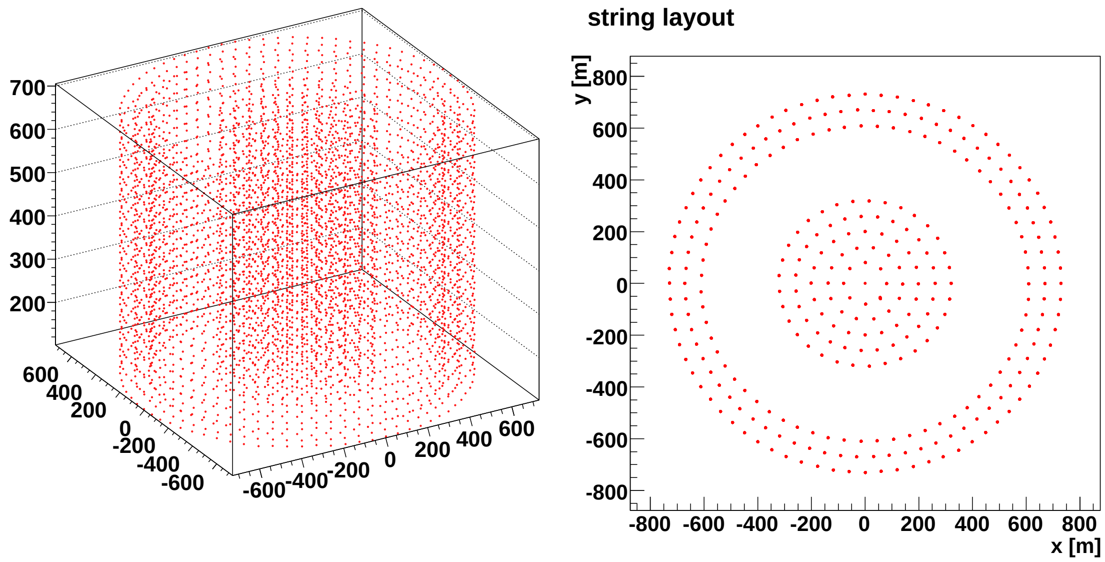

Figure 9.4: Left: *Ring3* geometry. Right: Sea floor layout of the strings used to simulate this geometry.

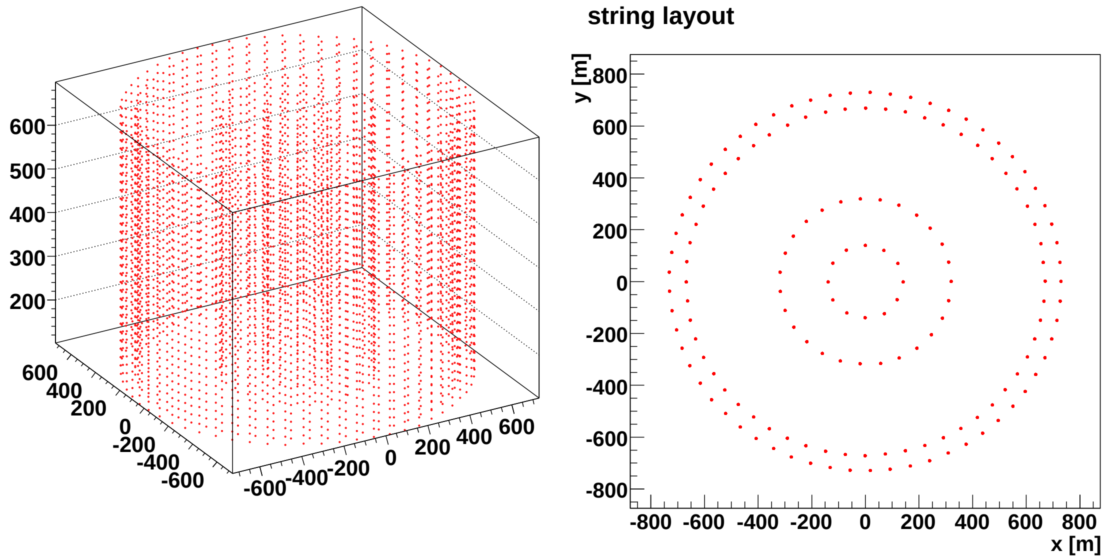

Figure 9.5: Left: *Ring4* geometry. Right: Sea floor layout of the strings used to simulate this geometry.

9.1.1 Results for detectors with ring geometries

Neutrino effective areas and effective area ratios for the different ring geometries, compared to the cuboid layout, are shown in Figs. 9.6 and 9.7. The latter figure also displays the angular resolution as a function of energy. The effective areas for all ring geometries are similar at the *minimal* and *hit* levels. Compared to the cuboid they are about 10% worse at energies above a few hundred GeV, but up to a factor of 2 better below at the *minimal* level. *Ring4* is even better at these low energies (about factor three). At the *hit* stage this is reduced to 25% (factor 2 for *ring4*). At the *moderate* stage the areas are comparable to the cuboid geometry below 100 TeV and massively better below 100 GeV. If the *trigger* criterion is applied the effective areas of the rings exceed the area of the cuboid for energies below a few TeV. *Ring1* is better here than the other rings, apparently due to a higher purity. At energies below 100 GeV *ring4* takes the lead again. The behaviour is similar for *selected* events. The angular resolutions are similar for all the rings and the cuboid, with a tendency to a better resolution for the rings at low energies.

The increased performance at low energies is a consequence of the denser spacing of the storeys along the strings. The slightly decreased efficiency at higher energies is a result of the decreased cross section area for events incident form very high or very low zenith angles.

This can be seen when looking at the effective areas and ratios as a function of the zenith angle, shown in Fig. 9.8. The overall shape of the effective area is the same as for the cuboid geometries (see section 8.1). However, the rings, especially *ring1*, lose efficiency towards $\cos\theta = -1$, i.e. upgoing events. For *selected* events *ring4* is even worse in this region. A tendency towards the same effect can be seen also for downgoing events.

The rings actually provide the advantages they were invented for. In order to check whether the same results can be achieved with less rings, two additional ring layouts were produced (see Figs. 9.9 and 9.10). These detector geometries have only two concentric rings with 145 strings (the outer two rings of *ring1*). The first one, called the *densering* has the same number of storeys as the others, resulting in a very dense instrumentation of the lines. The second one, called the *thinring*, has the same string setup as the other rings and therefore less storeys. The idea is to see if the 'ring effect' can also be used to reduce the number of storeys and still achieve similar efficiencies.

The results for these modified ring layouts are compared to the *ring1* and the standard cuboid in Figs. 9.11, 9.12 and 9.13. At the highest energies, the modified rings show an efficiency very similar to that of *ring1*. Below 1 PeV both of the modified rings start to become worse. The effective area of the *thinring* continually decreases, until it reaches about 50% of the area of the cuboid. However, especially at the *moderate* level, it starts to rise again for energies below 100 GeV (denser string instrumentation than cuboid). The *densering* loses only 10 to 20% (depending on selection step) compared to *ring1* and actually becomes better at the lowest energies well below 100 GeV. The angular resolution of the *thinring* is about 50% worse than that of the cuboid and the *ring1* at all energies. The resolution of the *densering* is only a bit worse than that of the *ring1* above 10 TeV, is comparable from 100 GeV to 10 TeV and better below. The zenith angle dependence of the effective areas of the modified rings is in principle the same as for the *ring1*, except that the drop for upgoing events is much more significant, due to the increased size of the 'hole' of the ring.

Apparently the reduction of the number of rings in the layout leads to a reduction in performance at most energies. The 'ring-effect' can not compensate for a smaller number of storeys (*thinring*) and the increased size of the uninstrumented volume in the center of the layout causes losses in efficiency for upgoing and also for downgoing events.

Section Summary

- At high energies the efficiency of a detector is defined by its cross section area.
- Ring geometries can be used to reduce the number of strings, but the overall number of storeys has to remain the same.
- If the width of the ring is too small the performance decreases (the 'hole' becomes too large).
- The ring geometries show good performance at lowest energies (E<100 GeV, below a few TeV for *selected* events) but are slightly worse than the cuboid (about 10% lower effective area and 10% higher angular resolution) for higher energies.

9.2 Clustered geometries

For the search for neutrinos from the annihilation of dark matter candidates in the Sun or the Galactic Center a detector with a low energy threshold and good low energy efficiency is necessary. The mass of the neutralino is generally assumed to be below 1 TeV, resulting in neutrinos of even lower energy. In order to optimise the detector for these low energies it would be possible to reduce the distances between the storeys in the detector. This would allow to get a reasonable number of hits in several different storeys, even for muons with low energy and therefore low track length and light output. Unfortunately, this reduces the volume of a homogeneous detector, reducing the efficiency for higher energies, where the small fluxes require a large detection volume.

A possible solution is a detector containing a number of clusters (of strings, or towers) that are densely instrumented. Low-energy events have an increased detection probability inside these clusters, while high energy events have the chance to hit several of these clusters, therefore still seeing a volume that is relatively large. The layout of a possible cluster geometry is shown in Fig. 9.14. It contains eight clusters of twelve strings each. Each string is equipped with 52 cylinder storeys with distances of 12 m. The string distance inside a cluster is 60 m. The radius of the inner ring of clusters is 360 m, that of the outer one 780 m. This amounts to a total number of 4992 storeys. This layout will be called *cluster1* in the following. In order to check the influence of the substructure of the string layout of one cluster, a second cluster geometry was simulated where the vertical structures are arranged in concentric rings (Fig. 9.15). It will be called *cluster2* in the following. A third geometry to be studied is called *cluster3*. It is an attempt to combine the benefits of the ring geometry with the one of a clustered detector by simply placing

minimal

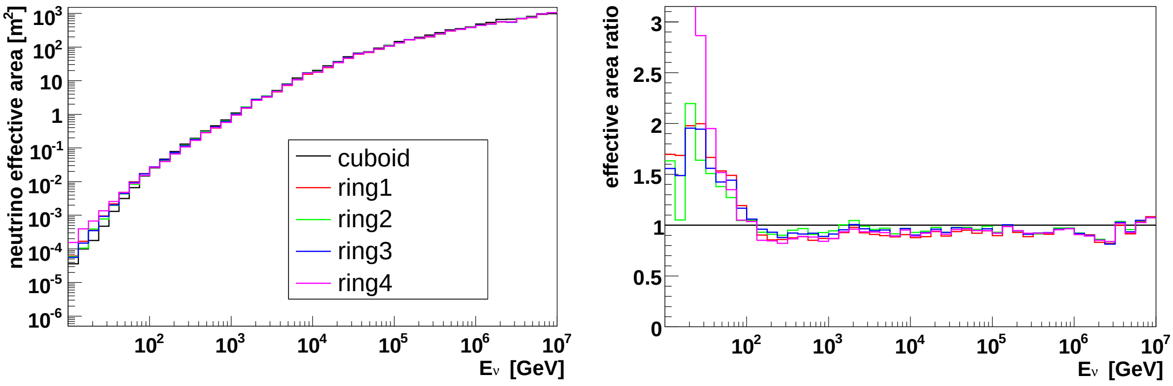

hit

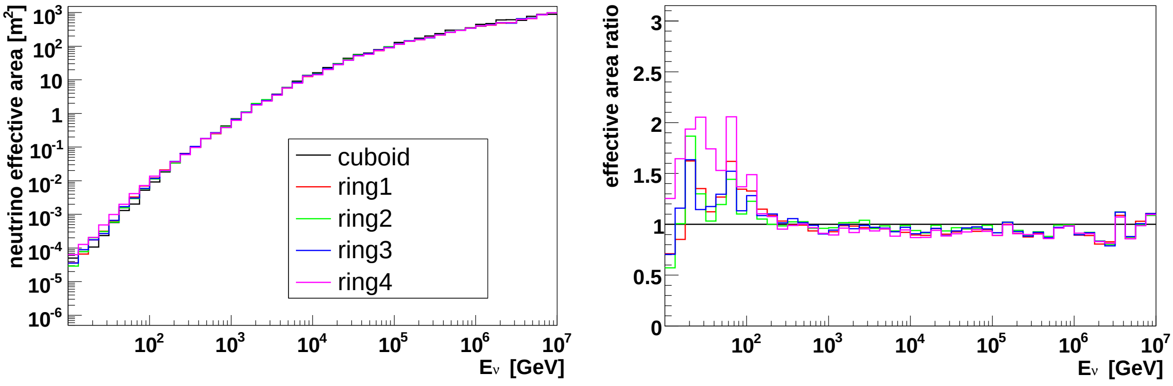

moderate

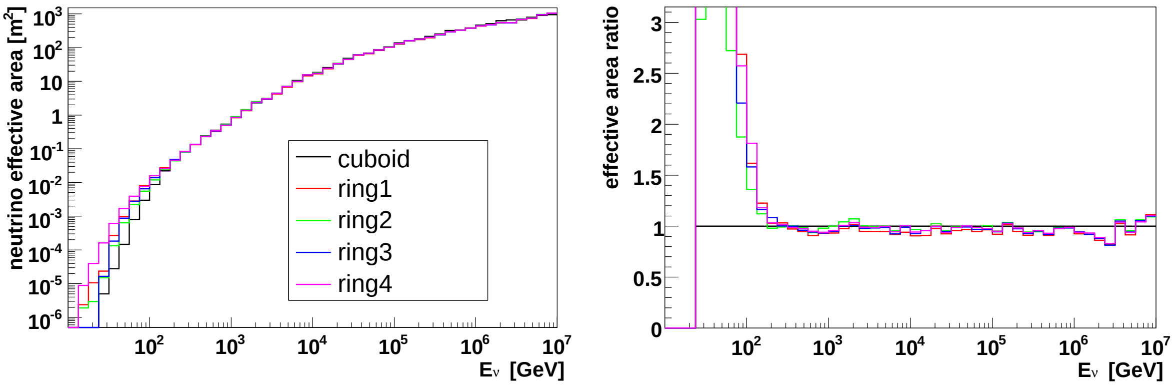

Figure 9.6: Neutrino effective areas and effective area ratios for detectors with ring geometries, for the *minimal*, *hit* and *moderate* criteria applied.

trigger

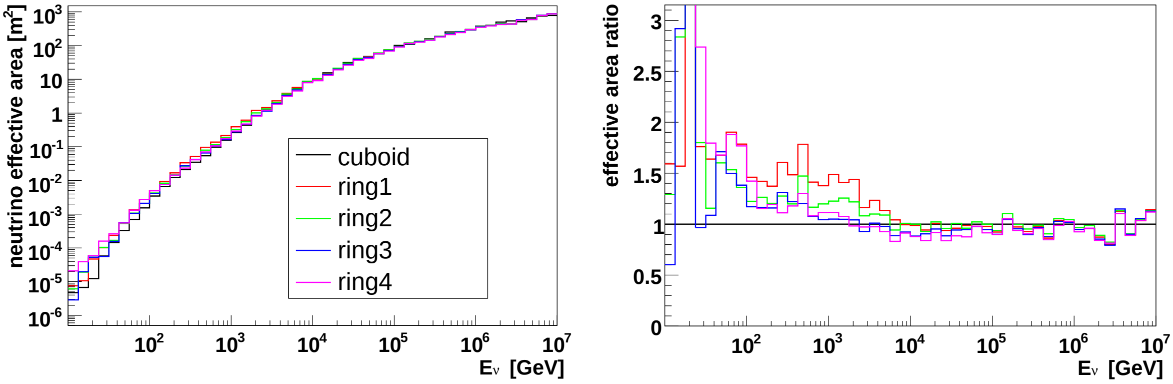

selected

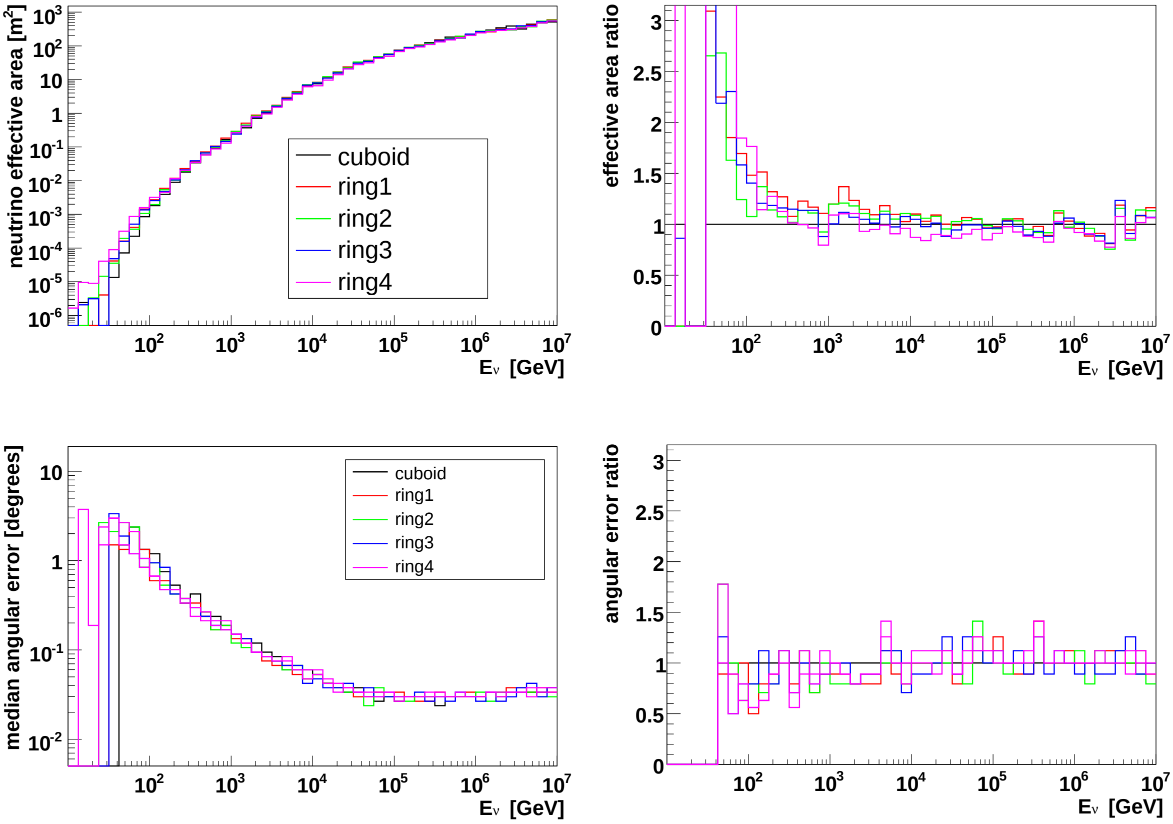

Figure 9.7: Neutrino effective areas and area ratios with the *trigger* criterion applied (top) and for *selected* events (middle) for detectors with ring geometries. Angular resolution and resolution ratios for *selected* events (bottom).

minimal

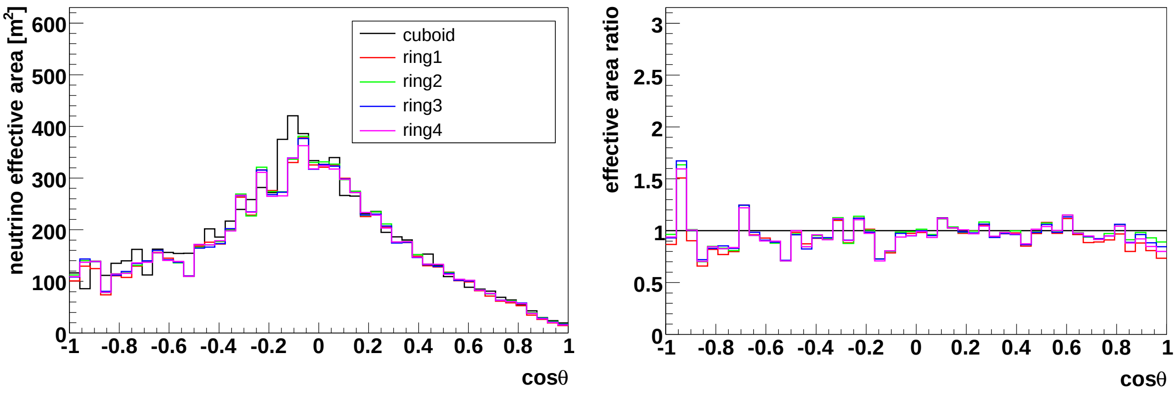

moderate

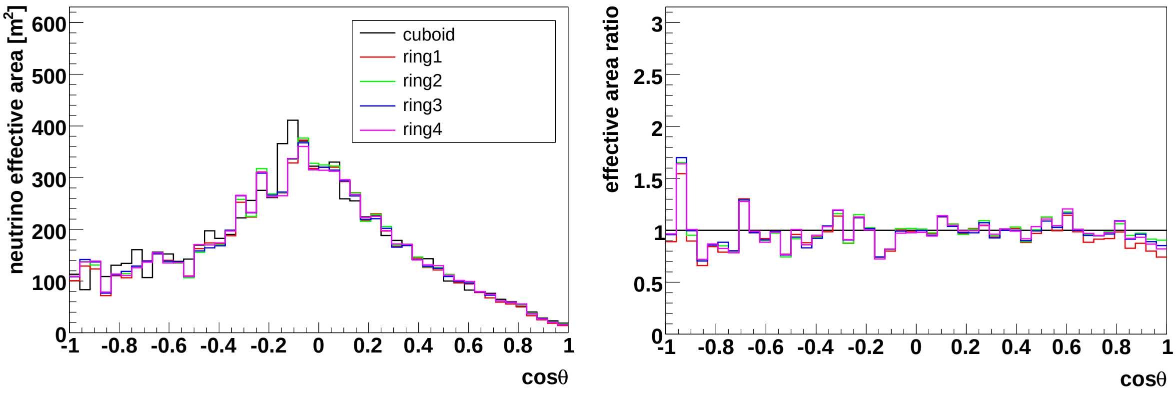

selected

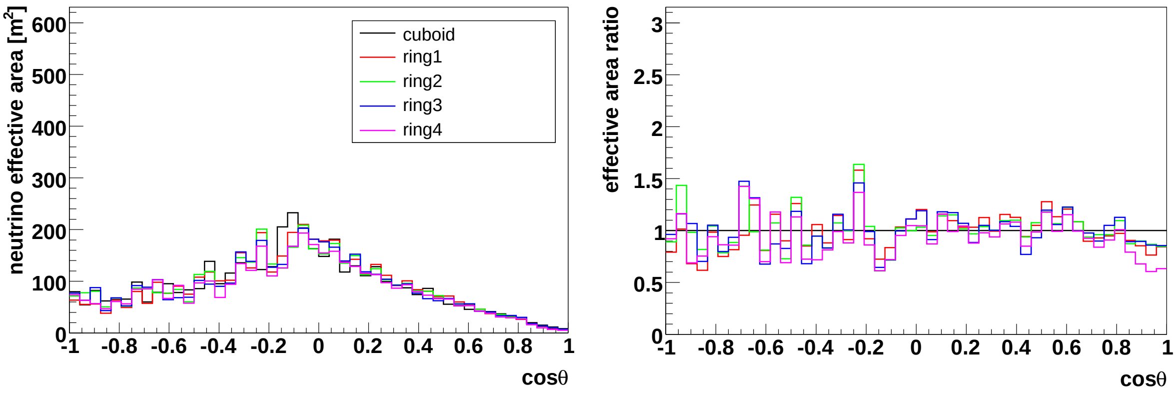

Figure 9.8: Neutrino effective areas and effective area ratios as a function of zenith angle for detectors with ring geometries, with *minimal*, *moderate* and *selected* criteria applied.

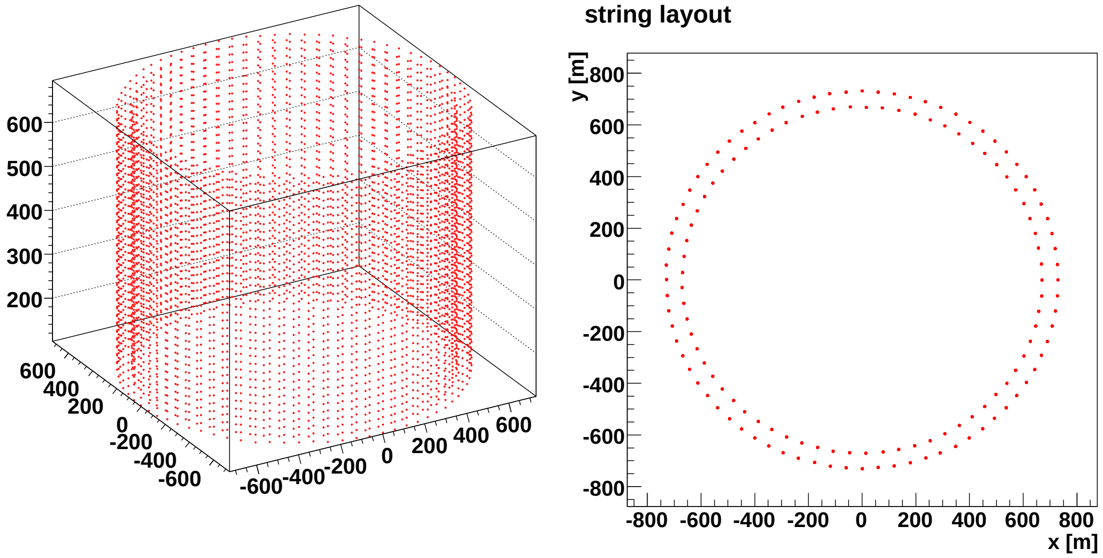

Figure 9.9: Left: *Densering* geometry. Right: Sea floor layout of the strings used to simulate this geometry.

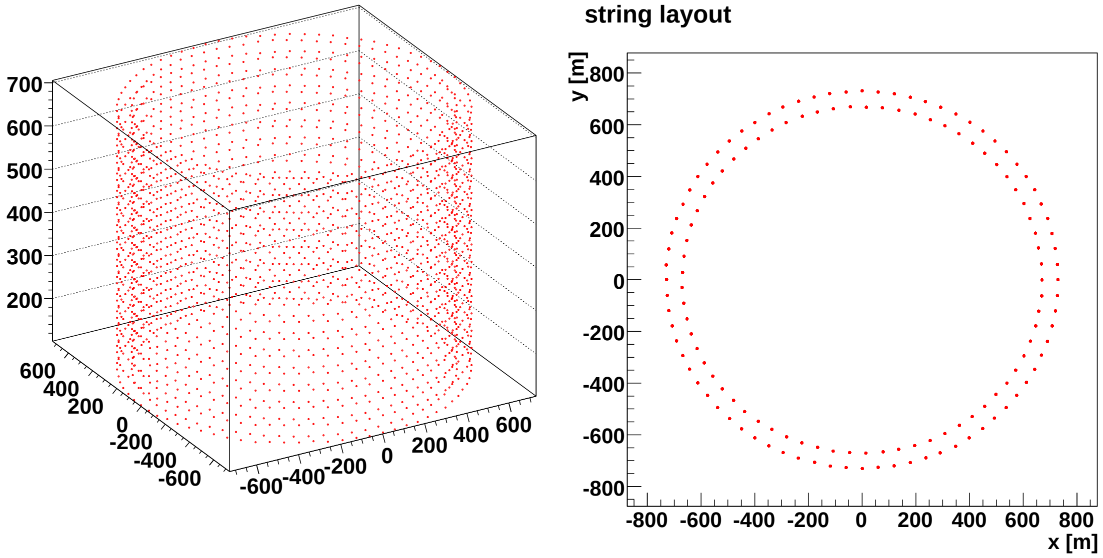

Figure 9.10: Left: *Thinring* geometry. Right: Sea floor layout of the strings used to simulate this geometry.

minimal

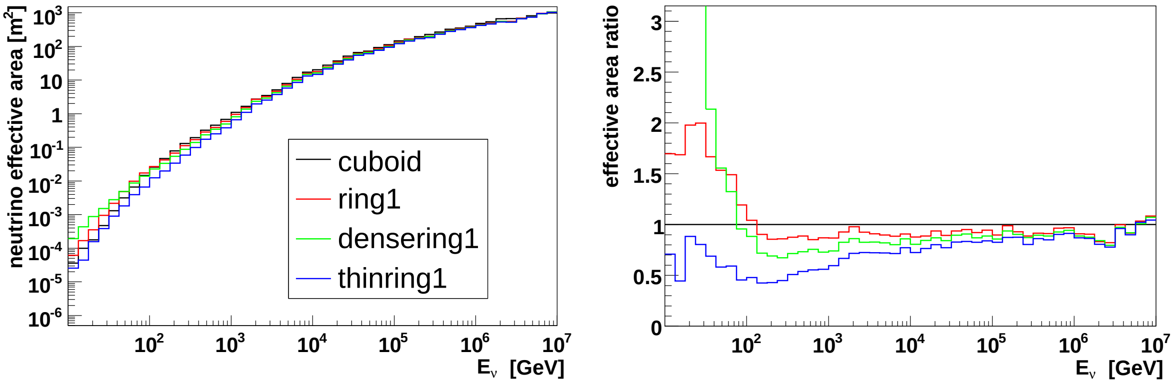

hit

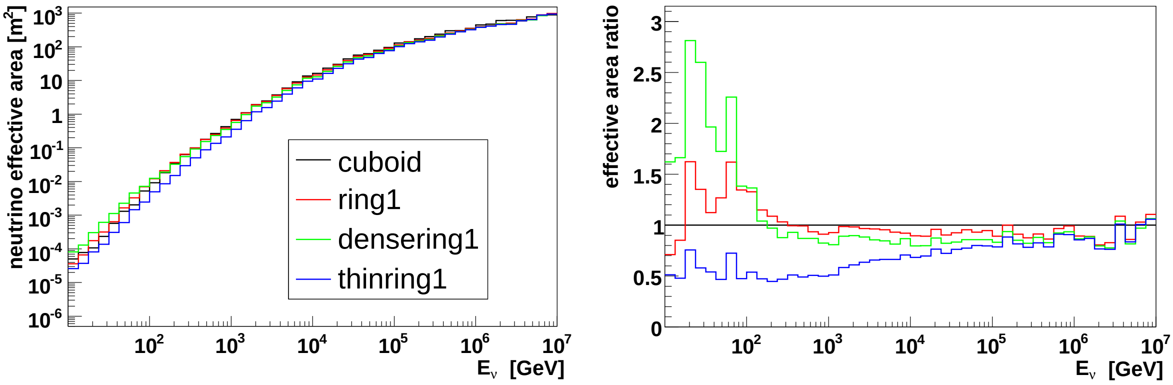

moderate

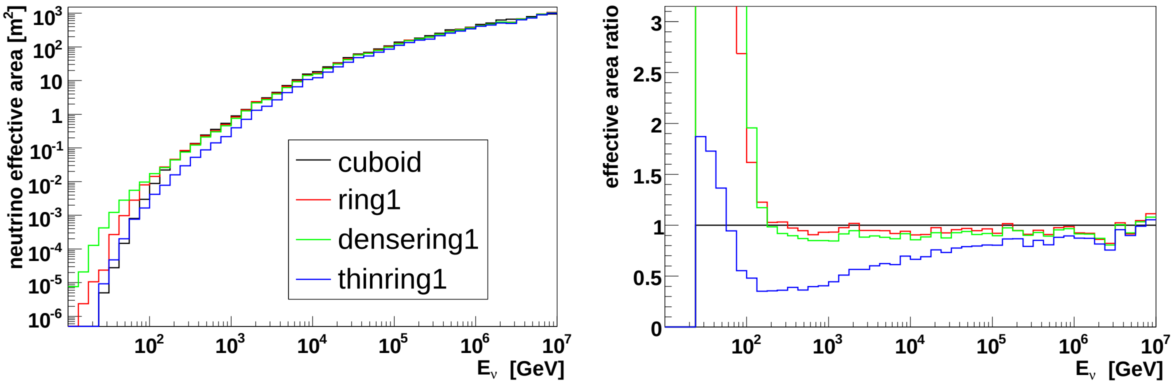

Figure 9.11: Neutrino effective areas and effective area ratios for detectors with alternative ring geometries, for the (from top to bottom) *minimal*, *hit* and *moderate* criteria applied.

trigger

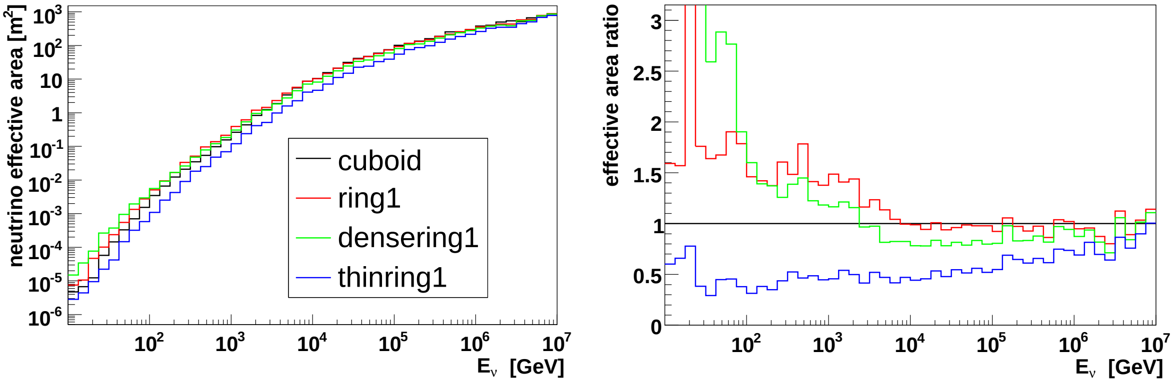

selected

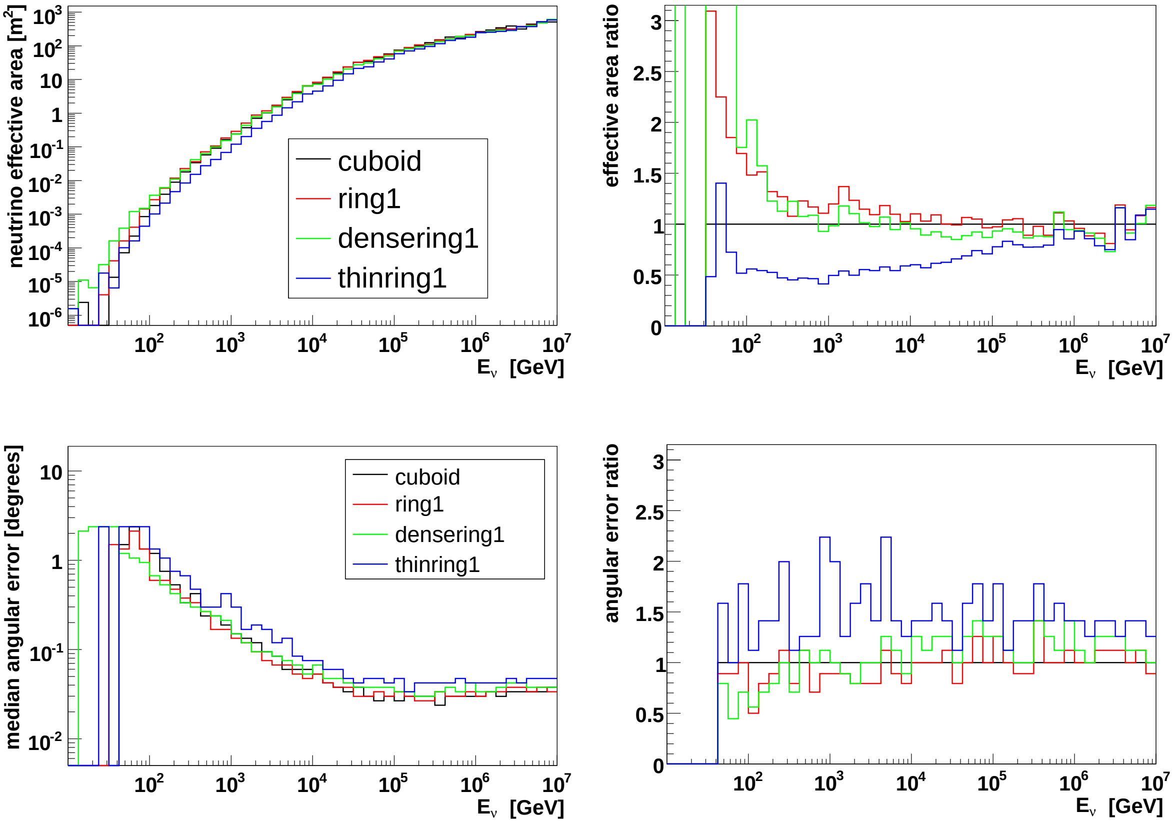

Figure 9.12: Neutrino effective areas and area ratios with the *trigger* criterion applied (top) and for *selected* events (middle) for detectors with alternative ring geometries. Angular resolution and resolution ratios for *selected* events (bottom).

minimal

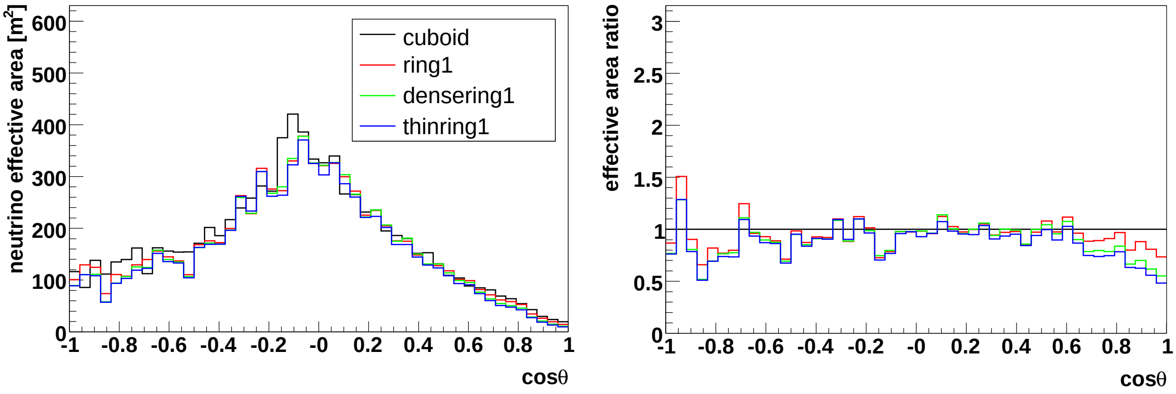

moderate

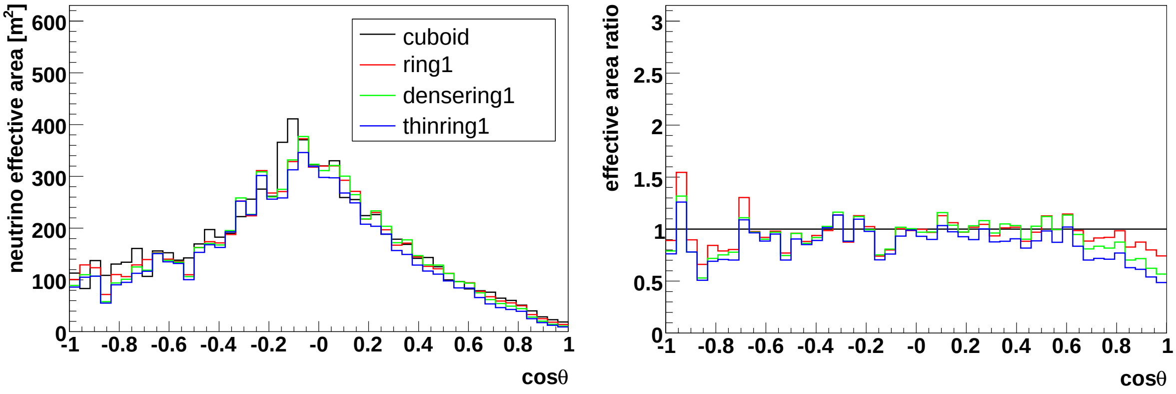

selected

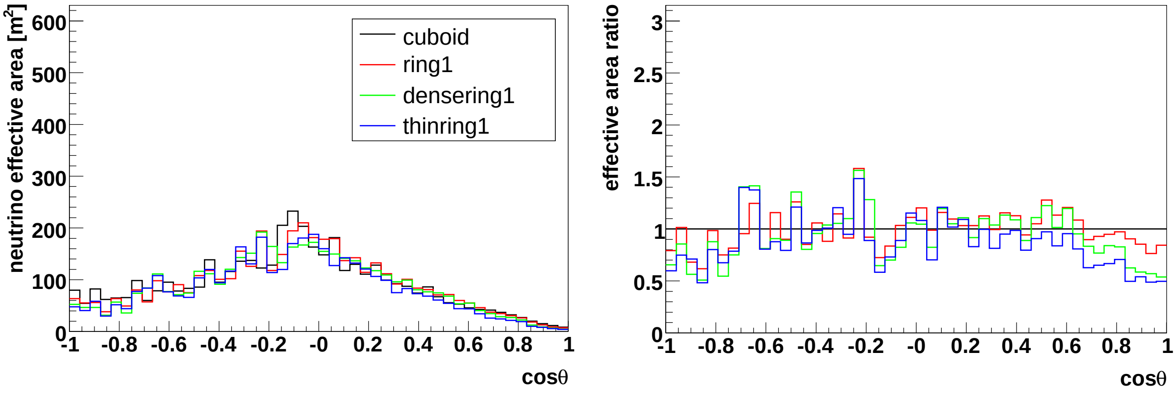

Figure 9.13: Neutrino effective areas and effective area ratios as a function of zenith angle for detectors with alternative ring geometries, with *minimal*, *moderate* and *selected* criteria applied.

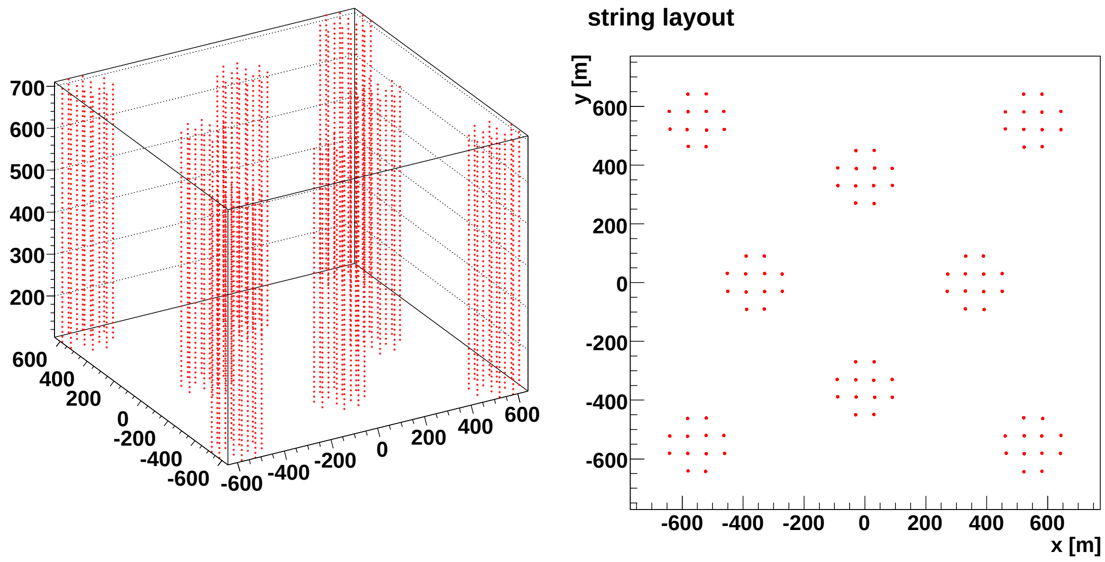

Figure 9.14: Left: *Cluster1* geometry. Right: Sea floor layout of the strings used to simulate this geometry.

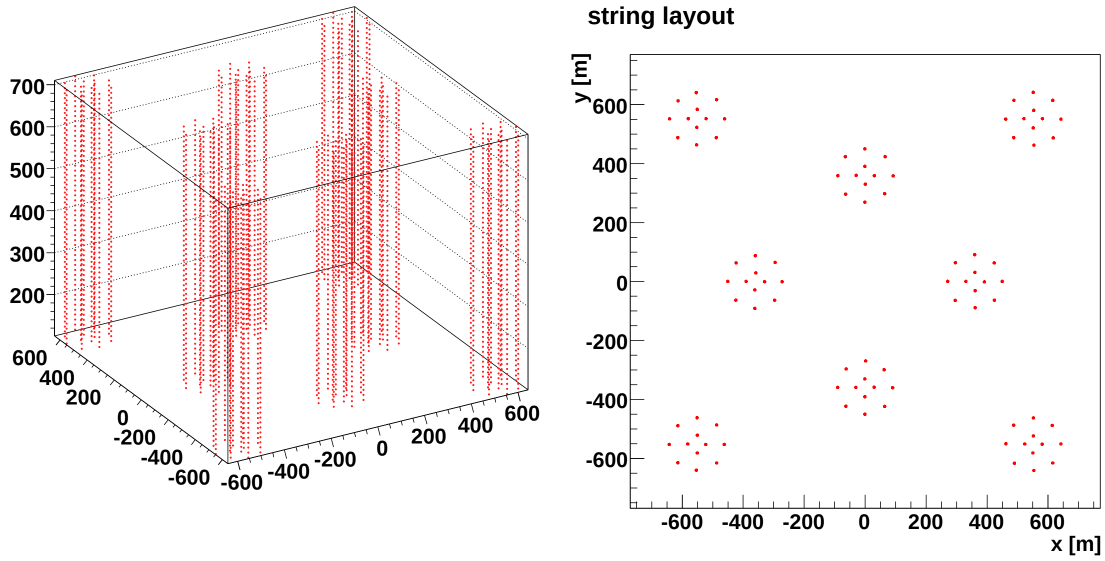

Figure 9.15: Left: *Cluster2* geometry. Right: Sea floor layout of the strings used to simulate this geometry.

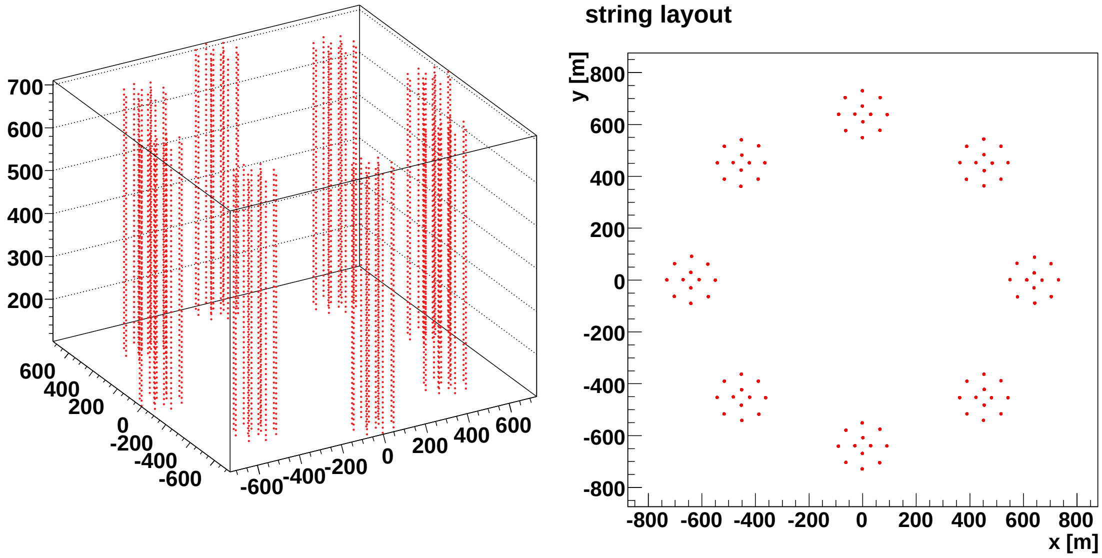

Figure 9.16: Left: *Cluster3* geometry. Right: Sea floor layout of the strings used to simulate this geometry.

the eight clusters in a single ring with a radius of 730 m. This layout is shown in Fig. 9.16.

9.2.1 Results for detectors with clustered geometries

The neutrino effective area, angular resolution and the respective ratios relative to the cuboid layout are shown in Figs. 9.18 and 9.19. The behaviour for all of the three cluster layouts is virtually the same. At highest energies above 1 PeV, the effective areas are about 20% worse than for the cuboid. The ratios drop towards lower energies and increase again below 100 GeV, where the clusters are massively superior. This holds at all selection steps. The only difference is at energies around 1 TeV. At the *minimal* stage the clusters have their minimal efficiency at these energies, with only 50% of the effective area of the homogeneous cuboid. At the *hit* and *moderate* levels this increases slightly to about 60%. With the *trigger* criterion applied and for *selected* events the clusters are comparable to the cuboid at these energies but still much worse at higher energies. The angular resolution behaves in a similar way as the effective area. It is worse than the resolution of the cuboid above a few TeV, and better below by a factor of two. The efficiency of the *cluster3* is a bit worse than for the other two layouts, especially at the highest energies and with the less strict selection criteria used.

The neutrino effective area as a function of the zenith angle is shown in Fig. 9.20. It is obvious that the largest loss of efficiency compared to the homogeneous cuboid happens at the extrema of the zenith angle, where the effective area is reduced by a factor of two compared to the cuboid. The geometric cross section of the clustered layouts is of course smaller for nearly vertical tracks, explaining this behaviour. For horizontal tracks *cluster1* and *cluster2* are almost comparable to the cuboid, while *cluster3* is still 10 to 20% worse.

The latter is caused by the smaller chance for a horizontal track to strike several clusters in a ring like structure.

Obviously, the cluster geometries do have increased performance at the lowest energies, but are significantly worse at higher energies. The question remains, whether there are events that hit several clusters and are selected. As the distances between the clusters are much larger than the absorption length in water, a related question is, whether a the group of clusters increases the performance through a synergy effect between the clusters, or whether the detector behaves like the sum of eight individual single-cluster detectors. The first question can be answered by looking at the distribution of the lever arm lengths of events satisfying the minimal criterion shown in Fig. 9.17 along with maps of the string layout, where some possible paths for a horizontal muon are marked. The fact that there are lever armlengths larger than approximately the length of one string shows that several clusters have been hit. Furthermore, several peaks can be found in this distribution, one just below 200 m, which is close to the diameter of a single cluster, and a double peak at about 600 m and between 750 and 800 m. The first corresponds to the height of the detector (and hence muons that pass it vertically), the second fits to the distance between a cluster of the outer ring and one of the inner ring. The next two peaks are at just over 1200 m and about 1700 m, distances that fit well to the length of one side of the instrumented volume and the diagonal of the string layout. The peak corresponding to the diameter of a single cluster is much higher than the others, which means that most events only hit one of the clusters. The same distribution is shown for the *cluster3* in Fig. 9.17 on the right. The distribution has peaks below 200 m and a double peak at 600 m and 660 m. As we have seen before, the first one of these corresponds to the diameter of a single cluster. The second fits the length of the strings and the distance between two neighbouring clusters in the ring. The following peaks correspond to distances between clusters further apart. The next-to-nearest-neighbour at 1080 m and the cluster directly at the opposite side of the ring structure at about 1460 m.

In order to check if the group of clusters is better than just eight individual clusters, it was compared to a single cluster with the effective area scaled by eight. The expectation at lowest energy is, that *cluster1* more or less behaves like eight individual clusters, as for low energy and therefore short muon tracks, the (densely) instrumented volume is the parameter defining the efficiency. As the energy and the muon range increase, the cross section area of the layout becomes more and more important. At the highest energies the single cluster multiplied by eight should therefore perform better than *cluster1*. Due to the arrangement of the clusters some of them are covered by others for horizontally arriving muons (which are dominant). Looking at the string layout, it is easy to see that for horizontal tracks only five of the eight clusters contribute to the cross section area of the detector. According to this simplified assumption, the multiplied single cluster should be about 40 to 50% better at the highest energies. In the medium energy range, where tracks are long, but the total light output is low (and proportional to the track length), the longer path length within the instrumented volume of *cluster1* should result in more collected photons and thus an advantage.

The results of the simulation of a single cluster multiplied by eight are compared to *cluster1* in Figs. 9.21 and 9.22. Indeed the results confirm the expectation, as the multiplied single cluster performs between 40 and 60% better at highest energies, depending

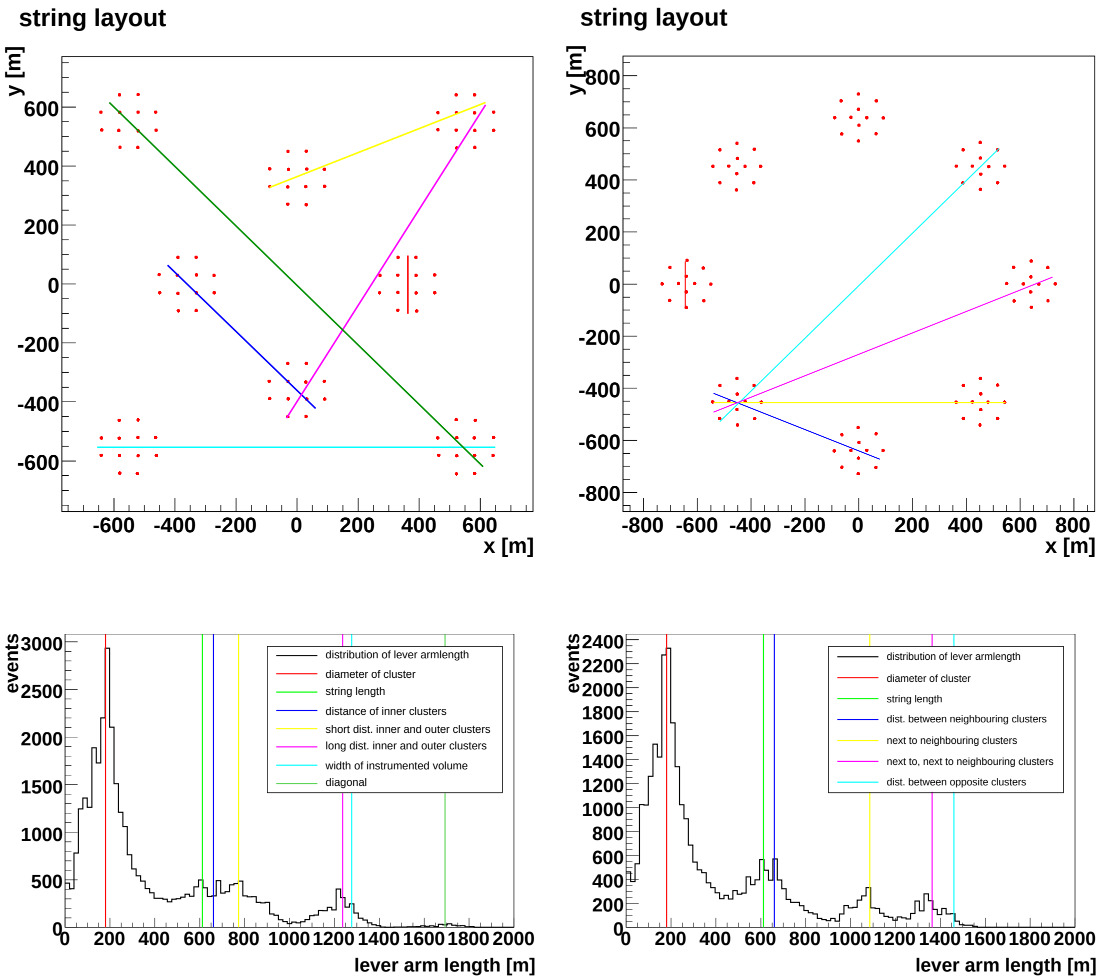

Figure 9.17: Distribution of the lever armlengths in the *cluster1* (bottom left) and *cluster3* (bottom right) detectors. The distances between clusters that appear in that geometry are marked with coloured lines in the string layouts of the detectors (top) and correspondingly in the distributions (bottom). The position of the peaks reflects well these distances.

on the actual criterion used. At energies between 100 GeV and 1 TeV *cluster1* has a larger effective area, as expected, and at energies below 100 GeV the scaled single cluster is slightly better again. The angular resolution is much better for the *cluster1*, as the average leverarm length is higher.

The effective area as a function of the zenith angle is shown in Fig. 9.23. The single cluster multiplied by eight is significantly better for horizontal events, while for events incident with very high or very low zenith angles the two effective areas are comparable. This also confirms the expectation, as for horizontal events the cross section area for *cluster1* is smaller than that of eight individual clusters, while for vertical events the cross section areas are the same. As the effective area is dominated by events above a few TeV, the effect of the different cross section areas dominates the zenith angle dependence.

Section summary

- Cluster geometries can be used to significantly increase the low energy performance (E<100 GeV), but at the cost of performance at medium and high energies.
- The arrangement of the clusters in the instrumented volume has no significant impact on the results.
- The layouts with eight clusters differ in performance from eight individual clusters. At energies below a few TeV (depending on selection) the eight-cluster geometry has higher effective area than eight individual clusters, above these energies it is lower. The angular resolution is better than for the individual clusters due to the longer leverarm achievable.

9.3 Variations of the cuboid geometry

In addition to the ring and clustered geometries, variations of the standard flat cuboid geometry have been considered. The first one is an attempt to apply the principle of the rings to a more rectangular layout. The reason is that a ring layout of strings is difficult to expand. As we will see in section 9.4, the extendability of a detector layout might play an important role in the future. With a ring structure this could be difficult. Therefore, the principle of a detector with a densely instrumented boundary and a hollow core was applied to the cuboid. The resulting layout, the *hollow cuboid*, is shown in Fig. 9.24. It is consists of 288 strings, each equipped with 17 storeys. The string distances are the same as in the standard cuboid, the storeys are spaced by 36 m. Three other variants of the cuboid were produced, that are shown in Figs. 9.25, 9.26 and 9.27. The idea for these concepts is to check if the number of strings in a homogeneous string layout can be reduced by just attaching more storeys to less strings, this corresponds to making the geometries more 'IceCube-like'. The detector layouts, called *cuboid2*, *cuboid3* and *cuboid4*, consist of 18×18, 15×15 and 12×12 strings, respectively. This results in 15 storeys per string with distances of 41 m for *cuboid2*, 21 storeys per string with distances of 28.5 m for *cuboid3* and 34 storeys per string with distances of 17.5 m for *cuboid4*.

minimal

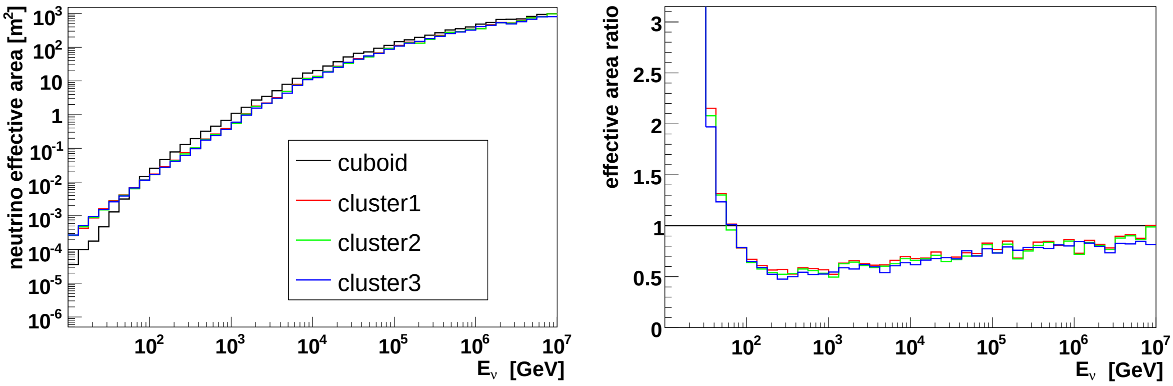

hit

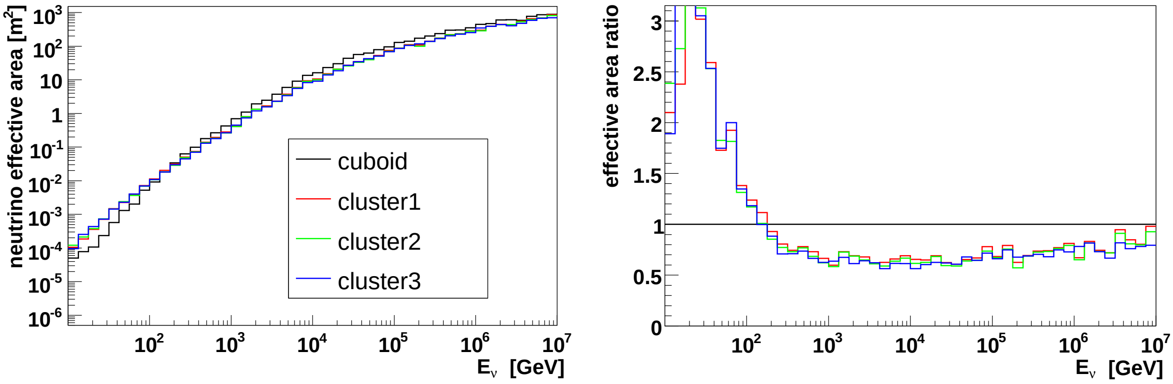

moderate

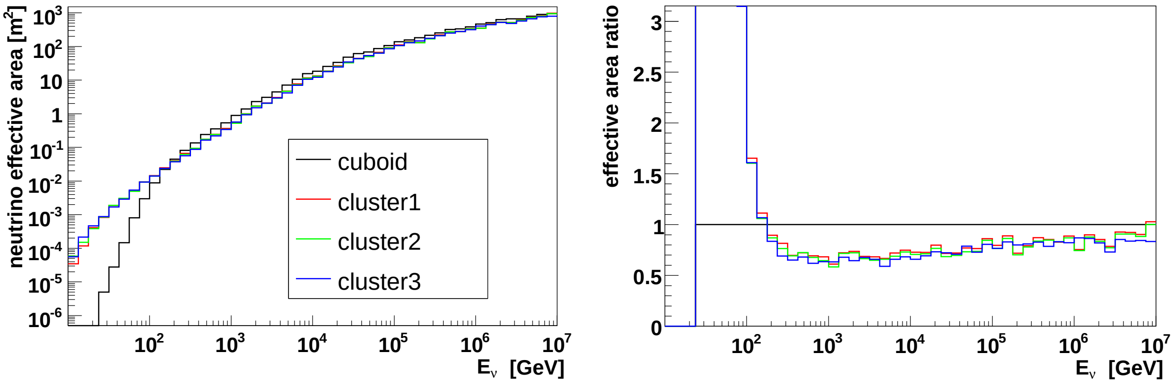

Figure 9.18: Neutrino effective areas and effective area ratios for detectors with clustered geometries, for the *minimal*, *hit* and *moderate* criteria applied.

trigger

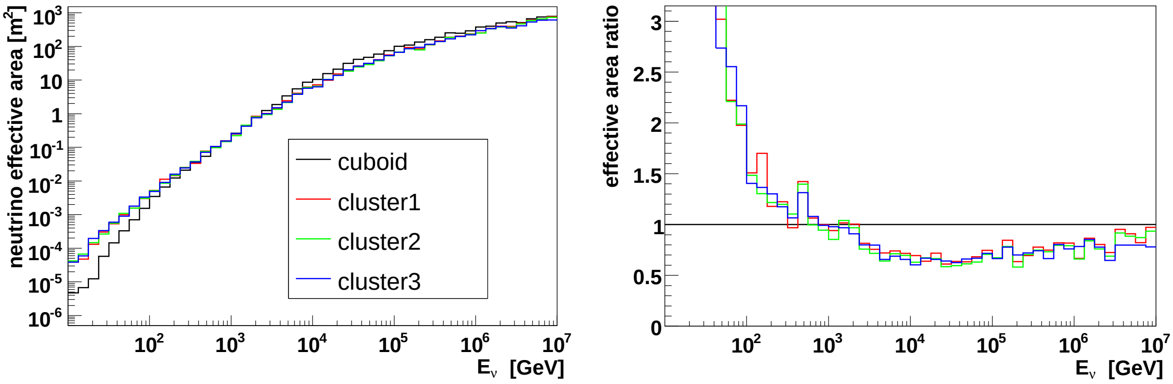

selected

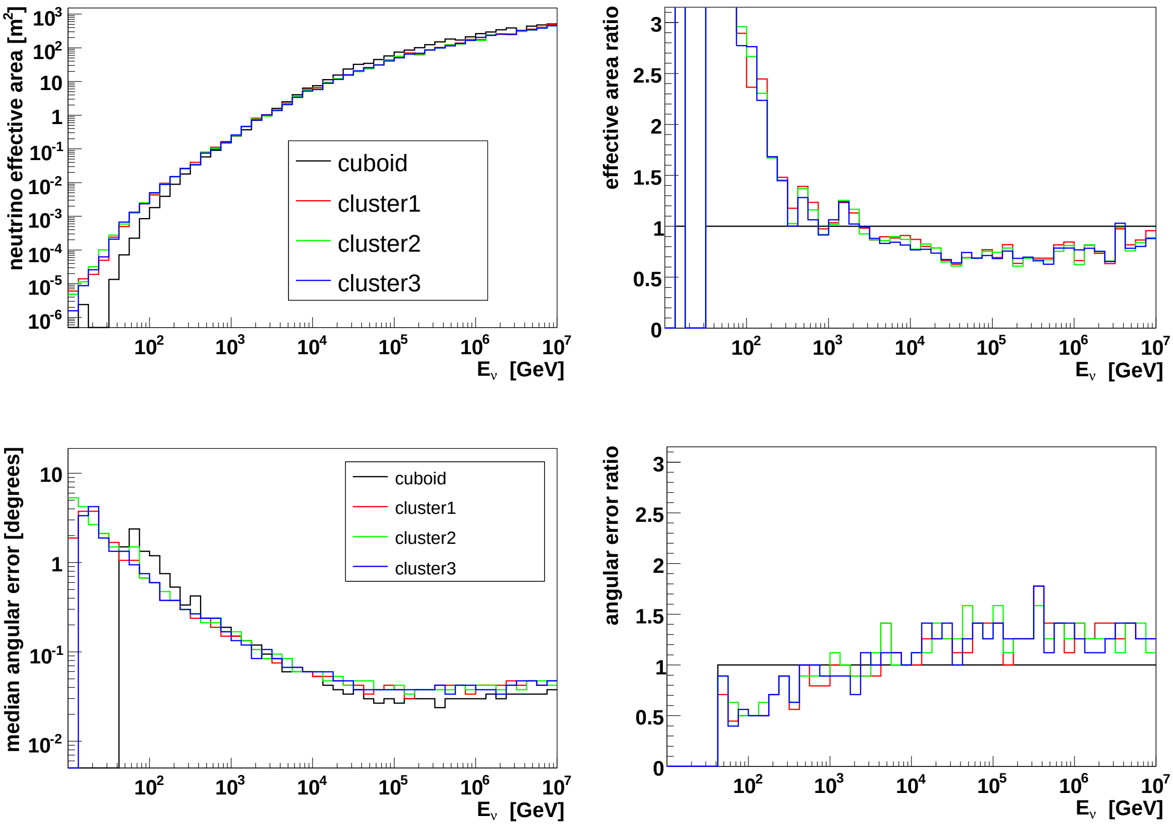

Figure 9.19: Neutrino effective areas and area ratios with the *trigger* criterion applied (top) and for *selected* events (middle) for detectors with cluster geometries. Angular resolution and resolution ratios for *selected* events (bottom).

minimal

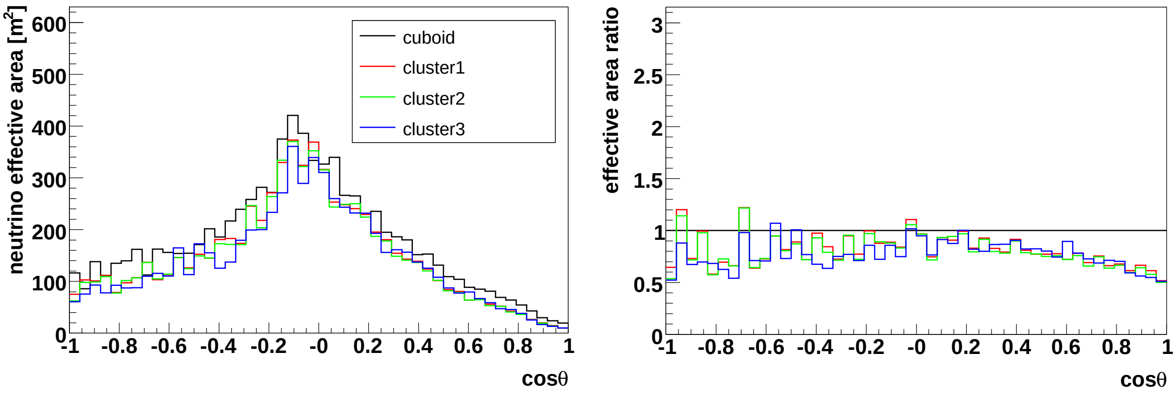

moderate

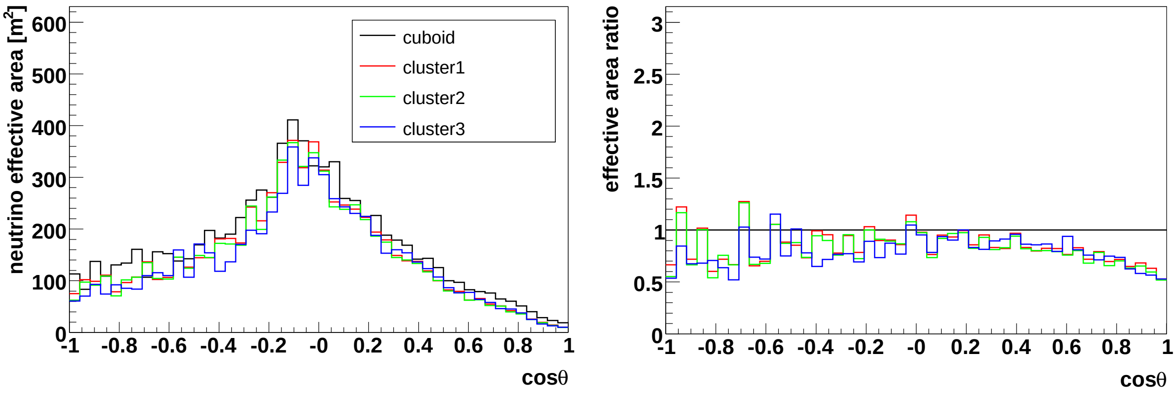

selected

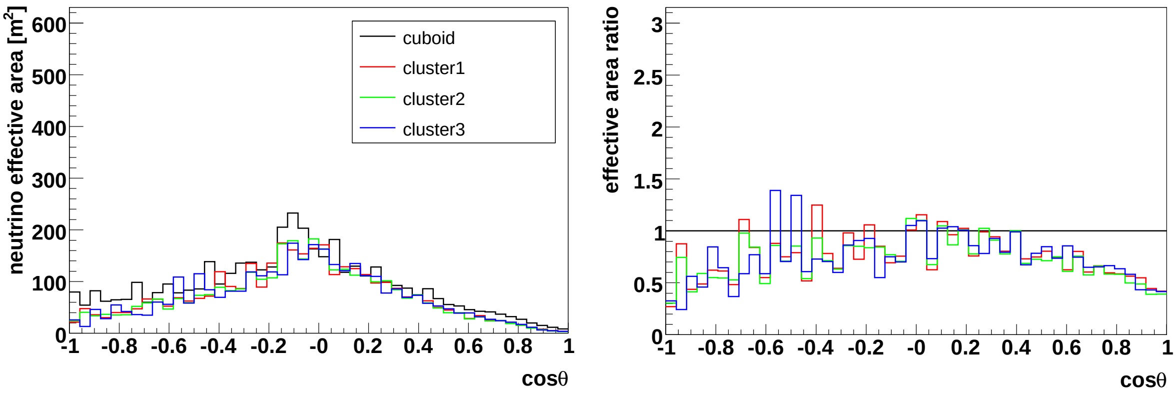

Figure 9.20: Neutrino effective areas and effective area ratios as a function of zenith angle for detectors with clustered geometries, with *minimal*, *moderate* and *selected* criteria applied.

minimal

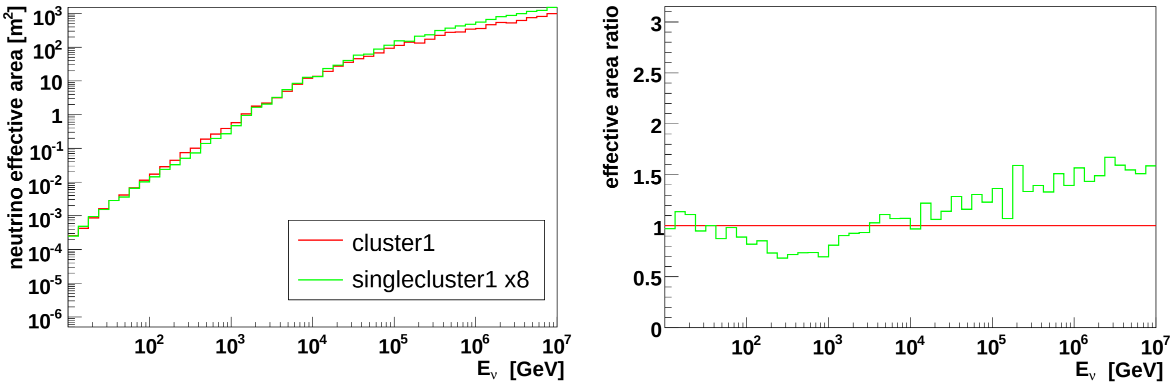

hit

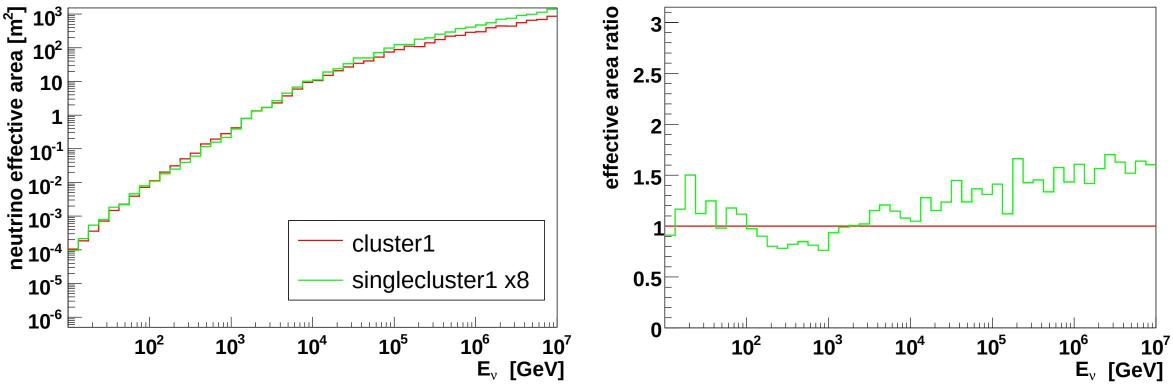

moderate

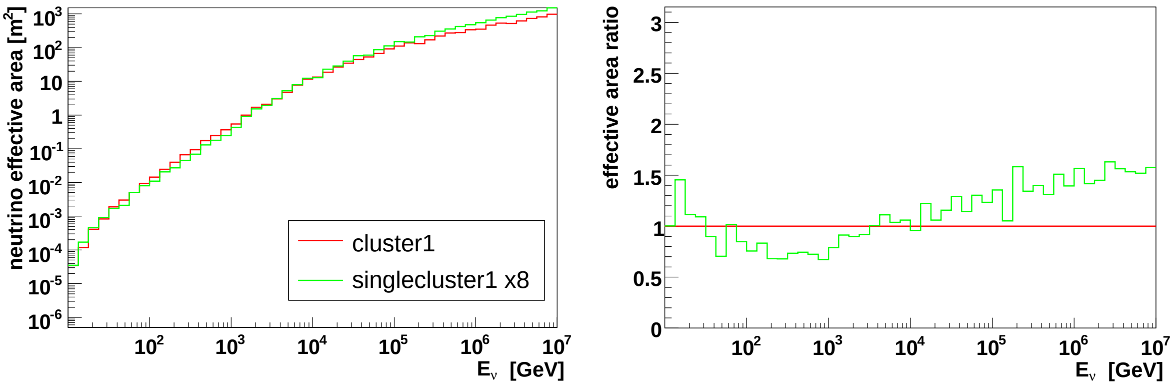

Figure 9.21: Neutrino effective areas and effective area ratios compared for the cluster1 and a single cluster scaled by eight, for the *minimal*, *hit* and *moderate* criteria applied.

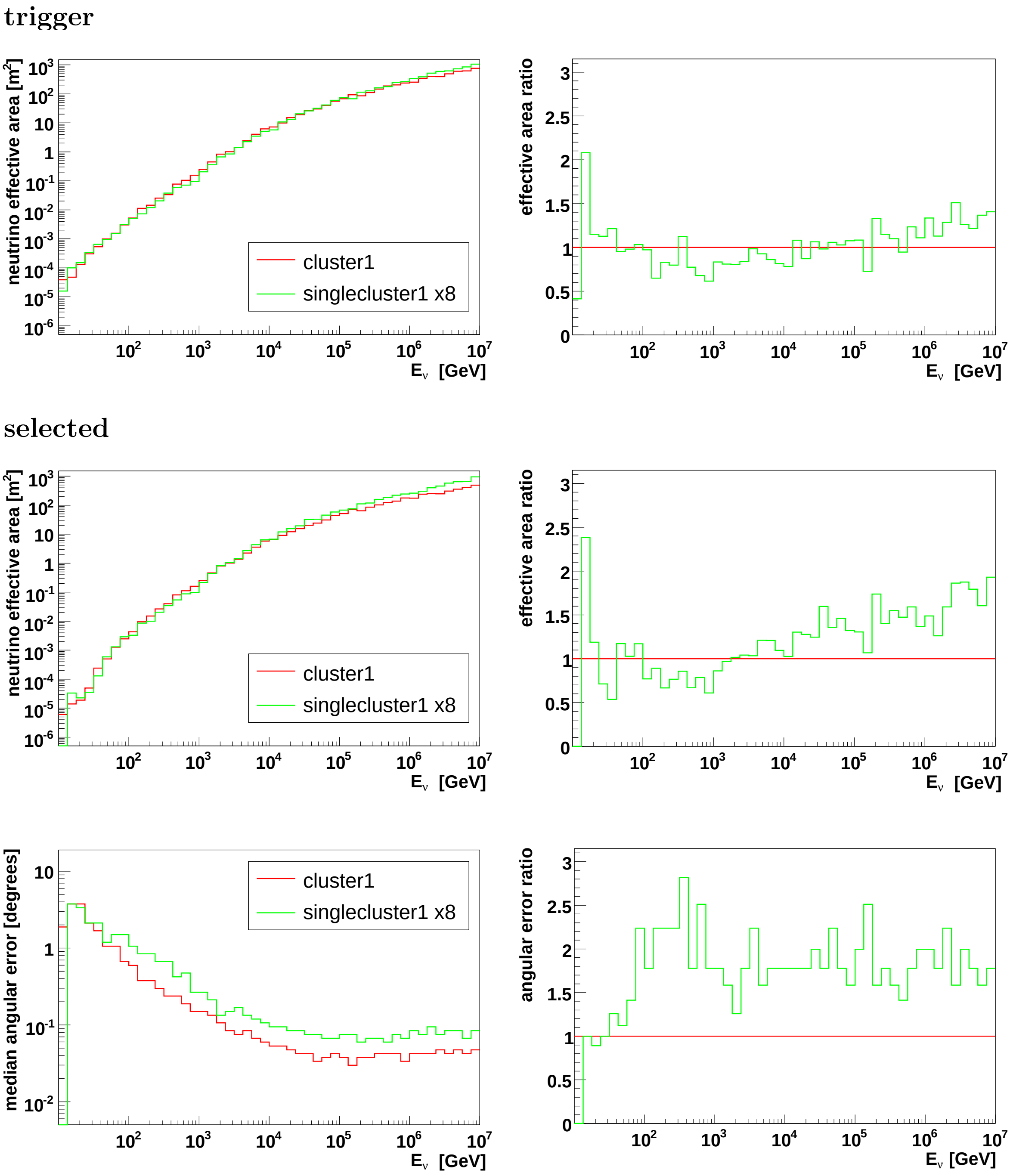

Figure 9.22: Neutrino effective areas and area ratios with the *trigger* criterion applied (top) and for *selected* events (middle) compared for the cluster1 and a single cluster scaled by eight. Angular resolution and resolution ratios for *selected* events (bottom).

minimal

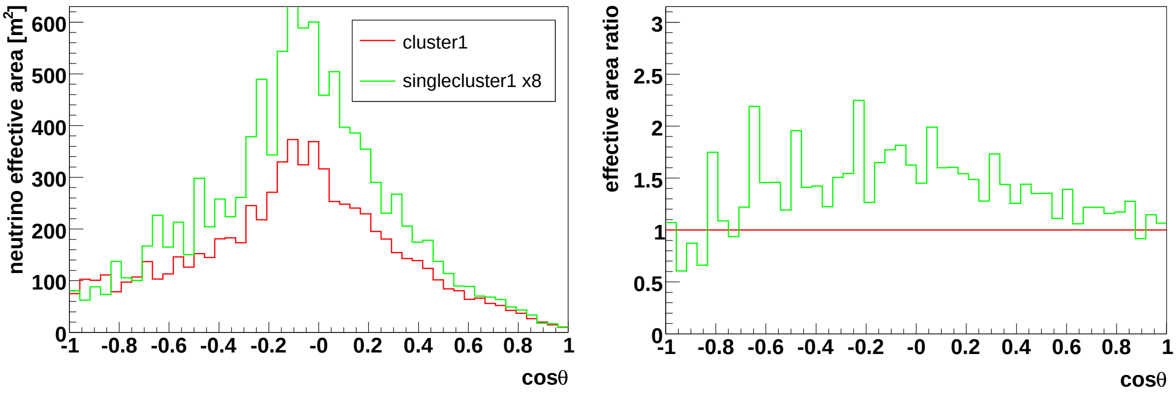

moderate

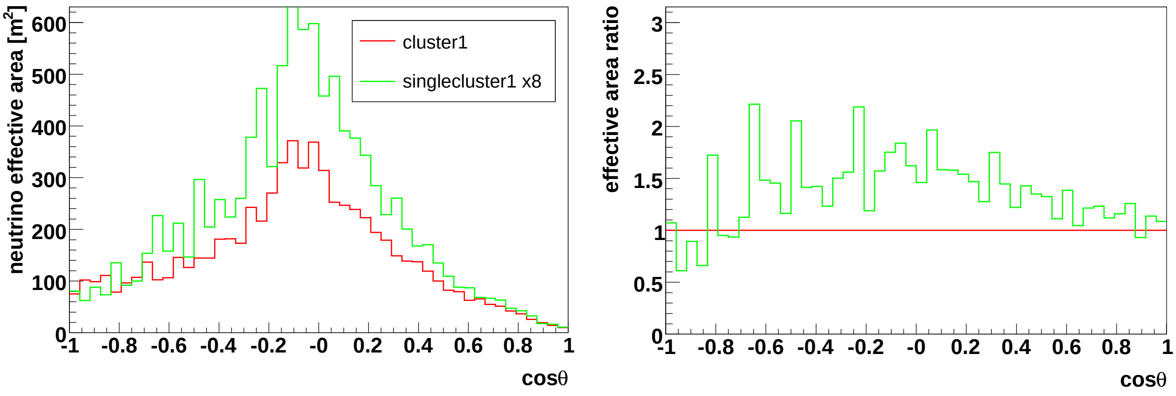

selected

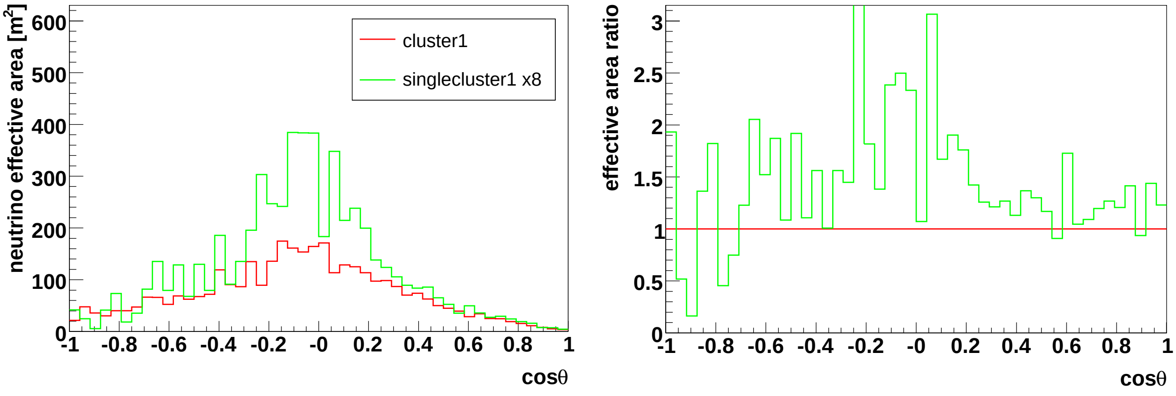

Figure 9.23: Neutrino effective areas and effective area ratios as a function of zenith angle compared for the cluster1 and a single cluster scaled by eight, with *minimal*, *moderate* and *selected* criteria applied.

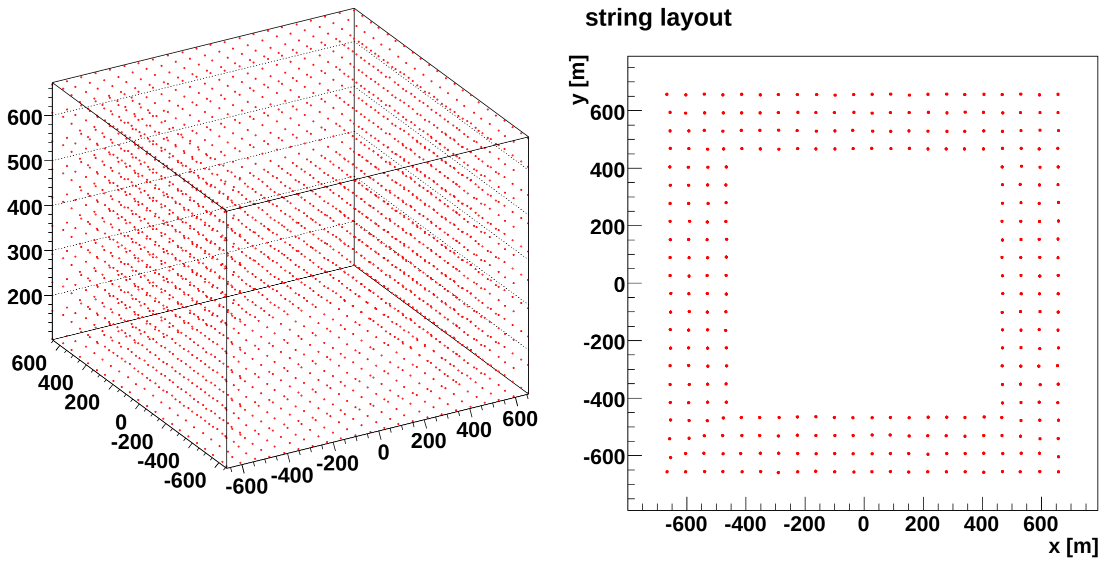

Figure 9.24: Left: *Hollow cuboid* geometry. Right: Sea floor layout of the strings used to simulate this geometry.

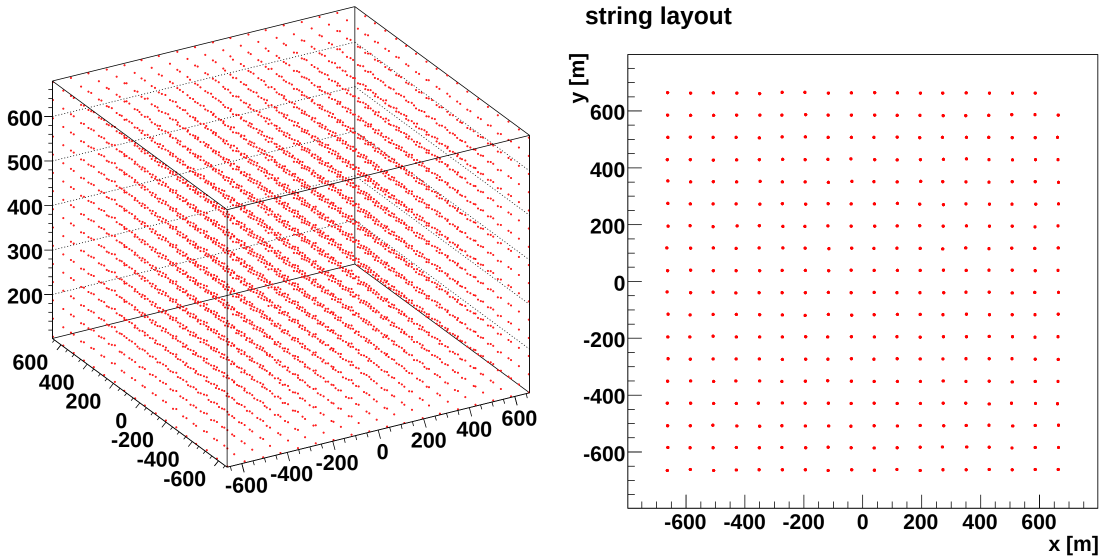

Figure 9.25: Left: *Cuboid2* geometry. Right: Sea floor layout of the strings used to simulate this geometry.

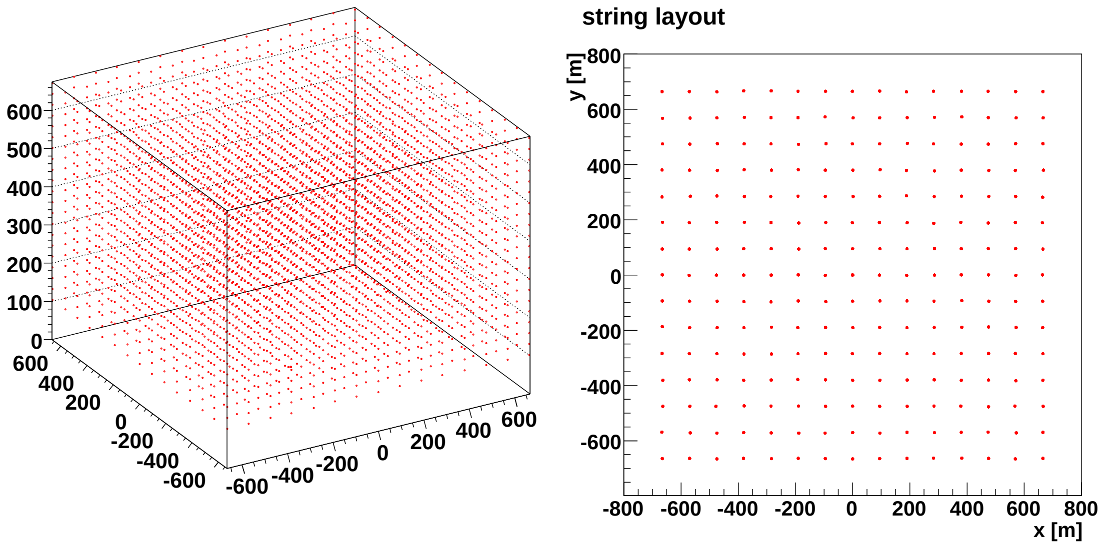

Figure 9.26: Left: *Cuboid3* geometry. Right: Sea floor layout of the strings used to simulate this geometry.

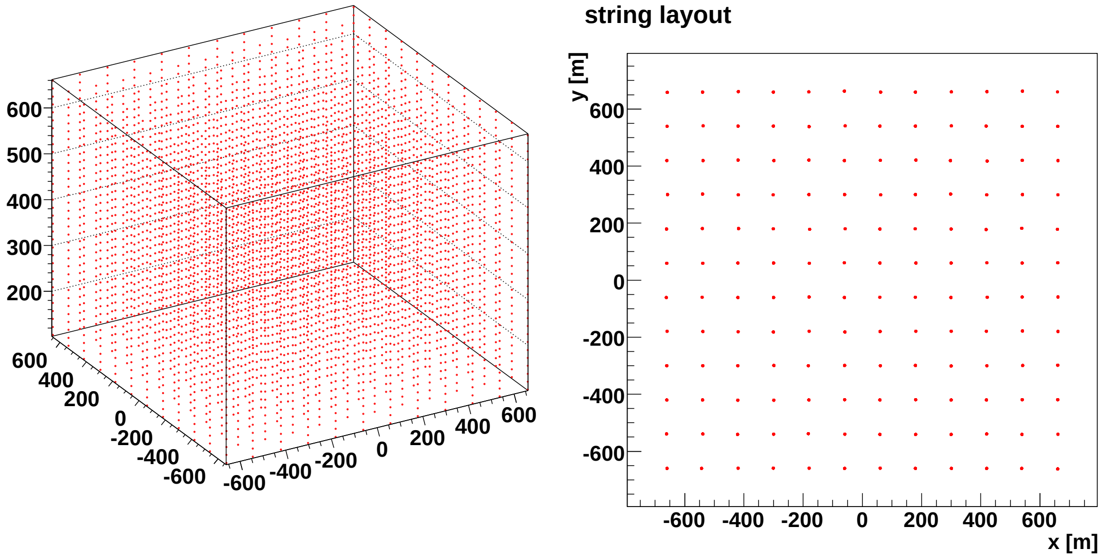

Figure 9.27: Left: *Cuboid4* geometry. Right: Sea floor layout of the strings used to simulate this geometry.

9.3.1 Results for the variants of the standard cuboid

The results of these variants are compared to the standard cuboid in Figs. 9.28, 9.29 and 9.30. At energies above a few hundred GeV, the effective area of the *hollow cuboid* is nearly identical to that of the standard cuboid for the *minimal*, *hit* and *moderate* criteria. At the *trigger* level and for *selected* events both are almost equal above a few TeV. Below these energies, the hollow version is actually better due the denser instrumentation of the strings. The difference varies from 30 to 40% below 100 GeV at the *hit* level, over ∼50% below 3 TeV at *trigger* level, to a factor of more than three below 100 GeV at the *moderate* level. Also, the angular resolution is better below a few TeV (to a maximum of 40% at 100 GeV). The zenith angle dependence of the effective area follows that of the ring geometries. It is very similar to the cuboid, with a slight disadvantage for down- and especially upgoing events, compensated by a slight advantage for horizontal events. Obviously, the *hollow cuboid* is a viable option, as it provides all the advantages of the ring geometries and apparently even with a slightly better performance.

The results for the *cuboid2*, *cuboid3* and *cuboid4* layouts are virtually identical to the results for the standard cuboid above 100 GeV. The only difference is a minimal advantage in efficiency and resolution for events at the very low end of the energy spectrum and a small loss of efficiency for the *cuboid3* (10%) and the *cuboid4* (20%) for *selected* events between 100 GeV and 1 PeV. This can be explained by looking at the zenith-angle dependence of the effective areas, showing that (as a consequence of the larger distance between the strings) the efficiency is reduced for vertical events.

As these cuboid variants decrease the number of strings even more than the ring layouts, they are also a viable (and probably even the better) option to save cost by reducing the number of structures.

Section summary

- A hollow cuboid geometry shows similar results as the rings.
- By reducing the number of strings in the cuboid layout and at the same time increasing the number of storeys on the strings, the performance can be kept almost constant, while drastically reducing the number of structures.
- If the string distances become too large, the performance around a few TeV is slightly reduced, due to a loss of efficiency for vertical events.

9.4 Beyond the cubic kilometer

In the early phase of the KM3NeT Design Study measurements with the HESS gamma-telescope showed, that a cubic kilometer of instrumented volume might not be sufficient for the detection of Galactic neutrino sources. Analyses like the one performed in [3] imply that indeed volumes larger by a factor of 2-5 or so will be necessary to collect enough statistics in neutrinos within a few years. The KM3NeT Design Study will focus on the

minimal

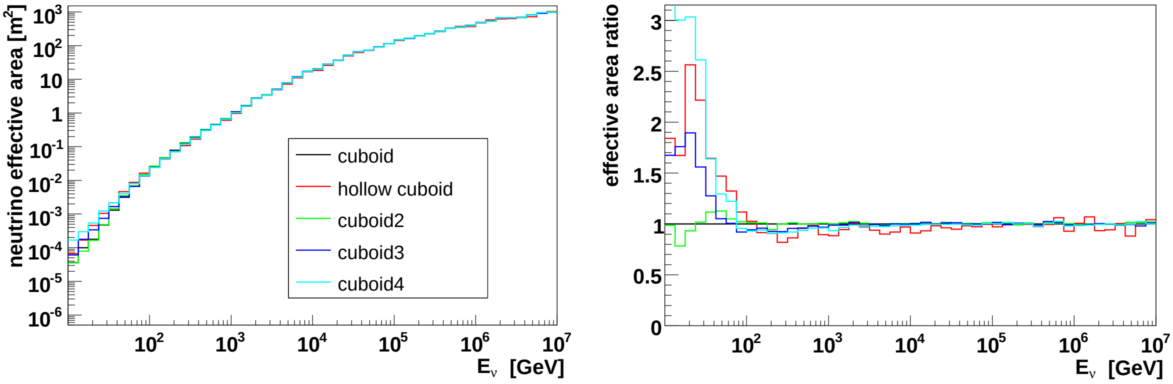

hit

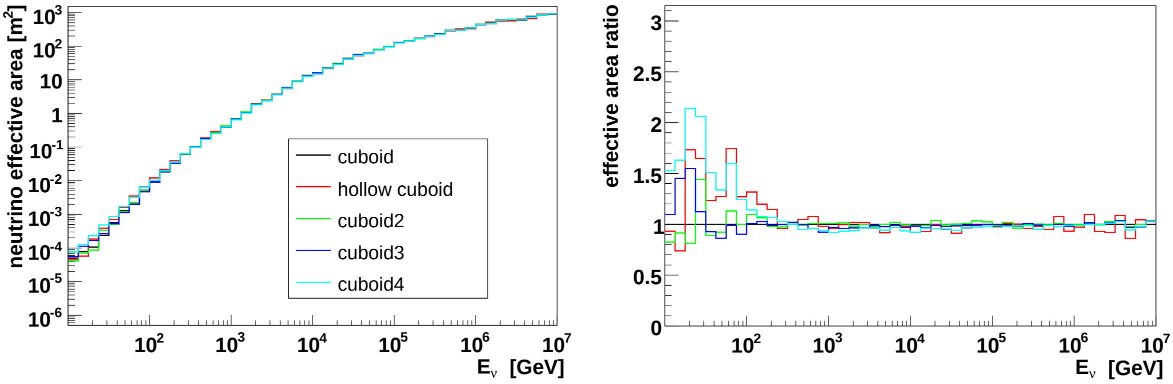

moderate

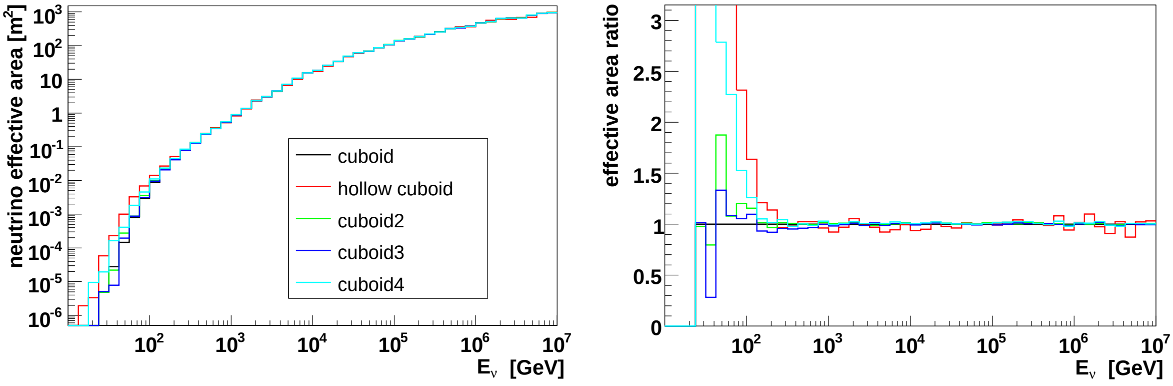

Figure 9.28: Neutrino effective areas and effective area ratios for the variants of the cuboid geometry, for the *minimal*, *hit*, *moderate* and *trigger* criteria applied.

trigger

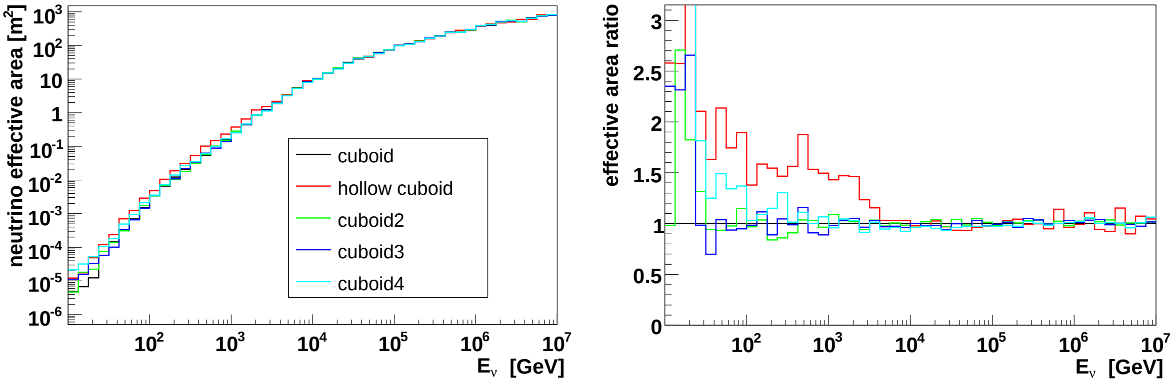

selected

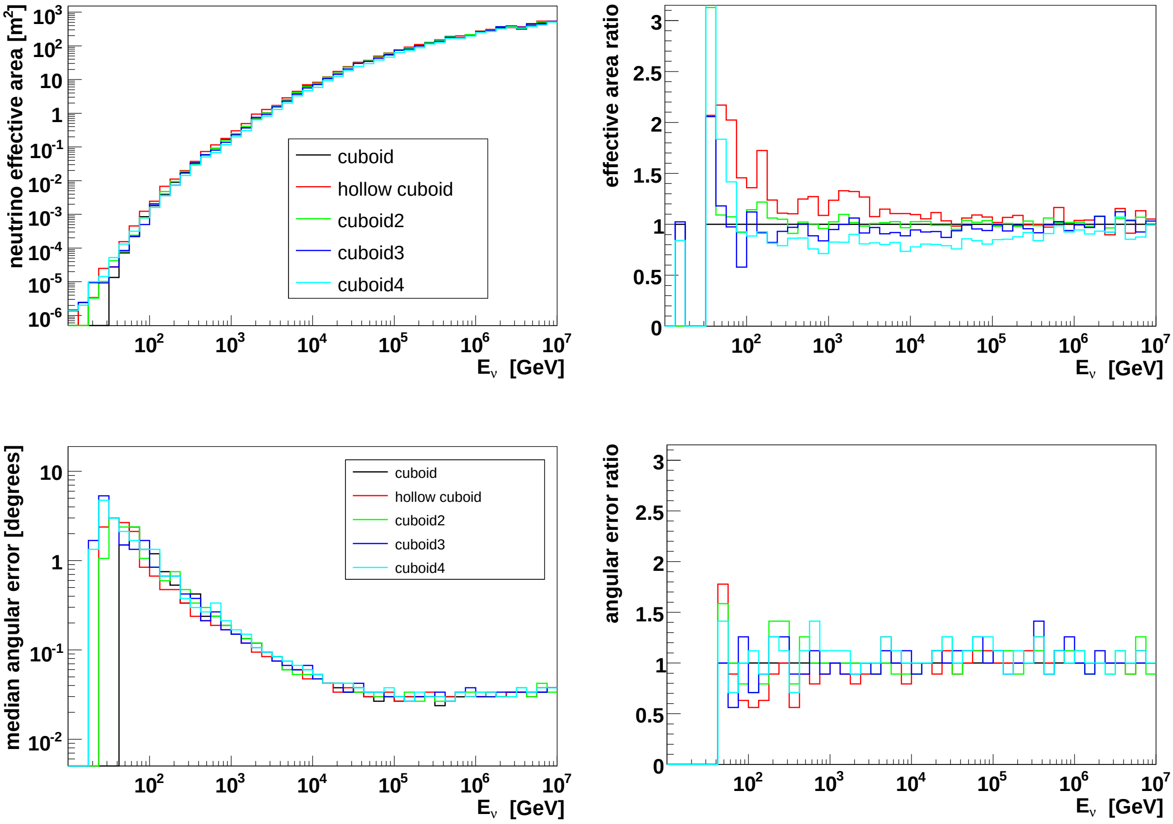

Figure 9.29: Neutrino effective areas and area ratios with the *trigger* criterion applied (top) and for *selected* events (middle) for variants of the cuboid geometry. Angular resolution and resolution ratios for *selected* events (bottom).

minimal

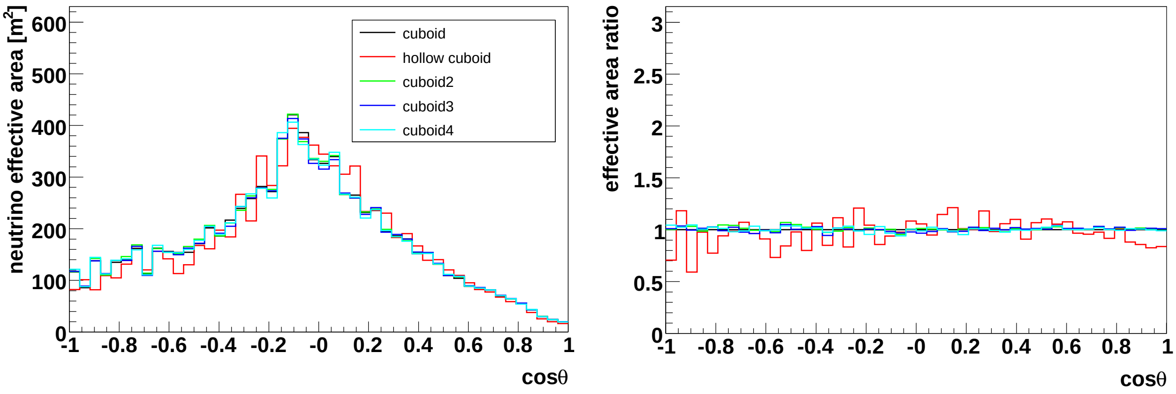

moderate

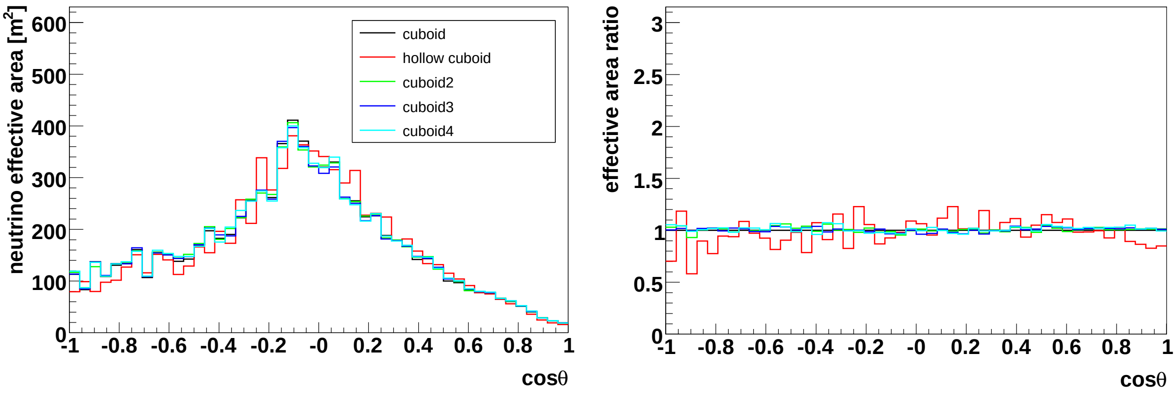

selected

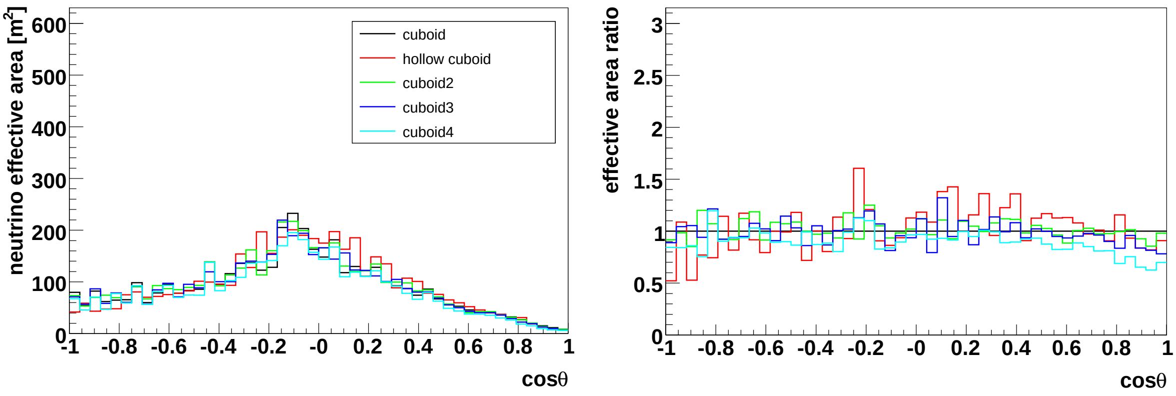

Figure 9.30: Neutrino effective areas and effective area ratios as a function of zenith angle for the variants of the cuboid geometry, with *minimal*, *moderate* and *selected* criteria applied.

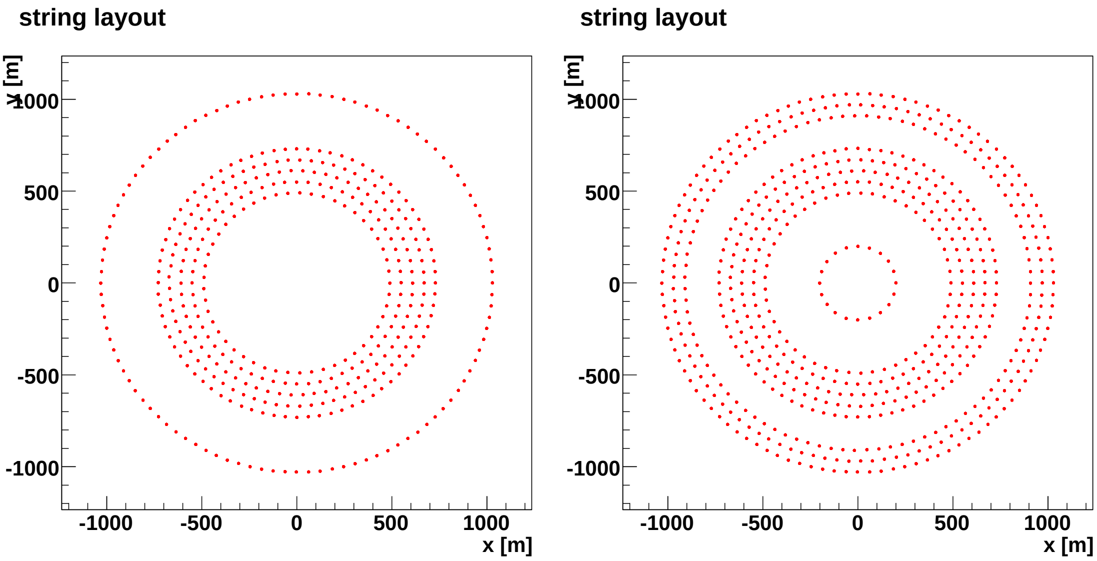

Figure 9.31: Left: String layout of the *ring1a* geometry. Right: String layout of the *ring1b* geometry.

design of a single cubic-kilometer telescope, but the possibility to extend the detector in the future is an important consideration.

Therefore, several extended geometries were simulated in this work, based mainly on the ring and cuboid structures. In addition, detector layouts with two cubic kilometers of instrumented volume were produced and simulated, implementing some basic concepts.

It should be noted that this study is just a series of tests, and cannot be a comprehensive study of extendable or enlarged geometries.

Extended detectors

The first extended geometry is based on the *ring1* geometry. The idea is to add a single additional ring with a larger radius, so that the overall volume is two cubic kilometers. In this case the number of storeys increases by about 30%. The resulting string layout is shown in Fig. 9.31 on the left side. This layout is called the *ring1a* in the following. The second geometry, shown on the right side of Fig. 9.31, doubles the number of storeys of *ring1*, by adding additional rings on the out- and inside of the standard ring geometry. It will be called the *ring1b*. A third extended layout, based on the hollow cuboid, is shown in Fig. 9.32. The volume and the number of storeys was doubled, by placing two hollow cuboids directly next to each other.

Detectors with two cubic kilometers of instrumented volume

These detector geometries are intended to have a larger volume without increasing the number of storeys. The first one is a *ring1* like geometry with a larger diameter to reach the instrumented volume intended. The number of strings and storeys is similar to *ring1*,

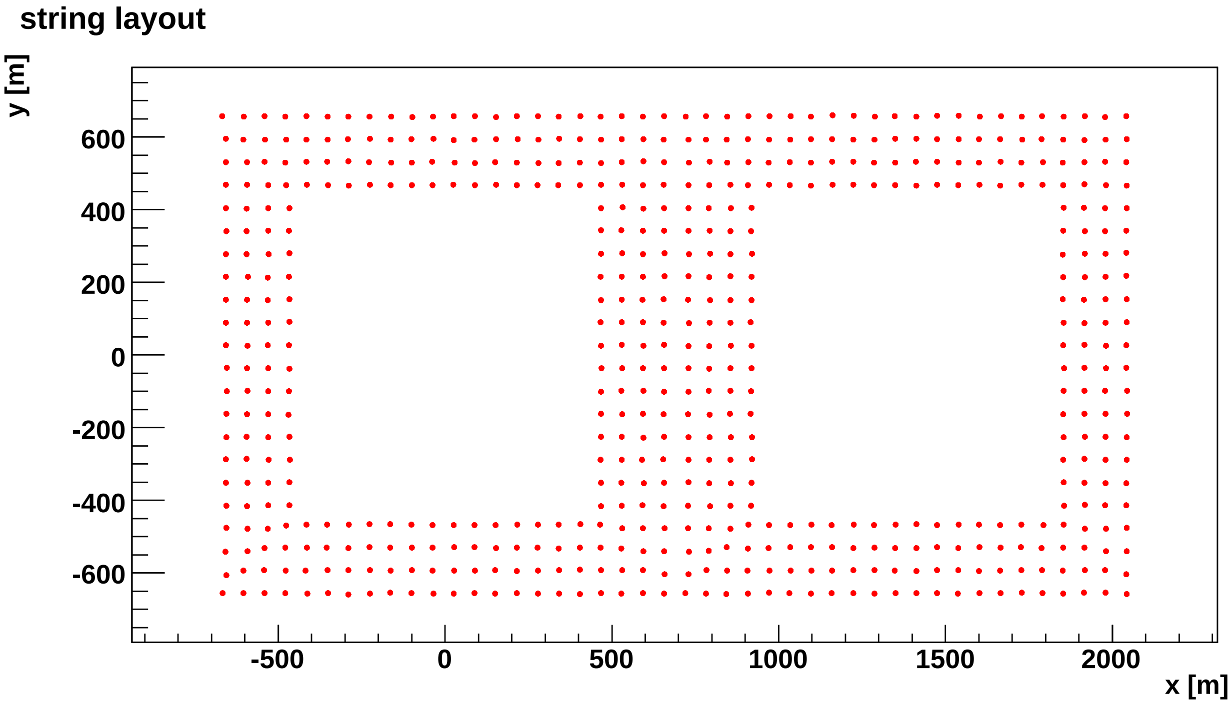

Figure 9.32: String layout of the double *hollow cuboid* geometry.

as it has 291 strings with 17 storeys per string and a string distance of 60 m within the rings. This layout is called the *large ring* and its string layout is shown in Fig. 9.33. For the next two geometries a common idea was used, although they are based on the cuboid and *ring1* geometries. The idea is to spread out the strings on the boundary of the detector, to increase the instrumented volume. In this way there is a rather dense core for the detection of low energy events, while with the thinned out boundary region a large volume for the detection of events with very high energies (and low fluxes) is created. The two string layouts are shown in Fig. 9.34. They will be called the *spread ring* and the *spread cuboid* in the following.

9.4.1 Results for extended detectors

The results for the extended detectors are given in the Figs. 9.35, 9.36 and 9.37. The effective area of the double *hollow cuboid*, under the *minimal*, *hit* and *moderate* criteria, is between 60% (at energies of several PeV) and 80% (at energies of a few TeV) higher than that of the standard cuboid. At energies below 1 TeV the extended detector with its doubled volume and number of storeys becomes increasingly superior with a maximum of more than factor three (a bit less in the *hit* case). For the same criteria *ring1a* has about 50% more effective area at the highest energies. The difference decreases towards lower energies, reaching its minimum (compared to the cuboid) at about 200 GeV. It is of course still superior to the cuboid at these energies, although only by 10 to 20%. For even lower energies the performance increases again, due to the denser instrumentation of the

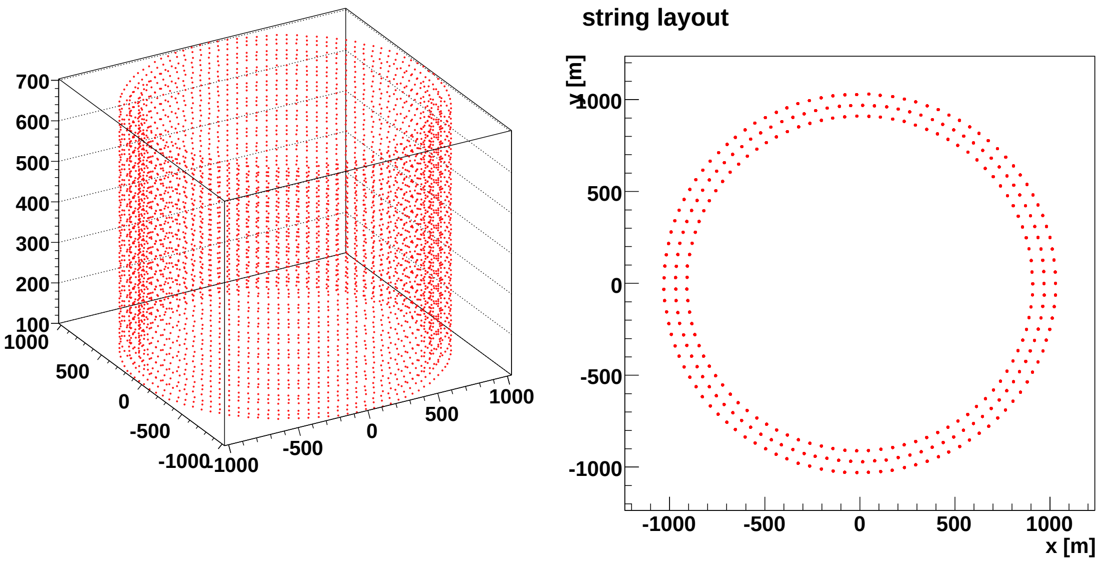

Figure 9.33: Left: *large ring* geometry. Right: Sea floor layout of the strings used to simulate this geometry.

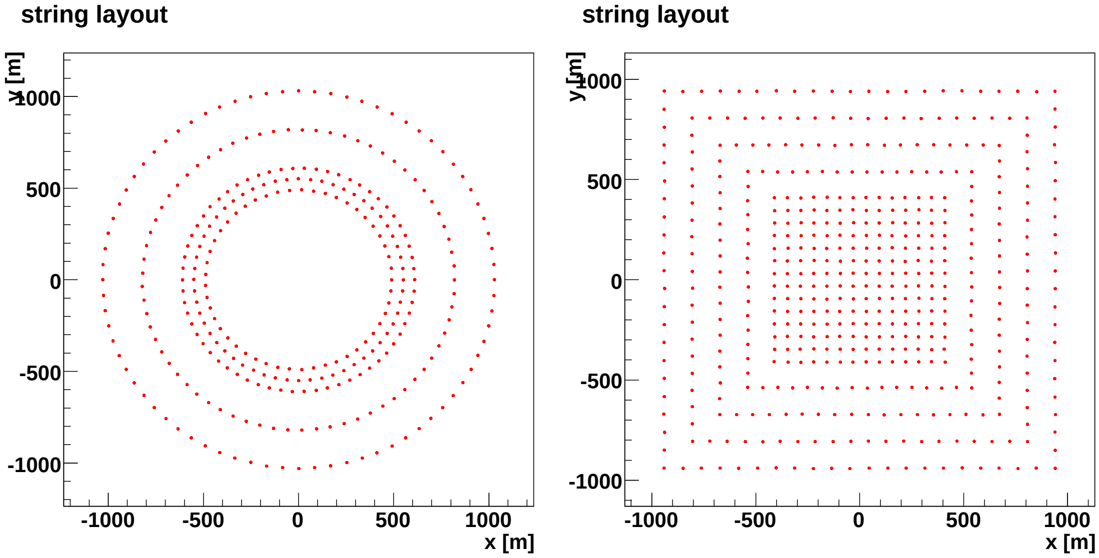

Figure 9.34: Left: String layout of the *spread ring* geometry. Right: String layout of the *spread cuboid* geometry.

strings compared to the cuboid. The *ring1b* geometry behaves like the *ring1a* at energies above 1 PeV. Towards lower energies it approaches the effective area of the double *hollow cuboid* and has almost the same efficiency below a few tens of TeV. This is interesting, as it has the same number of modules and the same volume as the double cuboid, but is still worse at the highest energies.

For *trigger* and *selected* events the relative behaviour of the three extended geometries is mostly similar to the other selection criteria, with an increased advantage for the double *hollow cuboid* at energies below a few TeV (here *ring1b* is worse, but still better than *ring1a*). The angular resolution is also very similar for these enlarged geometries, showing the same behaviour as the *ring1* (although *ring1a* seems to be a bit worse here). The zenith angle dependence of the effective areas is quite uniform for vertical and horizontal events. Only the double cuboid shows a slight decrease of efficiency for upward going events (at all selection levels), caused by the holes in the center.

The surface of the double hollow cuboid is a bit larger than that of *ring1b*, resulting in a larger average cross section area for horizontal events (for vertical events it is actually smaller, but the horizontal muons dominate). This explains the larger effective area at high energies of the double cuboid. At energies above 1 PeV nearly all events passing the instrumented volume area detected, which makes the cross section area of the detector the defining parameter. At lower energies the density of the instrumentation and the volume start to become more and more important and finally dominate at the low end of the energy spectrum. This explains the performance of *ring1b*, which is similar to *ring1a* at high energies (they have exactly the same instrumented volume and therefore the same cross section area) and similar to the double hollow cuboid at low energies (they have the same number of storeys).

Another interesting question is whether two separate and distant detectors provide better results than a single detector with the same volume and number of storeys. This question can be answered by comparing the double *hollow cuboid* detector with two *hollow cuboid* detectors, or in other words the effective area of a *hollow cuboid* scaled by two. The results for this comparison are shown in Figs. 9.38, 9.39 and 9.40.

At the *minimal* and *moderate* level the performance of the double *hollow cuboid* is comparable to that of the scaled *hollow cuboid* for energies below 1 TeV. At higher energies and at all other selection steps, the combined detector has an effective area between 10 and 20% smaller than two separate detectors. The reason for this is the fact that the potential interaction volume is larger for two separate detectors. The two components of the double *hollow cuboid* share the same interaction volume. At very low energies where the muon range is very small, the interaction volume for the double version is twice the one of a single *hollow cuboid*, at high energies, where the muon range is much larger than the detector dimension, it is only slightly larger. Two separate detectors on the other hand have twice the interaction volume at all energies. Additionally the cross section areas are different for the two cases. Two separate detectors have twice the cross section area of a single detector from all directions. The cross section area of the double *hollow cuboid* is smaller, as the two adjacent faces of the cuboids, do not contribute. The effect of the different cross section areas is also visible in the zenith angle dependence of the effective area. For horizontal muon tracks, the double cuboid is worse compared to the scaled cuboid, while for vertical tracks the effective areas are similar.

9.4.2 Results for detectors with increased volume

The neutrino effective areas at the various selection steps as a function of energy and of the zenith angle, as well as the angular resolution, are shown in Figs. 9.41, 9.42 and 9.43. They are in all cases compared to the standard cuboid and the *ring1* geometry All of the detectors with an increased volume have more effective area for high energies. The *spread cuboid* is about 50% better, followed by the spread ring and the large ring. The main difference between the selection modes is the energy, above which the larger detectors start to be better. For the *moderate* and the *hit* criteria this is about 1 TeV, for the *minimal* criterion it is 300 GeV. For the stricter *trigger* criterion and for *selected* events the increase in efficiency is slightly smaller and starts at higher energies around 10 TeV. This increase of effective area is of course a consequence of the larger volume of the detectors.

The behaviour below these energies is quite different for the detectors and selection steps. For low energies, the *large ring* detector has a very similar performance as the *ring1* at the *minimal*, *hit* and *moderate* level. The *spread ring* is clearly worse than the *ring1* and even the cuboid at energies around 100 GeV. At even lower energies it seems to gain a bit on the cuboid, but this is most probably a consequence of the low statistics at these energies. These observations can be explained by the different densities of the instrumentation. At very low energies, most of the events, that are selected are inside the instrumented volume. This volume is similar for the *large ring* and the *ring1*. It is larger for the *spread ring*, but the average distance between the storeys is larger, decreasing the low-energy performance. At the *trigger* level the *large ring* is worse than the *ring1* but still better than the cuboid. The *spread ring* compares well to the cuboid. For *selected* events *large ring* and *ring1* are very similar again, the same is true for the *spread ring* and the cuboid. The *spread cuboid* is clearly worse than the cuboid at low energies, which is a consequence of the larger average distance of the storeys in this geometry. Its area below 100 GeV varies between 10% of the cuboid effective area at the *moderate* level and 100% at the *hit* level and very low energies of tens of GeV.

The angular resolution of all the larger detectors is worse than for the standard cuboid detectors. At the highest energies, the *large ring* is the worst, below 1 PeV all of the detectors have a resolution about 50% worse than the cuboid. For horizontal tracks, the effective area of all the large detectors is very similar at all selection steps. The *spread cuboid* has similar performance as the cuboid for vertical tracks at the *minimal* and *moderate* levels. For *selected* events, the performance drops slightly for upgoing muons. For the *spread ring* this decreased effective area for vertical muon tracks is visible at all selection steps, which is a consequence of the 'hole' effect. This effect is even larger for the *large ring*, which has a much larger uninstrumented core. An interesting observation is the fact that for the spread detectors the efficiency for vertical tracks decreases for *selected* events (for the *large ring*, this effect is equally strong at all steps). The thinner instrumentation at the rim of the spread detectors obviously makes a (good) reconstruction of those vertical events difficult, which pass through this section of the detector.

Section summary

- Detectors with the double instrumented volume have higher effective areas at energies above 100 TeV, but not twice as high as the 1 km^3 *candidate* detectors. The exact amount of the increase depends on the overall photocathode area. Even detectors that also have twice the number of storeys reach an 80% increase only, as the cross section area (which dominates the performance at these energies) is not doubled with the volume.

- The behaviour at lower energies depends on the storey spacing and the overall photocathode area. Detectors where the number of storeys is also doubled achieve about a factor two here, detectors with the same number of storeys as the 1 km^3 *candidate* detectors are comparable to these.

- The angular resolution of the larger detectors is similar to the one of standard-size detectors if the number of storeys is doubled and worse if the overall photocathode area is similar.

9.5 IceCube comparable geometries

In the KM3NeT Design Study project, the software group decided on a common detector model for tests of different software packages. The selected model is a copy of the IceCube layout, equipped with ANTARES-like optical modules with 10"photomultipliers. The only exception is the angular acceptance, which was chosen to be proportional to $\cos(\theta)$ (flat disc). In order to provide results for the ANTARES software used in this work, this detector was also simulated. This provides the opportunity to test some of the general principles (geometries) considered in this work under slightly different conditions. Therefore a homogeneous cube, a ring and a cluster geometry were produced using the same string setup as in the IceCube layout. These resulting detector models are called IceCube comparable (ICC) detectors in the following. The string layouts for the original IceCube layout and the derived ICCcube, ICCring and ICCcluster models are shown in Figs. 9.44 and 9.45.

The main difference to the geometries considered before is the length of the string, which is 1000 m. This is probably not feasible for a real deep-sea detector, but its simulation serves as a test of principles. The ICCring and the ICCcube use IceCube-like strings, with 60 single downward-pointing optical modules with distances of 17 m. The ring has 80 strings as IceCube, the cube has 81 in order to create a nine by nine grid. The cluster has only 70 strings, but 68 OMs per string with distances of 15 m.

As the experience with the similarly equipped single OM cuboid has indicated bad statistics for *selected* events, a larger event sample containing 20×10^9 neutrinos was used.

minimal

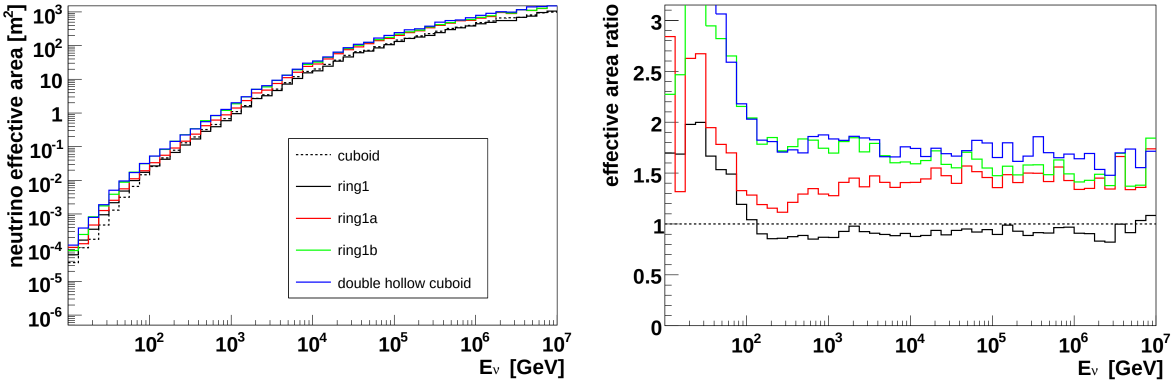

hit

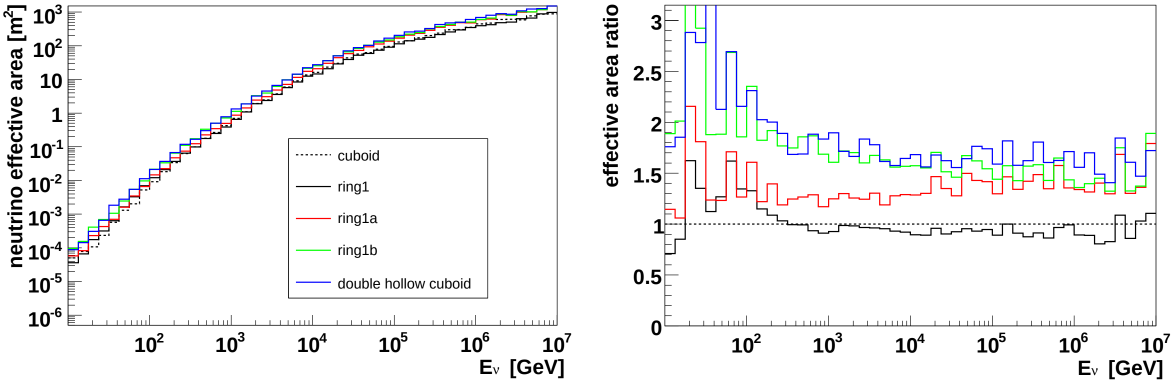

moderate

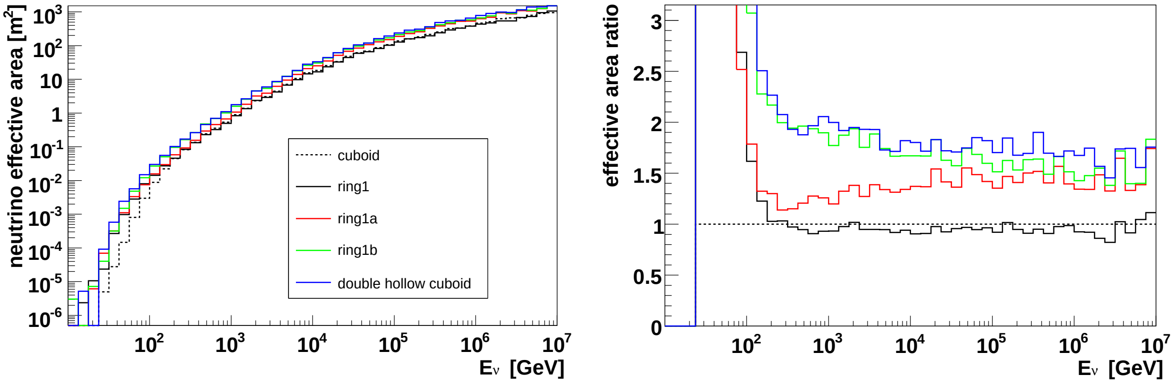

Figure 9.35: Neutrino effective areas and effective area ratios for detectors with extended geometries, for the *minimal*, *hit* and *moderate* criteria applied.

trigger

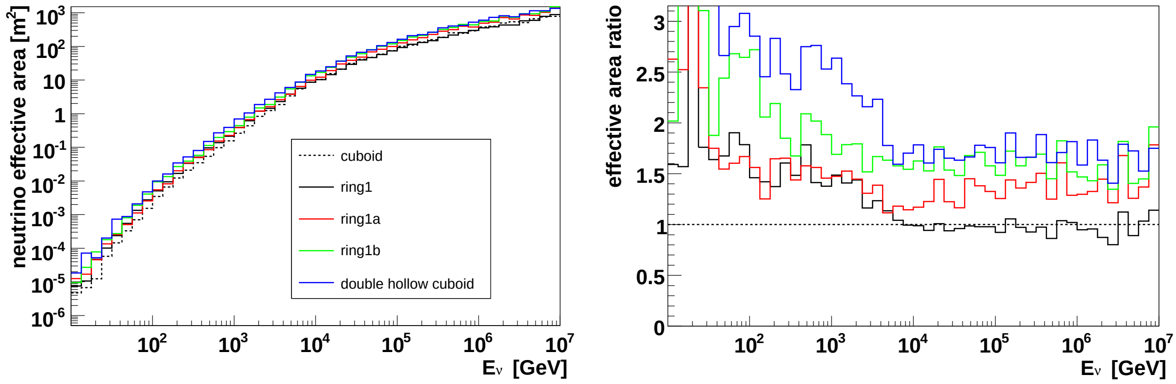

selected

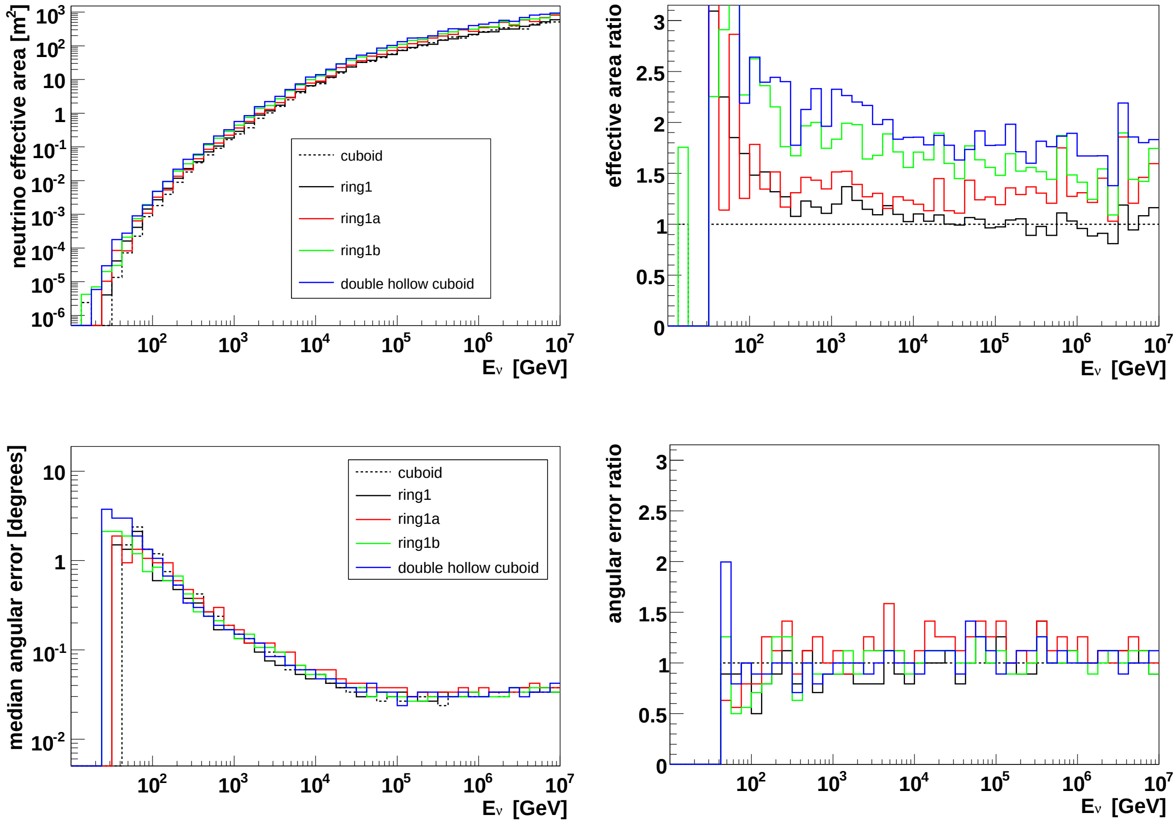

Figure 9.36: Neutrino effective areas and area ratios with the *trigger* criterion applied (top) and for *selected* events (middle) for detectors with extended geometries. Angular resolution and resolution ratios for *selected* events (bottom).

minimal

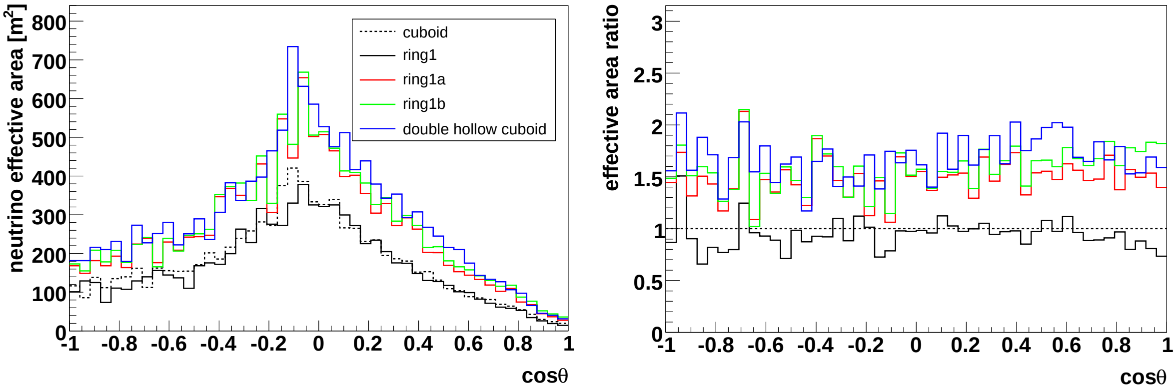

moderate

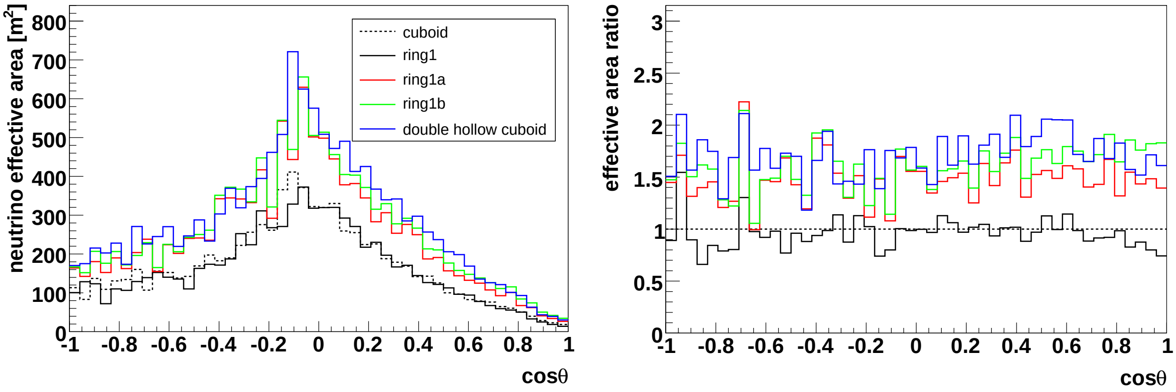

selected

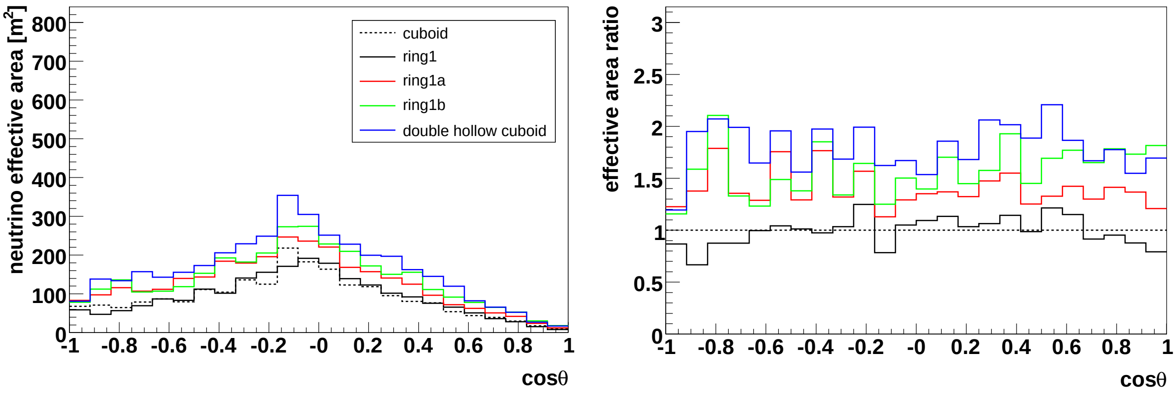

Figure 9.37: Neutrino effective areas and effective area ratios as a function of zenith angle for detectors with extended geometries, with *minimal*, *moderate* and *selected* criteria applied.

minimal

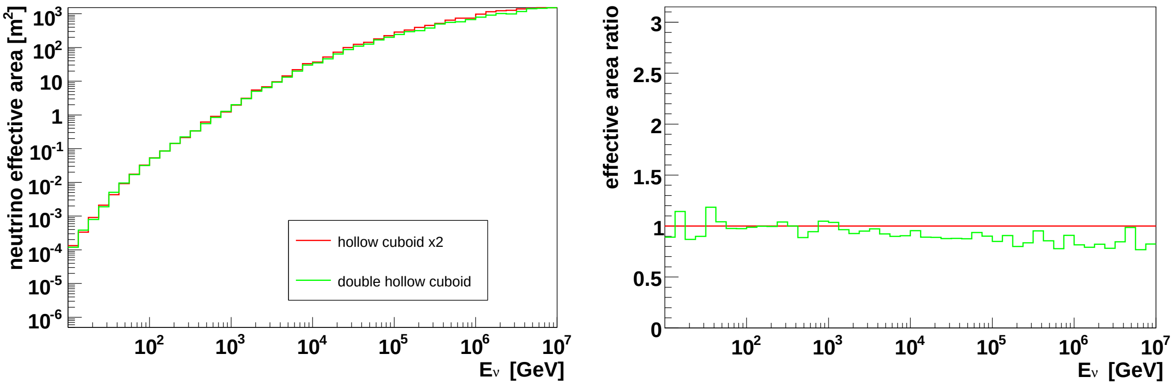

hit

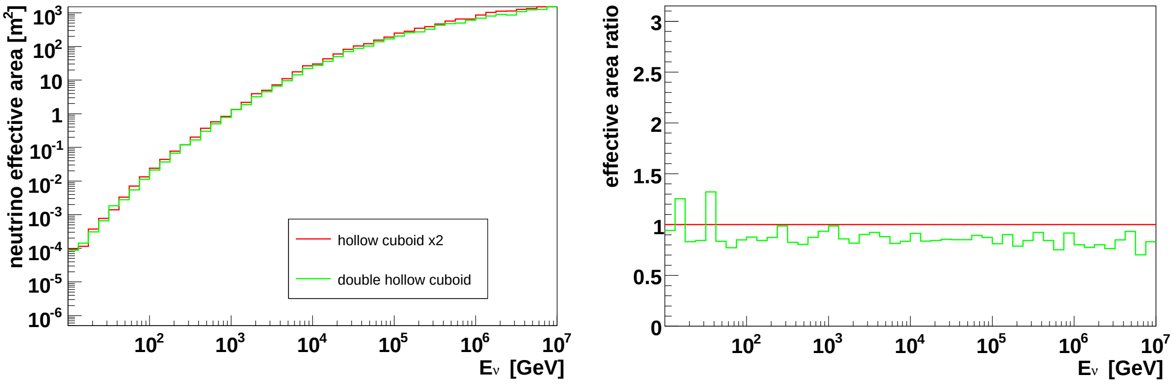

moderate

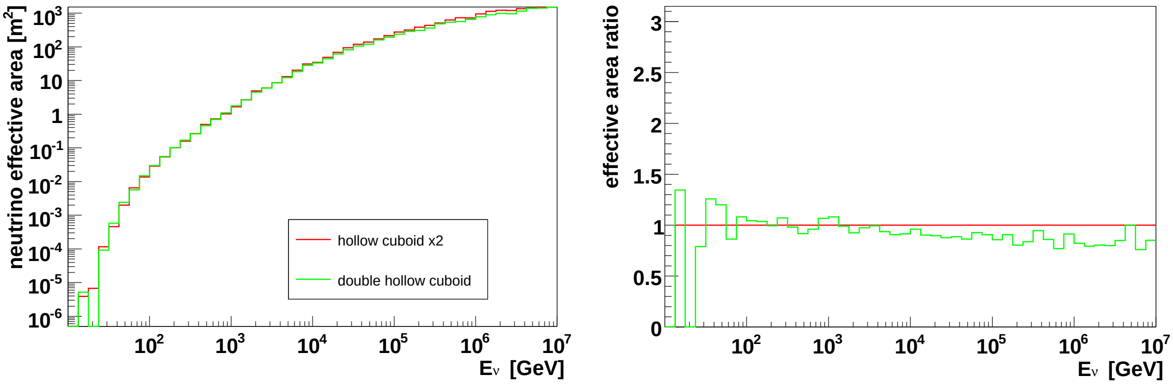

Figure 9.38: Neutrino effective areas and effective area ratios for the double hollow cuboid detector, compared to those of the hollow cuboid scaled by two, for the *minimal*, *hit* and *moderate* criteria applied.

trigger

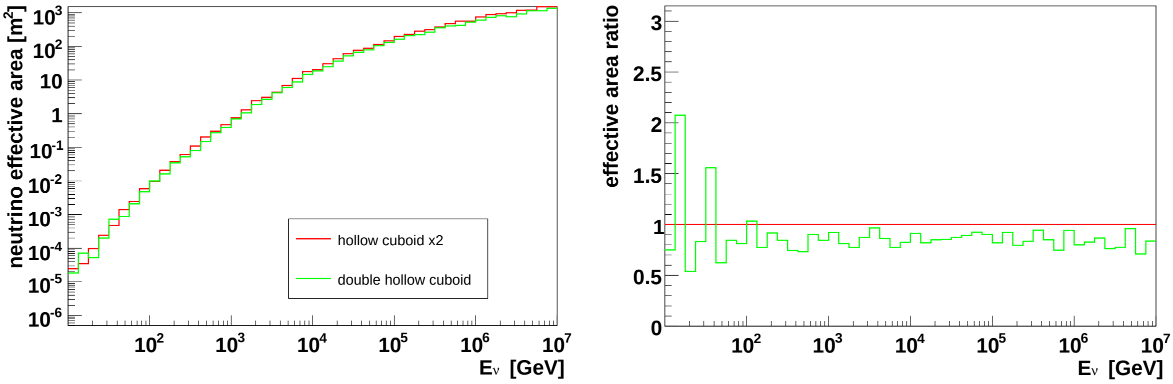

selected

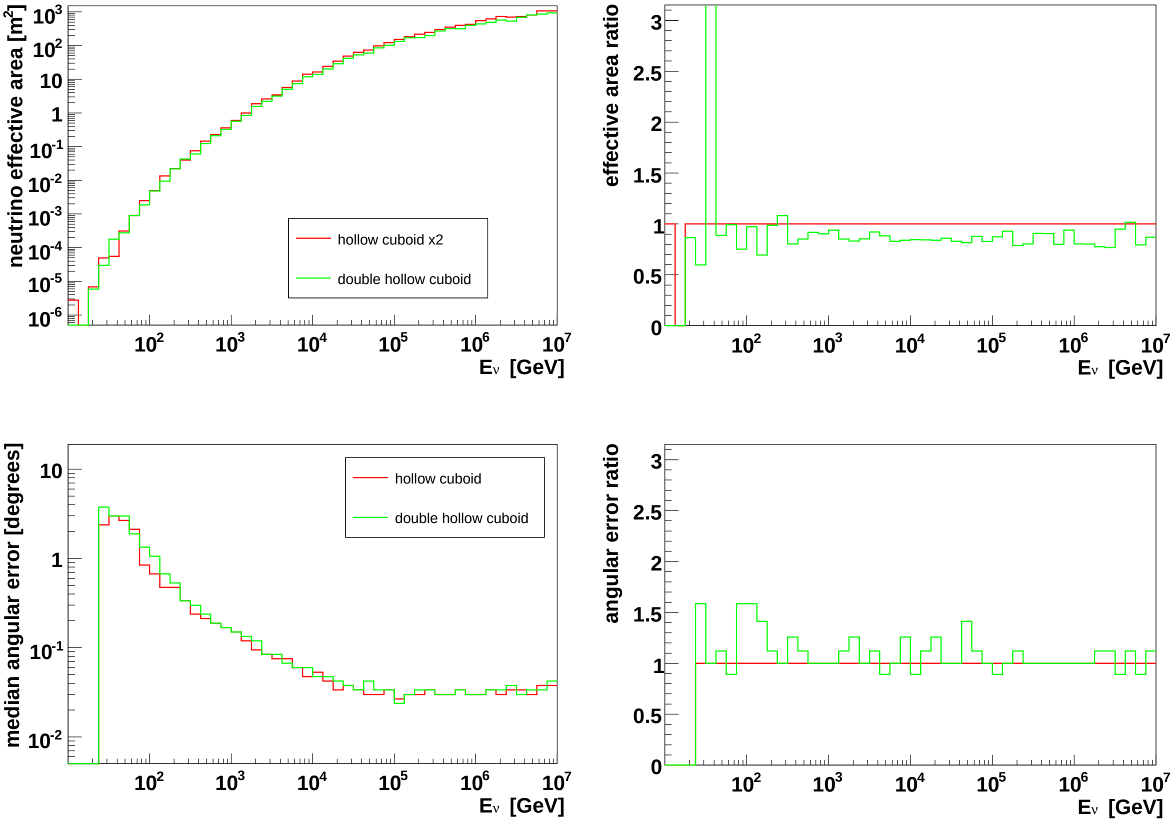

Figure 9.39: Neutrino effective areas and area ratios with the *trigger* criterion applied (top) and for *selected* events (middle) for the double hollow cuboid detector, compared to those of the hollow cuboid scaled by two. Angular resolution and resolution ratios for *selected* events (bottom).

minimal

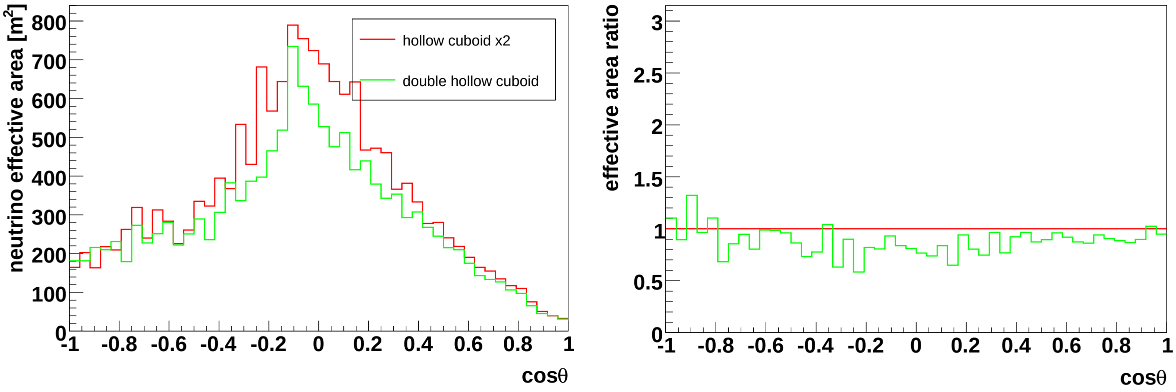

moderate

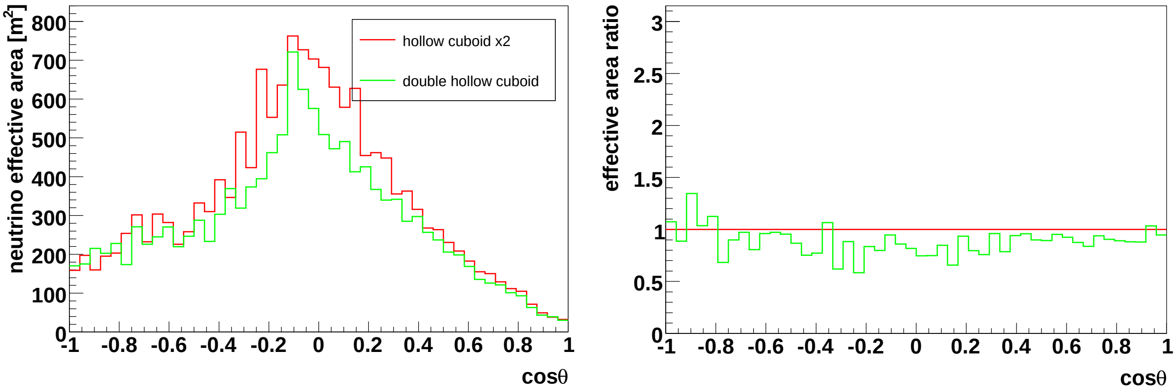

selected

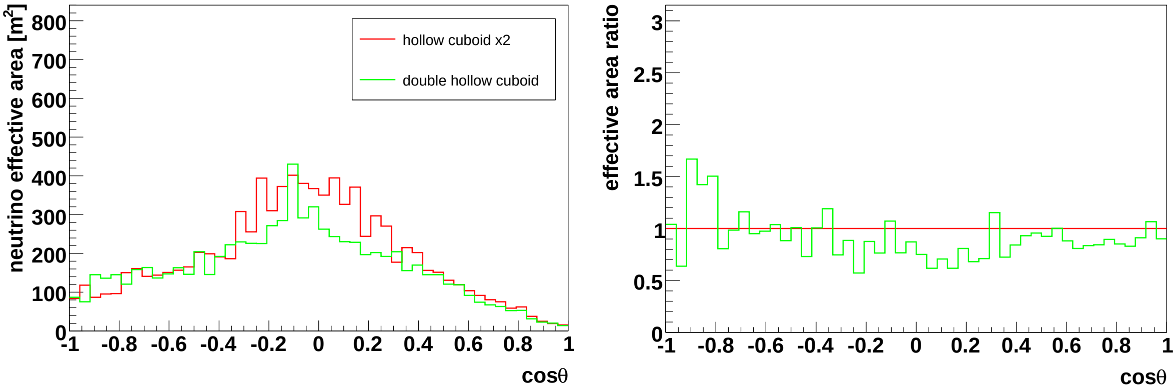

Figure 9.40: Neutrino effective areas and effective area ratios as a function of zenith angle for the double hollow cuboid detector, compared to those of the hollow cuboid scaled by two, with *minimal*, *moderate* and *selected* criteria applied.

minimal

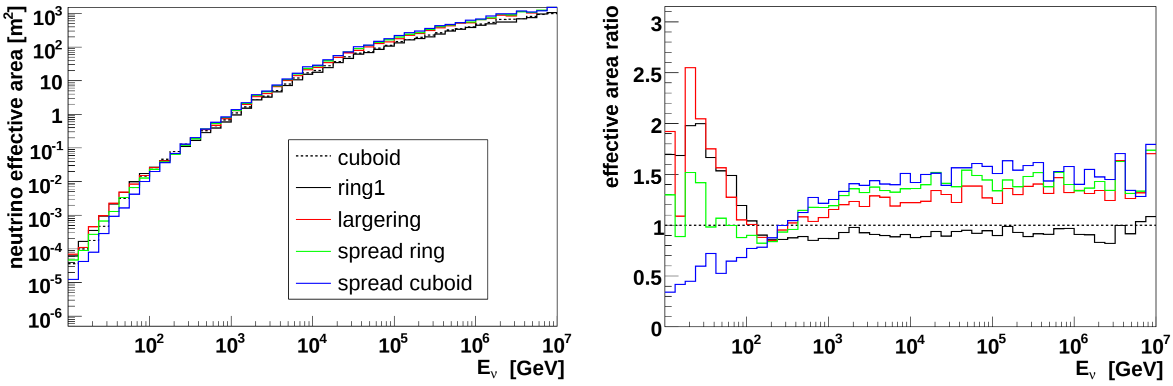

hit

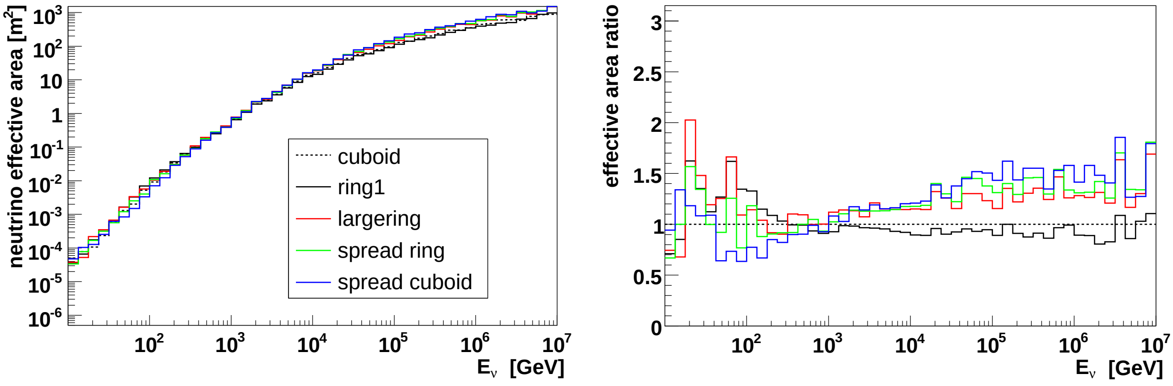

moderate

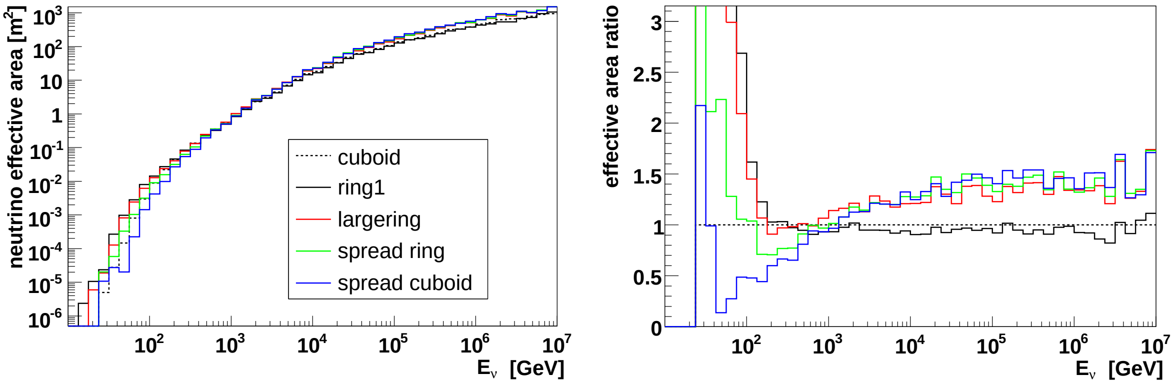

Figure 9.41: Neutrino effective areas and effective area ratios for detectors with increased volumes, for the *minimal*, *hit* and *moderate* criteria applied.

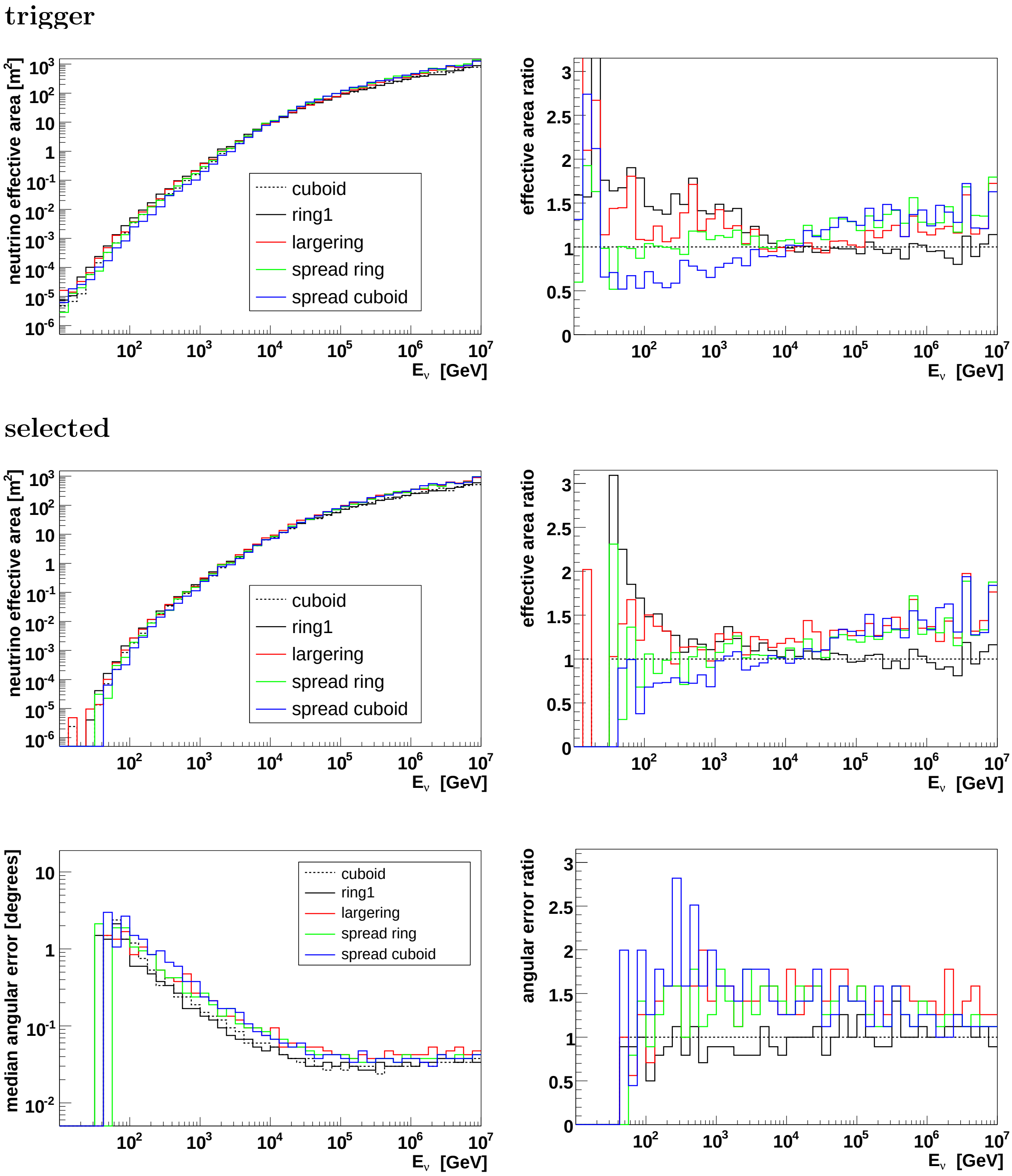
trigger

selected

Figure 9.42: Neutrino effective areas and area ratios with the *trigger* criterion applied (top) and for *selected* events (middle) for detectors with increased volumes. Angular resolution and resolution ratios for *selected* events (bottom).

minimal

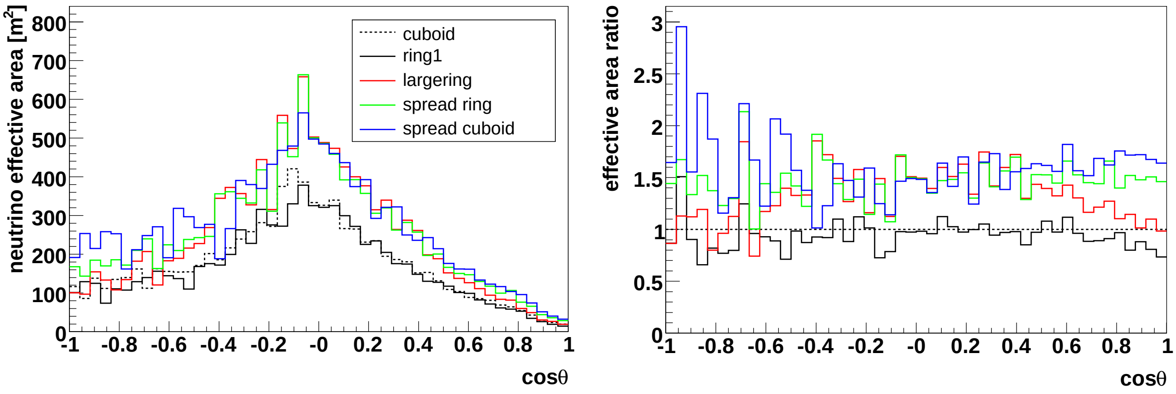

moderate

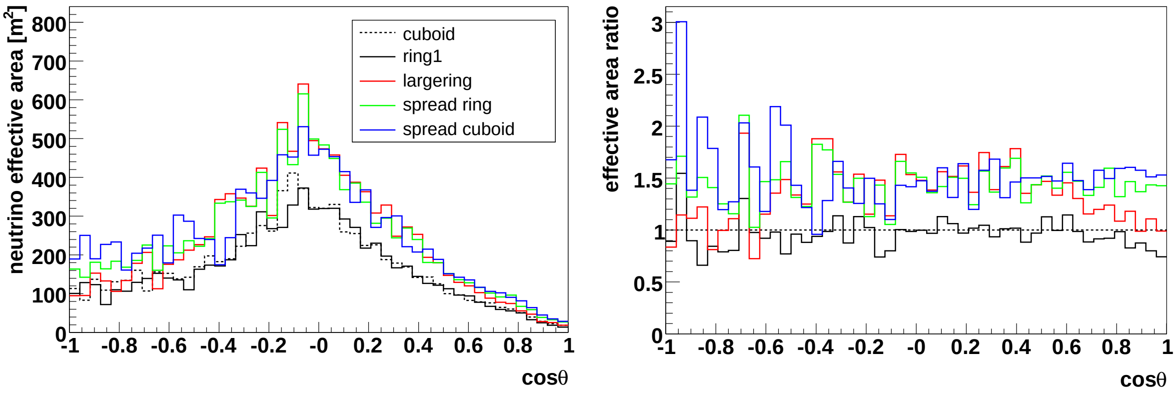

selected

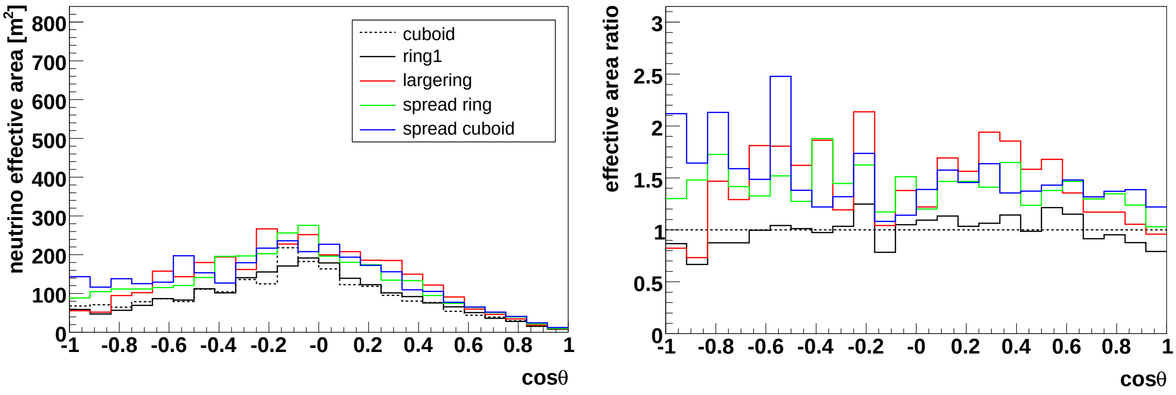

Figure 9.43: Neutrino effective areas and effective area ratios as a function of zenith angle for detectors with increased volumes, with *minimal*, *moderate* and *selected* criteria applied.

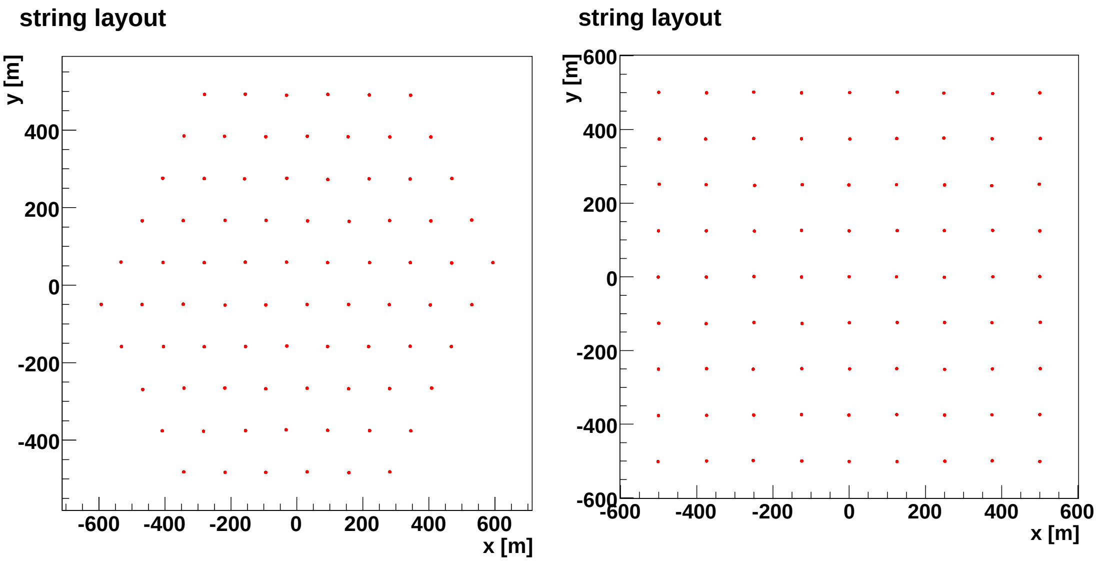

Figure 9.44: String layout of IceCube (left) and the ICCcube (right).

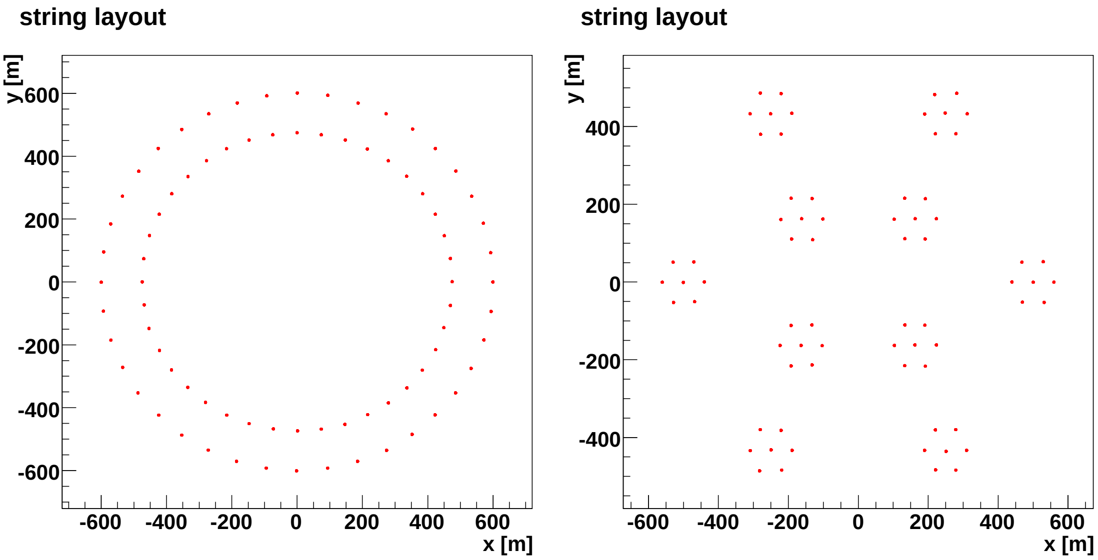

Figure 9.45: String layout of the ICCring (left) and the ICCcluster geometries (right).

9.5.1 Results for the IceCube comparable geometries

Neutrino effective areas and the ratios of the areas relative to the IceCube layout are shown in Figs. 9.46 and 9.47 as a function of neutrino energy. All of the ICC layouts have a larger effective area than the IceCube layout above 100 TeV for the *minimal*, *hit* and *moderate* criteria, the ring and the cube also at the *trigger* level. This is due to the simple fact that these geometries have a slightly larger instrumented volume. Therefore an enlarged version of the standard IceCube geometry with the same volume as the other ICC geometries was produced (with string distances of 134 m instead of 125 m). This layout, called km3IceCube, has effective areas very similar to those of the cube geometry at all selection steps. This shows that the arrangement (e.g. rectangular or hexagonal) of the strings does not influence the performance, as long as the distribution of the storeys is homogeneous and overall photocathode area and volume are similar. The second important observation is that the reconstruction algorithm does not work particularly well for these layouts. As with the single OM cuboid (see section 8.1), this is a consequence of the lack of local coincidences (as there are no coincidences with only one PM per storey). Even at the *trigger* level the event rates are very low. The general behaviour at the *minimal* and *moderate* levels is very similar. The effective areas of the ring and the cube are almost equal between 10 TeV and 10 PeV. Below this, the cube is a bit better, until at a few hundred GeV the ring has an advantage again (denser instrumentation). The effective area of the cluster is a bit worse than that for the ring and the cube, but below ∼1 TeV it starts to be massively superior. With the *hit* criterion applied this happens at higher energies around 10 TeV, the ring and the cube are comparable for energies below 100 TeV at this level. In the energy range between 1 TeV and 100 TeV the standard IceCube detector is comparable to the others, below it loses to the ring and the cluster, above it loses to the ring and the cube. At the *selected* level statistics are bad due to the inefficiency of the reconstruction algorithm for the storey type used. Nonetheless it can be seen that the cluster has a higher effective area in this case than the standard IceCube and ICCcube layout over the whole simulated range, in particular at medium and low energies ($<$ 100 TeV). The ring is also better at energies above a few TeV and comparable below. The IceCube, km3IceCube, and ICCcube geometries have similar effective areas. The behaviour of the angular resolution is similar to that of the effective areas. The cluster is the best at most energies, followed by the ring. The angular resolution of the IceCube layout is a bit better than the km3IceCube and the ICCcube geometry. Due to the low statistics for *selected* events more exact conclusions cannot be drawn.

The neutrino effective area as a function of the zenith angle is shown in Fig. 9.48. In principle the effective areas of ring, cluster and cube are better at all angles, except for upgoing events. Here the effective area of the cube drops a bit, while that of the ring decreases until it is comparable to that of the IceCube geometry. The area of the cluster drops more significantly to about 80% of the value for the IceCube layout. In the case of the ring and the cluster this is a consequence of the lower cross section area for vertical events. For *selected* events again statistics is too low to learn much from the result, although it seems that the cluster and the ring are better than the other geometries especially for up- and downgoing events, contrary to the results at other selection steps). This would hint on some reconstruction effect.

In principle the ICC versions of the cube, ring and cluster behave in the same way as for the standard geometries with MultiPMT cylinder storeys, which confirms the previous results. Except for the effect of the larger volume, the km3IceCube layout and the ICCcube geometry are very similar. The exact shape of the positioning of the strings (triangle or square) has little influence on the performance of the detector.

Section summary

- The relations between the different geometries is the same in the ICC and *candidate* cases.
- The exact shape of the positioning of the strings (triangle or square) has little influence on the performance of the detector.
- The reconstruction algorithm does not work well with single-PM storeys.

9.6 Conclusions

For an optimisation on the low energy part of the spectrum ($< 1\,\mathrm{TeV}$), clustered geometries can be used, but this comes at the price of performance losses at higher energies. In this context it should be noted that the energy reconstruction of track-like muon neutrino events at these very low energies is extremely difficult, a fact that makes the optimisation for these energies dangerous (as knowing the neutrinos energy is crucial for further analysis).

The proposed ring geometries produce results comparable to the homogeneous cuboid layout, but with some differences. The low-energy performance is increased because of the denser spacing of the storeys inside the rings volume. At higher energies the ring geometries are a bit worse due to the effect of the uninstrumented core (the hole in the middle) although the purity of the events and therefore the reconstruction probability is a bit higher inside the rings (their effective areas become very similar to the cuboid case at the *trigger* level and for *selected* events). A rectangular detector geometry using the same principles, the hollow cuboid, produces slightly better results than the rings. On the other hand, the main idea for the ring structures, the reduction of the number of strings necessary to fill the instrumented volume is implemented to a far greater effect in the cuboid variants that have less strings but more storeys per string. The *cuboid4* with only 144 strings (compared to the 484 of the standard cuboid) provides a similar performance at all selection steps, except for *selected* events (but this problem could be solved by a dedicated reconstruction algorithm). A similar attempt to further reduce the number of strings in the ring structures with the same method, the *densering* (or even the number of storeys as for the *thinring*), resulted in a significant loss of efficiency.

When attempting to increase the instrumented volume, the performance of the resulting detector model at high energies depends to a great extent on the geometric cross section area, whereas at low energies, the instrumented volume is more important. Of course the overall photocathode area is a further parameter with direct impact on the results. If the volume is doubled without also doubling the number of storeys, the effective

minimal

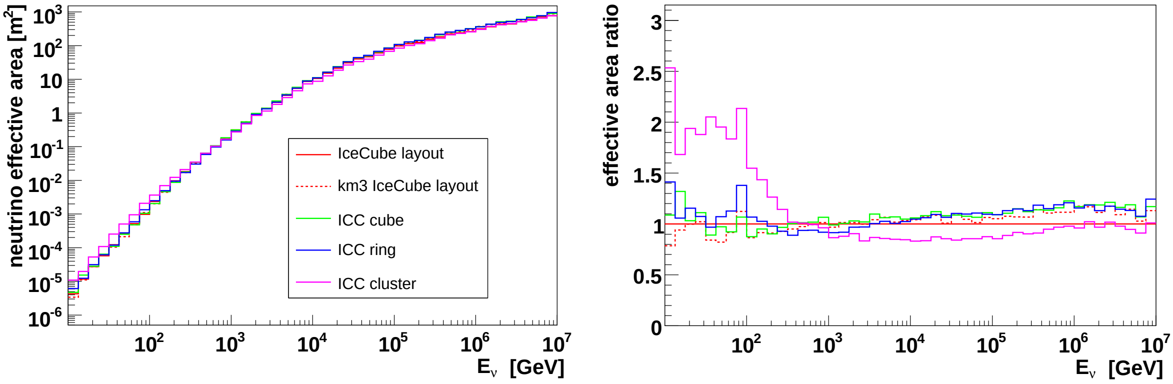

hit

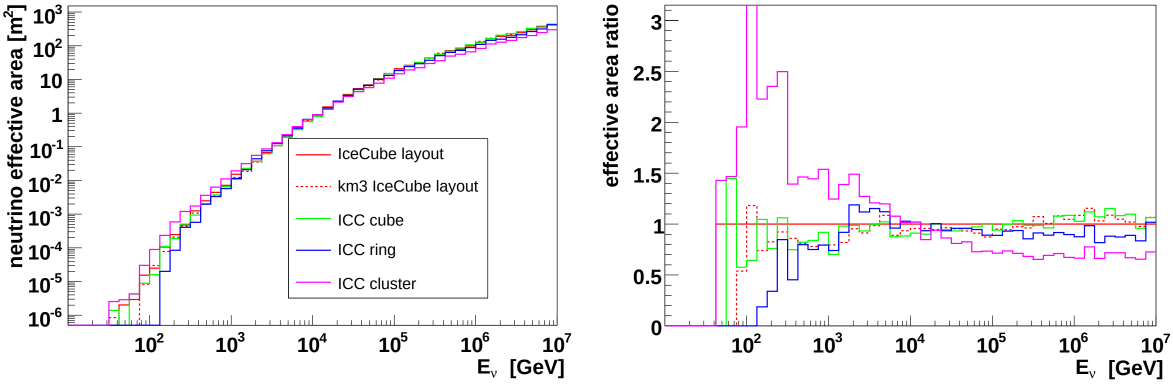

moderate

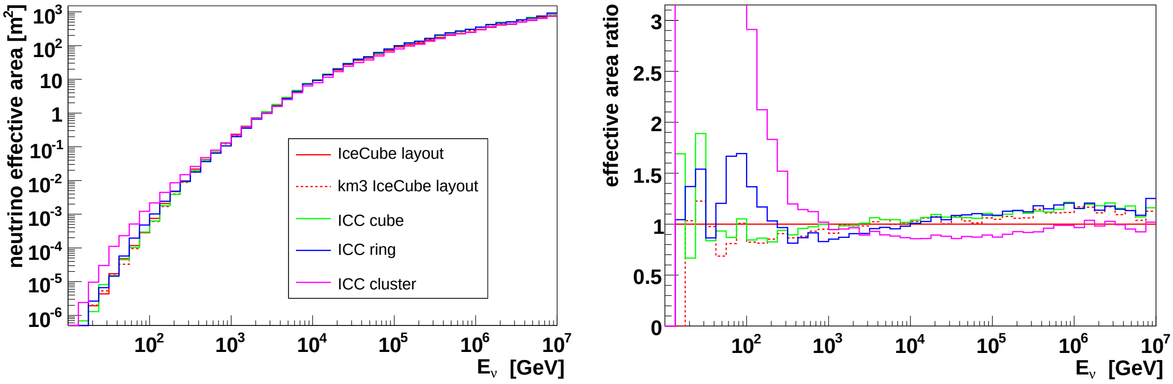

Figure 9.46: Neutrino effective areas and effective area ratios for the IceCube comparable geometries, for the *minimal*, *hit* and *moderate* criteria applied.

trigger

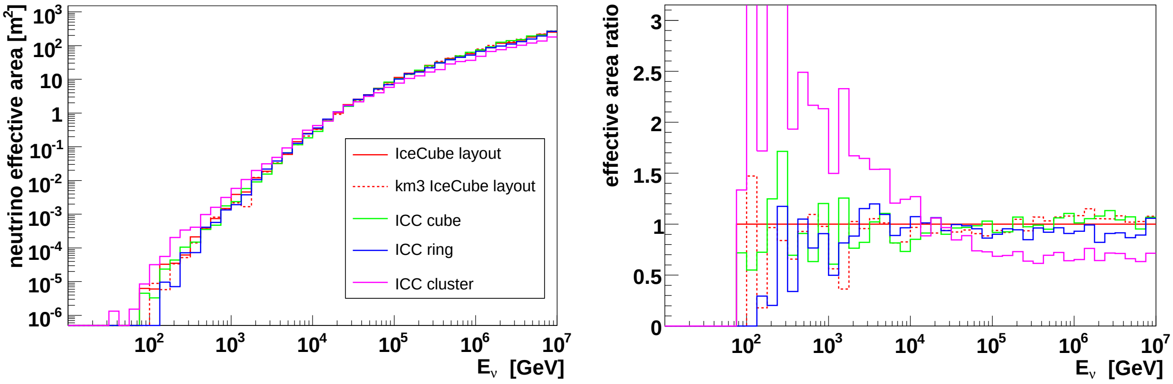

selected

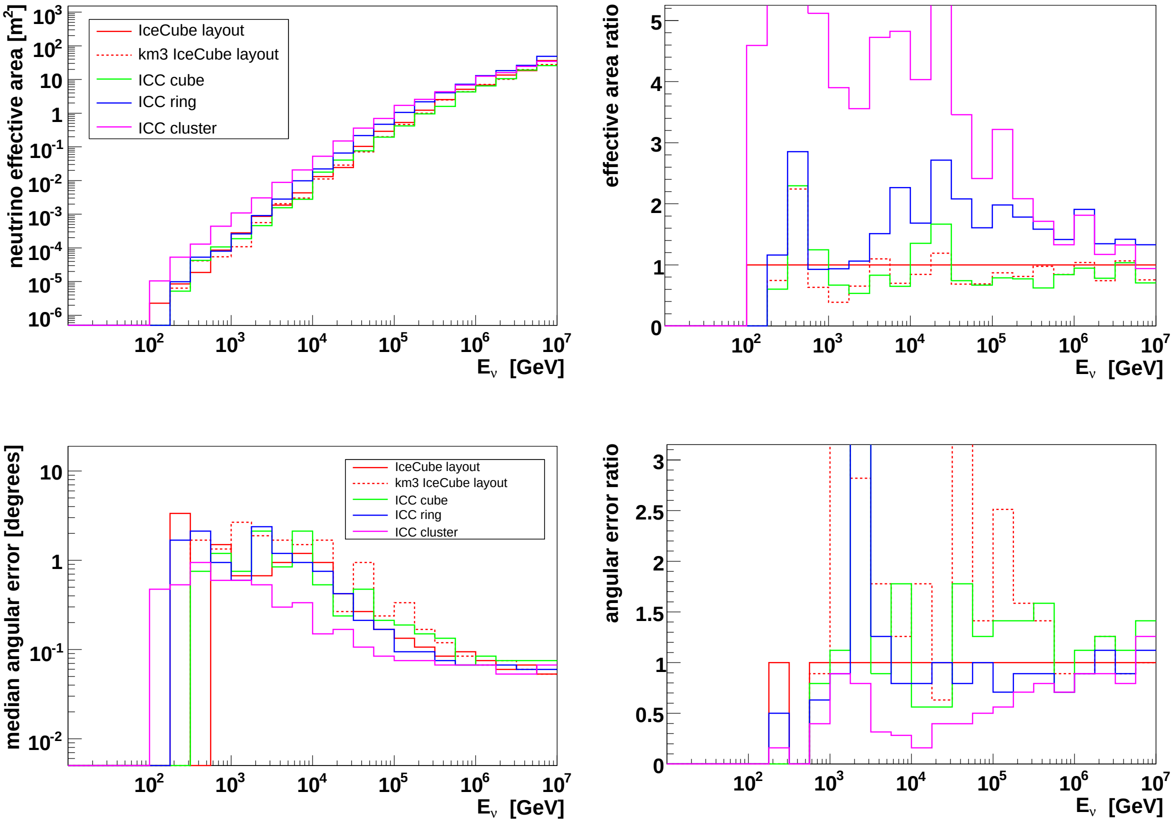

Figure 9.47: Neutrino effective areas and area ratios with the *trigger* criterion applied (top) and for *selected* events (middle) for IceCube comparable detectors. Angular resolution and resolution ratios for *selected* events (bottom).

minimal

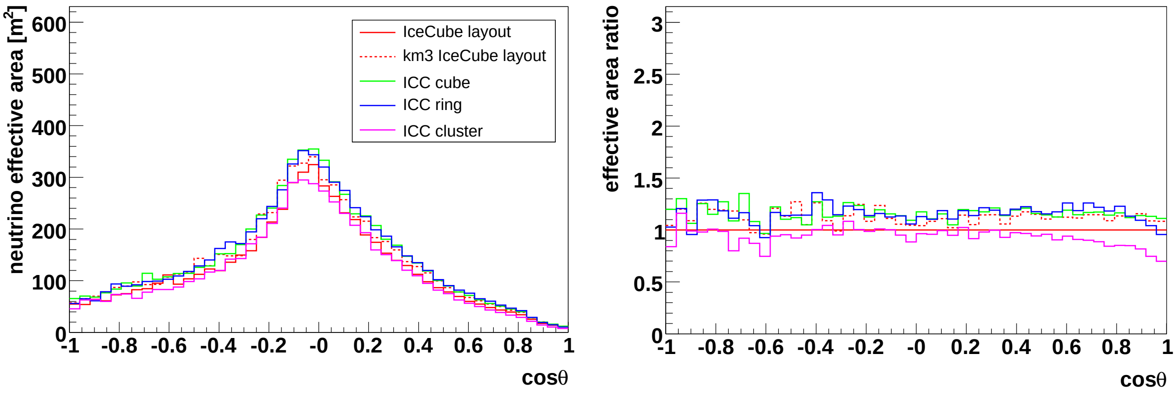

moderate

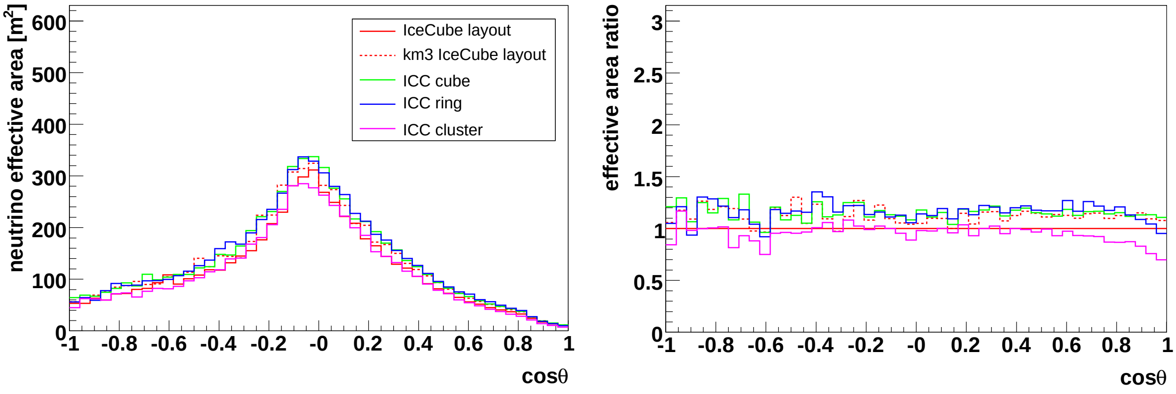

selected

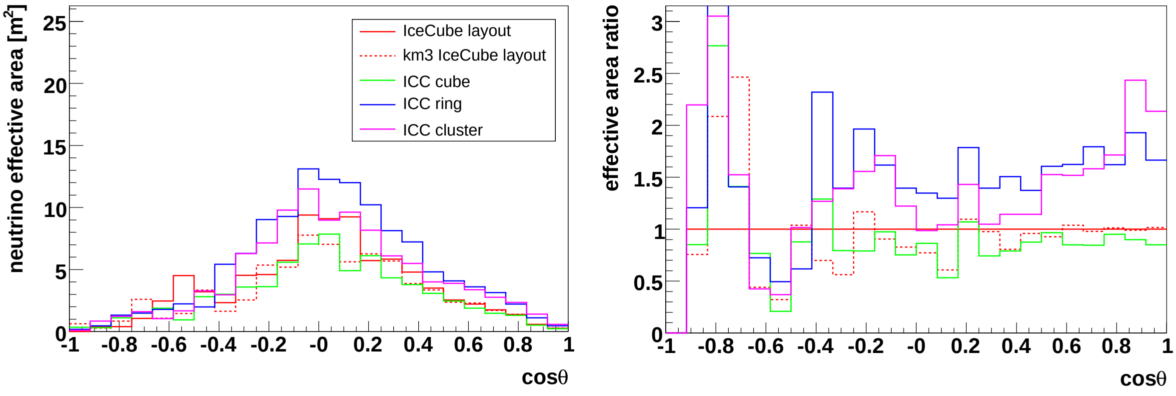

Figure 9.48: Neutrino effective areas and effective area ratios as a function of zenith angle for the IceCube comparable geometries , with *minimal*, *moderate* and *selected* criteria applied.

area increases at high energies due to the higher cross section area, but decreases at lower energies. This relates the desired volume of the detector with its energy threshold. If volume and number of storeys (and therefore photocathode area) are doubled, the effective area is more than doubled for very low energies and less than doubled at higher energies.

Considering these results, a detector with a geometry similar to the modified cuboids is probably the best choice. These layouts combine a good performance with a reduced number of strings.

9.7 The conclusion detector

The ultimate goal of this work is to find the optimal detector layout for further studies to be based on. It should combine the best possible efficiency with a small number of structures. From section 8.4 it appears to be a good choice to use the MultiPMT sphere stories with only one hemisphere instrumented with 21 3" PMs and increase the number of storeys per string. The cuboid in the corresponding *candidate* layout showed results, that were slightly better than for other photodetection setups with comparable photocathode area. From section 9.6 it is concluded that the cuboid layouts with reduced numbers of strings compensated by more storeys on the strings are the best option to reduce the number of structures. As the *cuboid4* is a bit less efficient at energies in the 10 TeV range, the use of the *cuboid3* layout is a good compromise. By combining the two results it should be possible to design a detector with a good performance that only requires 225 strings. The resulting layout, called the conclusion detector in the following, has 36 storeys per string with distances of 16.5 m. The distance between strings in the grid is 95 m. The simulation results for this detector model are shown in Figs. 9.49, 9.50 and 9.51. They are compared to the *candidate* cuboid with 21 PM sphere storeys (same storey type but more strings), the cuboid with cylinder storeys (reference detector for geometries) and the *ring1* geometry with cylinder storeys (different concept for the reduction of the number of strings).

The effective areas for the *minimal*, *hit* and *moderate* cases are better or at least comparable to the other detector models. At the *trigger* level the ring is better below a few TeV, which is a consequence of the lower average storey distance in the ring (including distances between storeys on neighbouring strings). At the *selected* level the *candidate* cuboid with the same type of storeys is clearly better.

The angular resolution of the conclusion detector is better than for the ring and the standard cuboid, and similar to the one of the *candidate* cuboid with the same storey type. At the *minimal* and *moderate* stage, the efficiency is better for upward going events, because most of the PMs are pointing downward. This holds for *selected* events, although the efficiency drops slightly for downward going neutrinos. This might be an effect of the reconstruction algorithm, which is optimised for a downward looking detector.

It appears that the proposed conclusion detector is a promising combination of efficiency and feasibility.

minimal

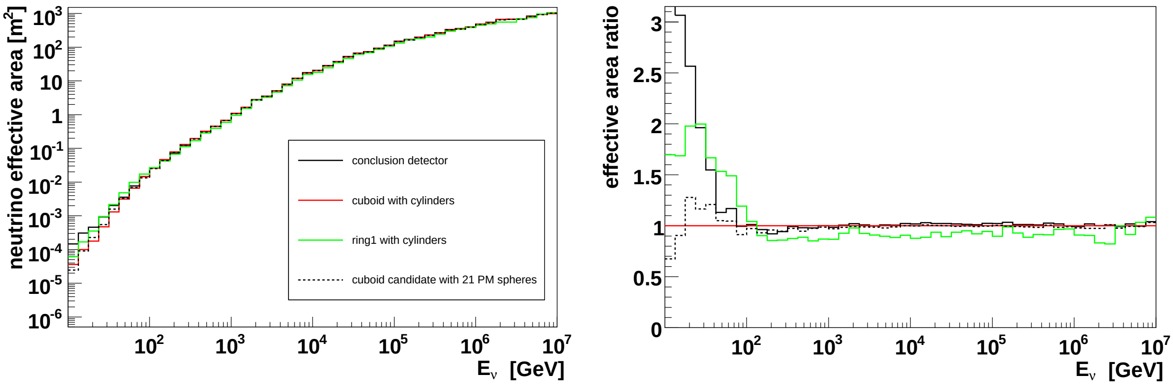

hit

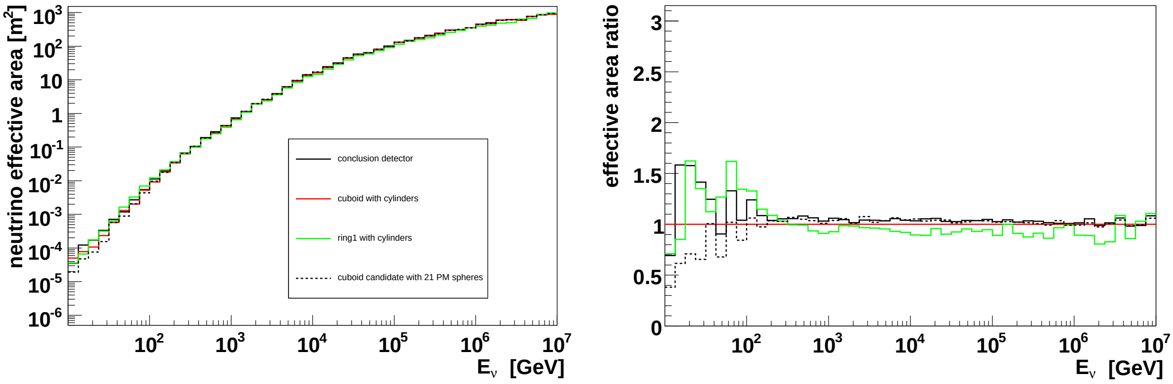

moderate

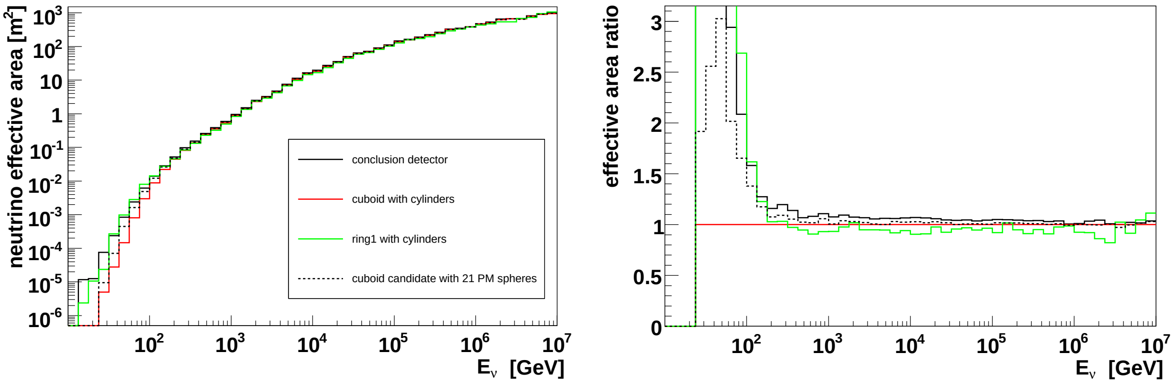

Figure 9.49: Neutrino effective areas and effective area ratios for the conclusion detector, for the *minimal*, *hit* and *moderate* criteria applied.

trigger

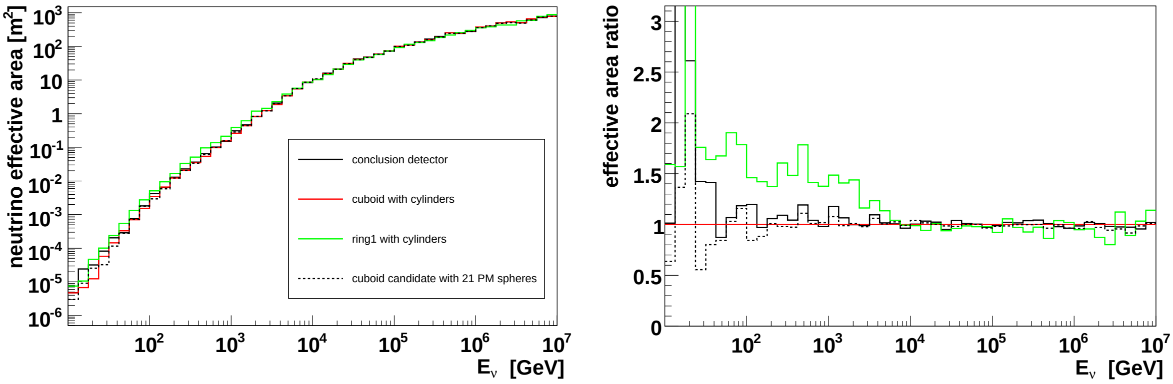

selected

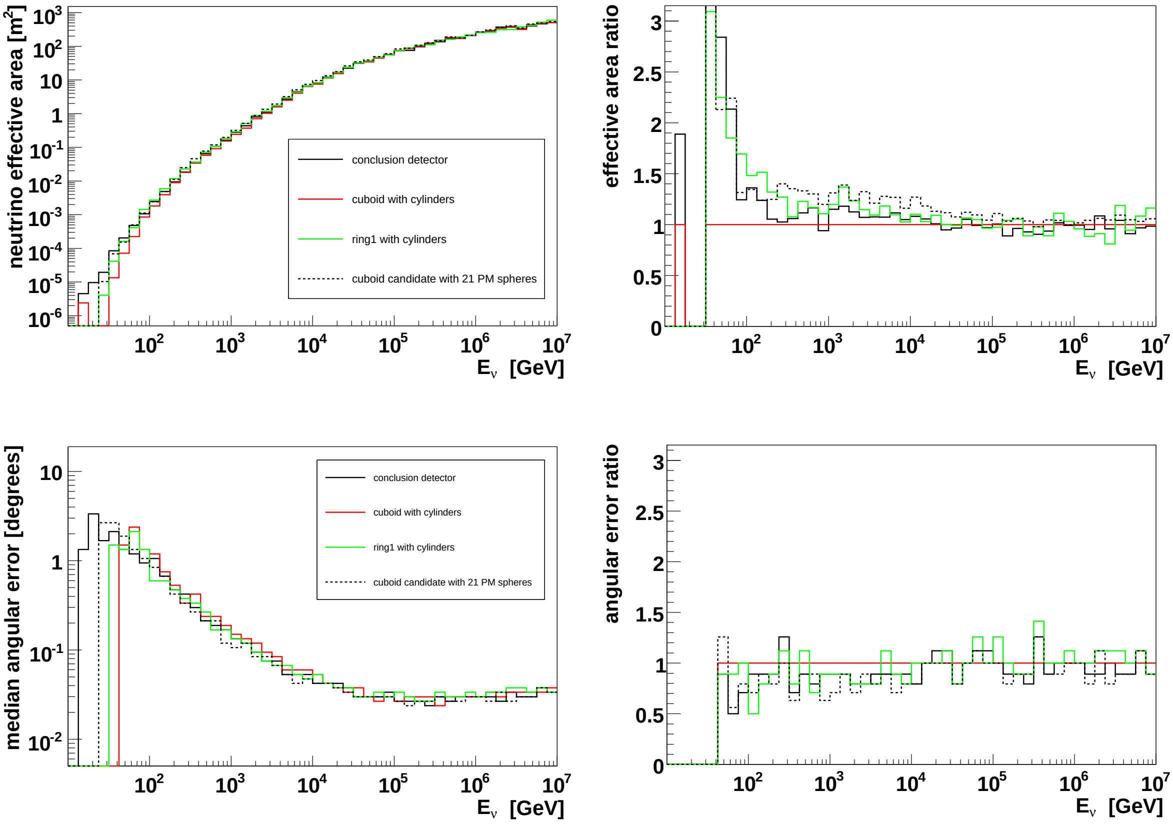

Figure 9.50: Neutrino effective areas and area ratios with the *trigger* criterion applied (top) and for *selected* events (middle) for the conclusion detector. Angular resolution and resolution ratios for *selected* events (bottom).

minimal

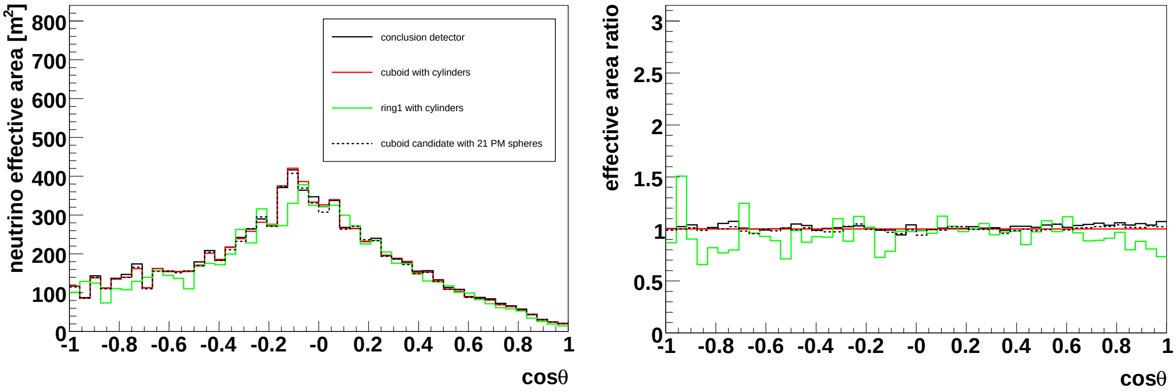

moderate

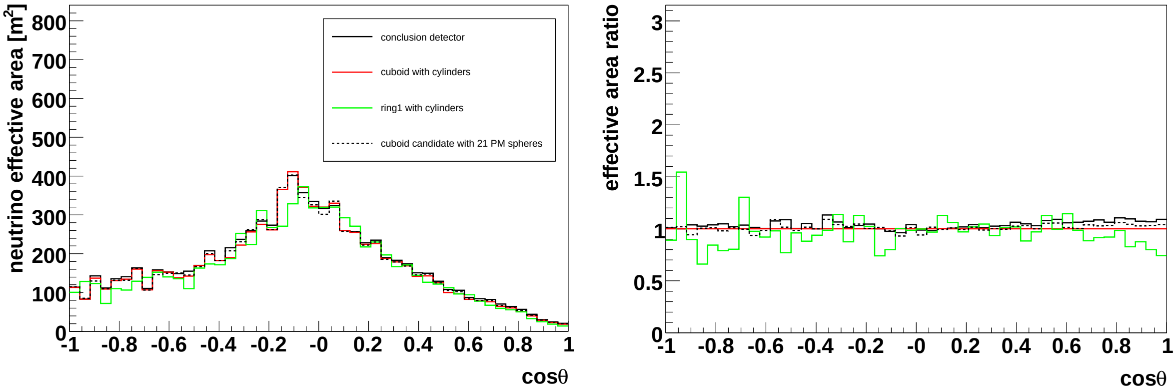

selected

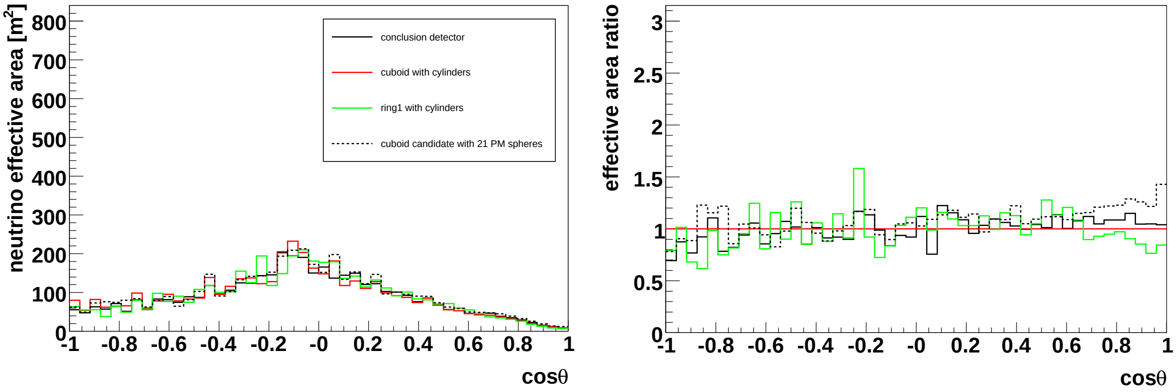

Figure 9.51: Neutrino effective areas and effective area ratios as a function of zenith angle for the conclusion detector with *minimal*, *moderate* and *selected* criteria applied.

Chapter 10

General analysis

This chapter summaries the results of studies that are not directly concerned with the simulation of candidate detectors for the KM3NeT project. In the first section, some of these candidates are compared to the ANTARES detector simulated under exactly the same conditions. This provides a 'sanity check' for the simulation results. The following section summaries the experiences with the reconstruction algorithm used, that have been acquired during the course of this work. Additionally, a very general study of the influence of string and storey distances on the performance of a detector is presented in the last section of this chapter.

10.1 Comparison with ANTARES

In the previous chapters potential candidate detectors for a future KM3NeT neutrino telescope were simulated and compared. In order to provide a sanity check on the absolute values of the effective areas, some of the KM3NeT candidate detectors were compared to a well-known neutrino telescope, the ANTARES detector. Additionally this provides a way to study possible reconstruction biases. As the reconstruction software was developed and optimised for ANTARES, it is expected to be most efficient for this layout. By comparing the ratios of the effective area at different selection steps and for the reconstructed events the extent of this bias can be analysed. In the following a rough estimate for the expected result of the comparison between ANTARES and the KM3NeT configurations is presented.

At high energies, as was mentioned before, the geometric cross section area of a detector is a very important factor. The cross section area 'seen' by an incident neutrino depends on its direction of incidence. However, it is a simplifying generic assumption that a cubic kilometer detector has a cross section area of one square kilometer, averaged over all directions. The ANTARES layout has a far larger cross section area for horizontal muons than for vertical ones, as it is shaped like a long cylinder. As was shown before, muons incident from the horizontal direction dominate the effective areas, as they have a large potential interaction volume and do not suffer absorption in the Earth at high energies. Therefore, it is a reasonable approximation that the horizontal cross section area of ANTARES, which is of the order of $0.1\,\mathrm{km}^2$ will dominate this comparison. As a consequence, the effective areas of the KM3NeT candidates at high energies should be about ten times larger than for ANTARES. Towards lower energies the properties of the photodetection system (PM properties, storey layout) and the size of the instrumented volume of the detector become more important. Passing muons still have very long track lengths at energies in the TeV range, but the light output is lower. Because of this the number of storeys that have a chance to be hit (which is proportional to the density of instrumentation) as well as the light detection and noise reduction capability (PMs, storey layout) start to dominate the performance. The volume of the KM3NeT candidate detectors is almost exactly one cubic kilometer, while that of ANTARES is approximately $0.03\,\mathrm{km}^3$, resulting in an expected performance factor of about 30. At the lowest energies, where the muon tracks start to become much shorter than the detector dimension, the density of the instrumentation gains in importance. Because of the cylindrical shape of ANTARES the ratio of the cross section area of a homogeneous cubic kilometer detector to the ANTARES area, is lower for horizontal events and larger for vertical muons.

The angular resolution in ANTARES is expected to be worse than for the cubic kilometer detector, as the average leverarm length for a given event is smaller. The candidates effective area as a function of the zenith angle should be better for vertically incident muons.

For this comparison, the ANTARES detector was simulated and analysed under the same conditions as the KM3NeT detector models.

10.1.1 Comparison of the simulation results

The Figures 10.1, 10.2 and 10.3 show the effective areas as functions of energy and zenith angle as well as the angular resolution of the cuboid detector equipped with ANTARES and MultiPMT cylinder storeys and of ANTARES. In the corresponding ratio plots all histograms were scaled to the results for the ANTARES detector.

At all selection steps, except at the *trigger* level, the cubic-kilometer detectors have an effective area eight to ten times larger than that of ANTARES at highest energies. At the *trigger* level they are ten to 15 times better. Towards lower energies this factor increases and reaches its maximum between 100 GeV and 1 TeV for the *minimal*, *hit* and *moderate* criteria. The cuboid with ANTARES storeys reaches factors between 20 (at *hit* level) and 30 (at *minimal* level), while the cuboid with cylinder storeys reaches more than 30. At the *trigger* level the effective areas of the candidate detectors are much better (factor 15 to 25) for all energies above 300 GeV. This hints at a higher purity for the larger detectors. For *selected* events the area of the candidates is only 15 to 20 times larger in the energy range of 1-10 TeV, which is interpreted to be a consequence of the reconstruction process, which apparently works better for the standard ANTARES detector. The cuboid equipped with cylinder storeys is clearly better than the cuboid with ANTARES storeys in this energy range at all levels, except for *selected* events, which further points towards a slight reconstruction bias toward the ANTARES storey layout. At energies below 100 GeV the difference is smaller, as the denser instrumentation of ANTARES starts to compensate for the smaller volume.

The angular resolution for the large detectors is a factor three better than that of ANTARES at energies above a few hundred GeV. Below this energy it becomes similar to ANTARES. At the low-energy end ($E <$100 GeV), the angular resolution is dominated by kinematics resulting in a similar performance for all detectors. The effective area of ANTARES compared to the cuboids is a factor of 15 to 20 smaller for vertically incident muons at all selection steps, and only a factor ten for horizontal events (about a factor of 7 to 8 for *selected* muon events, see Fig. 10.3).

The relations between the cuboids and ANTARES fit very well to the expectation in all the scenarios studied. There is slight evidence that the reconstruction process is biased towards ANTARES-like structures.

10.2 Experiences with the reconstruction algorithm

In this section observations are presented that were made when using the modified ANTARES reconstruction algorithm for cubic kilometer detectors. Some of the conclusions may be obvious, but they still might help in the creation of a dedicated KM3NeT reconstruction code.

The general setup and functionality of the reconstruction algorithm used in this work is described in section 5.5. As examples of cubic kilometer detectors, the cuboid with ANTARES, MultiPMT cylinder and ANTARES(20") storeys was used (to account for the different photodetection layouts) in addition to the *ring1* and *cluster1* geometries with ANTARES storeys (to account for the different classes of detector geometries).

10.2.1 Reconstruction efficiency

In order to successfully reconstruct an event, the algorithm needs at least 10 hits, and at least 2 hits that have an amplitude above two photo electrons or are part of a local coincidence. In order to check the efficiency of the algorithm it is straightforward to compare the number of events that fulfill these criteria with the number of events that are reconstructed. Another option, maybe more interesting, is the comparison of the number of reconstructed events with the number of events that fulfill the minimum hit criteria with hits produced by the muon (i.e. signal hits). All these events should be reconstructed by the algorithm. In Fig. 10.4 this last definition of the reconstruction efficiency is used to compare the different cubic kilometer candidates and the ANTARES detector. Also shown is the efficiency of the selection, i.e. the fraction of events that are reconstructed with an angular error of less than five degrees.

For the ANTARES detector, the reconstruction efficiency is close to unity, or at least above 90% for all energies. The cuboid with 20"PMs has a very similar efficiency, while for the cluster detector the reconstruction is slightly less efficient. The efficiency for the cuboids with cylinder and ANTARES storeys is a bit lower than for the other detectors above 100 TeV and drops drastically to less than 70% at a few hundred GeV. The efficiency for the cuboid with ANTARES storeys continues to decrease towards lower energies, while that of the cylinder-equipped cuboid starts to rise again (up to 90% at the lowest energies). The ring geometry with ANTARES storeys has an efficiency between the cluster and the cuboid equipped with the same storey type.

minimal

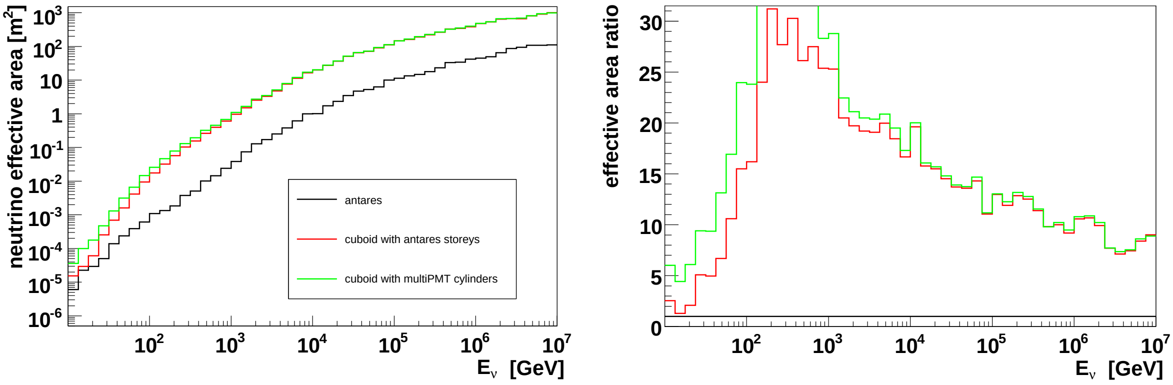

hit

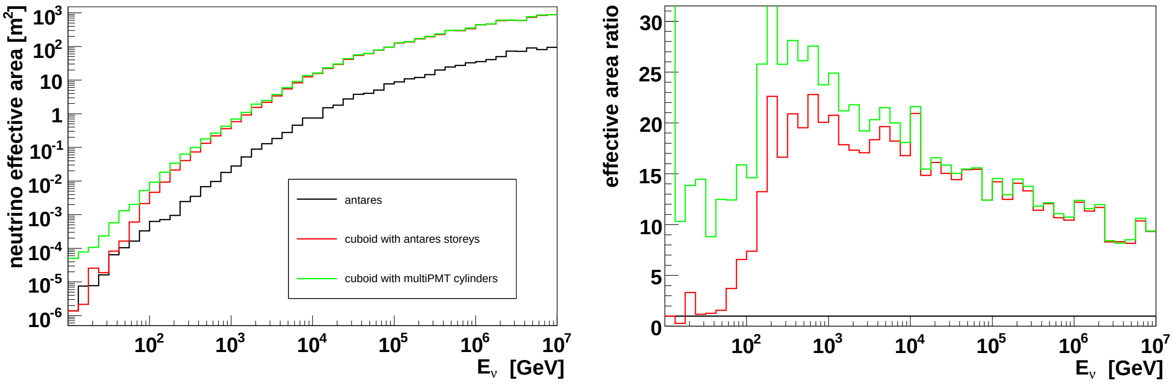

moderate

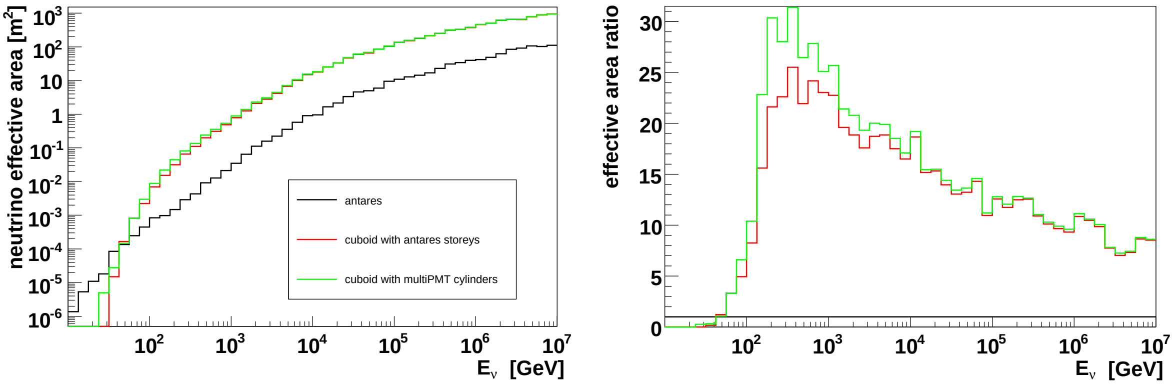

Figure 10.1: Neutrino effective areas and effective area ratios for the cuboid with ANTARES and MultiPMT cylinder storeys and the ANTARES detector, for the *minimal*, *hit* and *moderate* criteria applied.

trigger

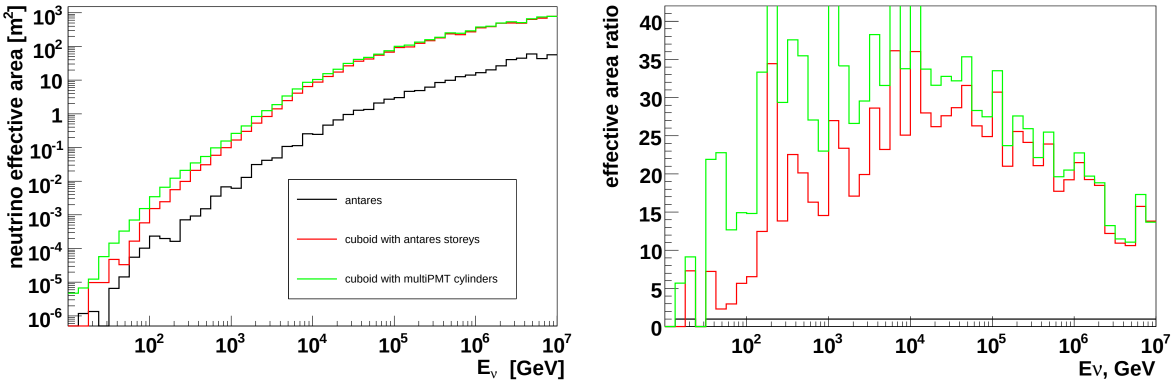

selected

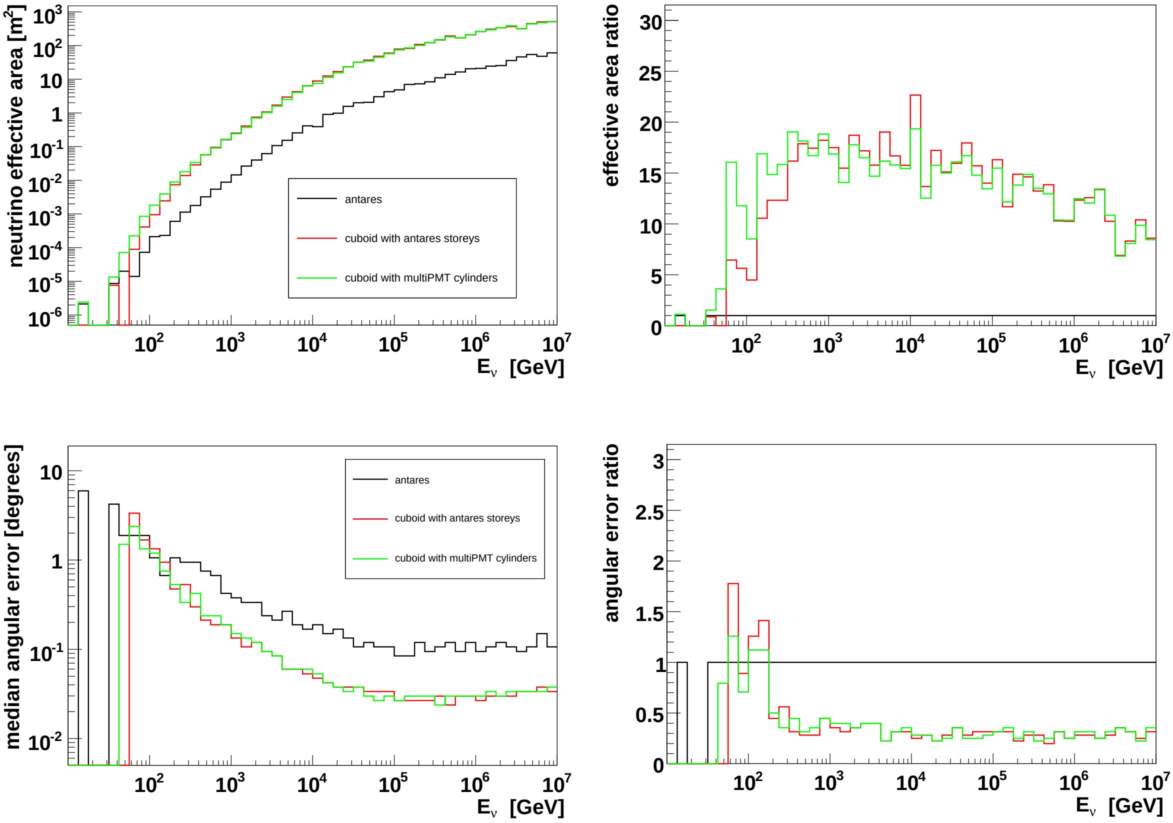

Figure 10.2: Neutrino effective areas and area ratios with the *trigger* criterion applied (top) and for *selected* events (middle) for the cuboid with ANTARES and MultiPMT cylinder storeys and the ANTARES detector. Angular resolution and resolution ratios for *selected* events (bottom).

minimal

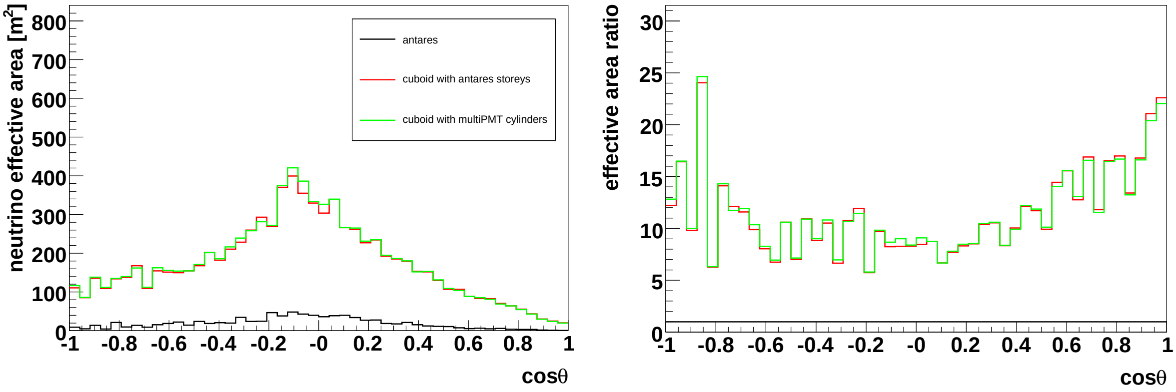

moderate

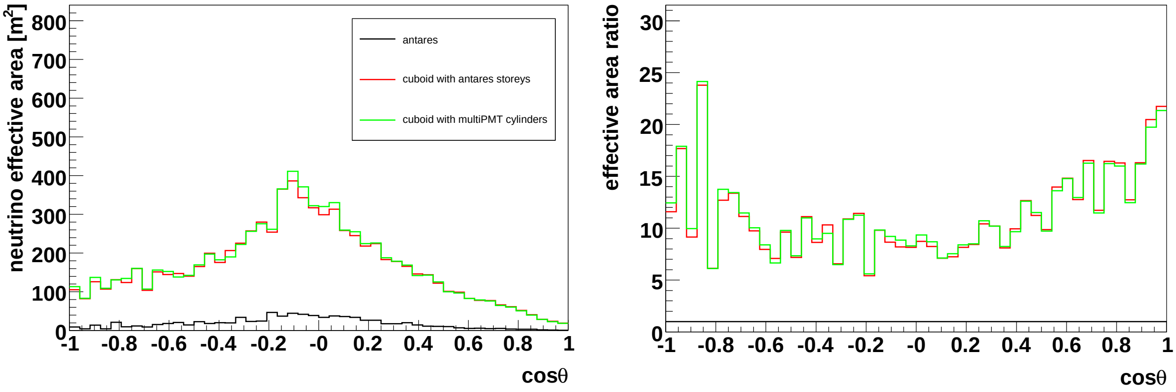

selected

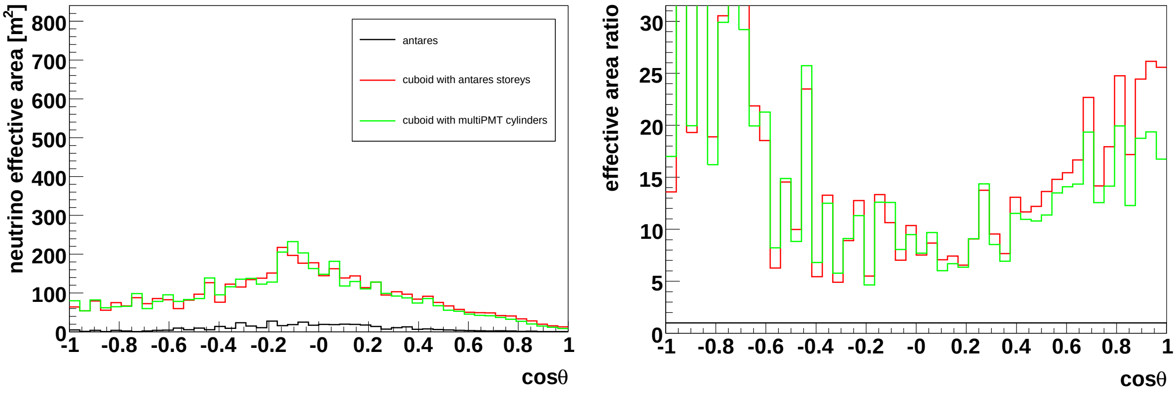

Figure 10.3: Neutrino effective areas and effective area ratios as a function of zenith angle for the cuboid with ANTARES and MultiPMT cylinder storeys and the ANTARES detector, with the *minimal*, *moderate* and *selected* criteria applied.

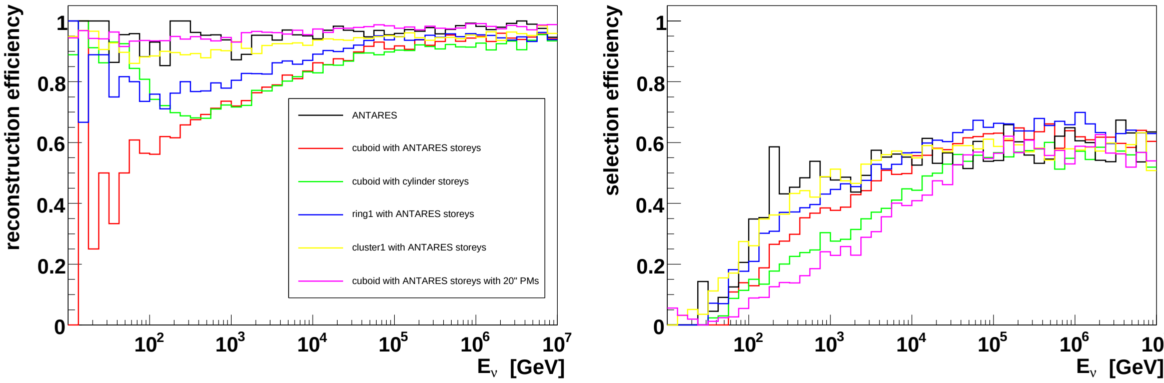

Figure 10.4: Left: Reconstruction efficiency for example candidate detectors and ANTARES. Right: Selection efficiency.

The selection efficiency is similar for all detectors at energies above 30 TeV. Below the detectors with ANTARES storeys are clearly better. Their efficiencies appear to depend on the storey distances, with ANTARES being the best, followed by the cluster, the ring and finally the cuboid. For the detectors with other storey types, the cylinder version is a bit better in this energy range. The reasons for this behaviour are difficult to isolate, as the general properties of the detector and storey layouts mix with reconstruction effects. The fact that the efficiency is close to unity for ANTARES implies that the algorithm is very well optimised for it. The fact, that the efficiency for other detectors is lower implies that most probably this reconstruction algorithm is not optimal for KM3NeT. The behaviour of the selection efficiency also strongly hints to a slight bias towards ANTARES-like structures.

10.2.2 The most common reasons for reconstruction failure

The next obvious question is why the reconstruction fails on events, that should in principle be reconstructable. In order to study this, the failure codes (see chapter 8) were investigated. Each failure code corresponds to a specific reason for the failure of the reconstruction process. Distributions of the failure codes for the example detectors, for events that produce 10 signal hits and 2 signal coincidences or large hits (thus meeting the reconstruction requirements), are shown in Fig. 10.5.

As can be seen from the failure code distributions, the most common reason for reconstruction failure is 'not enough hits for intermediate fit' corresponding to a failure of the intermediate fitting process, pointing to problems with the prefit. If the prefit is bad (points in the wrong direction), the starting point tracks can not be associated with the actual signal hits, resulting in the minimum hit number criterion not being met. This is obviously only a minor problem for the ANTARES layout, but for other detectors, especially the cuboid with cylinders, this has dramatic effects.

The effect might be related to the purity of the events. In the energy region where the efficiency of the cuboid is low, the purity of coincidences (used for the prefit) is also

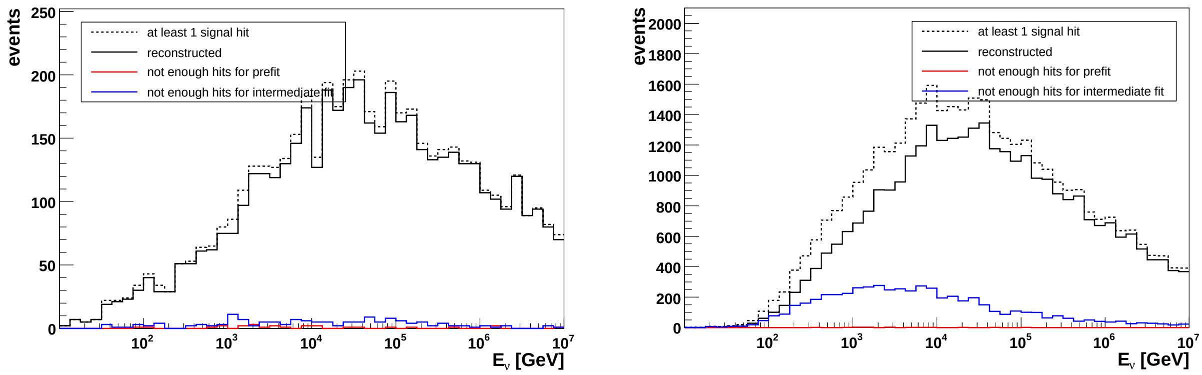
ANTARES

cuboid with ANTARES storeys

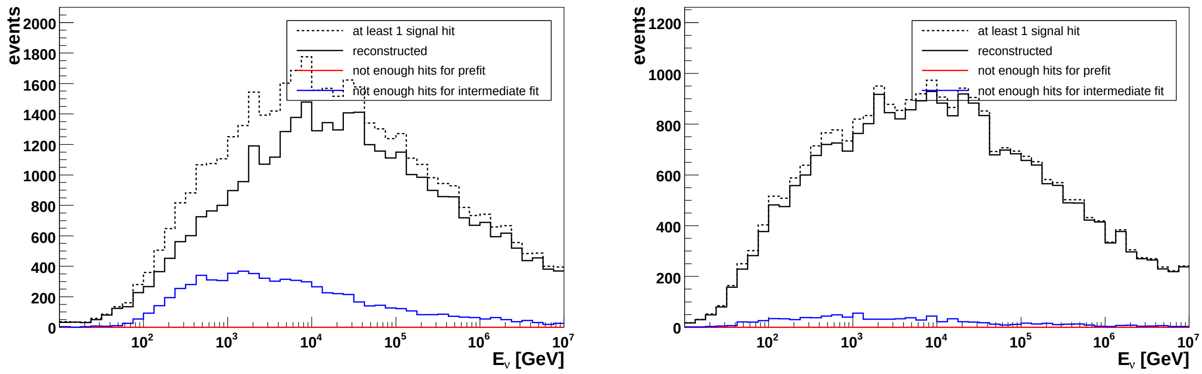
cuboid with cylinder storeys

cuboid with 20"PM ANTARES storeys

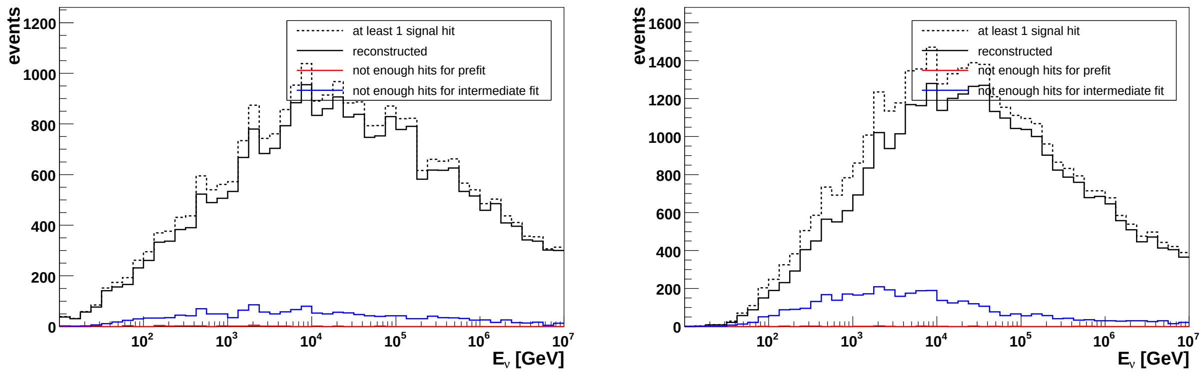
cluster1 with ANTARES storeys

ring1 with ANTARES storeys

Figure 10.5: Distributions of the reconstruction failure codes for the example detectors. Left column from top to bottom: ANTARES, cuboid with cylinder storeys, *cluster1* with ANTARES storeys. Right column from top to bottom: Cuboid with ANTARES storeys, cuboid with ANTARES storeys and 20"PMs, *ring1* with ANTARES storeys.

low, increasing the chance for a noise hit in a fake coincidence to spoil the prefit results. So the prefit plays a key role in the reconstruction process.

10.2.3 On the importance of the prefit

In order to illustrate the importance of the outcome of the prefitting procedure as an input for the following reconstruction steps, the code was modified to be able to use the Monte Carlo 'truth' information instead of the prefit. The effective areas (as a measure for the efficiencies) were compared for the case of a normal prefit and the prefit substituted by the true MC data (corresponding to a 100% efficient prefit) for *selected* events. These results are displayed in Fig. 10.6.

For all detectors the results with the Monte Carlo prefit are obviously much better. The amount of this increase is similar for ANTARES, *ring1* and *cluster1* with ANTARES storeys. The gain for the cuboids, especially the one with cylinder storeys is significantly larger.

The performance of the reconstruction for detectors equipped with MultiPMT storeys can thus be massively increased by either implementing a better noise suppression method and/or an optimised prefit strategy.

10.2.4 Conclusions for the reconstruction

This section only summaries some observations and experiences with the reconstruction algorithm. Nonetheless these experiences strongly hint at a bias toward ANTARES-like structures. This is of course no surprise, as the algorithm was designed and optimised for ANTARES.

It might be possible to tune the parameters used in the algorithm or even change the likelihood functions to better fit the properties of the different cubic kilometer detector models considered, but this is beyond the scope of this work. The better solution for the future is most probably to invest the effort and develop dedicated reconstruction software optimised for the challenges of a cubic kilometer detector.

10.3 Systematic studies on the detector geometries

This section summarises results of a study of the influence of the distances between the storeys on the performance of a detector. For this the dependence of the effective area on the distances between the strings and the storeys on a string was studied for the standard homogeneous cuboid, the *ring1* and the *cluster1* (equipped with cylinder storeys).

The question is where the increase of the instrumented volume is canceled by the loss of efficiency caused by interactions not recorded due to the sparse instrumentation. The expected effect is an increase of effective area at high energies, where the increased volume (and therefore increased cross section area) has the biggest effect, and a decreased effective area at low energies. Some of the resulting detector geometries are of course completely unfeasible. However, the intention of this section is to study general dependencies of parameters and not to find candidate detectors for KM3NeT.

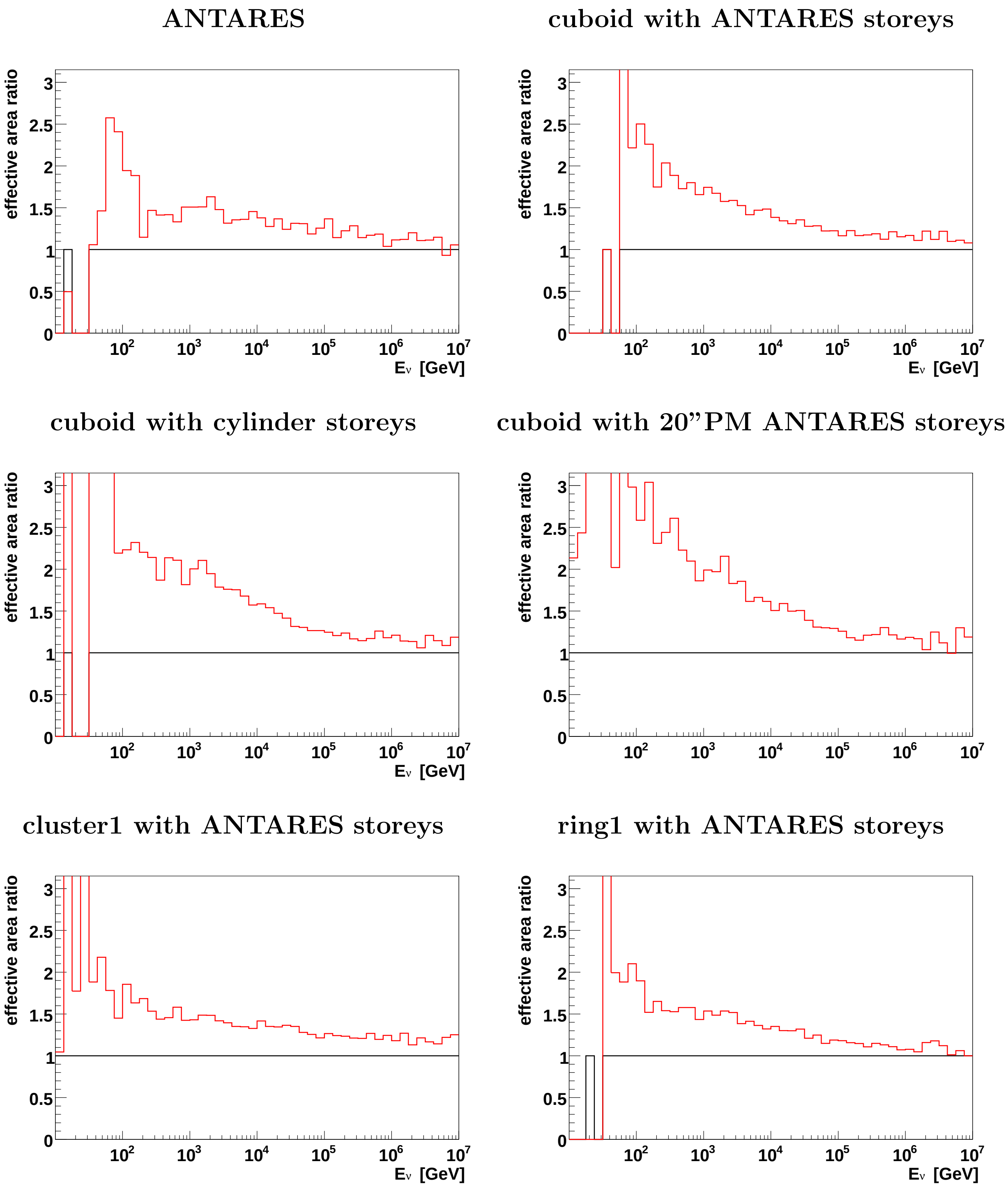

Figure 10.6: Comparison of the reconstruction efficiencies using the prefit (black) , and the true Monte Carlo information instead of the prefit (red). Left column from top to bottom: ANTARES, cuboid with cylinder storeys, *cluster1* with ANTARES storeys. Right column from top to bottom: Cuboid with ANTARES storeys, cuboid with ANTARES storeys and 20"PMs, *ring1* with ANTARES storeys.

In order to reduce the number of figures, only ratio plots are presented in this section.

10.3.1 Cuboid detector

New versions of the cuboid geometry (see Fig. 8.1) with string distances varying between 80 and 200 m in 20 m steps were produced and simulated. For the detector with a string distance of 80 m, three different versions with storey distances of 40, 60, and 80 m were simulated.

The outcome of the simulation for the cuboid detector with different storey distances is shown in Fig. 10.7 and the left column of Fig. 10.8. The ratios are given relative to the standard cuboid (string and storey distances 63 m). At all selection steps, the performance of the detector with the largest storey distance is about 50% better than the standard cuboid at high energies and worse to a varying extent at low energies. The detector with 60 m storey distance is only 25% better at high energies, but not quite as bad at low energies, while the cuboid with 40 m between storeys on a string is about 10 to 20% better at high energies and comparable (even better in the *trigger* case) at low energies. The difference between the selection steps is the energy region of the transition between the 'high' and 'low' energy behaviour. For the *minimal*, *hit* and *moderate* criteria it is between 100 GeV and 1 TeV. In the *trigger* case it is at 10 TeV and for selected events a bit lower at a few TeV. The angular resolution behaves in the same way. The cuboid with 80 m is the best at high energies (where it is comparable to the standard cuboid) followed by the 60 m version and then the short-stringed detector. Below a few TeV this relation turns around (now the 80 m version is the worst), although all three have about 50% higher median errors than the standard detector. Regarding the zenith angle dependence (see Fig. 10.8), the detectors with lower storey distances are better for vertical events than for horizontal events. These geometries have a lower cross section for horizontal events, as the strings are shorter and the detector therefore less high. This is combined with the effect of the denser instrumentation a vertical event sees in this case. The detector with equal string and storey distances is pretty uniform as is the standard cuboid.

For the modified string distances the behaviour is qualitatively the same, but the effect is larger. With increasing string distance, the effective area increases at high energies and decreases at low energies. This effect varies between an increase of 10% at high and a decrease of 10 to 20% (depending on selection step) at low energies for a string distance of 80 m and a factor of 4 to 5 at high and decrease of 50% or more at low energies for the maximum string distance considered. The crossover energy, where the area starts to exceed the one of the comparison detector, rises with the selection steps and also with the increasing string distance. The reason for this behaviour is the same as for the storey distance variations. Increased distance results in increased volume (or cross section area) and larger average distances between storeys. The effect is stronger because an increase in string distance increases the dimension of the detector in 2 dimensions, while an increase of the storey distance only increases the dimension in the z-direction.

At high energies the angular resolutions of all detectors are similar, but quickly spread towards lower energies. Here the resolution becomes clearly worse with increasing string distance (by a maximum factor of two to three). An increase of the volume in principle increases the potential lever arm length, resulting in a better resolution, but obviously this is more than cancelled by the lower density of the instrumentation.

The zenith-dependent effective area of the detectors with lower string distances is comparable to the standard cuboid. With increasing distance it drops for horizontal and for upgoing events relative to the rest of the distribution, which is still larger than for detectors with smaller volumes. For horizontal events, the increasing string distance reduces the number of storeys seeing these events, resulting in less hits and a lower efficiency. The fact that the area decreases for upgoing events but not for downgoing events points to the fact that the larger detectors detect more high-energy neutrinos, which are absorbed in the Earth with a large probability.

All these observations match the expectations very well.

10.3.2 Ring detector

The *ring1* geometry shown in Fig. 9.2 was used as a standard for this study. The string distance for the rings is defined as the distance between the strings in one concentric ring and between these rings. As the number of rings and strings stays the same, the radius of the rings increases with the string distance. Detectors with string distances of 80, 100 and 120 m have been simulated. For the 80 m version three additional versions with storey distances of 20, 40 and 60 m were produced. All the effective area ratios are relative to the respective result for the standard *ring1*.

The results for modified storey distances are shown in Fig. 10.10. The version with a storey distance of 20 m is comparable to the standard ring at energies above 100 GeV and a bit better below. Apparently the decrease of the storey distance compensates for the increase of the string distance. For larger string distances the behaviour is similar to the cuboid case. The detector with the largest storey distance is the best at high and the worst at low energies, the 40 m version is a bit worse at high and bit better at low energies (but still better/worse than the standard *ring1*). Even the amount of the advantage or disadvantage in effective area is similar to the cuboid case.

The behaviour of the angular resolution and the zenith angle dependence of the effective area (for the latter see Fig. 10.11) is also very similar to the cuboid case. In the horizontal direction the detectors with low storey distances and therefore lower height are a bit worse than in the vertical. This difference is not as strong as in the cuboid case, as the ring geometry suffers from the effect of the 'hole' that decreases performance for up- and downgoing events. The angular resolution of the 20 m version is the worst at high energies but stays more or less the same at lower energies. For the long string detector the resolution is better at high energies, but becomes increasingly worse for lower energies. The layout with 40 m storey distance has a resolution between these two.

The dependencies of effective area and angular resolution on the string distance are also very similar to the cuboid case, although the crossover energies are visibly lower. This is a consequence of the lower storey distances of the rings compared to the cuboids and the resulting better low energy efficiency. The same fact accounts for the lack of a decrease in effective area for upgoing events that was observed in the cuboid case. The rings have a better low energy performance and therefore the effect of absorption in the Earth is not as obvious (more events that have a low absorption probability in the earth

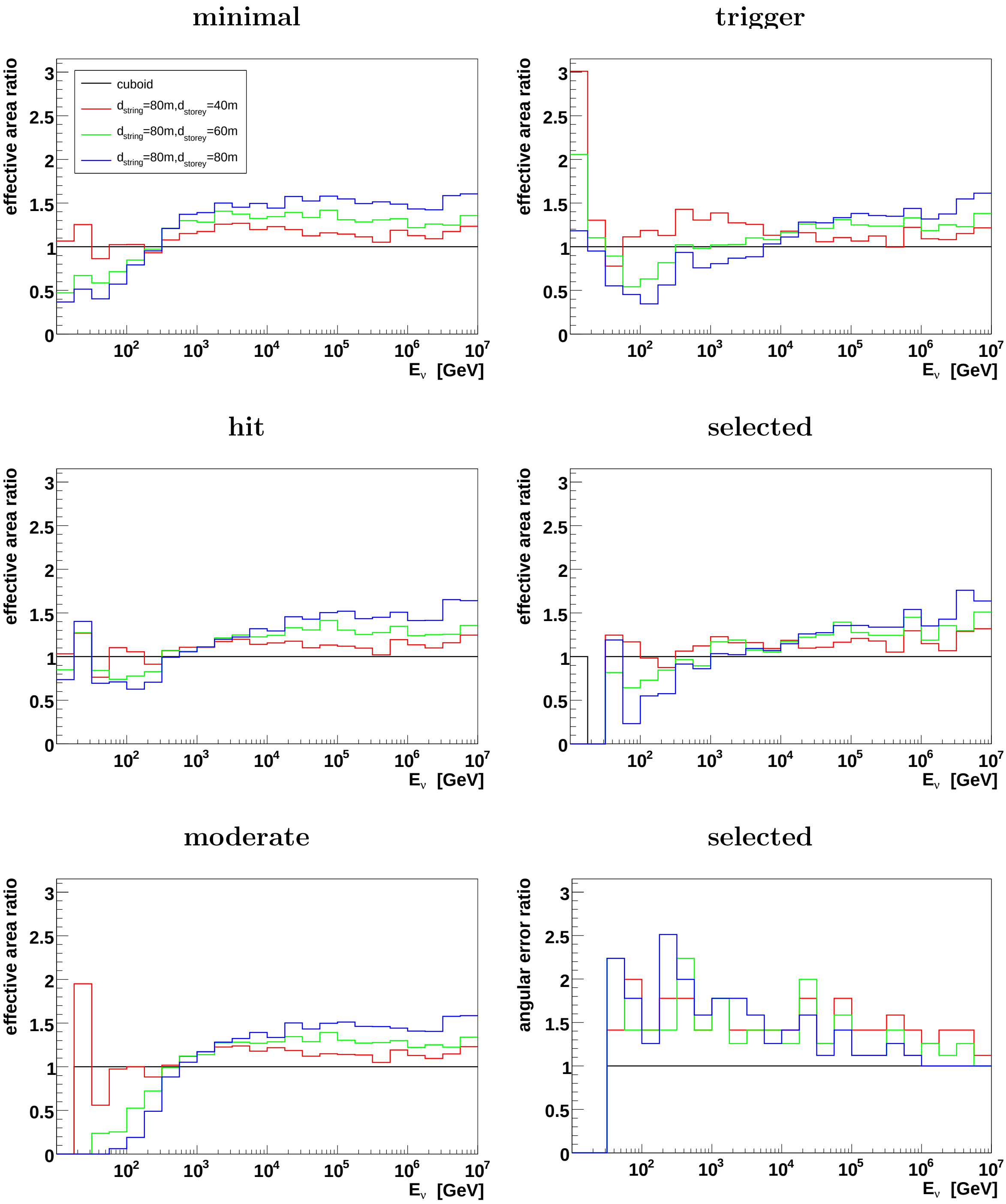

minimal

trigger

hit

selected

moderate

selected

Figure 10.7: Effective area and angular resolution ratios for the cuboids (MultiPMT cylinder storeys) with different storey distances. Left column from top to bottom: Effective area ratios at the *minimal*, *hit* and *moderate* levels. Right column from top to bottom: Effective area ratios at for *trigger* and *selected* events, angular resolution ratios for *selected* events

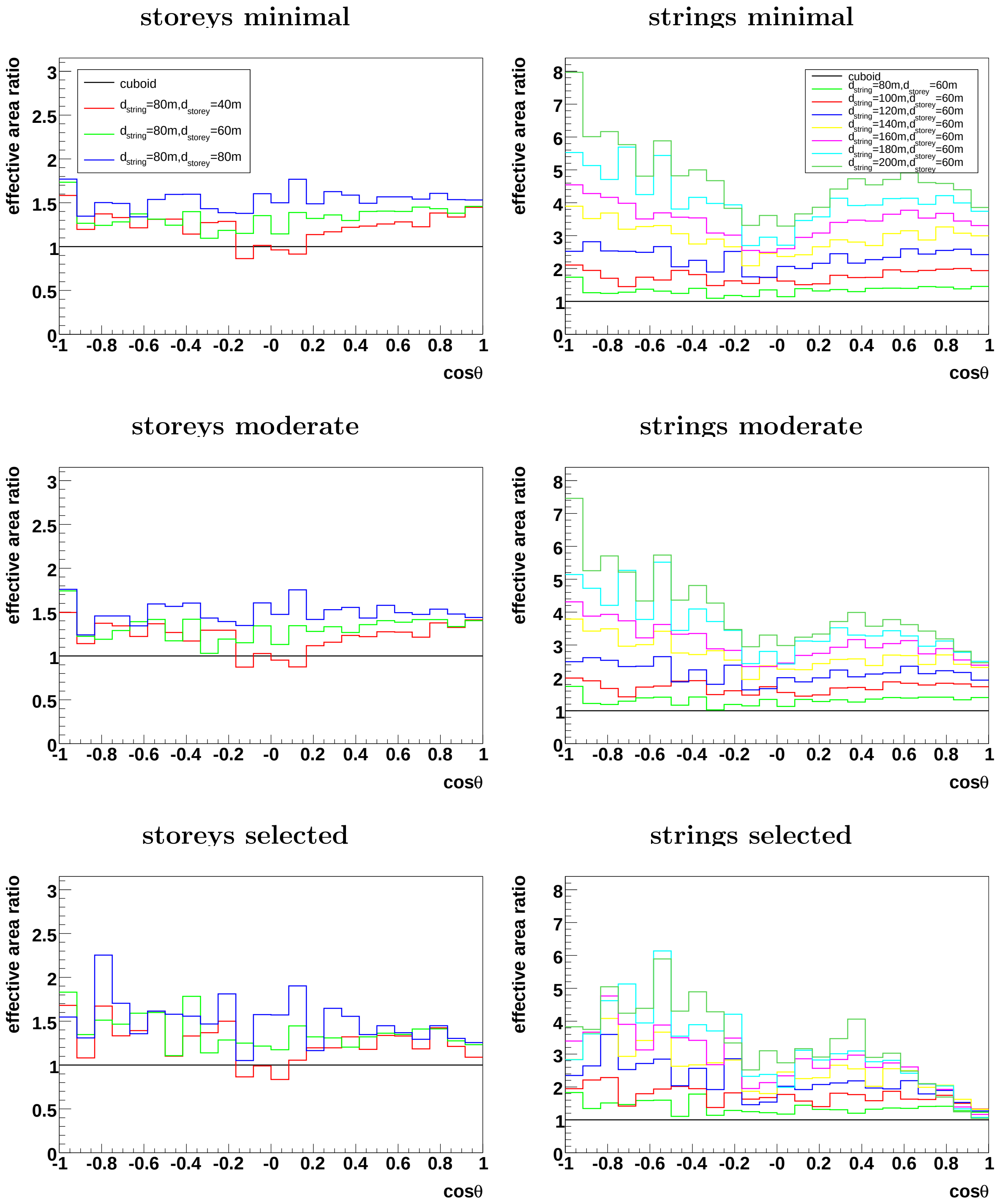

Figure 10.8: Effective area ratios as a function of zenith angle for the cuboids with different string and storey distances. Left column from top to bottom: Effective area ratios for cuboids with different storey distances at the *minimal*, *hit* and *moderate* levels. Right column from top to bottom: Effective area ratios for cuboids with different string distances at the *minimal*, *hit* and *moderate* levels.

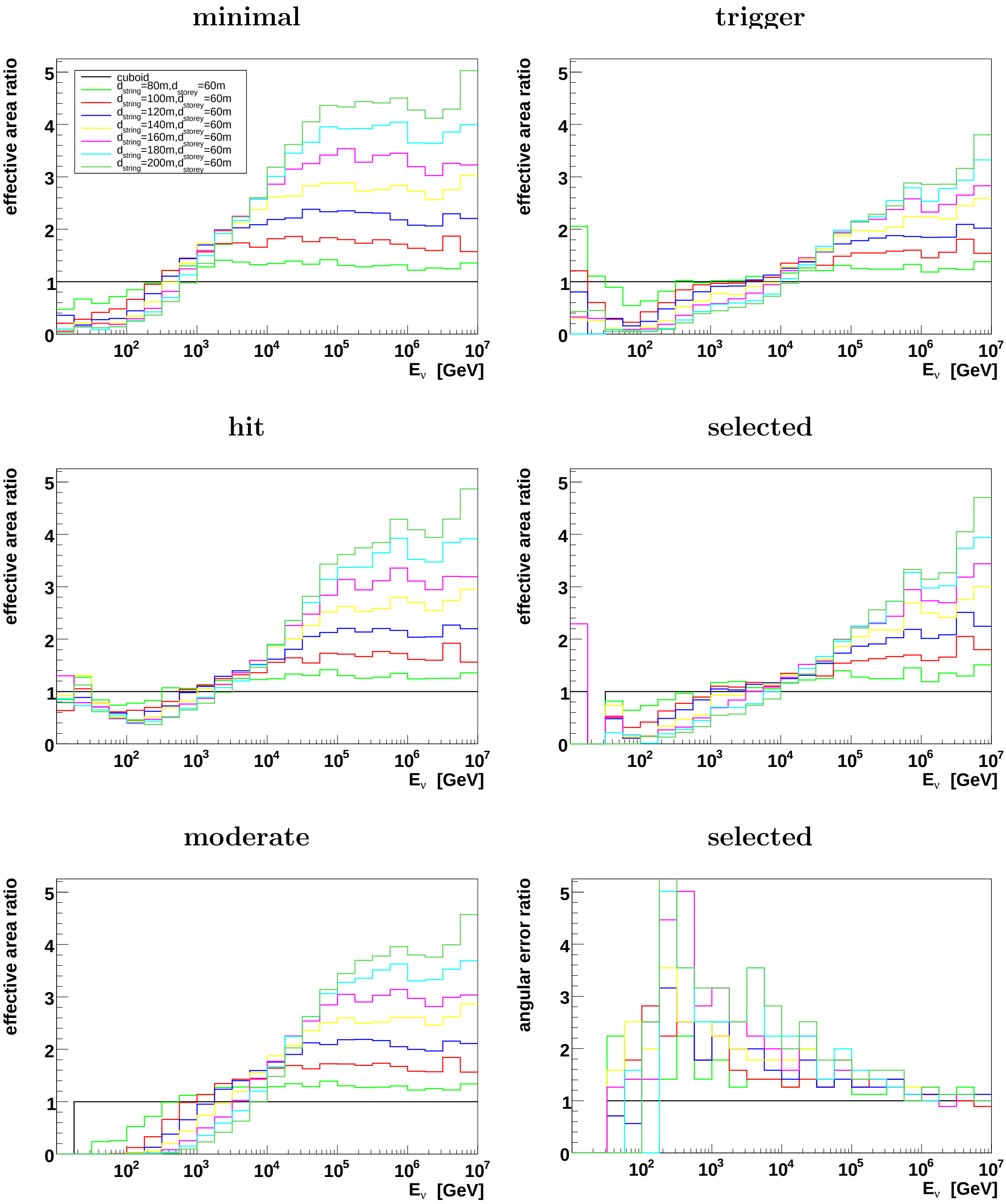
minimal

trigger

hit

selected

moderate

selected

Figure 10.9: Effective area and angular resolution ratios for the cuboids (MultiPMT cylinder strings) with different string distances. Left column from top to bottom: Effective area ratios at the *minimal*, *hit* and *moderate* levels. Right column from top to bottom: Effective area ratios at for *trigger* and *selected* events, angular resolution for *selected* events.

are detected). A hint of this decrease can be observed for *selected* events, as generally low energy events have a lower reconstruction probability (and higher angular errors). This results in a larger fraction of selected events having a high energy and therefore having a higher probability to be absorbed in the Earth.

Again, in the case of the ring detector, all of the observations match the expectations.

10.3.3 Cluster detector

In the cluster geometry there are three parameters that can be modified. The string distance within a single cluster, the average distance between the individual clusters, and the distance of storeys on the strings. Two cluster distances, 360 m and 540 m were used, together with string distances of 60, 80 and 100 m. For the detector model with cluster distance 360 m and string distance 60 m, storey distances of 6, 12 and 18 m were used (The configuration with 360 m, 60 m and 12 m is actually the standard *cluster1*). The results for the detectors with modified storey distances are shown in Fig. 10.13, with modified string and cluster distances in Fig. 10.15. The effective area ratios as a function of the zenith angle are given in Fig. 10.14 for both cases.

The detector with increased storey distance has a larger effective area at energies above a few tens of GeV (about 200 GeV for *trigger* and *selected* events). For smaller energies the effective area drops below that of the standard cluster. Again the increase is a consequence of the larger volume in this case, while the decrease at low energies results from the larger storey distance and therefore lower density of instrumentation. The detector with decreased storey distance shows the exactly opposite behaviour. While being only at 70 to 80% of the effective area of the *cluster1* for most energies, it gets better for the lowest energies. The exception here are the *selected* events, where there is no increase at lower energies. This might be a consequence of the low reconstruction efficiency at low energies. The reasons for the general behaviour of this detector version are the smaller volume, decreasing the effective area at most energies, and the denser instrumentation for events with very low energies. The angular resolution is actually worse than for the *cluster1* in both cases, although the larger version is a bit better than the 6 m one. The zenith angle dependence at the *minimal* and *moderate* level shows a very small increase for horizontal events for the detector with increased storey distance, while the detector with decreased distance is slightly worse for horizontal events than for vertical ones. This is again connected to the differences of the height of the detector. With denser string instrumentation, the 6 m version is of course less high than the other detector configurations, resulting in a decreased cross section area for horizontal muon events. For 18 m storey distance the situation is exactly opposite. The behaviour for downgoing events is difficult to judge due to low statistics, but it seems as if the effective areas behave similar for up- and for downgoing events.

If the string distance inside the clusters is increased, the effective area increases above some crossover energy, varying from a few tens of GeV at the *minimal* level to 20 TeV for *selected* events. Below this energy, the performance decreases. The reasons are basically the same as before (larger volume resulting in larger cross section area and lower density of instrumentation taking effect at low energies). The same is true for an increase of the average distance between the clusters, although the string distance is more relevant for

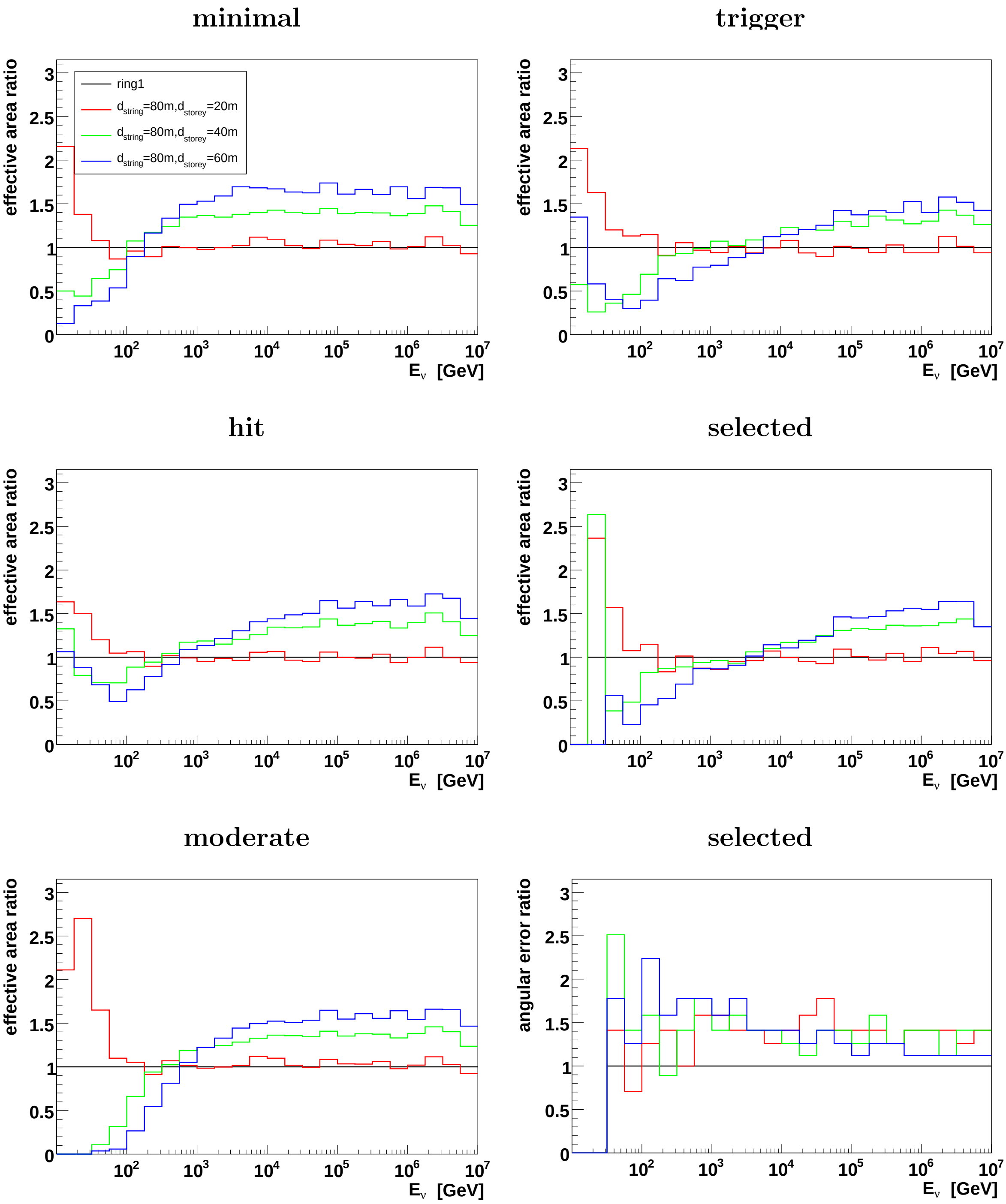

Figure 10.10: Effective area and angular resolution ratios for the rings (MultiPMT cylinder storeys) with different storey distances. Left column from top to bottom: Effective area ratios at the *minimal*, *hit* and *moderate* levels. Right column from top to bottom: Effective area ratios at for *trigger* and *selected* events, angular resolution ratios for *selected* events.

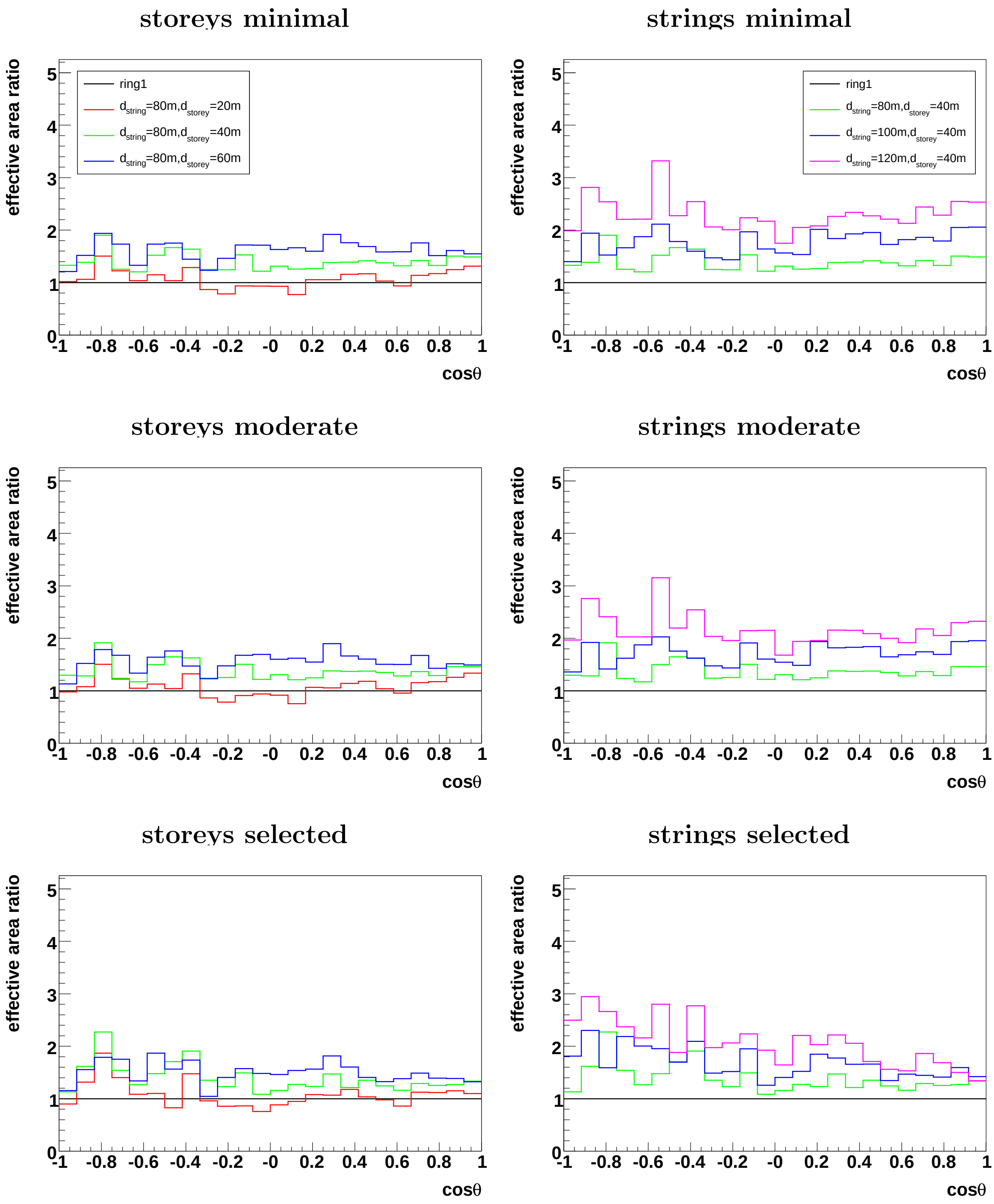
storeys minimal

strings minimal

storeys moderate

strings moderate

storeys selected

strings selected

Figure 10.11: Effective area ratios as a function of zenith angle for the rings with different string and storey distances. Left column from top to bottom: Effective area ratios for rings with different storey distances at the *minimal*, *hit* and *moderate* levels. Right column from top to bottom: Effective area ratios for rings with different string distances at the *minimal*, *hit* and *moderate* levels.

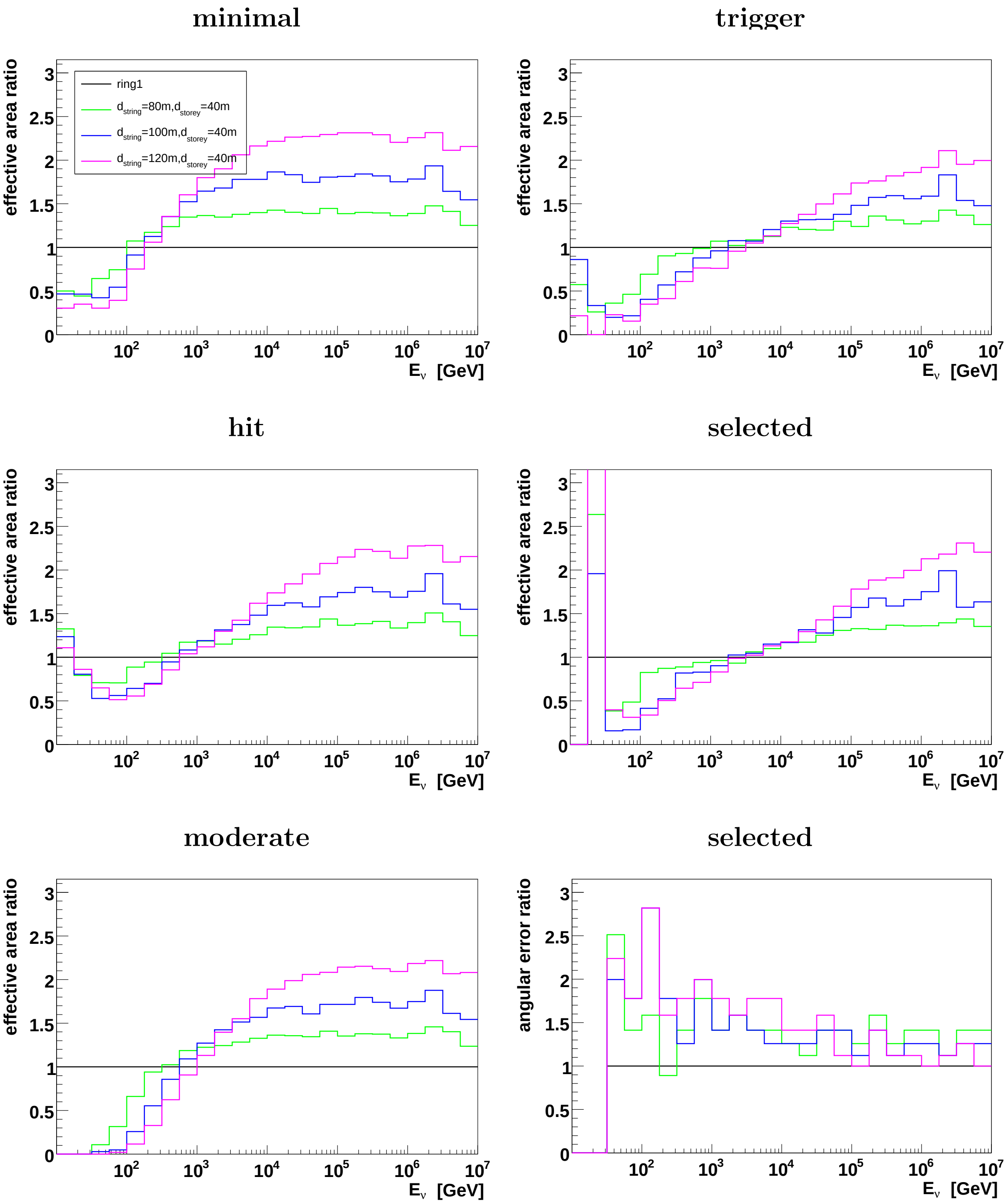

Figure 10.12: Effective area and angular resolution ratios for the rings (MultiPMT cylinder strings) with different string distances. Left column from top to bottom: Effective area ratios at the *minimal*, *hit* and *moderate* levels. Right column from top to bottom: Effective area ratios at for *trigger* and *selected* events, angular resolution ratios for *selected* events.

the performance at low energies. Generally the detectors with larger string distances are worse at low energies, regardless of the cluster distance. On the other hand this is no surprise, as the lowest energy events are most probably detected inside a single cluster (due to their short muon track length), which of course results in a limited influence of the cluster distance at low energies. The maximum increase at high energies is 50% for the largest version of the cluster detector (the one with string distance 100 m and cluster distance 540 m) at *minimal*, *hit* and *moderate* level. The effect is weakened in the *trigger* case and the reconstruction apparently has some problems with increased distances, as the performances for the larger detector decreases massively. The angular resolutions, though only about 25% worse at high energies, quickly degrade towards lower energies, where again the largest and therefore least densely instrumented detectors are the worst. The behaviour of the effective areas as a function of the zenith angle is comparable to the *cluster1* for all detector versions.

As for the ring and cuboid detectors, the behaviour observed for the different cluster models matches the expectations.

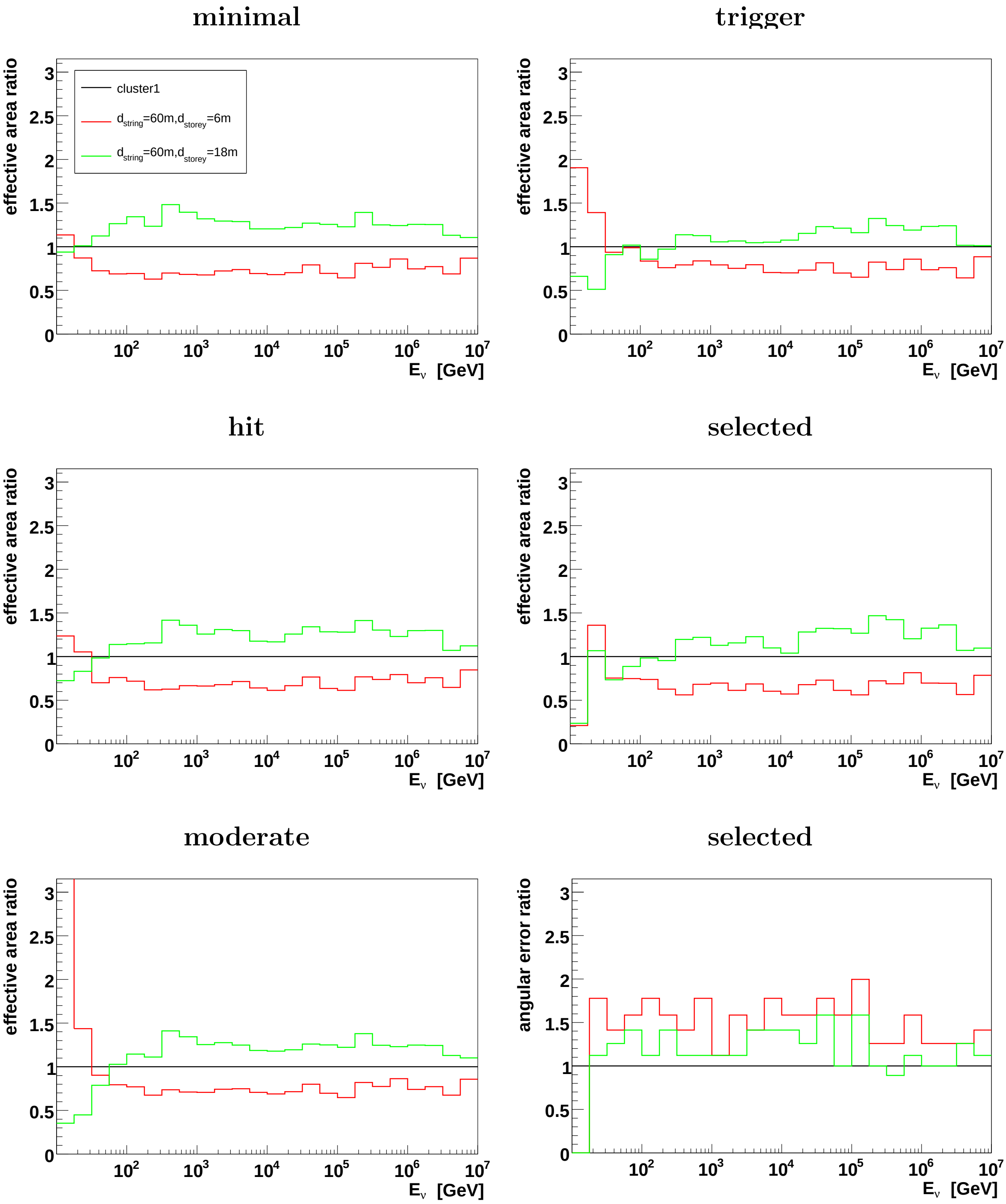

Figure 10.13: Effective area and angular resolution ratios for the clusters (MultiPMT cylinder storeys) with different storey distances. Left column from top to bottom: Effective area ratios at the *minimal*, *hit* and *moderate* levels. Right column from top to bottom: Effective area ratios at for *trigger* and *selected* events, angular resolution ratios for *selected* events.

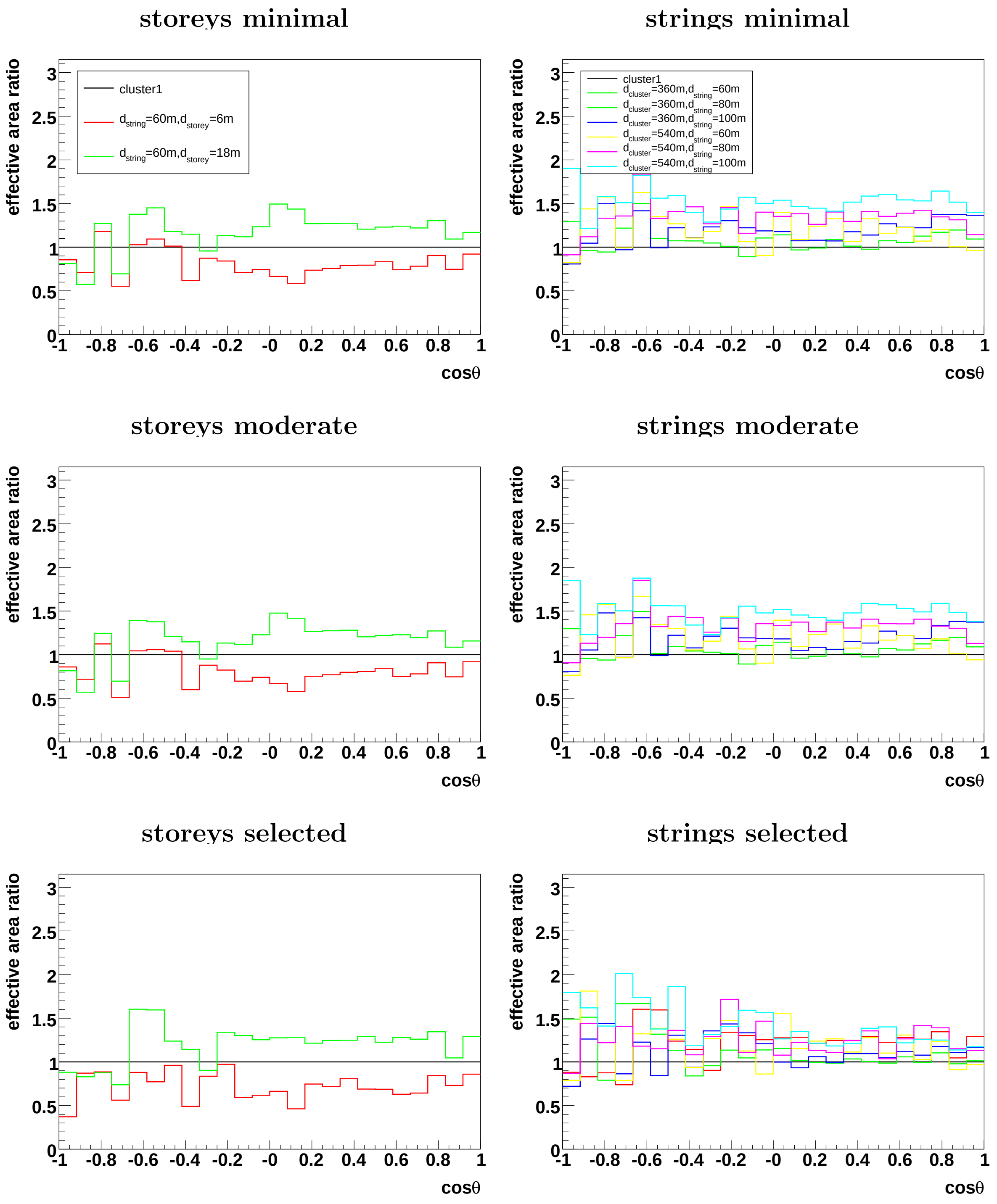

Figure 10.14: Effective area ratios as a function of zenith angle for the clusters with different cluster, string and storey distances. Left column from top to bottom: Effective area ratios for clusters with different storey distances at the *minimal*, *hit* and *moderate* levels. Right column from top to bottom: Effective area ratios for clusters with different string distances at the *minimal*, *hit* and *moderate* levels.

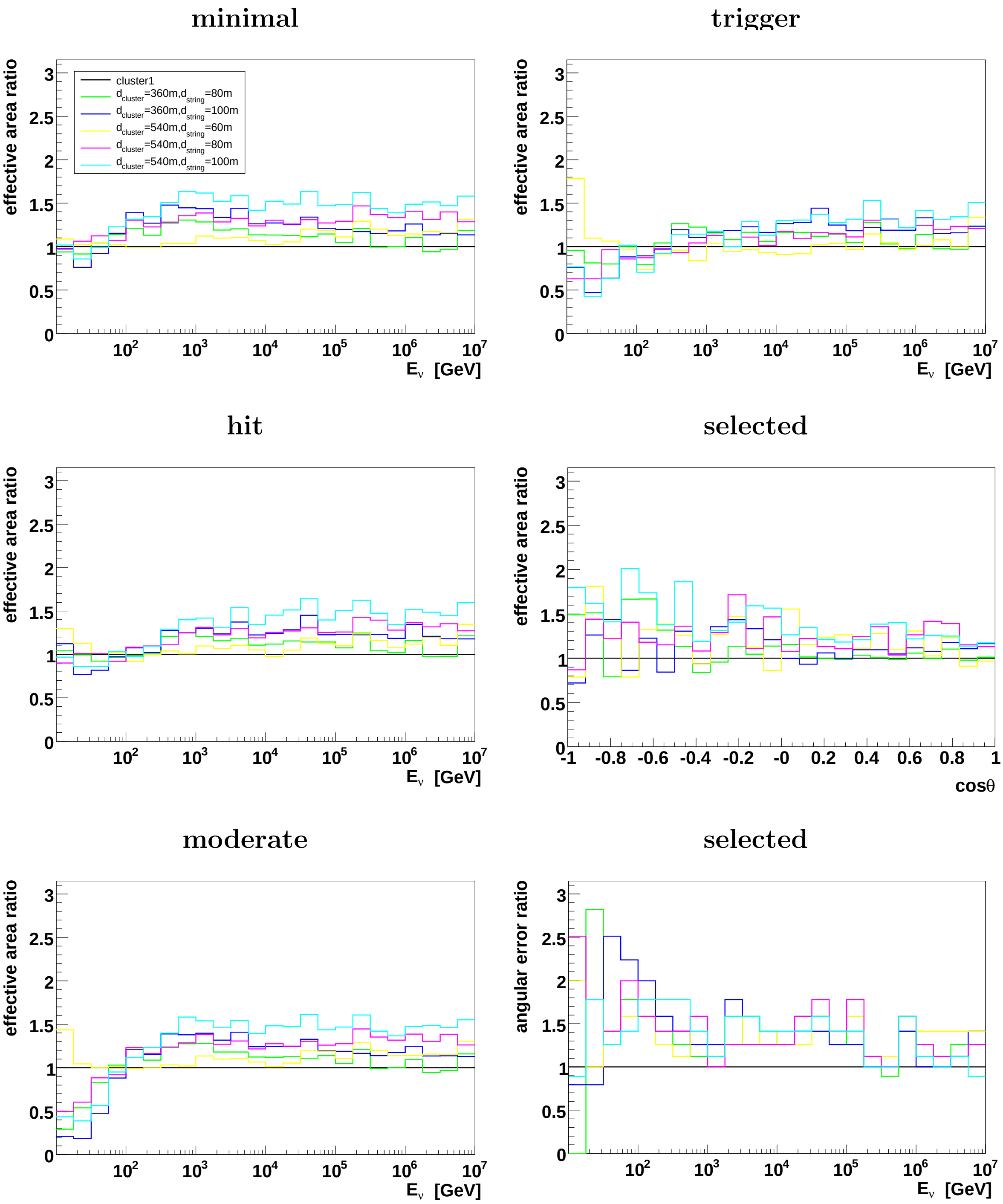

Figure 10.15: Effective area and angular resolution ratios for the clusters (MultiPMT cylinder strings) with different cluster and string distances. Left column from top to bottom: Effective area ratios at the *minimal*, *hit* and *moderate* levels. Right column from top to bottom: Effective area ratios at for *trigger* and *selected* events, angular resolution ratios for *selected* events.

Chapter 11

Sensitivities

In this chapter the results for some of the detector models are used to estimate the physics potential of KM3NeT. The selected detector models are the cuboid, the *ring1* and the *cluster1* equipped with cylinder storeys, covering the different geometry concepts, and the cuboid with ANTARES storeys (with 10"and 20"PMs), covering the photodetection concepts. Additionally the performance of the conclusion detector was studied.

In order to judge the physics performances the effective areas derived in chapters 8 and 9 were used to calculate event rates for the benchmark fluxes (see section 6.5); starting from these, achievable limits on the fluxes were calculated where appropriate, using the methods explained in section 6.4. The sensitivity of a neutrino telescope is generally defined as an upper limit on the neutrino flux, corresponding to the lowest flux that can be rejected at a given confidence level (usually 90%).

In the first section, upper limits on the diffuse neutrino flux are estimated and compared to the Waxman-Bahcall flux expectation. The sensitivity to point sources is the focus of the second section. Upper limits as a function of the source declination were calculated for a generic point source. Additionally, event rates for a promising Galactic source, SNR RX-J1713.7-3946, were calculated using the same method (and actually code) as in [3]. Finally event rates for three possible fluxes of neutrinos from dark matter annihilations in the sun were determined (see section 6.5 for details).

The different energy dependencies of the effective areas of the configurations considered define their sensitivity to the different physics goals; the use of the benchmark fluxes allows us to judge whether a detector configuration has high sensitivity for many different sources or whether it is very specialised on only a few of them. As many important factors, like atmospheric muon rejection (and in some cases even muon reconstruction), were not included, this chapter is not intended to provide a final definition of the sensitivity of KM3NeT. It should be noted that Monte Carlo energies are used throughout this chapter, i.e. no energy reconstruction has been applied.

11.1 Limits on the diffuse flux

In order to judge the sensitivity of a candidate neutrino detector to different diffuse flux models, an upper limit on the neutrino flux has to be calculated. The basics of this

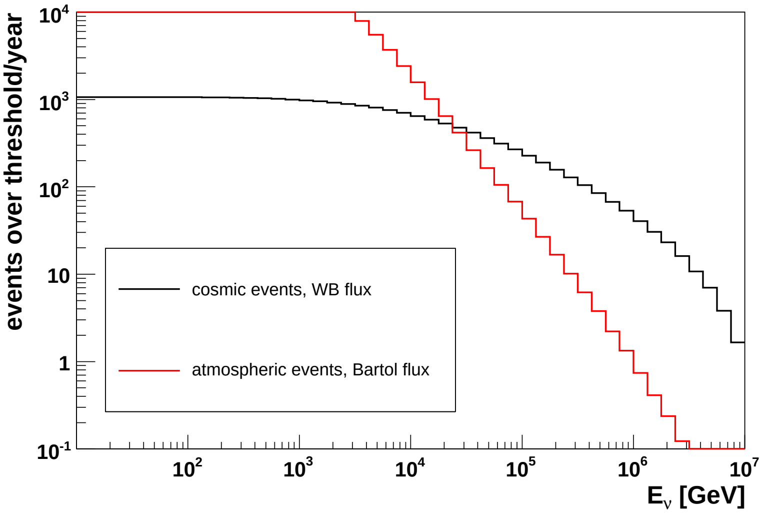

Figure 11.1: Integrated event rates for signal and background flux for the cuboid with cylinder storeys.

procedure are described in section 6.4.

The starting points are the event rates for a given detector for the atmospheric neutrino background flux and for a signal flux with a certain normalisation. The flux limits for an E^{-2} flux are calculated. The Waxman-Bahcall flux (equation 6.12), introduced in section 6.5, was used to calculate the signal event rates. The different parametrisations of the atmospheric neutrino flux are quite similar, at least when comparing their differences the uncertainties in the calculation of the effective areas of the detectors. Therefore the Bartol [1,62] flux was arbitrarily chosen for the calculation of the background event rates (see Fig. 4.8). Additionally a prompt neutrino flux inbetween the extrema of the different models was used, namely the QGSM model (see section 4.1.3). Effective areas for upward going muon neutrinos were used for the calculation of event rates (2π-case).

For each chosen energy, the integrated event rates (events above that energy) per year have to be calculated. Under the assumption that there is no signal present (only background events) the average upper limit N_{limit} of events has to be calculated, which corresponds the number of events that are consistent with a background fluctuatuion at the given confidence level. (see section 6.4). From this the model rejection factor (MRF),

$$MRF = \frac{N_{\mathrm{limit}}}{N_{\mathrm{model}}} \tag{11.1}$$

was calculated, where N_{model} is the number of events above threshold for the assumed signal flux. The minimum MRF defines the optimal energy cut and the resulting flux limit as explained in section 6.4. Example event rates (for the cuboid with cylinder storeys) are shown in Fig. 11.1.

In similar studies for existing neutrino telescopes muon event rates are used for this limit calculation procedure, as muon rates are the actual observable of the experiment. This allows to include all the (atmospheric muon) background rejection cuts. As there are no specialised cuts for the different detector models considered in this work yet (there

detector	**flux limit** (E^2 GeV s^{-1} m^{-2} sr^{-1})		
	minimal	**moderate**	**selected**
cuboid w cylinders	2.6×10^{-9}	2.6×10^{-9}	3.8×10^{-9}
cluster1 w cylinders	2.9×10^{-9}	2.9×10^{-9}	4.5×10^{-9}
ring1 w cylinders	2.7×10^{-9}	2.7×10^{-9}	3.8×10^{-9}
cuboid w ANTARES storeys	2.6×10^{-9}	2.7×10^{-9}	3.7×10^{-9}
cuboid w ANTARES storeys (20")	2.5×10^{-9}	2.5×10^{-9}	3.6×10^{-9}
conclusion detector (cuboid3 w 21 PM spheres)	2.6×10^{-9}	2.6×10^{-9}	3.8×10^{-9}

Table 11.1: Diffuse flux limits for a E^{-2} flux for different detector models at different selection steps, assuming one year observation time. Effective areas for upward going muon neutrinos and the Bartol atmospheric neutrino flux (including the QGSM parametrisation of the prompt flux) were used for the calculation.

is not even a dedicated reconstruction, which is beyond the scope of this work), neutrino event rates were used.

The results at different selection steps are given in table 11.1. The cuboid with the large 20"PMs is slightly better than the other models at all selection steps. The slightly increased effective area at high energies is the reason for this (also slight) advantage. Considering the fact that this detector has four times the photocathode area, this advantage is an artefact. At the three selection levels the cuboid detectors and the conclusion detector produce basically the same limits. Although the cuboid with ANTARES storeys has a slightly higher limit than the other detectors in the *moderate* and a slightly better limit in the *selected* case (possibly due to the effects of the reconstruction). The results for the *ring1* detector are also very similar. The reason for the similarity of the diffuse flux limits for the different detector configurations is the similarity of their effective areas at high energies (the optimal cut energies are between 200 and 280 TeV). Only the *cluster1* has worse limits, as its effective area at these high energies is lower than that of all the other detectors. With the exception of the extremely inhomogeneous cluster geometry, the details of the detector layout have little influence on the sensitivity to the diffuse cosmic neutrino flux.

The IceCube collaboration has published diffuse flux limits of

$$8.1 \times 10^{-9}\ E^2\ \mathrm{GeV\,s^{-1}\,cm^{-2}\,sr^{-1}},$$

for an E^{-2}-flux and one year observation time with an optimal energy cut of a few hundred TeV [5]. It should be noted that this limit includes all relevant selection and background reduction cuts, as well as an energy reconstruction. When comparing the limits, this should be kept in mind. Assuming a reduction of efficiency due to the application of the relevant cuts mentioned, the diffuse flux limit of a future KM3NeT detector will most probably be of the same magnitude as for IceCube.

In Fig. 11.2 the flux limit of the conclusion detector at the *selected* level is compared to Waxman-Bahcall flux expectation and the existing experimental limits.

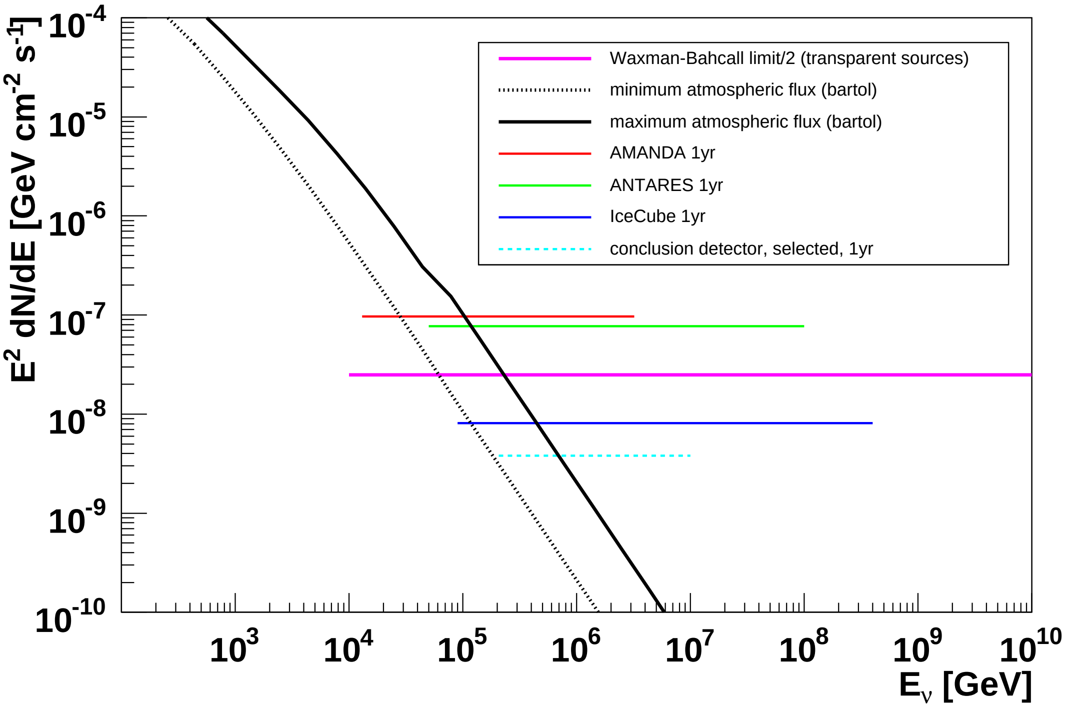

Figure 11.2: Comparison of the calculated diffuse flux limit for the conlcusion detector with results from different experiments and model fluxes. IceCube limit from [5], ANTARES limit from [6], AMANDA result from [7], Waxman-Bahcall flux from [8].

11.2 Point sources

The observation of neutrino point-like sources is one of the most important goals of a neutrino telescope. In order to estimate the performance of the different detector models, two methods are applied. The first is to calculate upper limits on the neutrino flux for a generic point-like (i.e. with an extension much below the angular resolution of the neutrino telescope) source as a function of its declination. A neutrino flux of

$$\frac{d\Phi_\nu}{dE_\nu d\Omega_\nu} = 1 \times 10^{-8} E^{-2} \mathrm{GeV cm^{-2} s^{-1} sr^{-1}} \tag{11.2}$$

was assumed for the source (no cutoff). The search cone is defined by the angular resolution of the detector. The Bartol flux [1,62] was used for the background of atmospheric neutrinos.

There are several approaches for point source searches. Here it is assumed that the position of the source is known. In this case, the number of atmospheric neutrino events is greatly reduced, as only neutrinos within the search cone form the background.

The efficiency for a given source declination depends on the visibility of the source, which in turn depends on the geographic latitude of the detector site. In the energy range interesting for point source searches (TeV energies, except for GRBs), the visibility is given by the proportion of the time the source is below the horizon, as above the horizon the atmospheric muon background is still far too high. Additionally the zenith angle dependence of the detector effective area is very important for the analysis. For this analysis the detectors were assumed to be located at the ANTARES site. However, the geographic coordinates of the other candidate sites do not differ drastically (all in the Mediterranean).

For every assumed declination of the source the event rates are calculated taking account of the zenith angle dependence of the effective area and of the atmospheric neutrino flux. The event rates are averaged with respect to the visibility of the source during a day. The atmospheric background is scaled according to the size of the search cone with an opening angle of twice the angular resolution. For simplicity, the angular resolution of the relevant detector at an energy of 1 TeV was chosen at all selection steps, where its is still dominated by kinematics. This is a conservative assumption. For the resulting rates, the limit calculation process, as described in sections 6.4 and 11.1 was repeated, resulting in upper limits as functions of the declination.

The results for the cuboid with cylinder storeys at the different selection steps are shown in Fig. 11.3. The results for different detector models are shown in Figs. 11.4, 11.5 and 11.6. The results for the conclusion detector are compared to the experimental or estimated limits of other experiments in Fig. 11.7.

The limits for the *minimal*, *hit* and *moderate* criteria are relatively close together. For *selected* events, the limits are about a factor two higher. The limits for the *trigger* case are between these extrema. Compared to the limits for ANTARES, the cuboid lowers the flux limits by a factor of 20 in the best case. When comparing the results of different detector layouts, the limits of the cuboids are close together at the *minimal* stage, while the ring is slightly and the cluster significantly worse. The problem of the ring and the cluster is their relatively low effective area in the range of a few TeV, which is the most relevant region of the spectrum for point source searches (except for GRBs which are assumed to produce neutrinos at higher energies). At the *moderate* level, the conclusion detector produces slightly lower limits, most probably because of its increased efficiency due to its larger number of storeys at this selection step. For *selected* events the cuboid with ANTARES storeys is clearly better than all the other detectors. This may be a consequence of the reconstruction algorithm combined with the fact, that the PMs in the ANTARES storeys point downward (at an angle of 45 degrees).

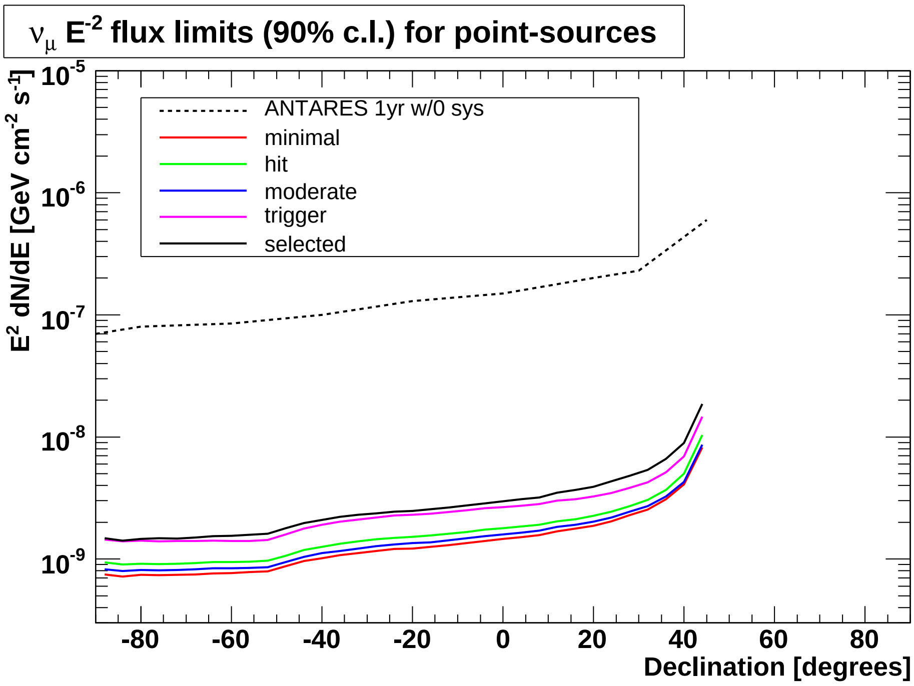

Figure 11.3: One year flux limits as a function of the source declination, for the cuboid with cylinder storeys at different selection steps, compared to the corresponding limits for ANTARES.

As an additional benchmark for the different detector layouts, event rates for the SNR RXJ1713.7-3946 were calculated using the identical procedure as in [3]. The neutrino flux from this source was derived from the spectrum of high energy gamma rays measured by the HESS experiment. The details of the method used are explained in [3]. The results for the different detector configurations are given in Table 11.2. The ranges of the event rates result from systematic uncertainties in the determination of the neutrino flux for the source (see [3] for details). All of the detector models provide signal event rates, comparable to the number of background events per year, with absolute numbers of about one to about three signal events per year. This would allow the detection of the source after several years of stable detector operation. Nonetheless there are some differences between the different detector models. The *cluster1* has lower event rates than the other layouts at all selection steps, due to its lack of efficiency in the TeV energy range. The conclusion detector and the cuboid with ANTARES(20”) storeys produce the largest number of events except for *selected* events, where both lose to the *ring1*. This is

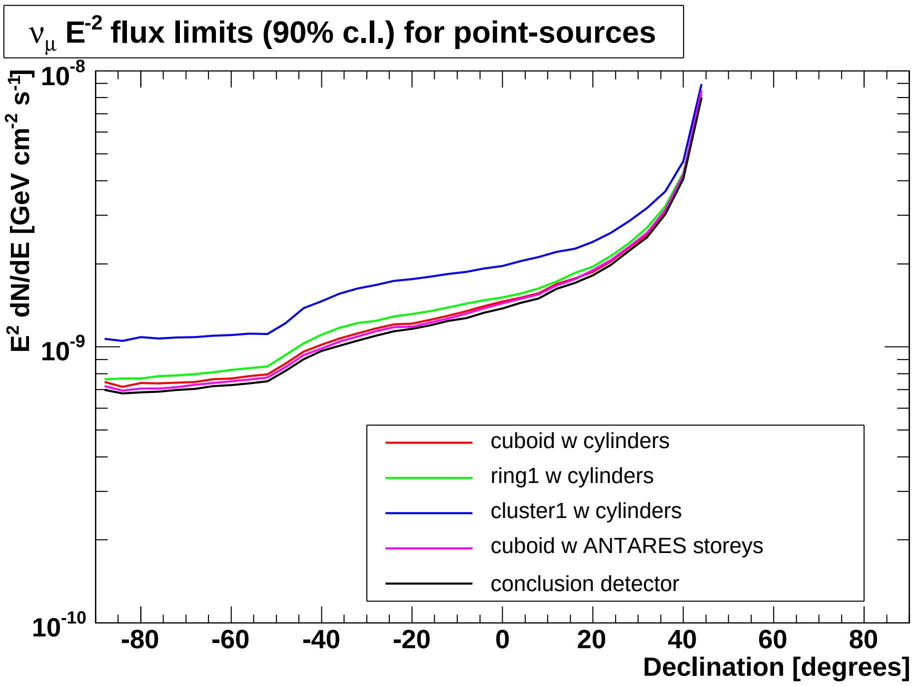

Figure 11.4: One year flux limits as a function of the source declination, for different detector models at the *minimal* level, compared to the corresponding limits for ANTARES.

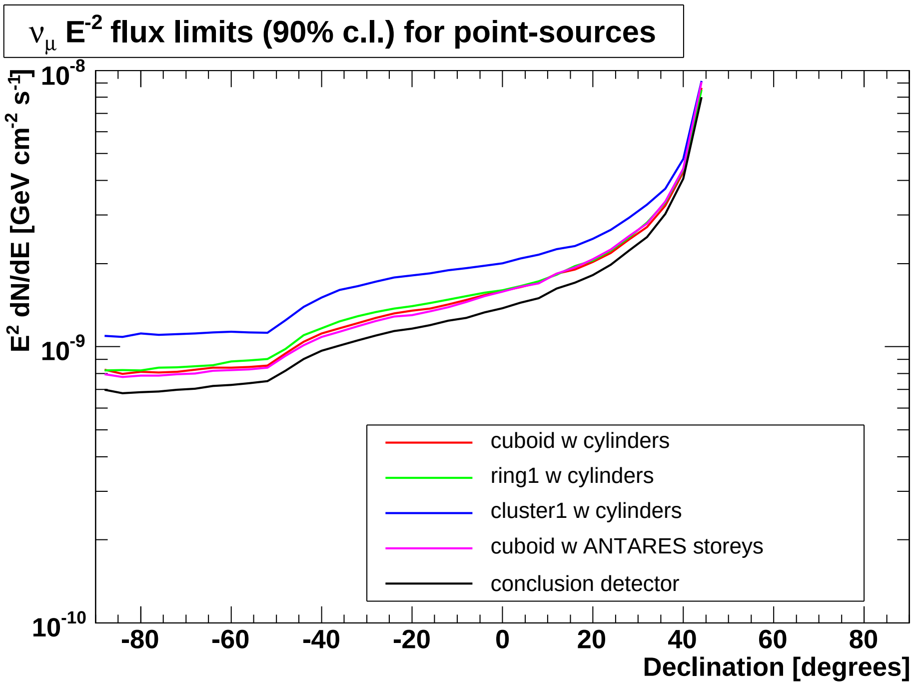

Figure 11.5: One year flux limits as a function of the source declination, for different detector models at the *moderate* level, compared to the corresponding limits for ANTARES.

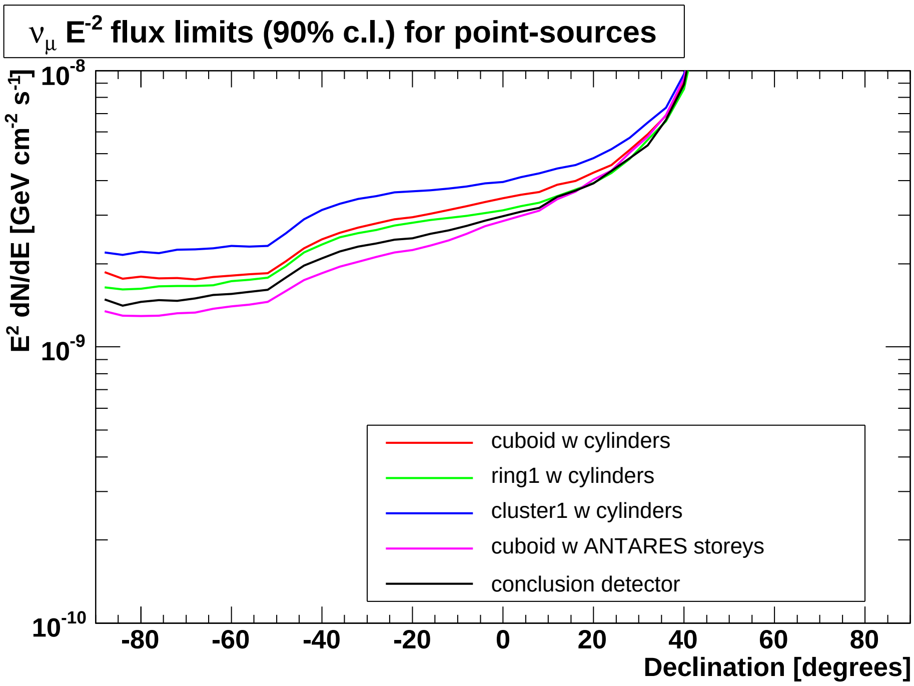

Figure 11.6: One year flux limits as a function of the source declination, for different detector models at the *selected* level, compared to the corresponding limits for ANTARES.

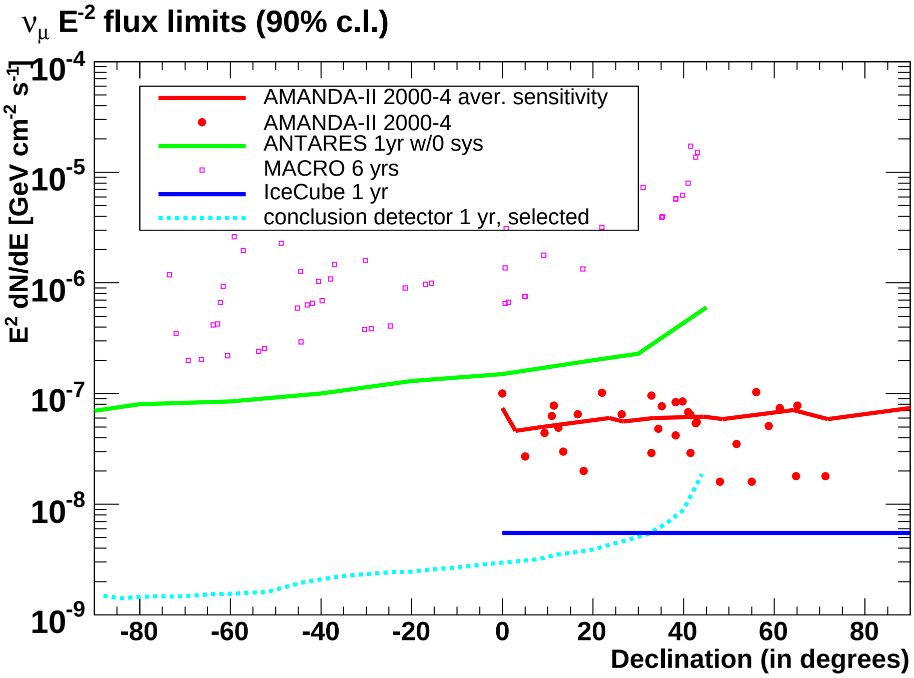

Figure 11.7: One year flux limits as a function of the source declination for the conclusion detector at *selected* level compared to other experiments.

detector	**selection step**	$\mathbf{N}_{\mathrm{src}}$	$\mathbf{N}_{\mathrm{atm}}$
cuboid w cylinders	minimal	1.8 - 3.6 (2.7)	10.7
	moderate	1.6 - 3.2 (2.4)	9.1
	selected	0.5 - 1.1 (0.8)	2.9
cluster1 w cylinders	minimal	1.1 - 2.3 (1.7)	6.5
	moderate	1.1 - 2.2 (1.7)	6.3
	selected	0.5 - 1.1 (0.8)	2.9
ring1 w cylinders	minimal	1.6 - 3.3 (2.5)	9.7
	moderate	1.5 - 3.0 (2.3)	8.7
	selected	0.6 - 1.3 (0.9)	3.4
cuboid w ANTARES storeys	minimal	1.7 - 3.4 (2.6)	9.8
	moderate	1.4 - 3.0 (2.2)	8.3
	selected	0.6 - 1.2 (0.9)	3.1
cuboid w ANTARES storeys (20”)	minimal	2.1 - 4.2 (3.2)	12.7
	moderate	1.9 - 3.9 (2.9)	11.6
	selected	0.6 - 1.2 (0.9)	3.1
cuboid3 w 21 PM spheres (conclusion detector)	minimal	1.8 - 3.7 (2.8)	10.9
	moderate	1.7 - 3.5 (2.6)	10.1
	selected	0.6 - 1.3 (0.9)	3.2

Table 11.2: Expected number of events from the SNR RX-J1713.7-3946 for different detector models and selection steps. The assumed observation time is 1 year, with an energy threshold of 1 TeV. The event number in parenthesis is the mean value.

due to its slightly higher effective area in the TeV region for that selection step. Except for the cluster, the differences between the various configurations are relatively small.

11.3 Neutrinos from dark matter annihilations in the Sun

To estimate the sensitivity of the detector configurations to neutrinos from annihilations of dark matter particles accumulated in the Sun, corresponding event rates were calculated. The fluxes used for this calculation have been introduced in section 6.5. These fluxes are for $\nu_\mu + \bar{\nu}_\mu$, while the effective areas are based on the simulation of ν_μ only. Due to the slightly different reaction cross sections for ν_μ and $\bar{\nu}_\mu$, the resulting event rates should be seen as a rough estimate.

For the calculation of the event rates the low-energy samples for the detectors were used to calculate effective areas for upgoing muons. The resulting integrated event rates for the different fluxes are shown in Figs. 11.8, 11.9 and 11.10 for the three different fluxes. For the bulk region flux the event rate per year for the conclusion detector reaches about 220 events at the *minimal* level. The lowest event rate is produced by the cuboid with ANTARES storeys at this stage, with about 90 events, while the other detectors are in between. At the *selected* level the event rates are between about 18 for the *cluster1* and just below two for the cuboid with ANTARES storeys. For the lower-focus-point flux the best detectors reach almost ten thousand events in the *minimal* and still about 4200 in the *moderate* case. The rate drops below one thousand for the cluster and *selected* events, while the other detectors produce only a few hundred events at this stage. Of course the chance for a detection depends on the background and is intimately related to the general problem, that almost all events for the bulk and lower-focus-point flux fluxes would be detected below about 130 GeV. At these energies energy reconstruction is extremely difficult. Not knowing the energy of the detected neutrinos with sufficient precision will significantly complicate the analysis since it effectively increases the background. Furthermore, the angular resolution at these lowest energies is dominated by kinematics and therefore not very good and intrinsically limited, thus again increasing the background. These problems might be less significant for the central-focus-point flux, as it extends to just above 300 GeV. However, the rates for this flux reach only about one thousand events for the best detectors, at the lowest energies and at the *minimal* level, which is much smaller than for the lower-focus-point flux. This drops to 700 at the *moderate* level and about 150 for *selected* events.

Of course this is only a rough estimate of the event rates for three example fluxes. The event rates appear to be high enough to allow the acquisition of sufficient statistics, but ultimately the background defines the probability of a detection. A detailed study on the detection potential is necessary to truly judge the sensitivity of km^3-detectors to neutrinos from dark matter annihilations. It should be kept in mind that for a real neutrino flux from dark matter annihilations similar to the bulk region flux, even with a detector layout optimised for low energies as the cluster, the detection of a dark matter signal might be difficult.

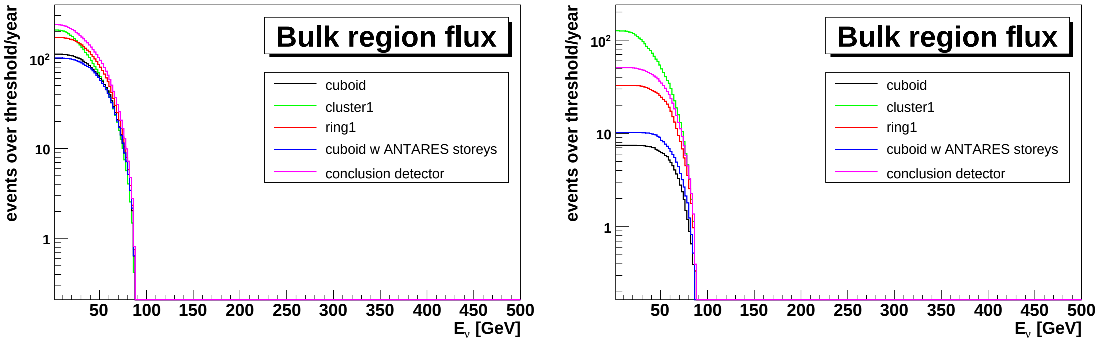
minimal

moderate

selected

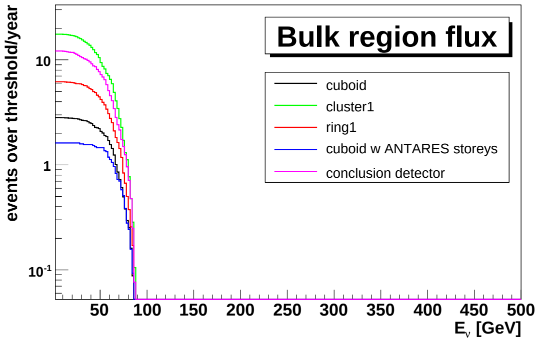

Figure 11.8: Integrated event rates for the bulk flux at different selection steps.

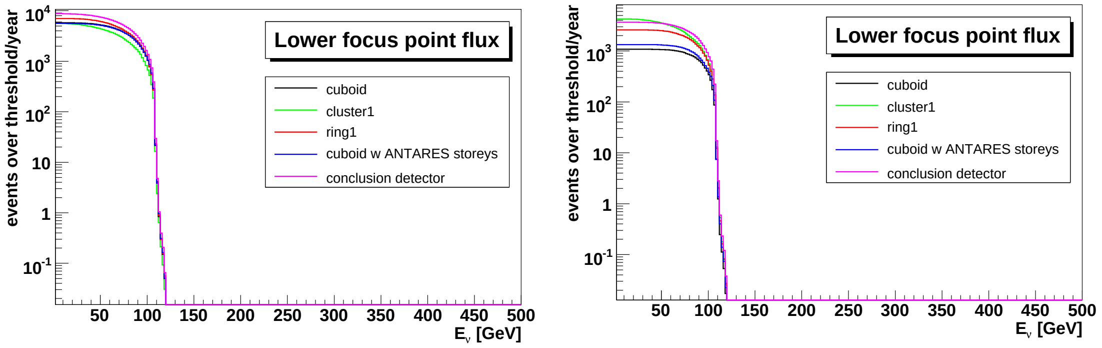

minimal

moderate

selected

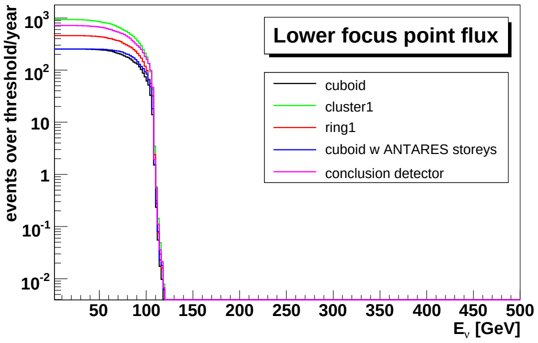

Figure 11.9: Integrated event rates for the lower focus-point-flux at different selection steps.

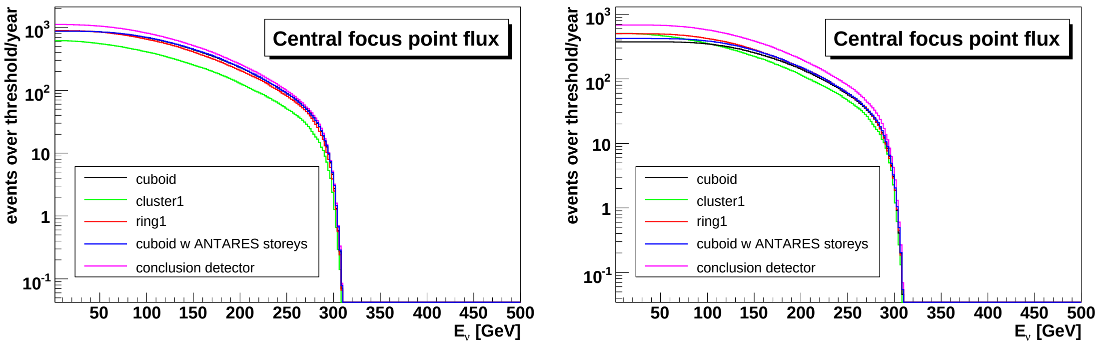

minimal

moderate

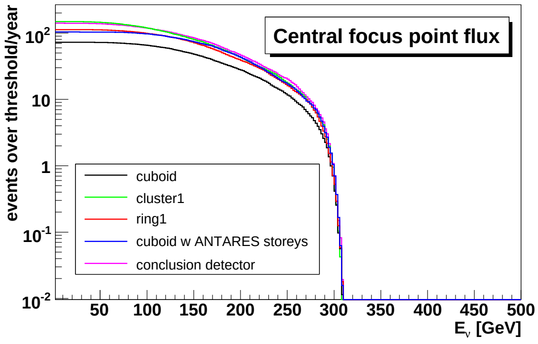

selected

Figure 11.10: Integrated event rates for the central focus-point-flux at different selection steps.

11.4 Sensitivity conclusions

For the sensitivity to the diffuse flux of cosmic neutrinos the effective area in the energy region of hundreds of TeV is the defining detector characteristic. As most detectors have similar effective areas at these high energies, the resulting sensitivities are very similar. Only the lower effective area of the *cluster1* at high energies results in a reduced worse sensitivity.

For the observation of point sources the effective area at energies of a few TeV and the angular resolution are the dominant properties of a detector. Here the cluster geometry is again the worst option. The ring also appears to be slightly worse than the other detectors (although not for *selected* events).

The cluster detector produces very high event rates for the considered fluxes of neutrinos from annihilations of dark matter in most of the cases. The conclusion detector produces good results here as well. The cuboids generally have the lowest event rates, followed by the ring and the other two configurations.

Most detectors produce similar results for the diffuse flux and for individual sources. The standard cuboid geometries produce the lowest event rates in the dark matter case. The cluster layout is clearly optimised on this, but produces the worst results for the rest of the physics goals. The conclusion detector seems to perform well at all the three tasks considered.

Part IV

Summary

Chapter 12

Summary and outlook

12.1 Motivation and methods

The aim of this thesis is to provide a starting point for the definition of a detector design for the KM3NeT neutrino telescope in the Mediterranean sea with an instrumented volume of cubic kilometer scale. A neutrino telescope is basically a three-dimensional array of photomultipliers, detecting the Cherenkov light produced by secondary particles originating from neutrino interactions with the surrounding medium. The detector medium is a large volume of sea water or ice, as large target volumes are required due to the low neutrino fluxes at high energies.

Neutrino astronomy aims to detect high-energy neutrinos from cosmic sources like Supernova-remnants, active galactic nuclei and gamma ray bursts. The detection of neutrinos from these sources will allow to study the properties of these sources and will help to find the origin of the cosmic rays. Several first-generation experiments are under construction or in operation to achieve this task - the BAIKAL, AMANDA, ANTARES and NESTOR experiments. While these experiments demonstrate the feasibility of the technique employed, it has become clear that for full scale high-energy neutrino astronomy, detectors with cubic kilometer volumes are necessary.

With the start of the construction of the IceCube telescope at the South Pole, the time frame for a similar-size experiment in the Northern Hemisphere is set. Because of the atmospheric muon background, a neutrino telescope is mostly sensitive to neutrinos traversing the Earth in an upward direction at most neutrino energies. Therefore two telescopes are needed to cover the whole sky, one in the Southern hemisphere to cover the northern sky and one in the Northern hemisphere to cover the southern sky. The latter has the advantage to provide most of the time visibility of the the Galactic Center, where many potential high-energy neutrino sources are located.

The European neutrino telescope community, represented by the ANTARES, NEMO and NESTOR collaborations, has joined forces for a design study for a cubic kilometer telescope in the Mediterranean Sea funded by the European Union in the Sixth Framework Programme. The project goal is a Technical Design Report, detailing all technical specifications for the construction of a deep sea cubic-kilometer neutrino telescope.

The first step of the design study is a phase of intensive simulation, to find detector geometries and photo-detection layouts, that are optimised for the specified physics goals. These are the detection of neutrinos from the cosmic diffuse flux, the detection of individual sources of cosmic neutrinos and the detection of neutrinos from annihilations of dark matter particles in the center of the Sun. This thesis represents a first step in this process. As the time schedule of the project is tight, it is not possible to write specific KM3NeT software from scratch at this stage. Therefore the software tools used by the ANTARES and NEMO collaborations were adapted to the task and used for the simulations. The software chain included a software model of the detector to be studied, the simulation of muon neutrino interactions, the propagation of the secondary muons to the detector site, the simulation of the detector response and the reconstruction of the incident neutrino's direction from the photon hits in the detectors PMs. With the exception of the reconstruction algorithm, all of these steps work well with the increased volumes and modified layouts of the detectors considered. However the reconstruction algorithm was optimised for the smaller ANTARES detector layout and is therefore presumably not an optimal solution. As the optimisation of the reconstruction for all the different detector models considered in this study is far beyond its scope of a PhD thesis, several reconstruction-independent selection criteria were introduced to guarantee a fair comparison between different concepts and to provide reasonable estimates of the detector performance (for a summary of these criteria see table 6.1). However, the application of the reconstruction process was necessary to find the angular resolution of the detectors studied. In order to compare different concepts, neutrino effective areas and angular resolutions were calculated, serving as a measure for the performance of a specific candidate detector layout.

12.2 Detectors and general studies

Two aspects of a neutrino telescope were studied. The first is the layout of a single cluster of photomultipliers, called a storey. This involves the properties and positions in the cluster of the PMs used. The PM properties that were modified are the photocathode area, the quantum efficiency and the angular acceptance. The second is the position of the storeys in the instrumented volume, or in other words the detector geometry. Except for the rate of the ^{40}K noise, the default site parameters included in the ANTARES code were used. The ^{40}K rate was set to the equivalent of 40 kHz for a 10" PM and the proportionate value scaled by photocathode area for smaller or larger PMs.

12.2.1 Photodetection

The different storey layouts were compared by placing them in a homogeneous cuboid grid. This cuboid grid equipped with standard ANTARES storeys was used as reference for the other storey types. For storey layouts with more or less photocathode area than the reference, additional detector geometries were produced, where the number of storeys per string was increased or decreased appropriately to reach the same overall photocathode area as the reference detector. These detector models are called *candidate* detectors. A summary of the detector model properties is given in table 12.2. The specifications of the

storey type	PMT type	#PMTs	total PMT area (m^2)
single PM	Hamamatsu R7081_20 10”	1	0.044
double PM	Hamamatsu R7081_20 10”	2	0.088
ANTARES	Hamamatsu R7081_20 10”	2	0.132
double ANTARES	Hamamatsu R7081_20 10”	6	0.264
MultiPMT cylinder	Photonis XP53X2 3”	36	0.140
MultiPMT spheres	Photonis XP53X2 3”	36	0.140
	Photonis XP53X2 3”	42	0.164
	Photonis XP53X2 3”	21	0.082
single 20”PM	Hamamatsu 20”	1	0.175
ANTARES 20”PM	Hamamatsu 20”	3	0.350

Table 12.1: Summary of storey types.

different storey types are summarised in table 12.1.

With similar PM properties and neglecting the background noise, detector models with a larger photocathode area are generally better. A detector with a large photocathode area collects more signal photons, but also more background photons, resulting in a relative degradation of performance for triggered and reconstructed neutrino events (see section 6.3 for selection criteria).

Storeys with only one PM per storey can not use local coincidences and have to rely on hits with large amplitudes to exclude noise hits in the prefit procedure. This results in poor performance at the reconstructed level. Assuming that a future reconstruction algorithm will use similar methods for the reduction of the background noise, this is a significant disadvantage.

Storeys composed of a larger number of smaller PMs appear to provide a feasible alternative to the common large hemispherical PMs. Their increased quantum efficiency helps to enhance the efficiency of a given detector lazout. A simplification of the readout process does not significantly deteriorate the performance of these MultiPMT storeys. The better two-photon separation capability of the small PMs was not even accounted for in this work. The geometrical layout of the small PMs within the storey has no effect on the detector performance.

Large hemispherical PMs (20”) increase the effective area especially at low energies (< 1-10 TeV). At higher energies the increase in performance is relatively small. The feasibility of their use greatly depends on the cost relative to the other structures studied. Assuming that the price for a photomultiplier scales with photocathode area, and considering the fact that the larger structures (larger glass spheres) required will also increase the cost, large hemispherical PMTs may not be the optimal solution.

The example of the *candidate* detector equipped with the 21 PMT sphere storey shows that a larger number of storeys per string can be an advantage for the reconstruction. The coverage of the instrumented volume with sensors is improved. As requiring six storeys to be hit, seems to be a reasonable condition for the reconstructability of a muon event, a larger number of storeys provides a significant advantage.

detector model	#strings	#storeys	instrumented volume (km^3)	total PMT area (m^2)
cuboid				
w single PM storey	484	4840	0.992	213
w double PM storey	484	4840	0.992	426
w ANTARES storey	484	4840	0.992	639
w double ANTARES storey	484	4840	0.992	1278
w MultiPMT cylinder	484	4840	0.992	680
w 36 PM MultiPMT sphere	484	4840	0.992	680
w 42 PM MultiPMT sphere	484	4840	0.992	793
w 21 PM MultiPMT sphere	484	4840	0.992	396
w single 20"PM storey	484	4840	0.992	847
w ANTARES 20"PM storey	484	4840	0.992	2541
candidate cuboid				
w single PM storey	484	14520	1.065	639
w double PM storey	484	7260	1.029	639
w double ANTARES storey	484	2420	0.992	639
w 42 PM MultiPMT sphere	484	3872	0.978	634
w 21 PM MultiPMT sphere	484	7744	0.984	634
ring1	312	4992	1.004	701
ring2	312	4992	1.004	701
ring3	312	4992	1.004	701
ring4	156	4992	0.999	701
cluster1	96	4992	1.007	701
cluster2	96	4992	1.007	701
cluster3	96	4992	1.025	701
densering	145	4930	1.007	692
thinring	145	2320	1.007	326
hollow cuboid	288	4896	1.008	687
cuboid2	324	4860	1.009	682
cuboid3	225	4950	1.008	695
cuboid4	144	4896	1.006	687
ring1a	416	6656	2.000	935
ring1b	624	9984	2.000	1388
double hollow cuboid	576	9792	2.016	1375
largering	291	4947	2.000	695
spread ring	312	4992	2.000	701
spread cuboid	484	4840	2.004	680
conclusion detector	225	8100	1.022	663

Table 12.2: Summary of detector configurations studied.

12.2.2 Geometry

The muon range in water increases above one kilometer at energies of about 1 TeV. Muons with energies above this threshold are most probably produced outside the instrumented detector volume and will enter the detector from outside. In order to exploit this effect, ring geometries have been simulated. The expected advantage is the reduction of the number of structures without significant loss of performance. The simulation shows that the low-energy efficiency is increased by the denser storey spacing, but the performance at higher energies is slightly decreased compared to homogeneous layouts. A reduction of the width of the instrumented ring further deteriorates the efficiency. Although the rings provide the expected advantage, a modification of the homogeneous cuboid is more efficient in this respect. By reducing the number of strings, and simultaneously increasing the number of storeys per string, the number of structures can be significantly reduced. Such a 'diluted' cuboid with only 144 strings provides similar effective areas as the standard cuboid with 484 strings.

Clustered geometries can be used to increase the performance at energies below 1 TeV. The low-energy efficiency is drastically increased, but at the cost of a significant loss of efficiency above 1 TeV. Such a detector configuration is more sensitive to neutrinos from annihilations of dark matter, but less sensitive to neutrinos from individual cosmic neutrino sources and the diffuse flux.

Also, several detector models with volumes of two cubic kilometers were simulated. If the photocathode area remains constant, the result was a loss of performance at lower energies(smaller than about 1 TeV) and a gain in performance at higher energies (larger than about 1 TeV). The efficiency at low energies depends on the instrumented volume and the density of the instrumentation, while at high energies it depends on the cross section area of the detector. Increasing the volume increases the area, but decreases the instrumentation density. More storeys therefore greatly increase the low-energy performance of these large detectors. It should be noted that at high energies the effective area is not doubled compared to the *candidate* detectors. The reason is, that the average cross section area defining the high energy efficiency is not twice as large.

An IceCube-like detector was simulated and compared with IceCube comparable versions of the geometries, studied in this work. The results prove that their general behaviour is also valid for the slightly different IceCube string and storey layout.

12.2.3 General studies

In addition to the simulation of KM3NeT *candidate* detectors, several additional simulation studies were conducted. The first was a comparison of some of the considered KM3NeT detector configurations with the results for the ANTARES detector. For this comparison the same simulation code and strategy as used for the *candidates* was used for the ANTARES detector. The resulting effective areas and angular resolution yield the expected relations, thus providing a sanity check for the results.

Furthermore the behaviour of the reconstruction algorithm used was analysed in order to investigate a possible reconstruction induced bias on the results. By comparing the reconstruction efficiencies and the causes of a failure of the reconstruction for different *can-*

didate detectors and the ANTARES layout, it was found that the reconstruction strategy is slightly biased toward ANTARES like structures. Detectors with ANTARES storeys (or at least ANTARES storey geometries) as well as detectors with similar string layouts yield slightly but still significantly better reconstruction results. It was shown that the prefit used in the reconstruction has a large impact on the quality of the reconstruction. By improving the prefit better results for the *candidate* detectors can most probably be achieved.

The influence of the string and storey distances in three different geometries has been studied. For this different detector models with increased distances were produced and simulated. An increase of the string and storey distances degrades the low-energy performance, while a decrease of these distance improves it. The reason is the shorter range (at energies below 100 GeV) and/or the low photon yield of low-energy muons. At increased distances and hence larger instrumented volume the high energy performance improves. The energy, where the degradation at lower energies changes to an increase also depends on the distances of strings and storeys (between 1 and 10 TeV).

12.3 Sensitivities

In addition to the effective areas and the angular resolutions, the physics potential was estimated using benchmark fluxes (see section 6.5). Using the Feldman-Cousins [109] method and the input from the simulation, including conventional and prompt atmospheric neutrino fluxes, upper limits on the diffuse neutrino flux were derived for some example KM3NeT *candidate* configurations. As for the diffuse flux the high-energy part of the neutrino spectrum is of interest, most of the detectors yield similar upper limits. Only those that are significantly worse at higher energies differ significantly. All of the calculated limits are well below the cosmic neutrino upper bound proposed by Waxman and Bahcall [8]. A comparison with the published diffuse flux upper limit of the IceCube experiment reveals that the best KM3NeT candidate detectors are a factor of two to three better than IceCube (also depending on selection). However, it should be noted that no energy reconstruction was applied in this work and no cuts to reduce the atmospheric muon background were included, resulting in a less than fair comparison.

In order to investigate the performance in searches for individual sources of cosmic neutrinos, upper limits for a generic point-like source were calculated depending on source declination. The conventional atmospheric neutrino flux was used for background simulation, while the prompt flux was neglected as it contributes significantly only at higher energies. The visibility of the source as a function of its declination, as well as the zenith angle dependence of the detector effective area and the atmospheric neutrino background were accounted for. At declinations, where the visibility is high, the resulting limits are slightly better for the best candidate detectors than for IceCube. Again it should be noted that true Monte Carlo energies were used for this study. In a further study, the code used in [3] was used to estimate event rates for neutrinos from the SNR RX-J1713-3946. For most detectors this yielded similar results of one to three neutrinos per year from this source, which would allow a detection after some years of observation. Only detectors having a smaller effective area in the TeV energy range (which is most relevant for the search for individual sources except gamma-ray-bursts), produce significantly less events.

The potential for the detection of neutrinos from WIMP annihilations in the Sun was analysed by calculating integrated event rates (events above energy threshold) for the benchmark fluxes. The results strongly depend on the events selection criteria and the flux used. In the most pessimistic case for the supersymmetric model used (MSSM), the case of the Bulk flux, the best detectors (low-energy optimised detectors) yield between 12 (18) events for reconstructed events and about 200 events for a minimal selection criterion. All of these events have energies below 100 GeV, where energy reconstruction is extremely difficult. In the most optimistic case the *candidates* yield between 700 (about 1000) events in the reconstructed case and almost 10000 events in the minimal case. The *candidates* with homogeneous instrumentation are generally less efficient at these low energies, due to the larger storey distances. The extremely inhomogeneous geometries, like the *cluster1* provide the best results for dark matter searches. Ultimately the probability of a detection depends on the true neutrino flux from the annihilations of dark matter. Nonetheless the *candidate* detectors might be able to constrain dark matter models significantly, although detailed studies (including energy reconstruction) are necessary to prove this.

12.4 Outlook

This thesis provides a detailed comparison of different potential KM3NeT detector configurations together with a preliminary estimate of their physics potential. However, as this study is based on the ANTARES simulation code, it is very important to simulate the proposed detector configurations with different software tools in order to corroborate the results. After a pre-decision on the detector layout, a dedicated reconstruction algorithm, including energy reconstruction, will have to be developed. Furthermore, the atmospheric muon background has to be included in the analysis, as well as the influence of the site parameters. Additionally, a realistic cost model has to be introduced in order to compare the physics potential based on actual costs of the detector layouts.

Only muon neutrinos were simulated in this work. For a complete design study also the performance of the candidate layouts for electromagnetic and hadronic showers has to be studied.

All this will allow to achieve a more realistic analysis of the absolute physics potential of the future KM3NeT neutrino telescope.

Appendix A

Detector summary

In this appendix, all of the detectors that have been simulated for this work are listed together with their properties.

cuboid detector

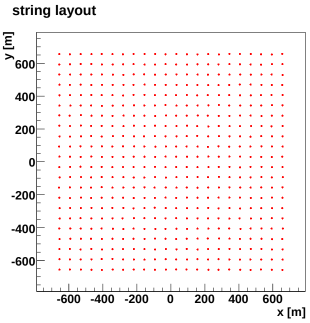

various
storeys

484 strings
string distance 63 m
10 storeys per string
total number of storeys 4840
storey distance 63 m
instrumented volume 0.992 km^3
total PMT area depends on storey type

candidate cuboid with single OM storeys

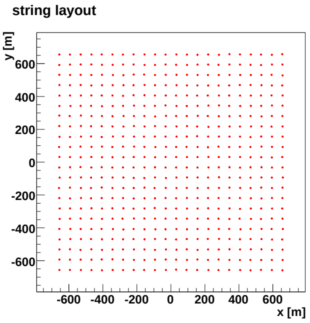

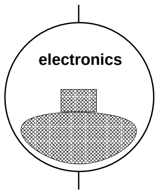

484 strings
string distance 63 m
30 storeys per string
total number of storeys 14520
storey distance 21 m
instrumented volume 1.065 km^3
total PMT area 639 m^2

candidate cuboid with double OM storeys

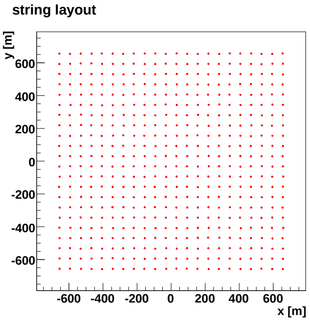

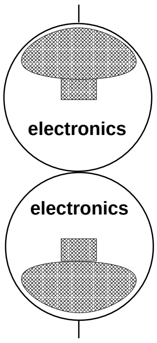

484 strings
string distance 63 m
20 storeys per string
total number of storeys 7260
storey distance 31.5 m
instrumented volume 1.029 km^3
total PMT area 639 m^2

candidate cuboid with twin ANTARES storeys

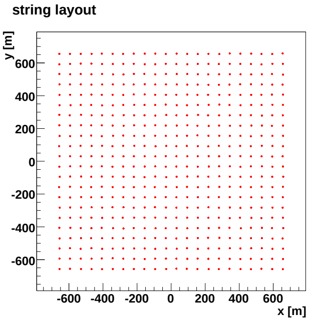

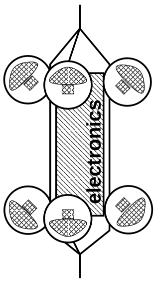

484 strings
string distance 63 m
5 storeys per string
total number of storeys 2420
storey distance 126 m
instrumented volume 0.992 km^3
total PMT area 639 m^2

candidate cuboid with 42 PMT sphere storey

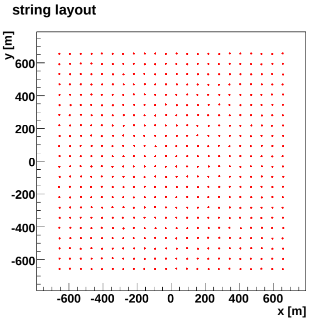

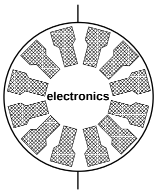

484 strings
string distance 63 m
8 storeys per string
total number of storeys 3872
storey distance 82 m
instrumented volume 0.978 km^3
total PMT area 634 m^2

candidate cuboid with 21 PMT sphere storey

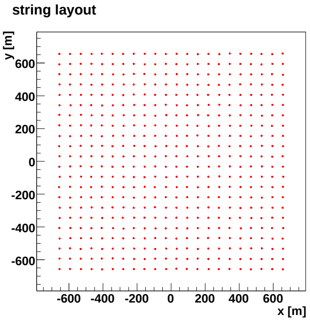

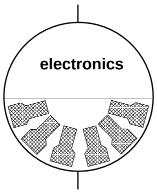

484 strings
string distance 63 m
16 storeys per string
total number of storeys 7744
storey distance 38.5 m
instrumented volume 0.984 km^3
total PMT area 634 m^2

ring1

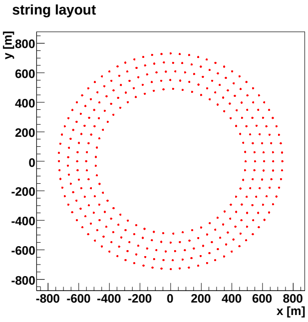

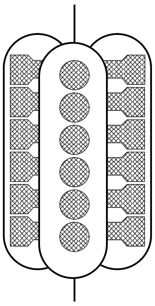

312 strings
string distance (within ring) 60 m
16 storeys per string
total number of storeys 4992
storey distance 40 m
instrumented volume 1.004 km^3
total PMT area 701 m^2

ring2

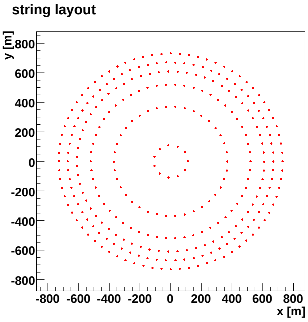

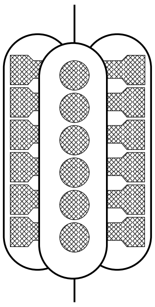

312 strings
string distance (within ring) 60 m
16 storeys per string
total number of storeys 4992
storey distance 40 m
instrumented volume 1.004 km^3
total PMT area 701 m^2

ring3

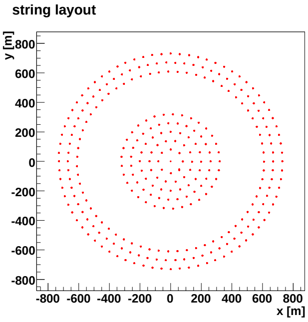

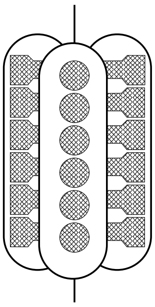

312 strings
string distance (within ring) 60 m
16 storeys per string
total number of storeys 4992
storey distance 40 m
instrumented volume 1.004 km^3
total PMT area 701 m^2

ring4

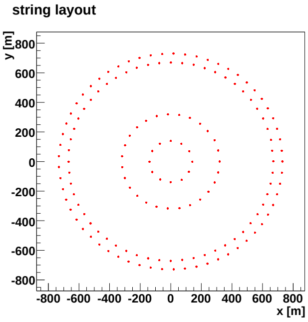

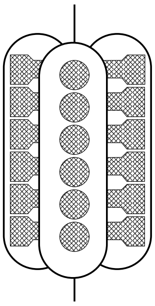

156 strings
string distance (within ring) 75 m
16 storeys per string
total number of storeys 4992
storey distance 19.25 m
instrumented volume 0.999 km^3
total PMT area 701 m^2

cluster1

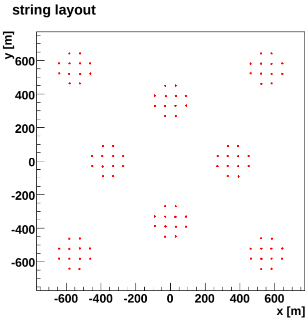

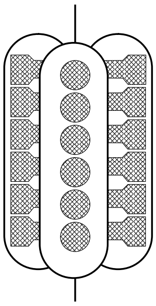

96 strings
string distance (within cluster) 60 m
52 storeys per string
total number of storeys 4992
storey distance 12 m
instrumented volume 1.007 km^3
total PMT area 701 m^2

cluster2

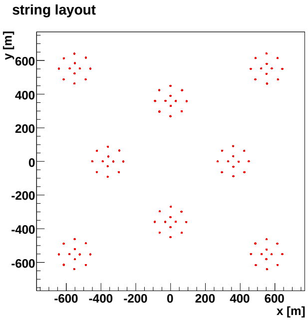

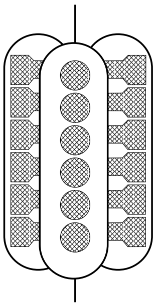

96 strings
string distance (within cluster) 60 m
52 storeys per string
total number of storeys 4992
storey distance 12 m
instrumented volume 1.007 km^3
total PMT area 701 m^2

cluster3

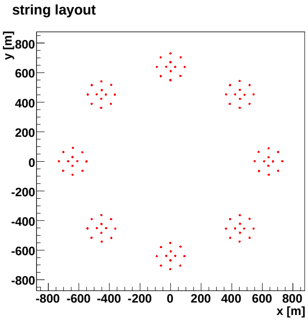

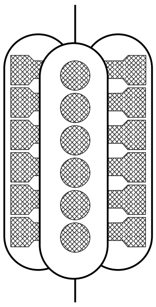

96 strings
string distance (within cluster) 60 m
52 storeys per string
total number of storeys 4992
storey distance 12 m
instrumented volume 1.025 km^3
total PMT area 701 m^2

densering

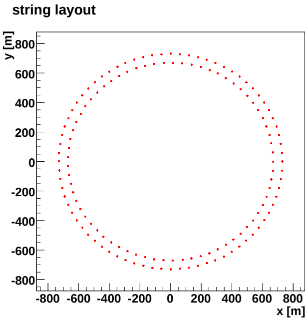

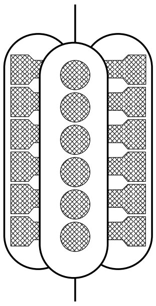

145 strings
string distance (within ring) 60 m
34 storeys per string
total number of storeys 4930
storey distance 18 m
instrumented volume 1.007 km^3
total PMT area 692 m^2

thinring

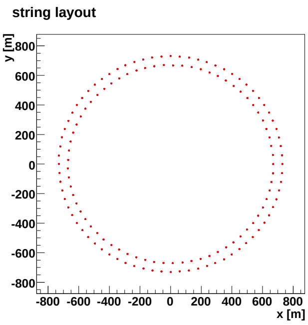

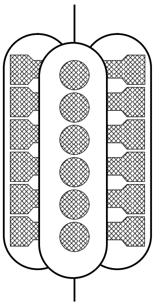

145 strings
string distance (within ring) 60 m
16 storeys per string
total number of storeys 2320
storey distance 40 m
instrumented volume 1.007 km^3
total PMT area 326 m^2

hollow cuboid

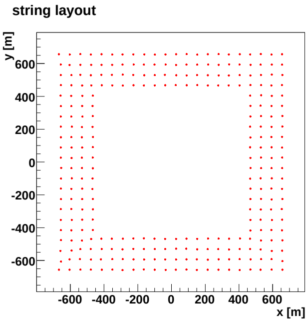

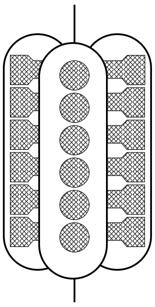

288 strings
string distance 63 m
17 storeys per string
total number of storeys 4896
storey distance 36 m
instrumented volume 1.008 km^3
total PMT area 687 m^2

cuboid2

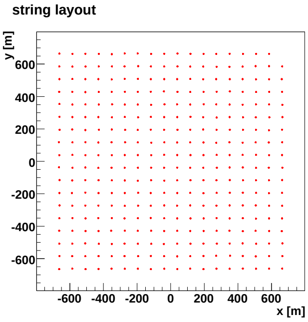

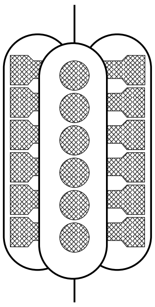

324 strings
string distance 78 m
15 storeys per string
total number of storeys 4860
storey distance 41 m
instrumented volume 1.009 km^3
total PMT area 682 m^2

cuboid3

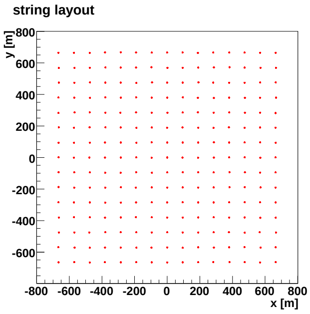

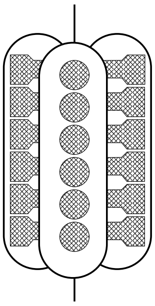

225 strings
string distance 95 m
21 storeys per string
total number of storeys 4950
storey distance 28.5 m
instrumented volume 1.008 km^3
total PMT area 695 m^2

cuboid4

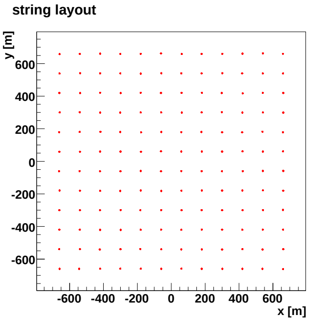

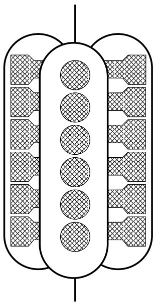

144 strings
string distance 120 m
34 storeys per string
total number of storeys 4896
storey distance 17.5 m
instrumented volume 1.006 km^3
total PMT area 687 m^2

ring1a

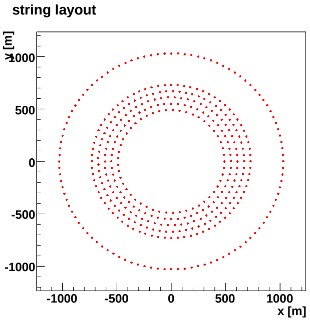

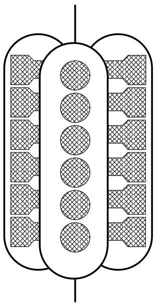

416 strings
string distance (within ring) 60 m
16 storeys per string
total number of storeys 6656
storey distance 40 m
instrumented volume 2.000 km^3
total PMT area 935 m^2

ring1b

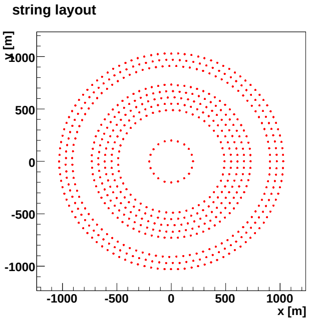

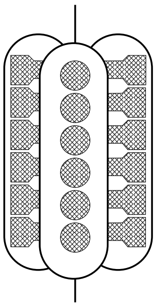

624 strings
string distance (within ring) 60 m
16 storeys per string
total number of storeys 9984
storey distance 40 m
instrumented volume 2.000 km^3
total PMT area 1388 m^2

double hollow cuboid

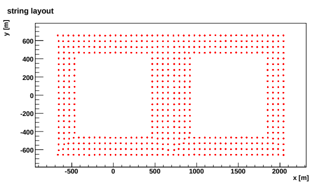

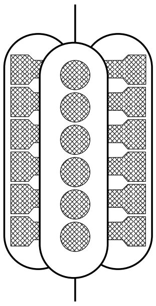

576 strings
string distance 63 m
17 storeys per string
total number of storeys 9792
storey distance 36 m
instrumented volume 2.016 km^3
total PMT area 1357 m^2

largering

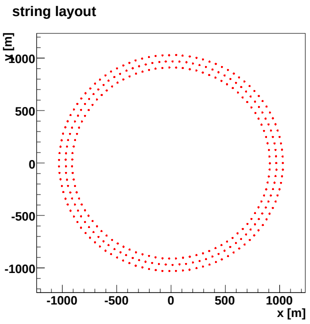

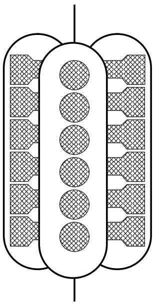

291 strings
string distance (within ring) 60 m
16 storeys per string
total number of storeys 4947
storey distance 37.5 m
instrumented volume 2.000 km^3
total PMT area 695 m^2

spread ring

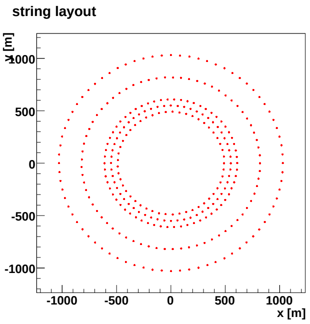

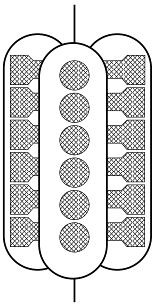

312 strings
string distance (within ring) 60 m
16 storeys per string
total number of storeys 4992
storey distance 40 m
instrumented volume 2.000 km^3
total PMT area 701 m^2

spread cuboid

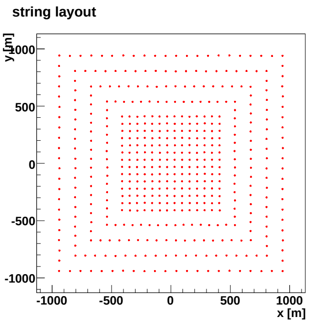

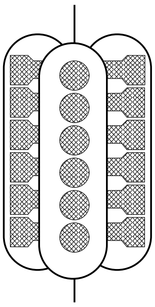

484 strings
string distance 63 m
10 storeys per string
total number of storeys 4840
storey distance 63 m
instrumented volume 2.000 km^3
total PMT area 680 m^2

Conclusion detector

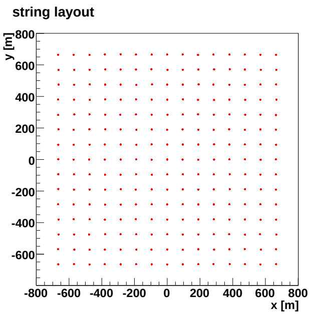

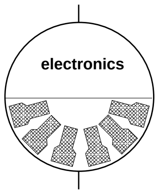

225 strings
string distance 95 m
36 storeys per string
total number of storeys 8100
storey distance 16.5 m
instrumented volume 1.022 km^3
total PMT area 663 m^2

Bibliography

[1] Barr, G. and Gaisser, T. K. and Stanev, T., Phys. Rev. **D39**, 3532 (1989).

[2] Costa, C.G.S., Astropart. Phys. **16**, 193 (2001).

[3] Kappes, Alexander and Hinton, Jim and Stegmann, Christian and Aharonian, Felix A. (2006).

[4] H. Motz, *Berechnung von Neutrinoflüssen und erwarteten Ereignisraten in ANTARES aus Neutrino-Annihilationen in der Sonne.* Ph.D. Thesis, University of Erlangen-Nürnberg, 2006.

[5] Ahrens, J. and others, Astropart. Phys. **20**, 507 (2004).

[6] De Dios Zornoza, J., ANTARES-Phys-2004-004 (2004).

[7] Bernardini, E., Nucl. Instrum. Meth. **A567**, 418 (2006).

[8] Waxman, Eli and Bahcall, John N., Phys. Rev. **D59**, 023002 (1999).

[9] H.Hanada and others, Nucl. Inst. Meth. **A 408** (1998).

[10] Aynutdinov, V. and others (2005).

[11] Silvestri, A., Int. J. Mod. Phys. **A20**, 3096 (2005).

[12] Spurio, Maurizio (2006).

[13] Aggouras, G. and others, Nucl. Phys. Proc. Suppl. **151**, 279 (2006).

[14] Achterberg, A. and others (2006).

[15] Distefano, C. (2006).

[16] European Union Sixth Framework Programme, *http://cordis.europa.eu/fp6/*, 2006.

[17] Horandel, Jorg R., Astropart. Phys. **21**, 241 (2004).

[18] Horandel, Jorg R. (2005).

[19] K. Greisen, Phys. Rev. Lett. **16**, 748 (1966).

[20] G. T. Zatsepin and V. A. Kuz'min, JETP Lett. **4**, 78 (1966).

[21] Antoni, T. and others, Nucl. Instrum. Meth. **A513**, 490 (2003).

[22] Teshima, M. Fujiyoshida 1988, Proceedings, Elementary-particle picture of the universe 193-204. (see Conference Index).

[23] T. Abu-Zayyad and others, Proc. 26th ICRC Salt Lake City, USA **3**, 264 (1999).

[24] Springer, R. W., Nucl. Phys. Proc. Suppl. **138**, 307 (2005).

[25] J.W. Cronin and others, Proc. 27th ICRC Hamburg Germany, p. 699 (2001).

[26] J.A. Hinton and others, New Astron.Rev. **48**, 331 (2004).

[27] Albert i Fort, J. and others (2005).

[28] *http://www.mpi-hd.mpg.de/hfm/HESS/*, 2006.

[29] F. A. Aharonian and others, to be published in Astronomy and Astrophysics (2005).

[30] W. I. Axford, F. Leer and G. Skadron, Proc. 15th ICRC, Plovdiv, Bulgaria **11**, 132 (1977).

[31] A. R. Bell, Mon. Not. R. Astr. Soc. **182**, 147 (1978).

[32] R. D. Blandford and J. P. Ostriker, Astrophys. J. 2 **228**, L29 (1978).

[33] G. F. Krymsky, Sov. Phys. Dokl. (translation) **22**, 327 (1977).

[34] J. G. Learned and K. Mannheim, Ann.Rev.Nucl.Part.Sci. **50**, 679 (2000).

[35] Aharonian, F. and others (2006).

[36] Aharonian, F. and others, Astron. Astrophys. **448**, L43 (2006).

[37] Bednarek, W., Astron. Astrophys. **407**, 1 (2003).

[38] C. Distefano and others, Astrophys.J. **575**, 378 (2002).

[39] A. Balenzano, F. Burgio and T. Montaruli, ANTARES-Phys-2003-006 (2003).

[40] Stecker, F. W. and Done, C. and Salamon, M. H. and Sommers, P., Phys. Rev. Lett. **66**, 2697 (1991).

[41] Szabo, A. P. and Protheroe, R. J., Astropart. Phys. **2**, 375 (1994).

[42] Waxman, Eli and Bahcall, John N., Phys. Rev. Lett. **78**, 2292 (1997).

[43] Bennett, D. P. and others (1995).

[44] Spergel, D. N. and others, Astrophys. J. Suppl. **148**, 175 (2003).

[45] M. Chikawa and others, Astrophys. J. **571**, L117 (2002).

[46] M. Ave and others, Phys. Rev. D **65**, 063007 (2002).

[47] S. Eidelman and others, Physics Letters B **592**, 1 (2004).

[48] The Homestake Collaboration, B. T. Cleveland and others, Nucl. Phys. B Proc. Suppl. **38**, 47 (1995).

[49] Super-Kamiokande Collaboration, S. Fukuda and others, Phys. Rev. Lett. **86**, 5651 (2001).

[50] Cristina Carloganu, ANTARES-PHYS-1998-013 (1998).

[51] F. Bernard, *Caractérisation des performances d'un télescope sous-marin à neutrinos pour la détection de cascades contenues dans le cadre du projet ANTARES.* Ph.D. Thesis, University of Marseille, 2000. CPPM-T-2000-02.

[52] Gandhi, Raj and Quigg, Chris and Reno, Mary Hall and Sarcevic, Ina, Phys. Rev. **D58**, 093009 (1998).

[53] J. D. Jackson, *Classical Electrodynamics.* John Wiley & Sons, Inc., 1998.

[54] B. Hartmann, *Reconstruction of Neutrino-Induced Hadronic and Electromagnetic showers with the ANTARES experiment.* Ph.D. Thesis, University of Erlangen-Nürnberg, 2006. FAU-PI1-DISS-06-001.

[55] Escoffier, S. and Cussatlegras, A.S., ANTARES-Phys-2006-007 (2006).

[56] Riccobene, G. (2003). Prepared for VLVnT Workshop on Technical Aspects of a Very Large Volume Neutrino Telescope in the Mediterrenean Sea, Amsterdam, The Netherlands, 5-8 Oct 2003.

[57] Anassontzis, E. G. and others, Nucl. Instrum. Meth. **A479**, 439 (2002).

[58] Aslanides, E. and others (1999).

[59] Cecchini, S. and Korolkova, E. and Margiotta, Annarita and Thompson, L. (2005).

[60] Gandhi, Raj and Quigg, Chris and Reno, Mary Hall and Sarcevic, Ina, Astropart. Phys. **5**, 81 (1996).

[61] Volkova, L. V., Sov. J. Nucl. Phys. **31**, 784 (1980).

[62] Gaisser, T. K. and Stanev, T. Contributed to the 24th International Cosmic Rays Conference (ICRC 95) 28 Aug - 8 Sep 1995, Rome, Italy.

[63] Honda, M. and Kajita, T. and Kasahara, K. and Midorikawa, S., Phys. Rev. **D52**, 4985 (1995).

[64] Battistoni, G. and Ferrari, A. and Montaruli, T. and Sala, P. R. (2003).

[65] Thunmana, M. and Ingelmana,G. and Gondolob, P., Astropart. Phys. **5**, 309 (1996).

[66] Aguilar, J. A. and others, Astropart. Phys. **23**, 131 (2005).

[67] G.A. Askariyan, Sov. Phys. JETP **14**, 441 (1962).

[68] Adams, Jennifer A. and others, AIP Conf. Proc. **689**, 3 (2003).

[69] Miocinovic, Predrag and others, ECONF **C041213**, 2516 (2004).

[70] *http://www.euso-mission.org*, 2006.

[71] G.A. Askariyan, Nucl. Instr. Meth. **164**, 267 (1979).

[72] Graf, Kay and others (2005).

[73] Sulak, L. and others, Nucl. Instr. Meth. **161**, 203 (1979).

[74] Albul, V. I. and others, Instrum. Exp. Tech. **44**, 327 (2001).

[75] Hunter , S.D. and others, Acoustical Society of America Journal **69**, 1557 (1981).

[76] Kurahashi, N. and others, Int. J. Mod. Phys. **A21S1**, 217 (2006).

[77] *http://pppa.group.shef.ac.uk/acorne.php*, 2007.

[78] T. Karg, *Detection of ultra high energy neutrinos with an underwater very large volume array of acoustic sensors: A simulation study.* Ph.D. Thesis, University of Erlangen-Nürnberg, 2006. FAU-PI4-DISS-06-002.

[79] Wischnewski, R., Talk presented at 2nd workshop on Very Large Volume Neutrino Telescopes, Catania, Italy (2005).

[80] *http://www.amanda.uci.edu*, 2006.

[81] Achterberg, A. (0500).

[82] Achterberg, A. and others, Phys. Rev. **D75**, 102001 (2007).

[83] *http://www.nestor.org.gr*, 2006.

[84] Aggouras, G. and others, Astropart. Phys. **23**, 377 (2005).

[85] *http://antares.in2p3.fr*, 2007.

[86] Karle, A., Talk presented at 2nd workshop on Very Large Volume Neutrino Telescopes, Catania, Italy (2005).

[87] Migneco, E., Talk presented at 2nd workshop on Very Large Volume Neutrino Telescopes, Catania, Italy (2005).

[88] Katz, Ulrich F. (2006).

[89] *http://www.km3net.org*, 2006.

[90] F. Cassol, ANTARES-SOFT-1999-007 (1999).

[91] F. Bailey, ANTARES-SOFT-1999-010 (1999).

[92] G. Ingelmann, A. Edin and J. Rathsman, Comput. Phys. Commun. **101**, 108 (1997).

[93] G. Barr, *The seperation of signal and background in a nucleon deacy experiment.* Ph.D. Thesis, University of Oxford, 1987.

[94] Antonioli, P. and others, Astropart. Phys. **7**, 357 (1997).

[95] Sokalski, I. A. and Bugaev, Edgar V. and Klimushin, Sergey I., Phys. Rev. **D64**, 074015 (2001).

[96] P. Lipari and T. Stanev, Phys. Rev. **D44**, 3543 (1991).

[97] S. Navas and L. Thompson, ANTARES-SOFT-1999-011 (1999).

[98] *GEANT Detector description and simulation tool*, 2006. Http://wwwinfo.cern.ch/asd/geant.

[99] *Geasim full detector simulation and tracking*, 2000. Http://antares.in2p3.fr/internal/software/geasim.html.

[100] E. Carmona and J.J. Hernandez, ANTARES-SOFT-2000-011 (1999).

[101] A. Heijboer, ANTARES-SOFT-2002-002 (2002).

[102] A. Heijboer, *Track reconstruction and point source searches with ANTARES.* Ph.D. Thesis, University of Amsterdam, 1987.

[103] D. Zaborov, ANTARES-SOFT-2002-008 (2002).

[104] D. Zaborov, ANTARES-SOFT-2004-004 (2004).

[105] Zaborov, D. (2003). Prepared for VLVnT Workshop on Technical Aspects of a Very Large Volume Neutrino Telescope in the Mediterrenean Sea, Amsterdam, The Netherlands, 5-8 Oct 2003.

[106] D.Bailey, ANTARES-SOFT-2001-007 (2001).

[107] D.Bailey, ANTARES-SOFT-2004-004 (2004).

[108] A. Dziewonski, *The encyclopedia of solid earth geophysics*, in *Earth Structure, Global*, ed. D. E. James, p. 331. Van Nostrand Reinhold, New York, 1989. As cited in [60].

[109] Feldman, Gary J. and Cousins, Robert D., Phys. Rev. **D57**, 3873 (1998).

[110] Agrawal, Vivek and Gaisser, T. K. and Lipari, Paolo and Stanev, Todor, Phys. Rev. **D53**, 1314 (1996).

[111] Naumov, Vadim A. (2002).

[112] Bahcall, John N. and Waxman, Eli, Phys. Rev. **D64**, 023002 (2001).

[113] Mannheim, Karl and Protheroe, R. J. and Rachen, Jorg P., Phys. Rev. **D63**, 023003 (2001).

[114] Sigl, Gunter and Lee, Sangjin and Bhattacharjee, Pijushpani and Yoshida, Shigeru, Phys. Rev. **D59**, 043504 (1999).

[115] Cirelli, Marco and others, Nucl. Phys. **B727**, 99 (2005).

[116] Aguilar, J. A. and others, Astropart. Phys. **23**, 131 (2005).

[117] Palanque-Delabrouille, N., ANTARES-SITE-2000-004 (2001).

[118] Hamamatsu Photonics K.K., *http://www.hamamatsu.com*, 2006.

[119] Kooijman, P., Talk presented at 2nd workshop on Very Large Volume Neutrino Telescopes, Catania, Italy (2005).

[120] Kooijman, P., Nucl. Instrum. Meth. A **567**, 508 (2006).

[121] Photonis imaging sensors, *http://www.photonis.com*, 2006.

[122] Flyckt, E. (2003). Prepared for VLVnT Workshop on Technical Aspects of a Very Large Volume Neutrino Telescope in the Mediterrenean Sea, Amsterdam, The Netherlands, 5-8 Oct 2003.

[123] Hamamatsu Photonics K.K., *http://www.hamamatsu.com*, 2006.

List of Tables

List of Figures

Danksagung

Mein Dank gilt all denen, die mich bei der Erstellung dieser Arbeit unterstützt haben.

Allen voran mein Betreuer Prof. Dr. Uli Katz, der mir die Möglichkeit gab an einem so interessanten Forschungsprojekt wie KM3NeT mitzuarbeiten. Viel guter Rat und nicht zuletzt eine gehörige Menge Motivation haben mir oft weitergeholfen.

Besonderer Dank gebührt weiterhin Dr. Alex Kappes, der mir während meiner Forschungsarbeit sehr oft sehr nützliche Ratschläge und Hinweise lieferte und schliesslich die fertige Arbeit ausserordentlich gewissenhaft korrekturgelesen hat (in seiner Freizeit!).

Furthermore, i would like to thank Dr. Rezo Shanidze, for a countless number of fruitful discussions about the topic and other things, as well as for being the nicest colleague imaginable.

I would also like to thank Prof. Dr. Els DeWolf for providing the 'Zweitgutachten' for my thesis.

Weiterhin danke ich den Kollegen der Erlanger ANTARES- und KM3NeT-Gruppen für ein angenehmes Arbeitsklima und all die kleinen Hilfen die sich über 3 Jahre so ansammeln.

Further thanks to the colleagues of the ANTARES and KM3NeT collaborations i have met during my time with these experiments for the fruitful atmosphere.

Zu guter letzt möchte ich meiner Lebensgefährtin Stefanie Scholz danken, die immer für mich da war (und ist).